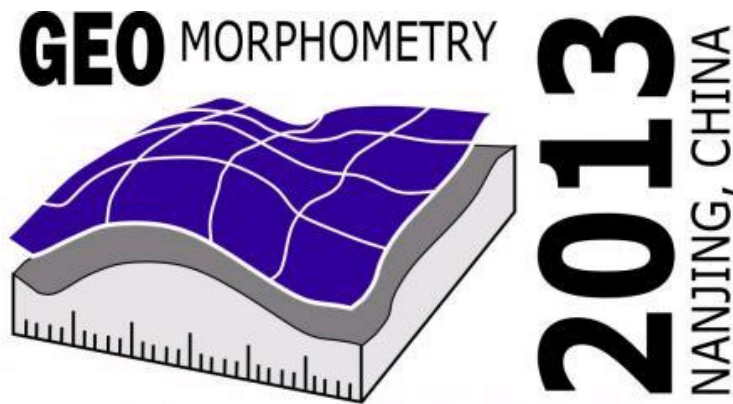


PROCEEDINGS OF GEOMORPHOMETRY 2013

16 October 2013 – 20 October 2013



Guoan Tang - Qiming Zhou
Tomislav Hengl - Xunjun Liu - Fayuan Li
(Eds.)

Hosted by
School of Geography
Key Laboratory of Virtual Geographical Environment, MOE
Nanjing Normal University, China

<http://geomorphometry.org/2013>

Foreword

On behalf of the organizers we would like to extend a warm welcome to all participants of Geomorphometry 2013 in Nanjing. The Geomorphometry 2013 conference continues a series initiated by the Terrain Analysis and Digital Terrain Modeling conference hosted by Nanjing Normal University in November 2006.

Geomorphometry 2013 brings together researchers to present and discuss developments in the field of quantitative modeling and analysis of elevation data. Geomorphometry is the science of quantitative land-surface analysis and description at diverse spatial scales. It draws upon mathematical, statistical and image-processing techniques and interfaces with many disciplines including hydrology, geology, computational geometry, geomorphology, remote sensing, geographic information science and geography.

For the conference, a total of 63 extended abstracts, with authors from 15 countries were submitted for review by the programme committee. Of these, a total of 56 were accepted for presentation at the conference. We believe that the conference programme offers a rich and varied insight into the key themes in geomorphometry today, with a mix of leading researchers in the field presenting methodological advances and young researchers presenting high quality reviewed work to an international audience.

The conference has four keynote speakers and four invited speakers. They are Dr. Ian Evans, Michael Hutchinson, Chenghu Zhou, Peter Guth, Josef Strobl, Benjamin Bräutigam, Qinke Yang and Alexander Brenning. Thank them for their contributions.

The conference also hosted three workshops with very different themes, entitled *Free and Open Source Geomorphometry Software*, *Watershed modeling with r.stream (GRASS GIS toolbox)* and *RiverTools 4.0*. respectively, providing attendees with the opportunity to get their hands dirty figuratively at the computer screen, and literally in the field!

Finally, we would like to thank all of those who make events such as this a success. Our programme committee and scientific committee, who on time and carefully reviewed a large number of papers, our keynote speakers, invited speakers, the workshop organizers, and all those who helped in the local organization, as well as the Nanjing Normal University for providing the conference facilities. Finally, and most importantly, we would like to thank the conference participants – without your work and participation there would be no conference. We hope your stay in Nanjing will be an enjoyable and stimulating one.

Guoan Tang, Qiming Zhou, Tomislav Hengl, Xuejun Liu and Fayuan Li

October 15th, 2013

Content

Oral presentation

Keynote speakers

- New Methods for Incorporating and Analysing Drainage Structure in Digital Elevation Models** 1

*Michael F. Hutchinson, Janet L. Stein, John C. Gallant,
Trevor I. Dowling*

- Land surface derivatives: history, calculation and further development** 5

Ian S. Evans

- The Giga Revolution in Geomorphometry: Gigabytes of RAM, Gigabyte-Sized Data Sets, and Gigabit Internet Access** 9

Peter L. Guth

Invite speaker

- The TanDEM-X Mission: Earth Observation in 3D** 13

*Benjamin Bräutigam, Manfred Zink, Irena Hajnsek,
Gerhard Krieger*

- Study on the Distributed Slope Length for Soil Erosion Prediction at Watershed Scale** 17

*Qinke Yang, Hongming Zhang, Chunmei Wang., Mudan Zhao,
Yongmei Liu, Lei Wang.*

- Leveraging geomorphometric data and statistical computing to gain complementary insights into complex Earth surface processes** 21

Alexander Brenning

Session 1 Creation of DEM

Content-based landscape retrieval using geomorphons	22
<i>Jaroslaw Jasiewicz, Pawel Netzel, Tomasz F. Stepinski</i>	
High-Res Digital Surface Modeling using Fixed-Wing UAV-based Photogrammetry	26
<i>Niels Anders, Rens Masselink, Saskia Keesstra, Juha Suomalainen</i>	
Effects of spatial resolution on slope and aspect derivation for regional-scale analysis	30
<i>Carlos H. Grohmann</i>	
Comparison of several methods for multi-scale DEM generalization in different landform areas	34
<i>Qiao Wan, Yumin Chen</i>	
An MPI-CUDA Implementation for The Compression of DEM	38
<i>Fei Zeng, Yumin Chen</i>	

Session 2 DEM attributes and objects : extraction & mapping

Land-surface segmentation to delineate elementary forms from Digital Elevation Models	42
<i>Lucian Drăguț, Ovidiu Csillik, Jozef Minár, Ian S. Evans</i>	
An automated method to extract typical karst landform entities from contour lines on topographic maps	46
<i>Fuyuan Liang, Yunyan Du</i>	
Application of supervised landform classification of 9-unit slope model for preliminary rockfall risk analysis in Gunung Kelir, Java	50
<i>Guruh Samodra, Junun Sartohadi, Guangqi Chen, Kiyonobu Kasama</i>	
Research on the classification of terrain texture from DEMs based on BP neural network	54
<i>Kai Liu, Guo'an Tang, Sheng Jiang</i>	

Research on Terrain Significance Index and Its Quantification Model based on Grid-DEMs	58
<i>Youfu Dong</i>	

Session 3 DEM attributes and objects: extraction & mapping

Mathematical Surfaces for which Specific and Total Contributing Area can be Computed: Testing Contributing Area Algorithms	61
<i>Scott D. Peckham</i>	

Simulating Loess Underlying Bedrock Paleotopographic strata for Landscape Evolution in the Loess Plateau Based on Digital Elevation Models	65
<i>Liyang Xiong, Guoan Tang</i>	

Terrain similarity characterizing approach based on two-dimensional continuous wavelet	69
<i>Shijiang Yan, Jie Wang</i>	

DEM based Extraction of LS factor: integrate channel networks and convergence flow	71
<i>Hongming Zhang, Qinke Yang, Wenting Han, Shangshang Yu, Shuqin Li, Xiaoyan Zhao</i>	

Research on 3D-Openness in urban area based on Urban Digital Elevation Model	75
<i>Wenhui He</i>	

Shoulder-line restricted loess slope segmentation	78
<i>Fayuan Li</i>	

Session 4 DEM analysis for and-cover modeling, hydrological modeling, soil-landscape modeling, environment modeling and other landform modeling

Land-Surface Segmentation as sampling framework for soil mapping	82
<i>Lucian Drăguț, Andrei Dornik</i>	
Development of gully and its controlling factors in the Loess Plateau of China using high spatial resolution imagery	86
<i>Zhen Li, Yan Zhang, Qingke Zhu, Yuanmei He, Wenjun Yao</i>	
From rills to gullies: how do we measure them?	89
<i>Sheng Li, Fangzhou Zheng, Zisheng Xing, Fanrui Meng, Rene Wackrow, David Lobb</i>	
Method for extraction continuous shoulder line in Loess watershed	92
<i>Yi Zhou, Jian Tian</i>	
Vegetation mapping using discrete-return and full-waveform airborne LiDAR data	95
<i>Dong Chen, Liqiang Zhang, Xiang Xu, Zhen Wang</i>	

Session 5 High performance computation and big data in terrain analysis; geo-computing and statistics analysis

Extraction and Analysis of Slope, Slope Length, and LS for National Soil Erosion Inventory in China	99
<i>Qinke Yang, Chunmei Wang, Minhang Guo, Mudan Zhao, Lei Wang, Yongmei Liu., Rui Li</i>	
Landscape planning of route-based visibility analysis	103
<i>Xiaodong Song, Gang Zhang</i>	
Extraction of drainage network from grid terrain datasets using parallel computing	107
<i>Ling Jiang, Guoan Tang, Kai Liu, Jianyi Yang</i>	
Mass elevation effect: concept and quantification	112
<i>Baiping Zhang</i>	

Session 6 Other fundamental problems of geomorphometry

- A Browser/Server-based Prototype of Heuristic Modelling Environment for Digital Terrain Analysis** 114
ChengZhi Qin, JingChao Jiang, LiJun Zhan, YanJun Lu, Axing Zhu
- Classification and formation environment of glacial valleys based on morphometric analyses** 118
Kosuke Naruse, Takashi Oguchi
- Floodplain delineation using cluster analysis of geomorphometric variables and class spectral statistics** 122
Mihai Niculiță
- Modeling hourly solar radiation over rugged terrains, based on DEM** 125
Jie Wang, Shijiang Yan, Yuhuan Cui
- Modeling of Topographic Spatial Structures Using Geo-statistical Method** 128
Chunmei Wang, Qinke Yang, David Jupp, Lei Wang, Rui Li.
- Monitoring topographical changes of island in the outlet of the Dongting Lake from 2000 to 2010 using time series of Landsat images** 131
Yi Yan, Fei Xiao
- Soil erosion and rill system evolution based on field observation in Kongshan Hill, South-west Jiangsu Province, China** 135
Zhenke Zhang, Yuexin Fu, Shengfen Li, Fayuan Li, Yingying Chen, Linghua Zhang
- Use of SRTM Data for a Quick Recognition of the Active Tectonic Signatures** 139
Biju John, K.S. Divyalakshmi, Yogendra Singh, C. Srinivasan
- Estimating shortwave radiation based on DEM and MODIS atmospheric products in rugged terrain** 143
Yanli Zhang, Xin Li

A Near-lossless Digital Watermarking Algorithm of DEM Based on DCT	145
<i>Hu Ding, Aili Liu</i>	
Implementation of a multiple flow algorithm into the dynamic ecosystem model LPJ-GUESS	147
<i>Jing Tang, Petter Pilesjö, Abdulghani Hasan</i>	
Snow distribution pattern and its influencing factors in a small watershed in Atlantic Canada	151
<i>Sheng Li, Yongbo Liu, Fangzhou Zheng, Zisheng Xing, Fanrui Meng, Karl Butle</i>	
Extraction of loess shoulder-line based on object-based image analysis	155
<i>Sheng Jiang</i>	
Scale-effect of Hypsometric Integral in Loess Plateau	159
<i>Shijie Zhu, Guoan Tang</i>	
The scale effect analysis of slope length based on DEM multi-scale representation	162
<i>Weiling Guo, Qinke Yang, Haijiang Wang, Rui Li</i>	

Poster

- Characterize the spatial patterns of perennial waterlogged cropland using the micro-geomorphology structure in Jiangnan Plain, middle reaches of the Yangtze River** 166
Fei Xiao, Yi Yan, Qi Feng, Xuan Ban.
- DEM Based Extraction and Analysis of Loess tableland** 170
Chiming Tong, Weiming Cheng, Wenjie Zhang
- Extend the Analysis window to improve the Geo-Computation** 176
Mingwei Zhao
- Transitional relation exploration for typical loess geomorphologic types based on slope spectrum** 180
Shangmin Zhao, Weiming Cheng
- Effectiveness of Mitigation Measures on Phosphorus Delivery** 184
Ting Zhang, Trevor Page, David M. Oliver
- Research on Terrain Landscape System based on Complex network** 188
Jian Tian
- Fractal analysis of the Loess Plateau in China** 192
Kamila Justyna Lis, Guoan Tang
- Generalizing Resolution-assignable DEM Based on Rational-dilation Wavelet Transform and Sampling Theory** 194
Haijiang Wang, Qinke Yang
- The elevation error of DEMs caused by grid size** 196
Lei Wang, Yongqing Long
- Construction of Information Capacity Model for Evaluation on the Land Surface Complexity using Remote Sensing Imagery** 199
Xuhong Wang, Zhe Zhang, Fei Li, Xiaoning Liu
- Vegetation Pattern Topographic Differentiation of YaoXian county, shaanxi province, China** 201
Xiaoyin Li

New Methods for Incorporating and Analysing Drainage Structure in Digital Elevation Models

Michael F.Hutchinson and Janet L. Stein
Fenner School of Environment and Society
Australian National University
Canberra, Australia
michael.hutchinson@anu.edu.au

John C. Gallant and Trevor I. Dowling
CSIRO Land and Water
G.P.O. Box 1666
Canberra, Australia
john.gallant@csiro.au

INTRODUCTION

Abstract—Digital elevation models (DEMs) play a key role in supporting fine scale representations of surface drainage structure. In fact, representing surface drainage structure has become a primary application of DEMs. It has directly driven the development of DEM interpolation techniques, such as the ANUDEM locally adaptive elevation gridding procedure (Hutchinson 1989; Hutchinson et al. 2009). High resolution remotely sensed elevation data sources, such as LIDAR and the Shuttle Radar Topography Mission (SRTM) DEM, have brought new challenges to DEM interpolation and applications. The inherent noise in remotely sensed elevation data needs to be appropriately smoothed to help remove drainage artifacts, especially in low relief landscapes. This smoothing also needs to be applied in conjunction with the enforcement of drainage structure using streamline data. The multi-grid structure of the ANUDEM algorithm is well suited to this task and has been upgraded to prevent corruption of stream heights by noisy elevation values. It has also been upgraded to accommodate the spatial complexity associated with high resolution streamline data. When incorporated onto a regular grid, these data can generate many spurious stream junctions and disjunctions that can significantly distort subsequent analysis of catchment structure. New procedures have been developed to make small shifts in the locations of gridded streamlines and streamline junctions to reduce the number of spurious coincident gridded streamline junctions while simultaneously maximizing the fidelity of the shifted gridded streamlines to the original data streamline network. New analytical methods for calculating specific catchment area from drainage enforced DEMs, an important DEM derivative for many hydro-ecological applications, have also been obtained (Gallant and Hutchinson 2011). Such methods are best understood by recognizing the vector field interpretation of specific catchment area.

Digital elevation models (DEMs), normally in the form of regular grids, play a central role in environmental modeling across a range of spatial scales [6]. A distinguishing feature for many of these applications, particularly those that operate at finer scale, is a primary requirement for information about terrain shape and drainage structure, rather than elevation. DEMs with connected drainage structure can be used to calculate hydrologically relevant topographic indices such as specific catchment area [2] and to support a wide range of hydro-ecological analyses [9,10]. The need for accurate representation drainage structure has led to the development of the ANUDEM elevation gridding procedure [4,7] where grid-based interpolation has been coupled with an automatic drainage enforcement algorithm to remove spurious depressions from the interpolated grid, together with a procedure to apply drainage structure in accordance with streamline data.

New remotely sensed elevation data sources, and the need for the systematic application of the catchments associated with streamline data to natural resource assessment, have led to two major upgrades to the ANUDEM procedure. These separately address the impacts of significant noise in dense remotely sensed elevation data and the impacts of spurious intersections in streamline data when incorporated into regular grids. Each of these upgrades is briefly described below.

The paper concludes with consideration of the calculation of specific catchment area from DEMs, a key terrain parameter for a wide range of hydro-ecological applications. It is shown that specific catchment area can be naturally interpreted as a two-dimensional vector field. This can simplify the theoretical derivation of the method recently obtained by Gallant and Hutchinson [2] and may offer further progress in the calculation and assessment of this terrain parameter.

NOISY REMOTELY SENSED ELEVATION DATA

Remotely sensed digital topographic data, from both airborne and spaceborne sensors, are an increasingly common source of fine scale digital elevation data. A major impetus for their use has been the goal of generating high resolution DEMs with global coverage. This has been achieved with the completion of the 3 second (90 m) DEM for the globe obtained from the Shuttle Radar Topography Mission [11]. These data have two generic limitations. The sensor normally cannot measure ground elevations underneath dense vegetation cover or underwater or under man-made structures, leading to significant errors, particularly in heavily vegetated areas. Secondly, all remotely sensed elevation data have significant random errors that depend on the inherent limitations of the observing instrument, as well as surface slope and roughness [3,11]. The product specification for the SRTM data was that 90% of the elevations had error within $\pm 16\text{m}$. These errors require appropriate filtering, without degrading shape and drainage structure, to maximize the utility of the data in environmental applications, particularly in areas with low relief or with significant surface cover. An additional feature of the errors associated with the SRTM data is that they are locally spatially correlated. This is due to the partially overlapping nature of the sensor footprint associated with each grid cell. The various impacts of these issues have been addressed, as described below.

Elevation data smoothing

The underlying interpolation algorithm of the ANUDEM program is described in [4,5,6]. It essentially fits a discretized thin plate smoothing spline to the data using a simple multigrid strategy to maximize computational efficiency. Elevation data are initially allocated to their corresponding grid points and the program then minimizes the sum of a user-specified roughness penalty and a weighted sum of squares of the residuals from the elevation data. The weighting of the residuals incorporates the natural discretization error associated with allocating data points to a regular grid and a user supplied estimate of the vertical standard error of the elevation data. The algorithm simultaneously respects local grid cell conditions associated with automated drainage enforcement, data streamlines, cliffs and lakes. The simultaneous application of data smoothing and these local grid cell conditions is a key factor in the quality of the resulting interpolated DEM.

For traditional elevation contour data sets, the vertical standard error of the data can be set to zero and then only the discretization error needs to be taken into account in the weighting of the data residuals. For remotely sensed elevation data, estimates of standard elevation are often available, although with mixed reliability. The latter can be calibrated within ANUDEM by experimenting with different levels of user

supplied vertical standard error. This has indicated, for example, that the $\pm 16\text{m}$ error specified for the SRTM data is an overestimate, as shown in [11], with experiments indicating that the standard error of the 1" data over Australia, after large errors due to vegetation cover are removed, is no more than around 2m.

An additional consideration for 1second resolution SRTM data is local correlation in the data errors for neighbouring grid cells. The multigrid algorithm within ANUDEM has played a role in detecting this local correlation, and in providing a simple method for taking it into account. Initial experiments assuming independent data errors yielded stable performance in the multigrid algorithm until the last and finest resolution was met. It can be shown that when elevation data values are averaged over larger grid cells, the cell to cell correlation in data error steadily diminishes until it becomes insignificant at the largest starting grid resolution for the multigrid interpolation procedure. It was found that by assuming a nearest cell to cell correlation of around 0.6, and by taking due account of this correlation in the data weighting applied at each grid resolution, stable behavior in the gridding process could be obtained. Effectively, the data smoothing applied at the last and finest grid resolution, relative to the amount of data smoothing applied at the second to last resolution, was larger than that appropriate for locally independent errors. The strong cell to cell correlation in these data also suggests that the 1 second resolution is somewhat finer than the true information content of the 1 second SRTM data.

Incorporating streamline data

In earlier versions of ANUDEM, where data errors were assumed to be zero, elevations on streamlines were initialized at each grid resolution by linearly interpolating along streamlines between grid points to which elevation data points had been allocated. Data points on streamlines that were higher than upstream data points were normally removed. This process becomes problematic when the elevation data have significant errors, giving rise to occasional upstream data points that are too low. These can remove accurate downstream elevation points and give rise to streamlines that are systematically too low with respect to the neighbouring landscape along extended sections of streamlines. This has been illustrated in [8].

The streamline initialization procedure has been revised to take initial streamline heights from the preceding coarser grid in the multi-grid interpolation process, rather than from the error prone actual data point heights that lie on the streamlines. The program then ensures that all initial heights on the streamlines linearly descend down each stream segment between successive stream junctions and disjunctions. The revised initialization gives rise to stable elevations on streamlines when applied to neighbouring tiles, as demonstrated in [8]. This is critical in

building a continent-wide high resolution DEM with consistent overall drainage structure from a series of overlapping map tiles.

SIMPLIFYING DATA STREAMLINES

The ANUDEM gridding process normally allocates each data streamline point to the centre of the closest grid cell. This process naturally perturbs the location of the points making up each streamline. This can generate many additional spurious stream junctions and disjunctions when close, but different, streams occupy the same grid cell. This is illustrated in Fig. 1 where data streamlines are plotted with their initial gridded representations. This shows several spurious junctions and two spurious disjunctions in the gridded streamline network. Complex networks, such as those arising in braided stream networks, can also lead to distinct data streamline junctions being allocated to the same grid cell. Finer grid spacings can reduce the number of spurious junctions but the problem is a generic one that can apply at any scale. On occasion the spurious junctions can be many grid cells removed from the real stream junctions. This can make determination of gridded representations of watersheds associated with data streamlines problematic. It can also make it difficult to automatically associate gauging stations with their respective catchments.

This problem was initially recognised in the production of the Australian national 9 second DEM and its associated flow direction grid [1]. This led to the development of the first version of a stream pre-processing procedure that could move a point in the gridded streamline segment to a neighbouring grid cell if this removed the spurious junction in the neighbouring grid cell. The move was also subject to the condition that the new location of the gridded streamline point was less than a user prescribed tolerance from the original data streamline point. An important aspect of this algorithm was to maintain simultaneous access to both the original data streamline segments and their gridded representations. This helped maximize the fidelity of the gridded streamlines to the original data streamline network. This stream pre-processing procedure substantially alleviated the problems associated with the gridded streamlines but its performance was sub-optimal, in part because the procedure attempted to simultaneously attend to both the generalization of the gridded stream segments, by removing unrealistic sharp corners, and the removal of spurious junctions and disjunctions. The procedure also did not consider making small shifts in the grid cell locations of data streamline junctions to reduce both the number of spurious junctions and disjunctions and the number of spurious coincident stream junctions.

This stream pre-processing feature has been revised to comprehensively address these issues. The process of stream generalization to remove sharp corners has been further

optimized and made separate from the process of removing spurious gridded stream junctions and disjunctions. The latter process has also been revised to optimize the choice of grid points to be moved and to remove the need for a user supplied distance tolerance. The revised procedure also explicitly minimizes the distance of the gridded streamline network from the data streamline network.

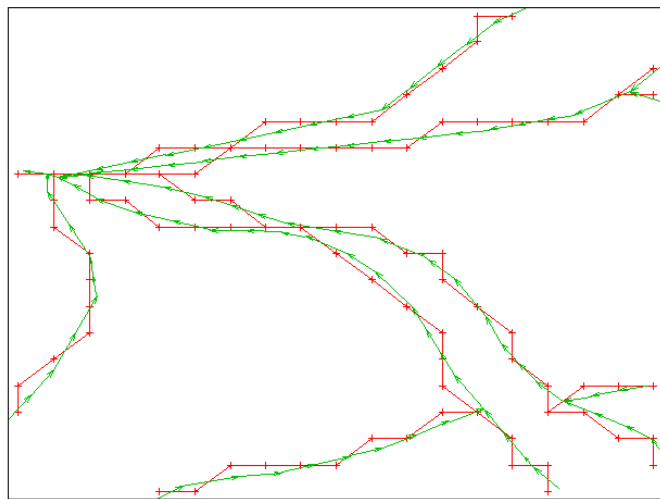


Figure 1. Streamline data in green and initial gridded streamlines at 1 second resolution in red.

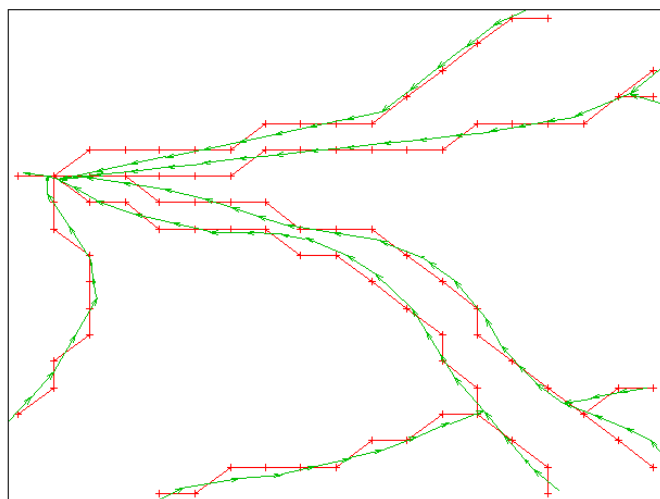


Figure 2. Streamline data in green and adjusted gridded streamlines at 1 second resolution in red.

Moreover, new procedures have been added to make small shifts in the locations of gridded streamline junctions to reduce the number of spurious coincident gridded streamline junctions.

Maximization of fidelity of the shifted gridded streamlines to the original data streamline network has been maintained as an important aspect of the new stream pre-processing procedures.

The result of applying the revised stream pre-processing procedure is illustrated in Fig. 2 where the spurious mid-stream junctions and disjunctions have been removed. The sharp junction in the southeast of Fig.1 has also been removed by shifting the stream junction one cell upstream to the east. The sum total of these small changes to the gridded streamline network can be quite large. For a 1second resolution DEM tile extending 150-151°E and 30-31°S in a low relief area of southeast Australia, containing a portion of the Namoi River, a total of 3600 spurious stream junctions and disjunctions were removed from a total of over 75,000 gridded stream segments. Of these spurious junctions and disjunctions, 1500 were removed by simple generalization of the gridded stream segments, and a further 2100 were removed by the stream shifting process described above.

SPECIFIC CATCHMENT AREA

Specific catchment area is a hydrological terrain parameter that is used widely in hydrological and ecological modeling, being directly associated with streamline patterns, areas of erosion and vegetation patterns. An important pre-requisite for its accurate calculation from a DEM is that the DEM respect the surface drainage structure of the landscape. This is a central motivation for the procedures described above. Gallant and Hutchinson [2] have recently obtained a differential equation for this quantity that can be solved using numerical methods. This has permitted assessment of various methods for calculating gridded representations of specific catchment area. All were found to overestimate specific catchment area on ridges and hilltops. The high spatial variability of specific catchment area makes its representation in gridded form problematic, on ridges and on streamlines.

One way to address this variability is to regard it as a two-dimensional vector field. It is natural to identify the downslope direction of the land surface as the direction of the vector form of specific catchment area. When so interpreted it can be readily shown that, away from depressions, the two-dimensional vector of specific catchment satisfies the fundamental identity

$$\text{div } \rho = 1$$

where ρ denotes the vector of specific catchment area and div denotes the divergence operator. This clarifies specific catchment area's precise role as a density of area. Moreover, by appealing to the standard formula for divergence with respect to orthogonal curvilinear coordinates it can be seen that equation (34) of [2] follows. This simplifies the derivation of the main result presented in [2].

The identity given above also suggests an alternative way to represent specific catchment area in grid form. This would be to replace current somewhat ill-defined gridded specific catchment values by appropriate line integrals of the vector field along the sides of each grid cell. This would overcome the near singularity of specific catchment area on streamlines and, away from depressions, could take advantage of the natural relationship between these integrals and the area of each grid cell. Further investigation is underway to determine an efficient method for calculating such integrals.

ACKNOWLEDGMENTS

Funding for this research has been provided in part by the Australian Bureau of Meteorology as part of the development of the Australian Hydrological Geospatial Fabric (Geofabric) <http://www.bom.gov.au/water/geofabric/>

REFERENCES

- [1] ANU Fenner School of Environment and Society and Geoscience Australia, 2008. "GEODATA 9 Second DEM and D8 Digital Elevation Model and Flow Direction Grid, User Guide", Geoscience Australia, 43 pp. http://www.ga.gov.au/image_cache/GA11644.pdf
- [2] Gallant, J.C., and M. F. Hutchinson, 2011. "A Differential Equation for Specific Catchment Area", Water Resources Research 47, W05535, doi:10.1029/2009WR008540.
- [3] Harding, D.J., J.L. Bufton, and J. Frawley 1994. "Satellite laser altimetry of terrestrial topography: Vertical accuracy as a function of surface slope, roughness and cloud cover", IEEE Transactions on Geoscience and Remote Sensing 32: 329-339.
- [4] Hutchinson, M.F. 1989. "A new method for gridding elevation and stream line data with automatic removal of spurious pits", Journal of Hydrology 106: 211-232.
- [5] Hutchinson, M.F., 2000. "Optimising the degree of data smoothing for locally adaptive finite element bivariate smoothing splines", ANZIAM Journal 42(E): C774-C796.
- [6] Hutchinson, M.F., 2008. "Adding the Z-dimension", In: J.P. Wilson and A.S. Fotheringham (eds), "Handbook of Geographic Information Science", Blackwell, pp 144-168.
- [7] Hutchinson, M.F., 2011. ANUDEM Version 5.3. Fenner School of Environment and Society, Australian National University, <http://fennerschool.anu.edu.au/publications/software/anudem.php>
- [8] Hutchinson, M.F., J.A. Stein, J.L. Stein, and T. Xu, 2009. "Locally adaptive gridding of noisy high resolution topographic data", In Anderssen, R.S., R.D. Braddock and L.T.H. Newham (eds) 18th World IMACS Congress and MODSIM09 International Congress on Modelling and Simulation. <http://www.mssanz.org.au/modsim09/F13/hutchinson.pdf>
- [9] Pusey, B. J., M.J. Kennard, J.L. Stein.,J.D. Olden, S.J. Mackay, M.F. Hutchinson. and F. Sheldon, 2008. (Eds.) "Ecohydrological regionalisation of Australia: a tool for management and science", Innovations Project GRU36, Final Report to Land and Water Australia. <http://lwa.gov.au/products/pn22591>
- [10] Stein, J.L., J.A.Stein and H.A. Nix, 2002. "Spatial analysis of anthropogenic river disturbance at regional and continental scales: identifying the wild rivers of Australia", Landscape and Urban Planning 60: 1-25.
- [11] Farr, T.G. et al., 2007. "The shuttle radar topography mission", Reviews of Geophysics 45, RG2004/2007.

Land surface derivatives: history, calculation and further development

Ian S. Evans

Durham University and University of Stefan cel Mare, Suceava.

i.s.evans@durham.ac.uk

Abstract— The use of derivatives in geomorphometry is reviewed. For first and second derivatives (slope and curvatures) of the land surface, represented by a square-grid DEM, use of a quadratic based on nine points is recommended. For detailed analysis of slope gradient, maximum slope (based on two points) may be useful: but only if the DEM is very accurate. For curvature, streamline (rotor) curvature should be added to profile and plan curvature. The system of local point-based variables in the gravity field is now extended to third derivatives.

1. INTRODUCTION: HISTORY

The importance of slope gradient in geomorphological processes and the description of land surface form has long been recognized (Young, 1972; Parsons, 1988). Traditionally it was measured directly in the field along profiles, using clinometers, levels or pantometers. This involved problems of sampling (Young, 1972) and the ground length over which it is to be measured: Pitty (1969) favoured the fixed slope length given by a 1.52 m pantometer, giving a ‘human scale’. Also, subtle differences can be observed between up-slope and down-slope measurements. Methods of measuring curvature tangential to the slope profiles were developed by Young (1972). Slope gradient was measured also from contour spacing on maps, and generalized maps of gradient were produced from contour density, e.g. counting contour intersections with a grid.

The calculation of derivatives from gridded height data was pioneered by geophysicists (e.g. Šalamon, 1963). This was applied to gridded models of the land surface by

Tobler (1969). Geophysicists also began consideration of the land surface as a scalar field, and systematic application of methods of mathematical analysis, a significant theoretical shift which was developed further by Krcho (1973). Drawing on the earlier work of Tobler and W.A. Wood, Evans (1972) demonstrated the value of derivatives in geomorphology, and attempted to simplify at-a-point geomorphometric variables in terms of two components (gradient, aspect) of the first derivative and two (plan and profile curvature) of the second. He showed their sensitivity to scale, represented by DEM grid mesh. Further work has dealt with various measurement scales or transformations for gradient and curvatures as distributed over areas. The value of all these derivatives has been amply confirmed, and their importance increases as new applications are found. Mitášová and Hofierka (1993) redefined plan and profile curvatures on the base of differential geometry theory (inverting the geomorphological sign convention), and more components of curvature have been added (Jenčo, 1992; Shary et al. 2002). Numerous variant definitions of curvature have complicated matters, reducing the simplification originally desired. Nevertheless, consistency of definition is highly desirable for a science to advance by making measurements which are comparable.

2. CALCULATION OF SLOPE (GRADIENT AND ASPECT)

Currently there is competition as to the value of different definitions, and debate about how variation with scale (or degree of generalisation) should be handled. For gradient

calculation from gridded DEMs, I suggest that both very local (D8: 2-point, 8-direction, maximum-slope), and slightly smoothed (9-point quadratic, omni-directional) values, are valuable – assuming data are sufficiently accurate. Onorati et al. (1992) illustrated differences between three methods for slope, for a 230 m grid of Italy, and chose a 3-point method. Zhou and Liu (2004) compared six methods for two mathematical surfaces, and demonstrated the desirability of using 8 points rather than 4 or 3: weighting by distance made little difference.

Although 2-point gradients (using steepest descent from the central point to any of the eight ‘Queen’s case’ neighbours) are very sensitive to data error, they do make full use of DEM detail and preserve the range of values, which is reduced by all methods that use more than 2 points. Conventionally the gradient is attributed to the source (central, upslope) grid point: if it were placed accurately, half-way between the two points, the resulting gradient values would be unevenly distributed, on an incomplete grid (with many holes). Fitting exact planes to each set of three adjacent points makes all directions (aspects) possible, rather than just eight ‘cardinal points’ of the compass, but the results relate to new points in the centres of the two sets of triangles produced from a square grid. Fitting planes to four points already involves some generalization of the DEM, and the results relate to new points displaced by half the grid mesh. Fitting to five points (a central point and four closest neighbours, ‘rook’s case’) increases generalization but does provide results at each of the original data points.

3. CALCULATION OF SLOPE AND CURVATURES

None of these (2, 3, 4 or 5 point algorithms) gives reliable estimates of surface curvature. This is why Evans (1980) adopted a full quadratic (6-parameter) equation fitted to nine points (3 x 3). Tests by Skidmore (1989), Eyton (1991), Guth (1995), Florinsky (1998) and Schmidt et al. (2003) have demonstrated the advantages of this method over several alternatives, even though it inevitably smooths sharp breaks. Wise (1998) also showed the advantages of the nine-point quadratic, especially for aspect estimation (n.b. slope is estimated from 8 points:

the central point is used only for curvatures). The quadratic provides better results for gradient (Florinsky, 1998) and for curvatures (Schmidt et al., 2003) than a 9-parameter partial quartic. Once error in the DEM is admitted, it seems undesirable to constrain the surface to pass through the central point, as this is affected by error as much as are the other eight. There may, however, be a case for weighting the central point more, and the corner points less, than the other four. Conversely, some algorithms use eight neighbours and ignore the central point, which seems perverse.

Shary et al. (2002) have suggested routinely fitting over 5 x 5 points, to smooth the errors in contour-based DEMs. The degree of smoothing should be related to the degree of DEM error: I suggest basing this on the ratio of standard error of altitude to the mean difference between adjacent points. We await calibration of the desirable degree of smoothing as a function of this ratio: it is probably best to smooth as necessary first, before fitting the nine-point quadratic.

Guth (1995) demonstrated that use of all eight neighbours reduced mean gradients to 78% of those from the ‘steepest adjacent neighbour’ (i.e. two-point) algorithm. This is roughly equivalent to the reduction when grid mesh is doubled.

Reference to the direction of gravity¹ distinguishes the use of derivatives in earth sciences, as distinct from broader mathematical schemes, although Shary et al. (2002) have demonstrated the use of principal curvatures. Evans (1980) used the 6-parameter quadratic as the basis for implementation of a 5-variable system of local point-based variables in the gravity field: altitude, slope gradient, slope aspect, profile curvature and plan curvature. Inevitably this attempt to simplify general geomorphometry has been followed by extension to greater complexity (Olaya, 2009), and it is clear that several additions are necessary (Evans and Minár, 2011). Improved computing capabilities permitted the very desirable extension to flow-line related positional variables (not dealt with here). For

¹ We generally assume that a land surface can be represented as a (single-valued) function, $z = f(x,y)$, with the z-axis parallel to the direction of gravity (e.g. Mitášová & Hofierka, 1993).

local variables, the most obvious omission was the third curvature variable: curvature of any surface in 3 dimensions can be completely characterised by three orthogonal variables, but there are many alternative trios of definition. If we keep profile and plan curvature (because of their clear relation to surface processes), the third curvature may be termed 'rotor curvature' (Florinsky, 1998) or 'streamline curvature' and describes the curvature of streamlines or the divergence of contour lines (Shary et al., 2002; Peckham, 2011). Tangential curvature, in a plane orthogonal to the surface and the flow line, is less useful because it is closely related to plan curvature (Peckham, 2011), especially on low gradients.

4. TRANSFORMATIONS OF FREQUENCY DISTRIBUTIONS

For most types of statistical analysis, it is important to check the shape of the frequency distribution of each variable. These vary between areas, even between adjacent areas (Minár et al. 2013). The venerable and developing literature on hypsometry shows that altitude can be right-skewed or left-skewed, so no single transformed scale will fit all study areas. Slope gradient in degrees or tangents is more often right- (positively-) skewed, so logarithmic transformation is appealing (Speight, 1971). This is because, even in mountain regions, deposition in fans, floodplains and lakes produces extra areas of low gradient. Where these are absent, however, distributions may be symmetrical or, where high relief pushes gradient toward a limiting value for slope stability, negatively skewed (Oguchi et al., 2011).

For real-world DEMs, the distribution of curvatures measured in degrees per unit length (100 m in Evans 1980) is always strongly peaked at the mode of zero. The presence of extremely positive and negative values can greatly bias calculation of product-moment correlations. (In profile convexity these extremes represent sharp breaks and concentrate in high-gradient areas; in plan convexity, they are not just across sharp channels and ridges but also on floodplains, where aspect is almost indeterminate.) To solve this, I have applied arctangent transformations to 'bring in' both tails. Unfortunately these require calibration of a constant multiplier, k :

Transform = $\arctan(k \cdot \text{convexity})$

k is chosen so as to minimise kurtosis, originally a rather clumsy trial-and-error process. Note that kurtosis on the negative side of normal (toward a rectangular distribution) is not usually a problem, as it is outliers or extreme values (long tails) that bias correlations and related statistics. Alternatives to the arctangent are the use of other sets of curvatures (would tangential or maximum and minimum curvature avoid the floodplain problem?) or of robust statistics, but it is hard to find applications of those approaches.

5. THIRD DERIVATIVES

First and second derivatives seemed adequate to cover applications in geomorphology up to 1980, but the work of Florinsky (2009) and of Minár et al. (2013) has now demonstrated several applications for the third derivative. Data unreliability has been the main deterrent to their use as yet, but this is improving and better computation techniques have been devised. These third derivatives are valuable in delimiting surface objects (such as elementary forms, forms homogeneous in one or more derivatives) and testing their tendency to a constant value of some derivative. Minár et al. (2013) show that as higher derivatives are taken, they concentrate increasingly around zero, as predicted by the concept of elementary forms. The increase is greater than for random or 'fractal' surfaces. Note, however, that as further derivatives of real land surfaces are taken, the resulting surfaces are rougher and rougher, unlike those of mathematically-defined polynomial surfaces. One promising application of third derivatives arises because, while zero values of tangential changes are widespread for both profile and tangential curvature, they coincide only on (sharp) ridges and valleys and both conditions are needed in delimiting these.

6. CONCLUSION

The system of first and second derivatives of land surface altitude in the gravity field has proved robust, popular and useful over the last four decades, and extended to the third derivative it should remain a cornerstone of general geomorphometry for decades to come. Applications are

legion (Hengl and Reuter, 2009), and increasing as DEMs at the fine scales relevant to surface processes become available. Uses for field-invariant variables, a further extension, have been proposed by Shary et al. (2002) and we hope to see numerous applications in future. Alternative systems for the analysis of rough surfaces, such as spectral and fractal analyses, are more difficult to implement in practice and to interpret. In fact our ability to differentiate representations of the land surface suggests that it cannot be truly fractal, as fractal surfaces are non-differentiable. With their more direct meaning – rates of change – derivatives remain intuitively appealing.

ACKNOWLEDGEMENTS

I am grateful to Jozef Minár, Lucian Drăguț and the reviewers for valuable comments.

REFERENCES

- Evans, I.S. 1972. "General geomorphometry, derivatives of altitude and descriptive statistics." In *Spatial Analysis in Geomorphology*, Edited by Chorley, R.J., Methuen, London, pp. 17–90.
- Evans, I.S. 1980. "An integrated system of terrain analysis and slope mapping." *Zeitschrift für Geomorphologie N.F., Supplementband* 36, 274–295.
- Evans, I. S. and Minár, J. 2011. "A classification of geomorphometric variables." *International Geomorphometry* 2011, 105-108. Geomorphometry.org.
- Eyton, J.R. 1991. "Rate-of-change maps." *Cartography and Geographic Information Systems* 18 (2), 87-103.
- Florinsky, I.V. 1998. "Accuracy of local topographic variables derived from digital elevation models." *International Journal of Geographical Information Science* 12 (1), 47-61
- Florinsky, I.V. 2009. "Computation of the third-order partial derivatives and derivation function from a digital elevation model." *International Journal of Geographical Information Science* 23 (2), 213–231.
- Guth, P. 1995. "Slope and aspect calculations on DEMs." *Zeitschrift für Geomorphologie N.F., Supplementband* 101, 31-52.
- Hengl, T., and Reuter, H.I. (Eds.) 2009. "Geomorphometry: Concepts, Software, Applications." *Developments in Soil Science*, 33. Elsevier, Amsterdam, 765 p.
- Jenčo, M. (1992): The morphometric analysis of georelief in terms of a theoretical conception of the complex digital model of georelief. *Acta Facultatis rerum naturalium Universitatis Comenianae. Geographica*, 33, s. 133-153.
- Krcho, J. 1973. "Morphometric analysis of relief on the basis of geometric aspect of field theory". *Acta geographica Universitatis Comenianae, Geographico-physica* 1, 11–233.
- Minár, J., Evans, I.S., Krcho, J. 2013. "Geomorphometry: quantitative land surface analysis." In: Shroder, J. (Editor in chief), Switzer, A.D., Kennedy, D.M. (Eds.), *Treatise on Geomorphology*. Academic Press, San Diego, CA, vol. 14, *Methods in Geomorphology*, pp. 22–34.
- Minár, J, Jenčo, M., Evans, I. S., Minár, J. Jr-, Kadlec, Krcho, J., Pacina, J., M., Burián L., Benová, A. 2013 "Third-order geomorphometric variables (derivatives) – definition, computation and utilization of changes of curvatures." *International Journal of Geographical Information Science*, 27 (7), 1381-1402.
- Mitášová, H., Hofierka, J. (1993): Interpolation by Regularized Spline with Tension: II. Application to Terrain Modeling and Surface Geometry Analysis. *Mathematical Geology* 25 (6), 657-669.
- Oguchi, T., Katsube, K., Lin, Z. And Chen, Y-G, 2011. "Characteristic slope angle of V-shaped valleys in humid steep mountains with frequent slope failure." *International Geomorphometry* 2011, 93-96. Geomorphometry.org.
- Olaya, V. 2009. "Basic land-surface parameters." In: T. Hengl and H.I. Reuter, eds. *Geomorphometry: concepts, software, applications*. *Developments in Soil Science*, 33. Amsterdam: Elsevier, pp. 141–169.
- Onorati, G., Chiarini, V., Crucilla, U., Poscolieri, M. and Ventura, R. 1992. "The DEM of Italy for geomorphology and structural geology: analysis of a DEM of the Italian peninsula." *Catena* 19, 147-178.
- Parsons, A.J. 1988. "*Hillslope form*." London: Routledge.
- Peckham, S.D. 2011. "Profile, plan and streamline curvature: A simple derivation and applications." *International Geomorphometry* 2011, 27-30. Geomorphometry.org.
- Pitty, A.F. 1969. "A scheme for hillslope analysis. I: Initial considerations and calculations." *University of Hull, Occasional Papers in Geography* 9.
- Šalamon, B. 1963. "Das typische Isoliniengrundfeld und seine Anwendung." *Studia geophysica et geodetica* 7, Praha.
- Schmidt, J., Evans, I.S., Brinkmann, J. 2003. "Comparison of polynomial models for land surface curvature calculation." *International Journal of Geographical Information Science* 17, 797–814.
- Shary, P.A., Sharaya, L.S., and Mitusov, A.V. 2002. "Fundamental quantitative methods of land surface analysis." *Geoderma* 107 (1), 1-32.
- Skidmore, A.K. 1989. "A comparison of techniques for calculating gradients and aspects from a gridded digital elevation model." *International Journal of Geographical Information Systems* 3 (4), 323-334.
- Speight, J.G. 1971. "Log-normality of slope distributions." *Zeitschrift für Geomorphologie N.F.* 15, 290 – 311.
- Tobler, W.R. 1969. "An analysis of a digitalized surface." In: Davis, C.M. (Ed.), *A Study of the Land Type*, University of Michigan, Department of Geography, MI, pp. 59–76. Report on Contract DA-31-124-ARO-D-456.
- Wise, S., 1998. "The effect of GIS interpolation errors on the use of DEMs in geomorphology." In: Lane, S.N., Richards, K.S., Chandler, J.H. (Eds.), *Landform Monitoring, Modelling and Analysis*. Wiley, Chichester, ch. 7, pp. 139–164.
- Young, A. 1972. "*Slopes*." Oliver & Boyd, Edinburgh. 288 pp.
- Zhou, Q., Liu, X. 2004. "Analysis of errors of derived slope and aspect related to DEM data properties." *Computers & Geosciences* 30, 369–378.

The Giga Revolution in Geomorphometry: Gigabytes of RAM, Gigabyte-Sized Data Sets, and Gigabit Internet Access

Peter L. Guth

Department of Oceanography
United States Naval Academy
Annapolis, MD 21402 USA
pguth@usna.edu

Abstract—Recent advances in computer technology herald a revolution in geomorphometry. Desktop computers and 64 bit operating systems can access massive data sets like the entire SRTM DEM from RAM. Multi-temporal lidar topography, with 1 m or 0.5 m grid spacing, can require gigabytes of data for relatively small project areas, but repeated surveys allow monitoring geomorphometric changes over time. As gigabit internet access reaches greater audiences, the need to download data before beginning analysis might be replaced with just-in-time delivery over the internet, or analysis as a service with downloading data. Traditional DEMs like SRTM could be viewed as almost all signal—they might be smoothed or filtered, but there was no way to remove whatever vegetation noise was present, and the user basically had to accept the dataset. With lidar the user can process the point cloud to remove vegetation, and can consider further removing boulders and similar features to get a generalized and more representative view of the landscapes.

Views of desert dune landscapes at three scales (1 km—100 m—1m) illustrate these changes. The half gigabyte global data set ETOPO1 easily loads into RAM. The largest dune fields appear at this scale, but few characteristics of the dunes appear and some suffer from aliasing. SRTM and ASTER GDEM have very similar 100 m real point spacing, and allow automated extraction of dune heights, spacing, and orientation for most dunes, although smaller dunes like many of those in Australia are at the limits for these elevations models. SRTM's collection over a short period captured a virtually instantaneous snapshot, whereas the ASTER GDEM's long temporal averaging smears out dune changes. The smallest dunes, such as those at White Sands, New Mexico, only appear well defined in lidar grids with 1 m resolution which can track dune migration and reveal spatial patterns.

I. INTRODUCTION

Increases in computer power, cloud delivery of both huge data sets and geospatial services, and increasing bandwidth all make this an exciting time for geomorphometry. This paper will look at three scales of data to show the increasing capabilities.

II. GLOBAL DEMS: ETOPO1 AND SRTM30

Global DEMs have come a long way from ETOPO5, which covered the entire globe, oceans and continents, in under 20 MB. Currently two data sets, ETOPO1 and SRTM30, cover the globe with about 500 MB and 2 GB respectively. ETOPO1 can load entirely into RAM, while SRTM30 must be subset or loaded into 64 bit software. For the purposes of geomorphometry, these data sets perform similarly, with data spacing of about 1 km.

The large linear dune fields of the world appear in these data sets, but at the limit for detection and quantitative geomorphometric analysis. Figure 1 shows the terrain classification of Iwahashi and Pike [1, 2] next to the SRTM30 for a region in the western Sahara. The dunes show up as noisy, alternating pixels in two categories. Attempts to use fabric analysis [3] on the dunes cannot differentiate them from linear tectonic ridges.

III. SRTM AND ASTER GDEM

The SRTM and ASTER GDEM have very similar effective resolutions. GDEM covers more the earth, although generally with more noise and other artifacts, but can improve on SRTM where the radar was shadowed or did not get returns in dry sand. With a 64 bit operating system, a desktop PC with 64 GB of RAM and clever indexing, could load the entire SRTM DEM into memory for rapid, random access.

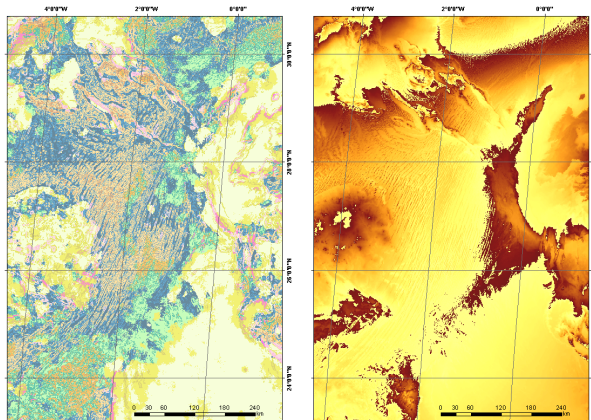


Figure 1. Classification of western Sahara from Iwahashi and Pike, compared to SRTM30 topography.

An automated algorithm can find dune spacing (crest separation), dune height, and crest orientation. Terrain fabric identifies the orientation of the dunes, and analysis of profiles perpendicular to the crests and pick out the crests and troughs and compute the spacing. Figure 2 shows crests picked in Niger, in a region with perpendicular dune orientations. Figure 3 shows dune heights in part of the Xianjang Desert of China.

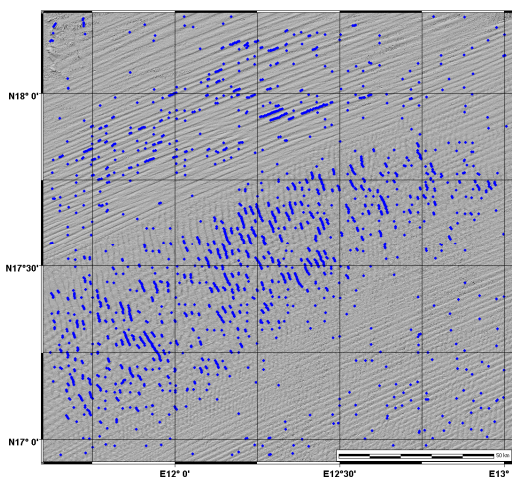


Figure 2. Dune crests identified in central Niger, with orthogonal trends.

IV. LIDAR DEMS AND DUNE MIGRATION

The real power released by current developments shows up with lidar data sets. Three lidar collections cover the White Sands dune field in New Mexico, in January 2009, September 2009, and June 2010. As point clouds in LAS format these require 5-9 GB of data storage each, with point densities of 4-6 points/m². Converted to gridded DTMs they require about 400 MB each.

Three methods were developed to track dune migration: (1) tracking the migration of dune crests; (2) assessing the shifts that provide the best correlation for subsets of the grids; and (3) identify slip face objects, and track their migration. All methods used a gridded DEM, and two require identification of the dune slip faces by locating slopes > 50%.

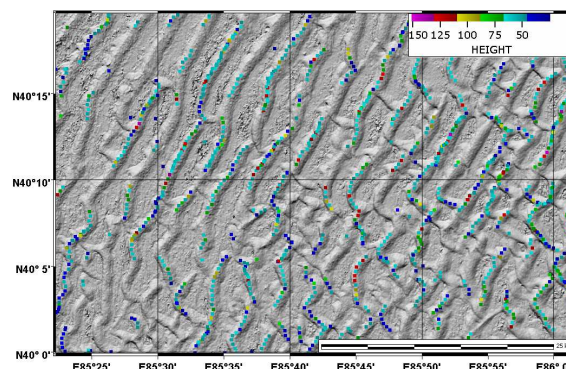


Figure 3. Dune heights computed along crests in Xinjiang Desert, China.

A. Migration from Identified Crests

The algorithm starts with the slip faces identified by slope, and picks the expected migration direction from the 8 principle cardinal directions, and then pick points on the opposite edge of the dunes as the dune crests of the dunes. It looks along profiles in the candidate direction starting from each crest point in the first DEM. If there is a crest in the other DEM within a maximum search distance, it will be the migrated crest. Positive numbers will be in the northerly or easterly direction.

B. Migration from Grid Correlations

This algorithm requires three parameters: the interval between computation points; the size of the regions, which can overlap; and the maximum distance to consider for shifting the two grids. Regions must be large enough to contain a significant proportion of dunes, as this will not work in flat interdune regions. The algorithm shifts one grid relative to the other, and computes the correlation coefficient between the elevation in the stationary grid and the shifted grid. The offsets for the highest correlation define the computed migration.

C. Migration from Slip Face Objects

This algorithm first detects the slip face objects, finding all connected regions on the map of slip faces from 50% slopes. The algorithm creates a grid with an ID for each object, and a database with the data about the object. The user selects a box region to search for the migrated slip face. The computer finds the shift with the largest percentage of the slip face matching a slip face in the second time period. The output notes the number of objects within this shift, as a dune can fragment as it migrates (Figure 5). The algorithm also performs a reverse analysis, from

the later DEM back to the original DEM. This provides similar results, but there are different numbers of slip faces in the two time periods, and some of the earlier slip faces may merge (Figure 5).

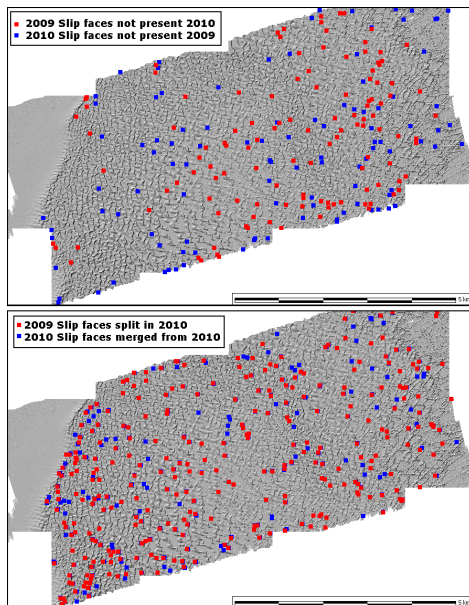


Figure 4. Slip faces without a simple 1:1 correspondence from January 2009 to June 2010.

V. RESULTS

Tables I and II summarizes the results. Figure 6 shows map depictions of the motion for all three methods. The grid correlation and slip face object methods produce very similar results, with a vector average rate of 5.1 to 5.4 m/year toward N70E, slightly more than the crest migration which only provides a component of the total motion. This is on the high end of reported figures (1-4-m/yr [4]). The most interesting result is the spatial pattern of migration shown in Figure 6, which shows the largest rates, approaching and some cases exceeding 10 m/yr along the western edge of the dune field, and a region in the center with lower rates than occur either to the east or west.

TABLE I. MIGRATION RATES FROM FIRST TWO METHODS

Method	Number	Average m/yr	Median m/yr	Vector Average m/yr
Grid Correlations	152	5.16	5.33	5.13 toward 68.9°
Crests, Motion E	59026	3.58	2.93	3.58 toward 90°
Crests, Motion NE	36181	4.73	4.17	4.73 toward 45°

TABLE II. SLIP FACE OBJECT ANALYSIS

Survey Date	Category	Number	Percentage	Vector Average m/yr
1/24/09	Total slip faces	2568		
	Trace forward	2446	95.25%	5.40 toward 72.2°
	Unique matches	2141	83.37%	5.22 toward 73.1°
	No match 2010	122	4.75%	
	Split forward	239	9.31%	
6/6/10	Total slip faces	2486		
	Trace backward	2381	95.78%	5.36 toward 72.2°
	Unique matches	2086	83.91%	5.16 toward 73.1°
	No match 2009	105	4.22%	
	Merge forward	271	10.90%	

VI. CONCLUSION

Huge data sets, large amounts of RAM on desktop computers, and large bandwidth for data downloads promise to change the practice of Geomorphometry: larger data sets, more details, and multi-temporal views. The rise of smartphones and tablets may drive analysis onto the web as a service, leaving visualization and data manipulation onto small clients.

ACKNOWLEDGMENT

White Sands LiDAR data acquisition and processing completed by National Center for Airborne Laser Mapping (NCALM - <http://www.ncalm.org>) funded by National Science Foundation Division of Earth Sciences, EAR-1043051. <http://dx.doi.org/10.5069/G97D2S2D>, G9Q23X5P and G9ZK5DMD.

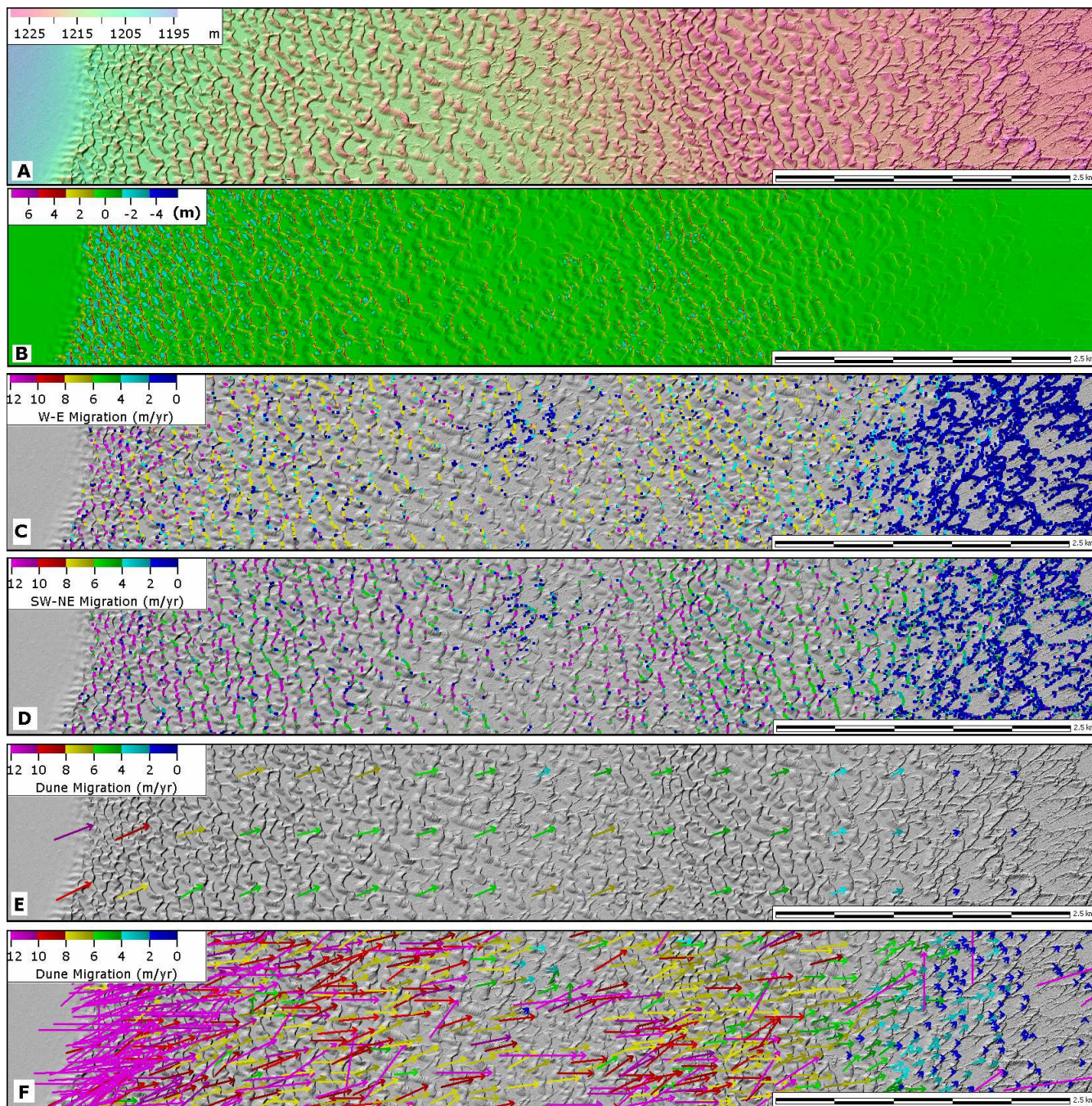
REFERENCES

[1] Iwahashi, J., and R.J., Pike, 2007, Automated classifications of topography from DEMs by an unsupervised nested means algorithm and a three-part geometric signature, *Geomorphology*, 86(3-4): 409-440.

[2] Iwahashi, J., 2010, Download site for automated terrain classification map using SRTM30: http://gisstar.gsi.go.jp/terrain/front_page.htm.

[3] Guth, P.L., 2011, Quantifying linear dune morphology: Examples with SRTM, GDEM, and multibeam bathymetry: in Hengl, T., Evans, I.S., Wilson, J.P., and Gould, M., eds., *Geomorphometry 2011*, Redlands, California, September 7-11, p.139-142. Online at <http://www.geomorphometry.org/system/files/Guth2011geomorphometry.pdf>.

[4] Kocurek, G.; M. Carr, R. Ewing, K.G. Havholm, Y.C. Nagar, and A.K. Singhvi, 2007, White Sands Dune Field, New Mexico: Age, dune dynamics and recent accumulations, *Sedimentary Geology*, 197(3-4), 313-331.



White Sands, New Mexico. A shows the dune elevations and morphology in January 2009; B the elevation difference between January 2009 and June 2010; C the computed east west component of dune migration of dune crests in 18 months; D the SW-NE migration over 18 months; E the migration using elevation correlations; and F the migration tracking features.

The TanDEM-X Mission: Earth Observation in 3D

Benjamin Bräutigam, Manfred Zink, Irena Hajnsek, Gerhard Krieger

Microwaves and Radar Institute
German Aerospace Center (DLR)
Oberpfaffenhofen, Wessling, Germany

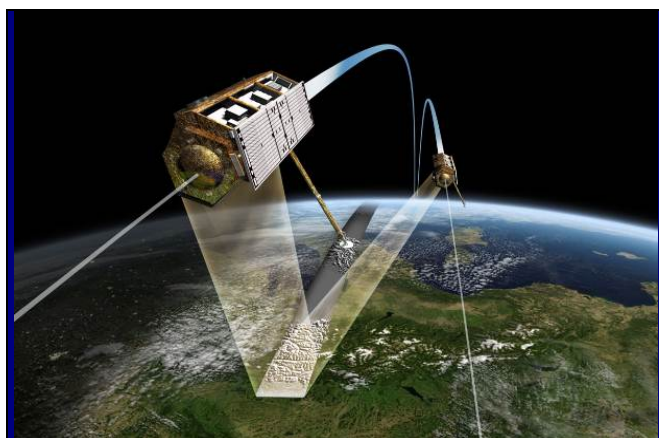
Abstract— TanDEM-X is an innovative radar mission which encompasses two formation flying satellites. Its primary goal is the generation of a global Digital Elevation Model (DEM) of unprecedented accuracy. The baseline between the satellites can be flexibly adjusted for single-pass SAR interferometry. The DEMs are produced by cross-track interferometry. Their high performance will be achieved by combining at least two global coverages into a homogenous mosaic of a global DEM. The final DEM consists of geo cells with 1° by 1° size. Delivery of DEM products to registered scientific and commercial users will commence in 2014. Furthermore, the secondary mission goals of TanDEM-X exploit the versatility of the two SAR instruments. Along-track SAR interferometry as well as bistatic and multi-channel SAR techniques are possible, providing unique capabilities for scientific researches in the field of remote sensing. This paper gives a status summary of the TanDEM-X mission with respect to the DEM generation and actual performance, its output products, and an outlook on future mission steps.

I. INTRODUCTION

Spaceborne remote sensing is the most efficient way to acquire global Digital Elevation Models (DEMs). Interferometric processing of synthetic aperture radar (SAR) acquisitions has already been used to form the SRTM product set, which provides DEM geo cells with up to 30 m horizontal resolution for latitudes between 58° South and 60° North [1]. Since 2010, Germany's SAR satellites TerraSAR-X and TanDEM-X are simultaneously operated by the German Aerospace Center (DLR) in order to acquire an updated DEM which exceeds the presently available global data sets in terms of resolution, coverage, and quality by orders of magnitude. Figure 1 shows the two satellites flying in close formation. The baseline between the two SAR sensors can be flexibly adjusted for single-pass SAR interferometry [2]. This provides the opportunity for accurate cross-track and along-track interferometry overcoming the limitations of atmospheric disturbance and temporal decorrelation in multi-pass data.

The primary mission goal is to cover the Earth's land masses at a spatial resolution of 12 m, and with relative/absolute height accuracies of down to 2 m/10 m, respectively (see Figure 1).

The DEM data will be the basis for a wide range of scientific research, as well as for commercial DEM production. Thanks to its unique capabilities, TanDEM X is furthermore well-suited to demonstrate novel bistatic and multistatic SAR techniques and Earth observation applications. This paper presents the general concept of how to acquire and to generate the TanDEM-X output products. The actual acquisition and performance status is given. At the end, an outlook on the future tasks and perspectives is provided.



Global Digital Elevation Model by TanDEM-X

Parameter	Specification	Requirement
Relative Vertical Accuracy	90% linear point-to-point error in 1° cell	2 m (slope < 20%) 4 m (slope > 20%)
Absolute Vertical Accuracy	90% linear error	10 m
Spatial Resolution	independent pixels	12 m (0.4 arc sec)

Figure 1. TerraSAR-X and TanDEM-X satellites flying in close orbit formation for the acquisition of a global Digital Elevation Model (DEM) with unprecedented resolution and accuracy.

II. TANDEM-X DEM GENERATION CONCEPT

A. Acquisition Strategy

TanDEM-X follows a systematic acquisition scenario based on the coordinated operation of two SAR satellites flying in close formation. The mapping strategy is to cover the land masses at least twice. The first global coverage is performed at satellite baselines in the order of 300 m, the second coverage is acquired with larger baselines in the order of 400 m [4]. The driving factor for this is the interferogram’s height of ambiguity, which is inversely proportional to the baseline

$$h_{amb} = \frac{\lambda r \sin \theta}{B} \quad (1)$$

where λ is the wavelength, r the slant range from the satellites to the illuminated ground target, θ the incident angle of the electromagnetic wave, and B is the perpendicular baseline component.

A lower height of ambiguity (i.e. larger baseline) improves the height accuracy, as the interferometric phase error is directly scaled by h_{amb} . On the other hand, a higher height of ambiguity increases the probability in selecting the correct ambiguity band during phase unwrapping. The correct ambiguity band contains the real elevation value, and its unambiguous determination is supported by radargrammetry [5]. To optimize the quality and to ensure a homogeneous performance, the acquisitions with larger height of ambiguity from the first coverage are used to support

the phase unwrapping of the second acquisitions with lower height of ambiguity [6].

This requires in turn frequent adjustments of the orbit formation parameters which are selected according to an optimized global data acquisition plan [7]. During the mosaicking process of the final DEM, the multiple acquisitions can be combined in order to achieve a high and homogenous performance [2].

B. TanDEM-X Data Output

TanDEM-X features the flexibility to command several bistatic modes with the two satellites. The standard mode for DEM acquisition is the bistatic StripMap mode in single HH polarization. Furthermore, dual-polarized acquisitions or Spotlight imaging are possible. Interferometric acquisitions in alternating bistatic or even simultaneous bistatic mode can be supported, at selectable baselines [8]. Experimental data takes with these modes can be chosen by the scientific TanDEM-X users.

In a first step, the bistatic data are processed to co-registered SAR (CoSSC) products of about 50 km length [9], for which a sophisticated synchronization and calibration scheme is applied [10], [11]. These products contain the monostatic and bistatic SAR image plus additional metadata for post-processing, of e.g. the coherence between both images or the interferogram. CoSSCs can be ordered by scientific TanDEM-X users [12].

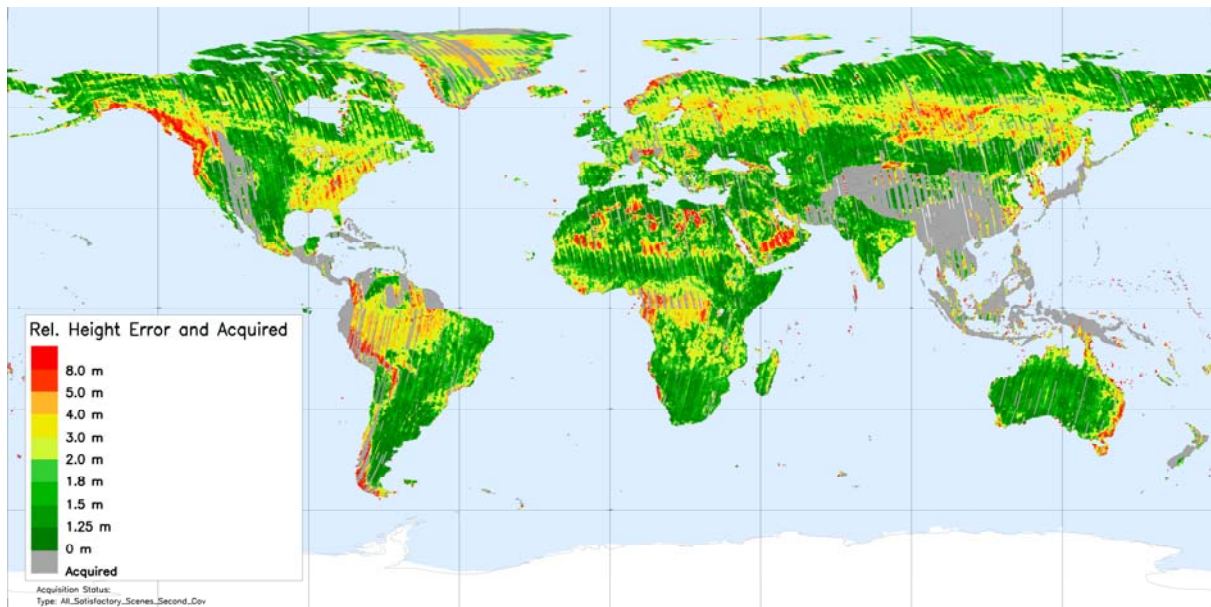


Figure 2. Mean relative height error per RawDEM acquired for the second global coverage (processing status August 2013). Green colors indicate areas where the height error is already within the 2 m requirement, yellow parts will be improved with the first coverage, red parts represent difficult terrain which requires additional acquisitions in the opposite viewing geometry. Grey parts have been acquired, but not processed yet.

For the DEM generation, each CoSSC is interferometrically processed and geocoded into a roughly calibrated “RawDEM” [5]. When all input data of a larger region (i.e. several thousands of square kilometers) are available, the tilts and offsets of the RawDEMs are calibrated against ICESat data. Finally, the mosaicking processor combines all elevation data and produces the output DEM geo cells of 1° by 1° size (ca. 110 km by 110 km at equator) [13]. The DEM products will also contain add-on layers like a height error map or a water indication mask. The detailed product and format specification can be found in [14]. Such output DEMs are provided to the commercial partner of DLR and are also available to the science community in the frame of dedicated TanDEM-X proposals.

III. DEM ACQUISITION AND PERFORMANCE STATUS

The global DEM acquisition started in December 2010 and the first global coverage (except Antarctica) was completed in January 2012. During processing of the first data sets it was analyzed that areas with strong topography variation, especially over forested regions, need an even larger height of ambiguity. Therefore, such areas have been re-acquired until April 2012 in order to have a robust basis for the DEM acquisitions of the second global coverage.

Up to July 2013, the Earth’s land masses have been mapped at least twice (except Antarctica, which has been mapped once). In the meantime, phase, delay and baseline calibration have reached such an accuracy level, that more than 90% of all individual RawDEMs are within ± 10 m accuracy compared to SRTM and ICESat data [11].

The mean coherence value derived from the CoSSCs is over 0.6 for 90% of all global DEM acquisitions and indicates the robustness of the SAR data [15]. The relative height error has been estimated from this coherence values and verified with sample repeat-pass DEMs [16]. Up to now, over 300,000 DEM scenes have been processed. A global status map of the relative height error only from the second year is depicted in Figure 2. A summary of the performance values from these acquisitions is given in Table I. The coherence and absolute height error percentages are derived from one value per scene. The relative height error percentage is evaluated on a 500 m pixel resolution. The final height performance will be achieved by combining the elevation measurements from several coverages in the mosaicking process.

Global DEM data acquisition with varying baselines will continue until mid 2014, concentrating on difficult terrain like mountains or valleys where shadowing and layover cause blind spots from a certain viewing angle. A change of the viewing angle is achieved by swapping the orbit formation, which has been performed in August 2013 [4]. First parts of the global TanDEM-X DEM will become available in 2014. Figure 3 shows an example TanDEM-X DEM at 12 m resolution compared to the SRTM DEM with 90 m resolution.

TABLE I. QUALITY OF DEM SCENES FROM SINGLE COVERAGES PROCESSED UNTIL MAY 2013.

	Coverage	
	First Coverage	Second Coverage
Coherence > 0.6 (for land masses)	90.9%	90.1%
Relative Height Error (flat areas < 2 m / mountains < 4 m)	66.4%	75.4%
	79.4%	84.9%
Absolute Height Error < 10 m (to SRTM / ICESat)	91.8%	89.0%

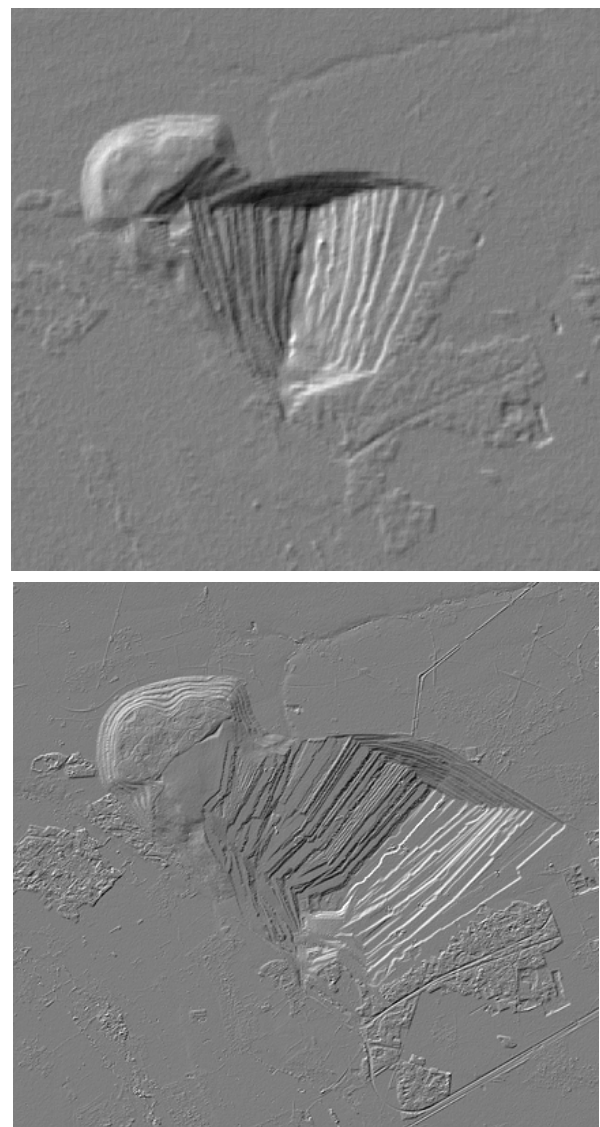


Figure 3. DEM of coal mine in Hambach, Germany. Top figure: SRTM in 2000; bottom figure: TanDEM-X in 2010.

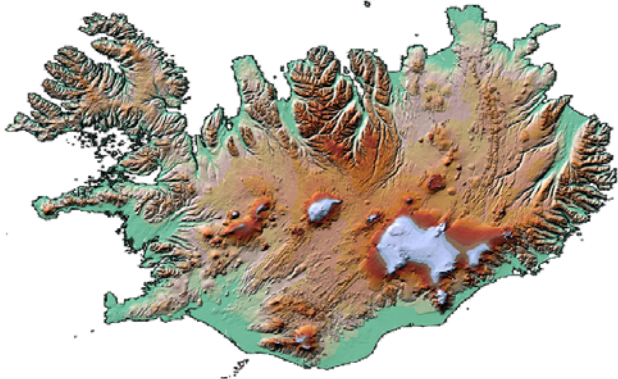


Figure 4. Mosaic of the intermediate DEM tiles of Iceland, provided by the Mosaicking and Calibration Processor [13]. Original resolution is 12 m.

IV. CONCLUSIONS AND OUTLOOK

The TanDEM-X mission is an innovative system for spaceborne radar remote sensing. A large single-pass SAR interferometer with adjustable baselines is realized by a close orbit formation. This enables the systematic acquisition of a global, highly accurate DEM. Furthermore, the demonstration of new bistatic and multistatic SAR techniques and applications is possible. Many innovative results have been obtained during the TanDEM-X commissioning phase [3], and CoSSC products are currently being investigated by scientific users around the world. Starting mid 2014, a dedicated scientific acquisition phase will be realized by TanDEM-X with the opportunity to acquire data at different baseline geometries and in different interferometric modes. The results and the experience from these experiments will be important for future formation flying SAR missions [18].

In 2013, DLR has started to calibrate the individual DEM acquisitions against ICESat data and mosaic the scenes into larger “tiles” of 1° by 1° size. These so-called intermediate DEMs have been generated on a regional basis, giving a first impression on the quality of the TanDEM-X data (see Figure 4). First parts of the global TanDEM-X DEM will become available in 2014. Scientific users can submit a TanDEM-X proposal in order to get CoSSCs, intermediate DEMs, and final DEMs. In parallel, the global DEM data are distributed to DLR’s commercial partner.

ACKNOWLEDGMENTS

The authors would like to thank all colleagues contributing to these mission results. Figure 2 has been provided by M. Bachmann from DLR.

REFERENCES

[1] The Shuttle Radar Topography Mission (SRTM) home page, <http://www2.jpl.nasa.gov/srtm>, last accessed 10 September 2013

[2] G. Krieger, A. Moreira, H. Fiedler, I. Hajnsek, M. Werner, M. Younis, M. Zink, “TanDEM-X: A Satellite Formation for High Resolution SAR Interferometry”, *IEEE Transactions on Geoscience and Remote Sensing*, vol. 45, no. 11, pp. 3317-3341, 2007.

[3] G. Krieger, M. Zink, M. Bachmann, B. Bräutigam, D. Schulze, M. Martone, P. Rizzoli, U. Steinbrecher, J. Walter Antony, F. De Zan, I. Hajnsek, K. Papathanassiou, F. Kugler, M. Rodriguez Cassola, M. Younis, S. Baumgartner, P. López-Dekker, P. Prats, A. Moreira, “TanDEM-X: A radar interferometer with two formation-flying satellites”, *Acta Astronautica*, Volume 89, August–September 2013, pp 83-98

[4] B. Bräutigam, P. Rizzoli, M. Martone, D. Borla Tridon, M. Bachmann, D. Schulze, G. Krieger, „ TanDEM-X Acquisition and Quality Overview with Two Global Coverages”, *IEEE International Geoscience and Remote Sensing Symposium (IGARSS)*, Melbourne, Australia, 2013.

[5] C. Rossi, F. Rodriguez Gonzalez, T. Fritz, N. Yague-Martinez, M.Eineder, “TanDEM-X calibrated Raw DEM generation”, *ISPRS Journal of Photogrammetry and Remote Sensing*, Vol. 38, pp. 12-20, 2012

[6] M. Lachaise, U. Balss, T. Fritz, H. Breit, “The Dual-Baseline Interferometric Processing Chain for the TanDEM-X Mission,” *International Geoscience and Remote Sensing Symposium (IGARSS)*, Munich, Germany, 2012.

[7] C. Ortega, D. Schulze, D. Polimeni, P. Rizzoli, M. Bachmann: “TanDEM-X Acquisition Planning,” *9th European Conference on Synthetic Aperture Radar*, Nuremberg, Germany, 2012.

[8] J. L. Bueso Bello, C. Grigorov, U. Steinbrecher, T. Kraus, C. Gonzalez, D. Schulze, B. Bräutigam, “System commanding and performance of TanDEM-X scientific modes,” *9th European Conference on Synthetic Aperture Radar*, Nuremberg, Germany, 2012

[9] T. Fritz, “TanDEM-X Experimental Product Description”, TD-GS-PS-3028, Issue 1.2, DLR Public Document

[10] H. Breit, M. Younis, U. Balss, A. Niedermeier, C. Grigorov, J. Hueso Gonzalez, G. Krieger, M. Eineder, T. Fritz, “Bistatic synchronization and processing of TanDEM-X data,” ,” *International Geoscience and Remote Sensing Symposium (IGARSS)*, Vancouver, Canada, 2011

[11] M. Bachmann, J. Hueso Gonzalez, G. Krieger, M. Schwerdt, J. Walter Antony, F. De Zan, “Calibration of the bistatic TanDEM-X interferometer,” *European Conference on Synthetic Aperture Radar (EUSAR)*, Nuremberg, Germany, 2012.

[12] I. Hajnsek and Th. Busche, “TanDEM-X: Science Activities”, *IEEE International Geoscience and Remote Sensing Symposium (IGARSS)*, Melbourne, Australia, 2013

[13] B. Wessel, A. Gruber, A. Wendleder, M. Huber, M. Breunig, U. Marschalk, D. Kosmann, A. Roth, “Production Chain towards First Calibrated and Mosaicked TanDEM-X DEMs,” *IEEE International Geoscience And Remote Sensing Symposium (IGARSS)*, Vancouver, Canada, 2011

[14] B. Wessel, “TanDEM-X DEM Products Specification”, TD-GS-PS-0021, Issue 2.0, DLR Public Document

[15] M. Martone, B. Bräutigam, P. Rizzoli, C. Gonzalez, M. Bachmann, G. Krieger, “Coherence Evaluation of TanDEM-X Interferometric Data,” *ISPRS Journal of Photogrammetry and Remote Sensing*, Vol. 38, pp. 21-29, 2012.

[16] P. Rizzoli, B. Bräutigam, T. Kraus, M. Martone, G. Krieger, “Relative height error analysis of TanDEM-X elevation data,” *ISPRS Journal of Photogrammetry and Remote Sensing*, , Vol. 38, pp. 21-29, 2012

[17] B. Bräutigam, P. Rizzoli, M. Martone, M. Bachmann, T. Kraus, G. Krieger, “InSAR and DEM Quality Monitoring of TanDEM-X,” *International Geoscience and Remote Sensing Symposium (IGARSS)*, Munich, Germany, 2012.

[18] G. Krieger, I. Hajnsek, K. Papathanassiou, M. Younis, and A. Moreira, “Interferometric Synthetic Aperture Radar (SAR) Missions employing Formation Flying”, *Proceedings of the IEEE*, 98(5):816-843, 2010.

Study on the Distributed Slope Length for Soil Erosion Prediction at Watershed Scale

Yang, Q. K.,^{1,2} Zhang, H. M.,³ Wang, C. M.¹, Zhao M. D.,¹ Liu Y. M.¹ Wang, L.¹

and Water Conservation Chinese Academy of Sciences
 Ministry of Water Resources, Yangling, Shaanxi, China;
 3. College of Information Engineering, Northwest A & F University Yangling, Shaanxi, China)

(1. College of Urban and Environment, Northwest University, Xi'an, Shaanxi, China; 2. Institute of Soil

Abstract—As the most mature and practical soil erosion prediction models so far in the world, USLE and its derivative models, including RUSLE and CSLE, have been widely applied in the soil erosion inventory and mapping at watershed and regional scale. In the models the impacts of terrain on soil erosion is represented by Length Slope factor (LS), which calculate based on DEM derived slope degree and slope length layers. The extraction of slope and slope length themes, especially the latter, of a watershed for each location is difficulty and key issue in the application of USLE to soil erosion assessment and mapping at watershed and regional scale. The issues reviewed and discussed in this paper include; (1) slope length (USLE slope length), at the slope scale, for soil erosion prediction is a specified term introduced by USLE to represent the influence of slope length to sheet and rill erosion, so the slope length is different from similar concepts in geomorphology and hydrology which is really a flow length in hydrology. (2) Slope length of the distributed basin soil erosion (watershed slope length, in short, WSL) refers to the slope length of erosion of any point within the basin that is consistent with the process of erosion, transportation and settlement of the slope soil within the basin when actual topographical conditions of the basin are taken into consideration; (3) The WSL is an extension of USLE slope length from hill slope to a compound terrain parameter in 3-D dimensional landscape, and orient to the USLE application directly in soil erosion survey and mapping. (4) There are 4 algorithms proposed by researchers, and there are more or lees differences between them, of which the cumulative runoff algorithm by Hickey and Van Remortel is much better than others. (5) the extraction of WSL is mainly influenced by four factors, including DEM resolution, flow direction algorithm, partitioning strategy of DEM datasets, and cut-off methods of slope length; (6) The issues should be further studied include principles and software tools for WSL extraction, variance structures and statistical distribution, uncertainties and applicability analysis of the WSL in the soil erosion study at watershed and regional scale.

Key words—USLE, distributed slope length, DTA, GIS

1 INTRODUCTION

As the most popular soil erosion assessment model, USLE (and RUSLE, CSLE) has been used widely in watershed and regional scale soil erosion survey and mapping^[1-5]. The influence of terrain to soil erosion was measured by length slope factor (LS

factor for short) witch calculated on slope length and slope gradient^[6-8]. And the calculation of slope length based on DEM is one of the difficult questions for the application of USLE in soil erosion survey and mapping at watershed and regional scale. In this paper, slope length at watershed scale discussed systematically, including the concept of distributed slope length for soil erosion prediction at watershed scale (watershed slope length, WSL for short), extraction method, and it's influence factors, in order to improve the calculation method of WSL and boost the study on quantitatively soil erosion assessment and modeling at watershed scale.

2 CONCEPT OF DISTRIBUTED SLOPE LENGTH FOR SOIL EROSION PREDICTION AT WATERSHED SCALE

2.1 Concept of Slope Length for Soil Erosion Prediction

In soil erosion research, slope length is the horizontal distance from the source of runoff to a deposition place where slope decrease to some degree or to an well-defined channel (including nature and man-made channel)^[14]. In field survey, it is measured through several typical profiles^[7]. As in Fig.1, the distances from A' to B' and B' to C' (λ_1 and λ_2) refers to slope length for soil erosion prediction. And the distance from A' to any point between A' and B' or the distance from B' to any point between B' and C' refers to distributed slope length for soil erosion prediction at watershed scale.

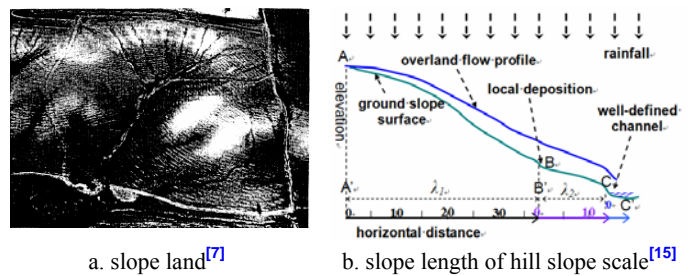


Fig. 1 concept of slope length in USLE

2.2 Concept of Distributed Slope Length for Soil Erosion Prediction at Watershed Scale

In order to use USLE at larger scale, some research should be taken on LS factor at watershed scale [9-11, 13, 16]. According to these researches, the distributed slope length for soil erosion prediction at watershed scale is suitable to the process of soil erosion -- transportation --deposition in watershed and could be calculated at any point in the watershed [17] (Fig. 2 & Fig. 3). In some researchers' options, it could be taken place by specified catchments area [10, 13, 18]

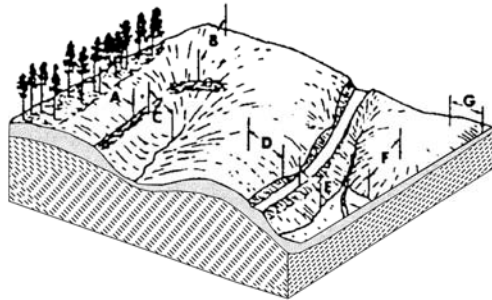


Fig. 2 concept of WSL (Wilson, 1986)

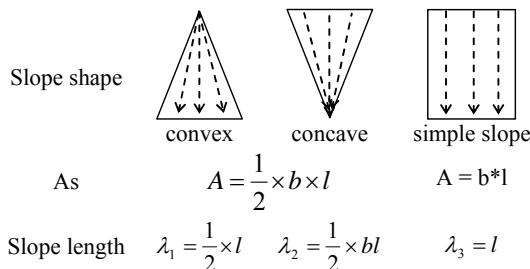


Fig. 3 slope shape and slope length

3. ALGORITHMS OF DISTRIBUTED SLOPE LENGTH FOR SOIL EROSION PREDICTION AT WATERSHED SCALE

Varied algorithms of slope length had been developed according to varied understanding of slope length, including the simplified algorithm proposed by Tang [19, 20], Hickey's cumulative runoff algorithm [21, 22], the algorithm based As [10, 13, 23], algorithm based on flow length [24], and the method based on classification of terrain proposed by Gallant [25]. The differences among the varied algorithms are shown in Fig.4. And Hickey's algorithm seems to be better. In order to calculate distributed slope length for soil erosion prediction at watershed scale, the authors developed a software named LS_Tool based on algorithms proposed by Hickey and van Remortel [21, 22], and partial code provided by Remortel.

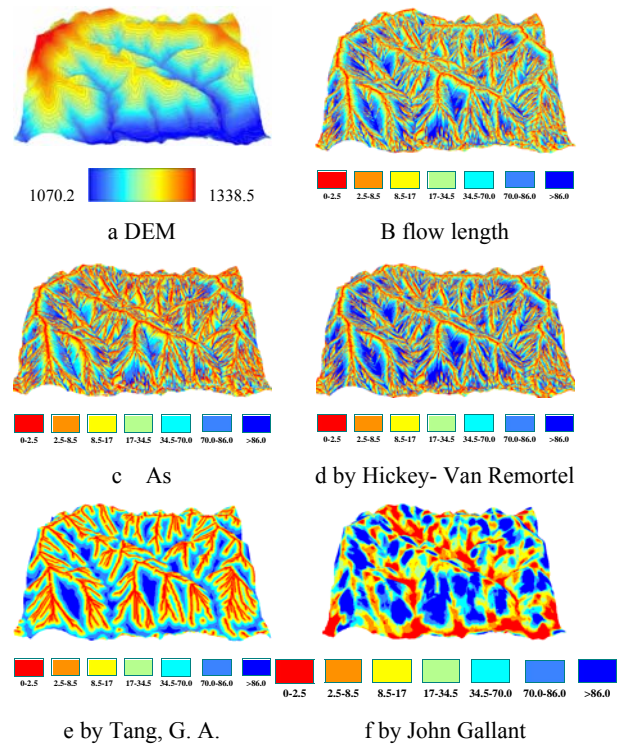


Fig. 4 simple comparisons of SWL algorithms

4. IMPACT FACTORS OF DISTRIBUTED SLOPE LENGTH FOR SOIL EROSION PREDICTION AT WATERSHED SCALE

The studies show that, the extraction of WSL was mainly influenced by resolution of DEM [27-29], flow direction algorithm [26] and slope length cut off methods. With resolution became coarser, WSL increased. And WSL based on single flow direction algorithm is shorter than that based on multiple flow direction algorithm, and the variance of surface is larger than the latter (Tab.1).

Tab.1 Relationship between terrain parameters and flow direction algorithms [26]

terrain parameters	mean	variance
single flow direction algorithm		
As (m ² /m)	287.15	30.27
multiple flow direction algorithm		
As (m ² /m)	354.25	24.05

5. ABOUT FURTHER STUDIES

Considering the importance of WSL in soil erosion assessment and mapping, several topics should be researched in the future, including algorithms of WSL, spatial and statistic characteristics of WSL, uncertainties of WSL and the applicability analysis of WSL.

ACKNOWLEDGMENT

This research was supported by Natural Science Foundation of China project (Estimating Spatially Distributed Slope Length at Watershed for Soil Erosion Assessment41071188; and Re-scaling of Slopes Derived from Lower Resolution DEMs for Regional Soil Erosion Modeling, 40971173)

REFERENCES

- [1]Lu, H., Prosser, I. P., Moran, C. J., Gallant, J. C., Priestley, G., Stevenson, J. G. Predicting sheetwash and rill erosion over the Australian continent [J]. *Australian Journal of Soil Research*, 2003, 41(6): 1037-1062.
- [2]Yang, D., S. Kanae, T. Oki, T. Koike, K. Musiak. Global potential soil erosion with reference to land use and climate changes [J]. *Hydrological Processes*, 2003, 17: 2913-2928.
- [3]Hammad, A. A. Watershed erosion risk assessment and management utilizing revised universal soil loss equation-geographic information systems in the Mediterranean environments [J]. *Water and Environment Journal*, 2009, 25(2): 149-162.
- [4]CHENG Lin, YANG Qinke, XIE Hongxia, WANG Chunmei, GUO Wei-ling. GIS and CSLE Based Quantitative Assessment of Soil Erosion in Shaanxi, China [J]. *Journal of Soil and Water Conservation*, 2009, 23(5): 61-66.
- [5] XIE Hongxia, LI Rui, YANG Qinke, LI Jing, LIANG Wei. Effect of Returning Farmland to Forest (Pasture) and Changes of Precipitation on Soil Erosion in the Yanhe Basin [J]. *Scientia Agricultura Sinica*, 2009, 42(2): 569-576.
- [6]Wischmeier, W. H., Smith, D. D. Predicting rainfall erosion losses: A Guide to conservation planning [M]. *USDA Agric. Handb. No 537*, 1978.
- [7]Renard, K. G., Foster, G. R., Weesies, G. A., McCool, D. K., Yoder D. C., et al. Predicting rainfall erosion by Water: A Guide to conservation planning with the Revised Universal Soil Loss Equation (RUSLE) [M]. In: *USDA Agric. Handb. No 703* [M] 1997.
- [8]Liu, B. Y., Zhang, K. L., Xie, Y. A empirical soil loss equation [M]. In: *Process of soil erosion and its environment effect volume II 12th ISCO* [M] Beijing: Tsinghua press, 2002. 143-149.
- [9]Williams, J. R., Berndt, H. D. Determining the universal soil loss equation's length-slope factor for watersheds [M]. In: *Soil Erosion: Prediction and Control* [M], Foster, G. R., Editor: *Soil Conservation Society of American*, Iowa, 1977. 217-225.
- [10]Moore, I. D., Burch, G.J. Physical basis of the length-slope factor in the Universal Soil Loss Equation [J]. *Soil Science Society of America Journal*, 1986, 50(5): 1294-1298.
- [11]Wilson, J. P. Estimating the topographic factor in the universal soil loss equation for watersheds [J]. *Journal of Soil and Water Conservation*, 1986, 41(3): 179-184.
- [12]Griffin, M. L., Beasley, D. B., Fletcher, J. J., Foster, G. R. Estimating soil loss on topographically nonuniformed field and farm units [J]. *Journal of Soil and Water Conservation*, 1988, 43(4): 326-331.
- [13]Moore, I. D., Wilson, J.P. Length-slope factors for the Revised Universal Soil Loss Equation: Simplified method of estimation [J]. *Journal of Soil and Water Conservation*, 1992, 47(5): 423-428.
- [14]Smith, D. D., Wischmeier, W. H. Factors affecting sheet and rill erosion [J]. *American Geographer Union Trans*, 1957, 38: 889-896.
- [15]Horton, R. Erosional Development of Streams and Their Drainage Basin; Hydrophysical approach to quantitative morphology [J]. *Geological Society of America Bulletin*, 1945, 56(3): 275-370
- [16]Rodríguez, J. L., G., 1 and Martín C. Giménez Suárez2 Estimation of Slope Length Value of RUSLE Factor L Using GIS [J]. *Journal of Hydrologic Engineering*, 2010, 15(9): 714-717
- [17]YANG Qinke, GUO Weiling, ZHANG Hongming, WANG Lei, CHENG Lin, LI Jun. Method of Extracting LS Factor at Watershed Scale Based on DEM [J]. *Bulletin of Soil and Water Conservation*, 2010, 30(2): 203-206.
- [18]Moore, I. D., Wilson, J.P. Reply to comments by Foster on "Length-slope Factors for the Revised Universal Soil Loss Equation: Simplified Method of Estimation" [J]. *Journal of Soil and Water Conservation*, 1994, 49(5): 174-80.
- [19]TANG Guoan, CHEN Zhengjiang, ZHAO Mudan, LIU Wanqing, LIU Yongmei. The Spatial analysis Method of GIS Based on ARCVIEW [M]. Beijing: *Science Press*, 2004. p174-175.
- [20]CAO Longxi, FU Suhua. A Comparison of Methods for Computing Slope Length Based on DEM [J]. *Bulletin of Soil and Water Conservation*, 2007, 27(5): 58-62.
- [21]Hickey, R., Smith, A., Jankowski, P. Slope Length Calculations from a DEM Within ARC/INFO GRID [J]. *Computers, Environment and Urban Systems*, 1994, 18(5): 365-380.
- [22]van Remortel, R. D., Maichle, R. W., Hickey, R. J. Computing the LS factor for the Revised Universal Soil Loss Equation through array-based slope processing of digital elevation data using a C++ executable. [J]. *Computers & Geosciences*, 2004, 30(9-10): 1043-1053.
- [23]Desmet, P. J. J., Govers G. A GIS procedure for automatically calculating the USLE LS factor on topographically complex landscape units [J]. *Journal of Soil and Water Conservation*, 1996, 51(5): 427-433.
- [24]JIN Bei, LIU Xuejun, ZHEN Yan, LI Haoshu. Analysis of Slope Length Extracted from Grid-based Digital Elevation

- Model in ArcGIS Environment [J]. JOURNAL OF GEO-INFORMATION SCIENCE, 2010, 12(5): 700-706.
- [25] Gallant, J. Terrain scaling for the Continental Scale Soil Erosion Modeling [C]. In: Proceedings of MODSIM 2001: International Congress on Modelling and Simulation. Canberra, Australia: Modelling and Simulation Society of Australia and New Zealand: 925-930. Canberra. 2001.
- [26] Wolock, D. M., McCabe, G. J. . Comparison of Single and Multiple Flow Direction Algorithms for Computing Topographic Parameters in TOPMODEL [J]. Water Resources Research, 1995, 31(5): 1315-1324.
- [27] Guo Weiling, Yang Qinke, Cheng Lin, Li Jun. Re-scaling method of slope length factor in the soil erosion assessment of regional scale [J]. Science of Soil and Water Conservation, 2010, 8(4): 73-78.
- [28] Sørensen, R., Seibert, J. Effects of DEM resolution on the calculation of topographical indices: TWI and its components [J]. Journal of Hydrology, 2007, 347(1-2): 79-89.
- [29] Pradhan, N. R., Ogden, F. L., Tachikawa, Y., et al. Scaling of slope, upslope area, and soil water deficit: Implications for transferability and regionalization in topographic index modeling [J]. Water resources research, 2008, 44(12): W12421.
- [30] Gertner, G. Z. Uncertainty Propagation and Partitioning in Spatial Prediction of Topographical Factor for RUSLE [C]. In: Fourth International Conference on Spatial Uncertainty. Amsterdam. 2000.
- [31] Wang, G., Fang, S., Shinkareva, S., Gertner, G., Anderson, A. Spatial uncertainty in prediction of the topographical factor for the Revised Universal Soil Loss Equation (RUSLE) [J]. Transactions of the ASAE, 2002, 45(1): 109-118.
- [32] Wang, G., Gertner, G., Parysow, P., Anderson, A. B. Spatial prediction and uncertainty analysis of topographical factors for the Revised Universal Soil Loss Equation (RUSLE) [J]. Journal of Soil and Water Conservation, 2000, 55(3): 374-384.
- [33] Wang, G. X., Gertner, G. Z., Fang, S., Anderson, A. B. A methodology for spatial uncertainty analysis of remote sensing and GIS products [J]. Photogrammetric engineering and remote sensing 2005, 71(12): 1423-1432.

Leveraging geomorphometric data and statistical computing to gain complementary insights into complex Earth surface processes

Alexander Brenning
Canada University of Waterloo
brenning@uwaterloo.ca

Novel analysis and prediction methods developed at the intersection between computer science and statistics have been gaining popularity in recent years in Earth surface process modelling using geomorphometric predictor variables. These newer approaches promise to improve predictive performances by overcoming the limitations of statistical models, making better use of highly correlated and interacting predictors such as terrain attributes calculated at different resolutions. However, these possible (yet not guaranteed) improvements come at the cost of potentially overfitting to the training data, making the interpretation of empirical relationships difficult, and all this at a high computational cost. This talk discusses the potential and pitfalls of novel statistical and machine-learning methods in the context of landslide susceptibility modeling based on (mainly) geomorphometric predictor variables. Spatial cross-validation and permutation-based variable importance measures are presented as key tools in this context. Their open-source implementation in the statistical software R and integration with GIS software are introduced. It is argued that traditional statistical and newer machine-learning techniques can provide complementary insights into complex environmental relationships.

Content-based landscape retrieval using geomorphons

Jaroslav Jasiewicz
 Geocology and Geoinformation Institute
 Adam Mickiewicz University
 Dziegielowa 27, 60-680 Poznan, Poland
 jarekj@amu.edu.pl

Pawel Netzel
 Department of Climatology and Atmospheric Protection
 University of Wroclaw
 Kosiby 6/8, 51-621, Wroclaw, Poland
 netzelpl@ucmail.uc.edu

Tomasz F. Stepinski
 Space Informatics Lab
 University of Cincinnati
 Cincinnati, OH 45221-0131, USA
 stepintz@uc.edu

Abstract—We introduce a concept of content-based landscape retrieval (CBLR). Our CBLR system retrieves morphometrically similar landscapes from a large DEM thus acting as a search engine for landscapes. The system works on the principle of query-by-example, a reference landscape is given and the system outputs a map showing degree of similarity between a reference and all the other local landscapes across the spatial extent of the DEM. Landscape is defined as pattern of landform elements. A DEM is converted into a map of landform elements using the geomorphons method. The core of the CBLR is the similarity function between two landscapes that encapsulates a degree to which their patterns of landform elements correspond to each other. The search relies on exhaustive evaluation of similarity using an overlapping sliding window approach. In the featured case study we use our method to delineate a spatial extent of the characteristic landscape formed by the end moraine associated with the latest glaciations across the country of Poland. Good agreement is found between the region delineated by our method and a range of end moraine manually delineated from geomorphic, geological, and paleogeographical information. The CBLR can be implemented as a GeoWeb application and serve as a rapid and convenient tool for exploration of very large DEM datasets.

I. INTRODUCTION

Large archives containing medium resolution (10-100 m/cell) digital elevation models (DEM) datasets of continental or global extent are now readily available (see, for example, DEM Explorer <http://ws.csiss.gmu.edu/DEMExplorer/>). Popular datasets include The Shuttle Radar Topography Mission (SRTM) and Aster Digital Global Elevation Map (GDEM). However, at present, these archives are predominantly used to access topographic information for sites for which a prior knowledge of

their relevance already exists. The full informational potential of these archives is not fulfilled due to lack of intelligent methods aimed at their exploration and knowledge discovery. Possible approaches to the development of such methods include terrain classification and query-by-example. Previous work [1-3] has focused on development of algorithms capable of automatic delineation of physiographic units from a DEM. Resultant maps indeed utilize the entire dataset, but tend to be too generalized to allow for meaningful exploration and discovery.

In this paper we propose a content-based landscape retrieval (CBLR) system – a query-by-example method that identifies all locations in a DEM characterized by landscapes that are similar to a given example or a set of examples. The word “content” in the CBLR indicates that a query is based exclusively on quantitative values extracted from the DEM and not on any metadata. Proposed system is a modification of our earlier work [4] on query and retrieval of similar land cover scenes from the National Land Cover Dataset 2006 and is inspired by Content-Based Image Retrieval (CBIR) systems extensively studied [5] in the context of natural image retrieval. By not being restricted to a set of pre-defined classes, the CBLR system has much higher discriminating power than auto-generated physiographic maps. This makes it a great tool for exploration of large DEMs with capacity for meaningful discovery. Ultimately, the system is envisioned as a web-based real time “search” application for landscapes.

In our context, “landscape” means a pattern of landform elements over a scene of interest. In the rest of this paper we use term landscape in this specific morphometric meaning. Two scenes have similar landscapes if they have similar patterns of landform elements. Thus, the CBLR system must consist of a method of delineating landform elements, a similarity function

capable of comparing spatial patterns of those elements, and an implementation of spatial query. For automatic delineation of landform elements we use the geomorphons method [6]. This robust and computationally efficient method converts DEM into a geomorphometric map (gmphMap) – a categorical raster indicating the most common landform elements. The gmphMap can be thought of as an interpreted map of topography and is ideally suited for our CBLR system. (For an example of a gmphMap and its comparison to a physiographic map see <http://sil.uc.edu/dataeye/>). We developed a pattern similarity function appropriate to morphometric landscapes and designed a spatial retrieval system to execute a query and display its results.

II. METHODOLOGY

A. Mapping landform elements

The input to the method is a DEM dataset over the region of interest (for example, a given country, continent, or the entire globe). The first step is to convert a DEM to the gmphMap. This is achieved using a public domain GRASS module *r.geomorphons* (<http://sil.uc.edu/downloads.html>). Geomorphons are pattern recognition-based method for delineation of landform elements. The method yields the gmphMap – a raster of the same size as the input DEM with each cell assigned one of ten common landform elements labels: flat, peak ridge, shoulder, slope, spur, hollow, footslope, valley and pit. The method has two parameters: the search radius L and the flatness threshold t . The search radius determines the maximum spatial scale at which any landform element is extracted and the flatness threshold is a angle of a slope below which a terrain is considered flat.

B. Similarity between two landscapes

A “tile” T is defined as a small subset of the entire gmphMap. For convenience we use square-shaped tiles with the of size n by n cells. Each cell is labeled by one of 10 landform elements labels. A spatial pattern of different labels (commonly visualized by different colors on the gmphMap) constitutes a landscape. Note that the size of the tile indicates a spatial extent over which landscape is captured. A query Q is a particular tile containing a landscape of interest.

Like in most CBIR methods, we don’t calculate similarity between two tiles directly from the values of their cells, but rather from the histograms of their “primitive features.” Histograms are widely used in the CBIR because of their rotational invariance. Primitive features are elements of pattern that are counted to form a histogram. For example, they could be just individual cells; counting cells of different labels produces a histogram reflecting “composition” of landscape. However, in this paper we use pairs of neighboring cells as primitive features (4-connected neighborhood is assumed). Because there are 10 different labels in the gmphMap, there are 55 different possible pairs, examples include: flat-flat, flat-slope, slope-peak, etc. Pairs are extracted

for each tile and counted to form a histogram that encapsulates the pattern of the tile. By showing which connections between landform elements are most common such histogram emphasizes a texture of a given landscape.

Calculating similarity between two landscape tiles T and Q reduces to calculating similarity between the two histograms T^h and Q^h representing their patterns. It is customary to compare histograms using distance (dissimilarity) rather than a similarity metric. Choosing the best distance metric is largely empirical decision dependent on the actual retrieval system. In this paper we use normalized Wave Hedges distance metric [7] which takes values from 0 (identical histograms) to 1 (histograms do not share bins). The formula for Wave Hedges similarity (1-distance) is:

$$\text{sim}(T^h, Q^h) = \frac{1}{n} \sum_{i=1}^n \frac{\min(T_i^h, Q_i^h)}{\max(T_i^h, Q_i^h)}, \text{ if } \max(T_i^h, Q_i^h) > 0$$

The measure compares corresponding bins of two histograms and compute a fraction equal to (smaller bin)/(larger bin). If the two bins are both 0 the fraction is equal to 1. The bin comparison values are summed and the sum is divided by the number of bins. An overall similarity is built from similarities between individual features. Note that such similarity measure is not sensitive to absolute composition of landform elements in a landscape; for example, two landscapes dominated by the flat element may still be measured as significantly different if other, minor elements are different.

C. Query execution

A query over the entire dataset uses a square grid with the resolution of k cells superimposed on the entire spatial extent of the DEM. This grid forms a basis for a similarity map resulting from the query. The query is executed by means of exhaustive evaluation - the value of similarity is calculated between the query tile and all the local tiles assigned to a similarity grid. If $n > k$ the local tiles overlap. The resulting similarity raster (much coarser than an original DEM) can be displayed as a map showing how a degree of similarity to a query varies over the entire region.

III. CASE STUDY

In order to demonstrate a practical application of our CBLR system we applied it to a DEM covering the country of Poland. The input is a 1" integer DEM which was converted by adaptive smoothing to the 30m resolution floating-point terrain model. The final DEM has the size of 21,696 by 24,692 cells. The gmphMap was calculated using search radius $L=40$ cells (1200m) and flatness threshold $t=0.8$ degree. Fig. 1 shows resultant

gmphMap; individual landform elements cannot be seen at this level of resolution, but different physiographic units can be recognized by different tones of colors resulting from different composition and patterns of landform elements. The territory of Poland exhibits a number of different landscapes. In particular, the northern parts of the country is occupied by postglacial landscape and the southern parts by uplands and mountains.

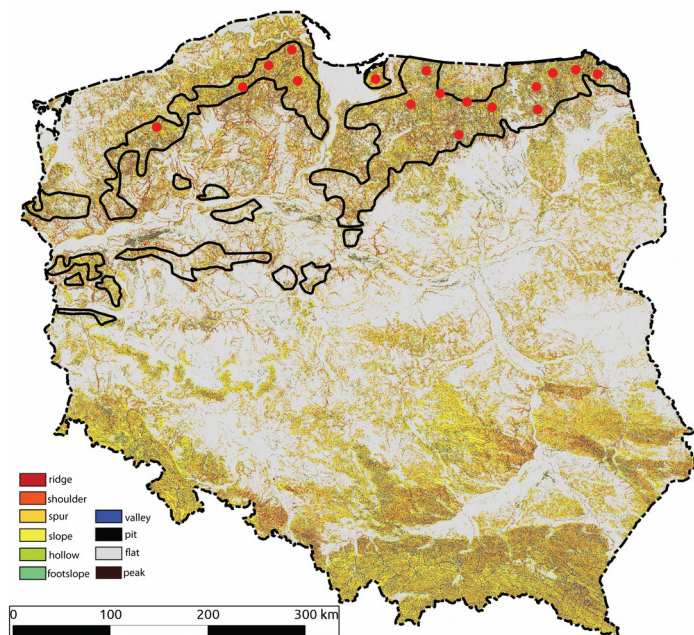


Figure 1. Geomorphometric map (gmphMap) of Poland calculated from the 30m resolution DTM using geomorphons method. Black contours indicate a range of end moraine according to Kondracki [8] and the red dots show location of our queries.

We demonstrate the ability of the CBLR system to delineate a spatial extent of a given landscape by applying it to calculate a region corresponding to end moraine resulting from glacial activity in the marginal zone of Pomeranian/Brandenburg phase. Such landscape, characterized by broad ridges and hills, is a very young surface not yet transformed by a denudation process. Therefore we expect that its morphometric landscape is sufficiently unique for the CBLR system to discriminate it from older surfaces which are also dominated by ridges and hills. On Fig. 1 the black contours indicate the range of end moraine landscape as manually delineated [8] on the basis of geomorphological as well as geological and paleogeographical information. This serves as a reference to our results.

The execution of a query was constructed using $n=512$ and $k=64$ cells. This means that we assess landscape on spatial scale of ≈ 15 km and we use similarity grid having size of ≈ 2 km. Thus, we sample local landscape with a high degree of

overlapping. In its basic form a query-by-example works by choosing a single reference landscape and calculating a similarity map showing spatial distribution of similarity between this single example and the local landscapes. However, in a landscape formation, like the end moraine, not every location has exactly the same character of landscape as local variations are present. Therefore, it makes more sense to select a number of different queries, calculate similarity map for each one individually and integrate the results to obtain a region with local landscapes defined by similarities with all examples.

We have selected 17 examples (queries) from the end moraine range; their locations are shown by red dots on Fig. 1. The resultant similarity maps were combined in two different ways. In the first the minimum from amongst all 17 local similarity values was assigned as an overall local similarity. Such procedure delineates areas which are most similar to *all* examples. The resultant map is shown on the left panel of Fig. 2. In the second, the median of all 17 local similarity values was calculated and assigned as an overall local similarity. Such procedure delineates areas whose *expected* similarity to the queries is high. The resultant map is shown on the right panel of Fig. 2. Both similarity maps cover the entire area of Poland, areas with high values (red colors) delineate a range of end moraine landscape. We observe that our median method delineated a region with high overlap ($>70\%$) with a manually delineated reference. Small areas in southern Poland also show high average similarity despite having no geological connection with end moraine. As expected, the minimum method is more restrictive, but its map does not show high values of similarity beyond the putative range of end moraine. Overall, the delineation of end moraine is good considering that our method takes into account only the DEM without any additional geologic information.

IV. CONCLUSIONS

The CBLR offers a search engine-like capabilities for landscapes embedded in large DEMs. In most applications a query is taken from the same DEM, but it may be taken from another source including a simulated landscape. In addition, a query may not correspond to any landscape at all, but rather be just a histogram of features designed to test a specific hypothesis. Unlike other, more familiar search tools, the CBLR does not output a short list of best-matching landscape locations, but rather a similarity map showing a degree of similarity between a query and every other landscape in the DEM. Such presentation of search results is more appropriate for spatial dataset where geographical context matters.

The CBLR is an ideal tool for rapid exploration of large DEMs. For such a tool to be practical it needs to be implemented as a GeoWeb application so it can be accessed by anyone. We plan on offering such application in the near future; it would work similarly to LandEx [9] (<http://sil.uc.edu/landex/>) - our existing tool for searching land cover across the United States.

The performance of the CBLR system depends predominantly on selection of features and a form of pattern similarity function. In addition to the features and the similarity function presented here we have also experimented with features described in [4] and the Jensen-Shannon similarity function. Such choice gives similar results in application to the case study

presented here, but for other searches its performance was worse. Future research will evaluate other combinations of features and similarity functions. Note that search results will depend on the spatial scale of landscape; a scale used in this paper is about 50% larger than that advocated by Hammond [10] and within a range of macro landforms.

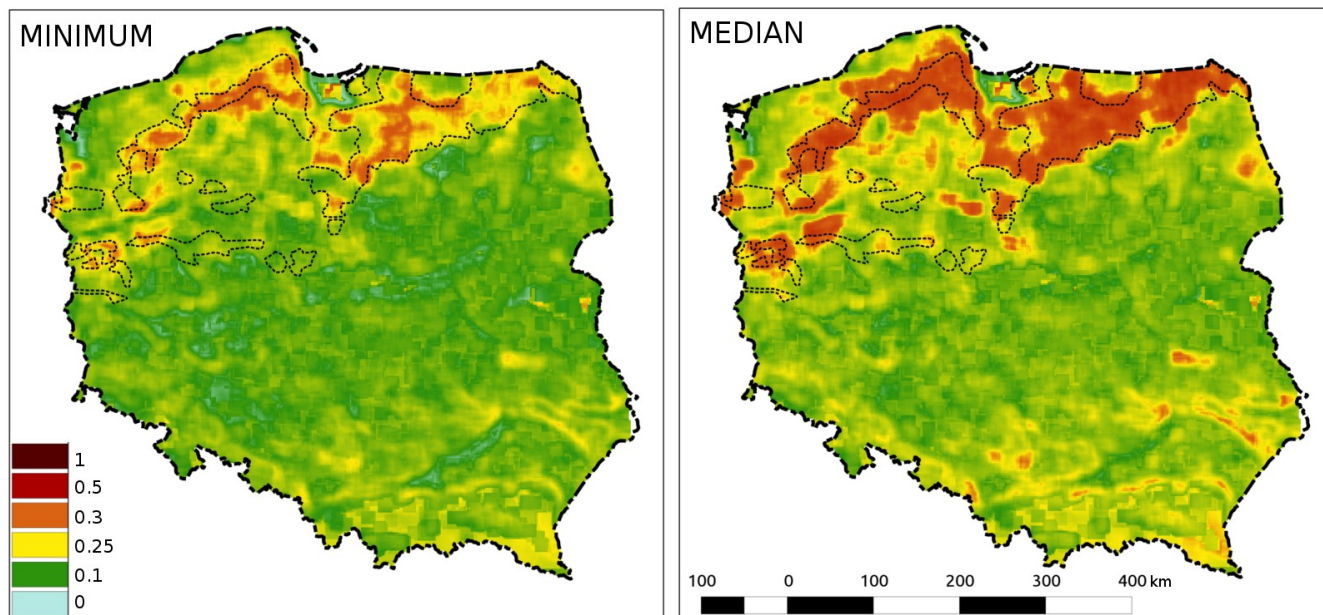


Figure 2. Landscape similarity maps constructed to delineate the range of end moraine landscape. (Left) Map obtained by taking a minimum similarity from all the queries. (Right) Map obtained by calculating a median similarity. Black contours indicate a range of end moraine according to Kondracki [8]

ACKNOWLEDGMENT

This work was supported partially by the National Science Foundation under Grant BCS-1147702 and National Science Centre DEC-2012/07/B/ST6/012206 and UC Space Exploration Found.

REFERENCES

[1] Dikau, R., Brabb, E.E, Mark, R.M., 1991."Landform classification of New Mexico by computer." Open File Report 91-634. U.S Geological Survey. .
 [2] Iwahashi, J., Pike, R., 2007. "Automated classification of topography from DEMs by an unsupervised nested-means algorithm and three-part geometric signature." *Geomorphology* 86, 409-440.
 [3] Dragut, L., Eisank, C., 2012. "Automated object-based classification of topography from SRTM data." *Geomorphology* 141-142, 21--23.
 [4] Jasiewicz, J., Stepinski, T.F. 2013. "Example-Based Retrieval of Alike Land-Cover Scenes From NLCD2006 Database." *IEEE Geoscience and Remote Sensing Letters* 10(1), pp. 155-159

[5] Datta, R., Joshi, D., Li, J., Wang, J.Z. 2008. "Image Retrieval: Ideas, Influences, and Trends of the New Age." *ACM Computing Surveys*, 40,1 —60.
 [6] Jasiewicz, J., Stepinski, T.F. 2013. "Geomorphons -a pattern recognition approach to classification and mapping of lanforms." *Geomorphology* 182, pp. 147-156.
 [7] Cha, S.-H. 2007. "Comprehensive survey on distance/similarity measures between probability density functions." *International Journal of Mathematical Models and Methods in Applied Sciences*, 1(4), 300-307.
 [8] Kondracki, J., 2002. "Geografia regionalna Polski." 3rd Edition. Wydawnictwo Naukowe PWN, Warszawa.
 [9] Stepinski, T.F, Netzel, P., Jasiewicz, J., Niesterowicz, J. 2012. "LandEx - A GeoWeb-based Tool for Exploration of Patterns in Raster Maps, GIScience 2012 Conference. <http://www.giscience.org/proceedings/>
 [10] Hammond, E.H. 1964. "Analysis of properties of land form geography: an application to broad-scale land form mapping." *Annals of the Association of American Geographers* 54, 11-19.

High-Res Digital Surface Modeling using Fixed-Wing UAV-based Photogrammetry

Niels Anders, Rens Masselink, Saskia Keesstra
Soil Physics and Land Management
Wageningen University
Wageningen, The Netherlands
niels.anders@wur.nl

Juha Suomalainen
Lab for Geo-Information Science and Remote Sensing
Wageningen University
Wageningen, The Netherlands

Abstract—High-res multi-temporal digital terrain data is a potential valuable source for geomorphological research and/or monitoring studies, yet often difficult and costly to obtain. Unmanned Aerial Vehicles (UAVs) provide a promising and flexible platform for the acquisition of multi-temporal digital surface models (DSMs) and orthorectified airphotos. In this research we demonstrate preliminary results with UAV-based photogrammetry with a fixed-wing aircraft, and we assess the quality of derived DSMs and terrain properties in a geomorphologically active agricultural catchment near Pamplona, N-Spain. In 4 sequential flights 200 ha was captured at 3 cm ground sampling distance (GSD ~ 185 m flight altitude) with which a 12 cm DSM was created. Subsequently, a single flight at 90 m altitude enabled creating a DSM of 7 cm spatial resolution of a subarea. Both datasets have been compared by visualizing small rills and a superficial landslide. Results suggest that 3 cm GSD was found sufficient for identifying small-scale geomorphological activity. Yet, small rills and tractor tracks which are potentially interesting for hydrological or hydrogeomorphological studies required smaller GSD. The preliminary results show high potential of the utilization of UAVs in different domains of geomorphological research.

I. INTRODUCTION

Digital Surface Models (DSMs) are recognized tools in geomorphology. Modern technology to generate high-res digital surface models is frequently based on LiDAR data or photogrammetry using aerial stereophotos. Data acquisition can however, be costly, especially when repeated flight campaigns are required. Yet, multi-temporal data can potentially be very valuable for e.g. mapping geomorphological features and analyze their change over time [1,2] or for analyzing effects of land management to landscape development.

Unmanned Aerial Systems (UAS) provide a promising tool for the acquisition of such multi-temporal aerial stereophotos and

high-resolution digital surface models. A UAS often comprises an Unmanned Aerial Vehicle (UAV) with autopilot navigation and desktop software. In general two types of light-weight UAVs are currently commercially available, i.e. multicopters and fixed-wing aircrafts. Multicopters can often carry more payload, resulting in the possibility of installing more advanced sensing systems [e.g. 3], but their coverage area is limited [e.g. 4] due to their relatively low flight speed and high battery drain. Fixed-wing UAVs, equipped with light-weight digital cameras are therefore more suitable for capturing stereographic images of larger areas.

This study presents experiences with a fixed-wing UAV and shows first results on digital surface modeling and the visualization of geomorphological features. It shows the entire work flow of UAV photogrammetry and illustrates the effect of flight altitude on the detail of derived digital surface models and terrain properties in a gully system and a landslide complex.

II. STUDY AREA

The UAS was tested in the agricultural catchment of Latxaga, near the municipality of Beortegui, approximately 20 km east of Pamplona, N-Spain (Fig. 1). The catchment area is approximately 200 ha, altitude ranges from 500-690 m.a.s.l. and mean annual precipitation is 800-850 mm. The area is underlain by marls with mostly clayey soils. The area is characterized by sheet, rill and occasional gully erosion. The relatively flat valley bottoms provide temporal storage of sediment coming from adjacent hillslopes. After wet periods shallow landslides are common.

III. MATERIALS AND METHODS

A MAVinci Sirius 1 fixed-wing UAV was used with on board a Panasonic Lumix GX1 16 MP digital camera and 20 mm lens. The wing span is 1.6m and the total weight of the aircraft

including camera is approximately 2.6 kg. Average ground speed approximates 60 km/h depending on wind conditions. The camera is able to collect 8-bit JPEG and RAW images but in this study only JPEG images were used. The work flow and characteristics of the Sirius I model are typical for fixed-wing solutions.

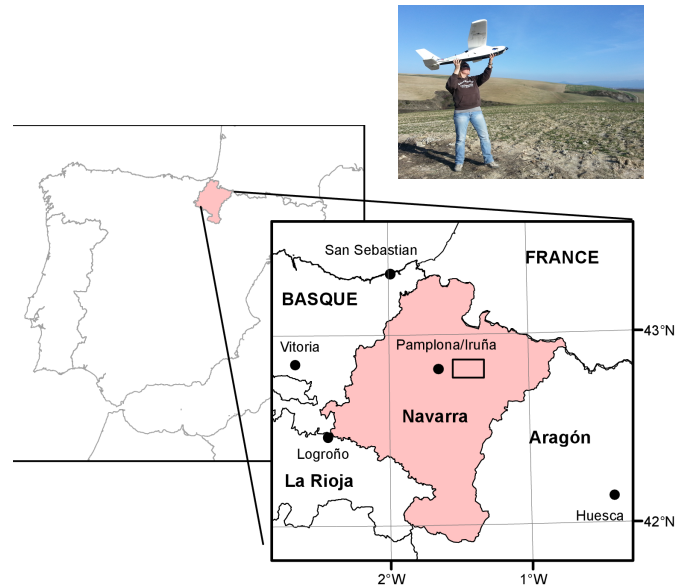


Figure 1: Left and bottom) The study area is located in the Latxaga catchment, approximately 20km east of Pamplona, Spain; Top-right) Typical hand-launch of the UAV in the study area.

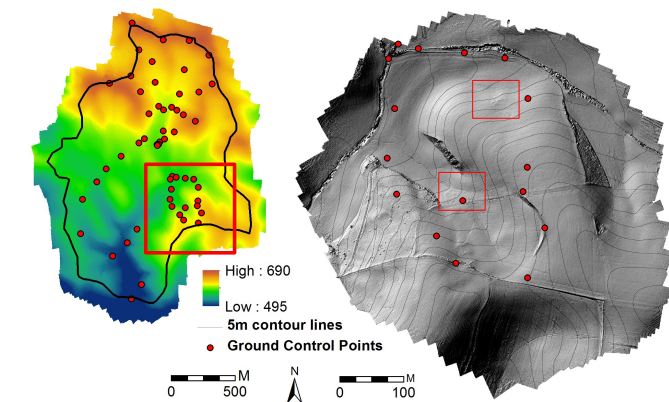


Figure 2: Left) 12 cm DSM of the entire catchment area (200 ha), highlighted by the black outline. The red rectangle shows the location of the detailed study area; Right) 7 cm DSM of a subset (20 ha) of the catchments area. The red rectangles show the locations of the subsets in Fig. 3

The UAV comes with desktop software to prepare flight plans (i.e. 3D GPS waypoints) based on amount of overlap and camera specifications. The flight lines are optimized for minimizing flight time, wind direction or topography. Flight plans were prepared to obtain 85% image overlap in flight direction and 60% side overlap. The UAV is launched by hand and flight lines are followed with an autopilot GPS waypoint navigation. Images were taken at specific time intervals to obtain the predefined overlap. Maximum flight time is typically 45-60 minutes with a single battery, depending on wind condition. To ensure sufficient time for safe landing, flight time was maximized to 35 minutes. To reach 3 cm ground sampling distance (GSD) for the entire catchment flights were carried out at an average altitude of 185 m above the surface. A smaller area was selected for higher resolution imagery (1.6 cm GSD) which was flown at 90 m. In total 50 ground control points (GCPs) were collected, including 10 GCPs in the selected area, which have been used for DSM alignment and accuracy assessment.

Post-processing was carried out with Agisoft PhotoScan Professional 0.9 on a modern processing PC (6-core Intel Xeon processor, 40 GB RAM, 4 GB GeForce GTX680 videocard). PhotoScan is able to semi-automate the processing of ortho-photos and digital surface models. The work flow consists of 1) image matching and calculating tie points to create a sparse point cloud using 'Structure-from-Motion' [5] (automated, uses embedded GPS and camera orientation), 2) positioning of GCPs in the images to georeference and fine-tune the initial point cloud (assisted, estimated GCP location is projected on top of raw images which eases GCP positioning), 3) calculating geometry from the initial tie points using multi-view stereopsis [6] to create a dense point cloud and digital surface models (automated), and 4) texture rendering for creating orthophotos (automated).

IV. RESULTS

With the current setup it was possible to capture the entire 200 ha catchment with 3 cm GSD in a single day, in four sequential flights, totaling approximately 5000 images (Fig. 2-left). Post-processing took 36 hours and DSM resolution was automatically optimized to 12 cm resolution. The estimation of optimal cell size is done in the PhotoScan software and is based on average point density. Despite registration of detailed topographic variation (Fig. 3-bottom) absolute deviations from dGPS points were considered too high (~45 cm) for monitoring applications on subtle geomorphological activity.

A single flight at an average flight altitude of 90 m above the ground surface collected approximately 1200 images with 1.5 cm GSD covering approximately 35 ha. Post-processing required about 12 hours and optimal DSM cell size was determined at 7 cm. Also here, the absolute deviations from dGPS points were considered too high (~35 cm). Table 1 summarizes the DSM specifications per altitude and the standard deviation from dGPS.

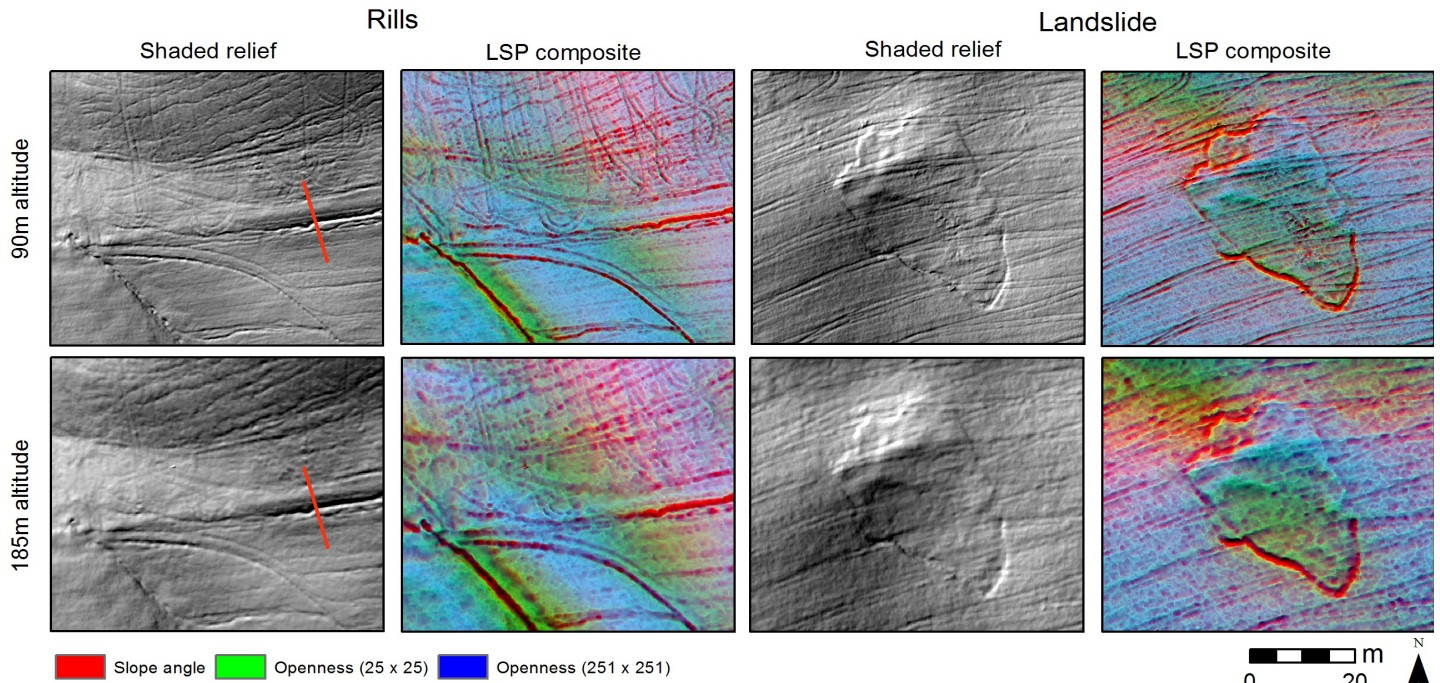


Figure 3: The left figures show the shaded relief images and the right figures show the LSP composites. The red line in the left figures shows the location of the profiles in Fig. 4. Especially the LSP composites show high detail of geomorphological features such as gullies, rills and landslides in the area.

TABLE I. SUMMARY OF FLIGHT AND DSM SPECIFICATIONS

Flight altitude [m]	GSD [cm]	DSM cell size [cm]	Standard deviation [cm]
90	1.5	7	35
185	3	12	45

In Fig. 3 the gray scale subplots show shaded relief maps of rills and a landslide. The color plots show a false-color composite (or Land Surface Parameter, LSP, composite) of slope angle (as red) and topographic openness measured with a 25 x 25 and 251 x 251 cells moving window (as green and blue, respectively). The LSP composites clearly show the topographic variation in high detail. The upper and lower figures in Fig. 3 represent the 7 and 12 cm DSM, respectively. Especially the 7 cm DSM contains subtle features such as rills and tractor tracks. Also landslides are captured in high detail showing sharp edges near the back scarp and the deposition area.

Fig. 4 presents cross profiles of various rills of different dimensions. It is evident that the largest/deepest rills are registered well in both DSMs. The terrain attribute profiles indicate that smaller rills are not well visible in the 12 cm DSM and require higher spatial resolution.

V. DISCUSSION

At the time of writing, vertical accuracies of the 7 and 12 cm surface models are 35 and 45 cm, respectively, which are too high for measuring subtle topographic changes or monitoring studies regarding e.g. rill erosion measurements. Earlier research [7] shows that overall accuracy can be as low as 2-4 cm with low flight altitude (40-50m) and high overlap (75-95%). Slightly more noise was expected due to higher flight altitudes and higher relief which results in higher variability in GSD. However, Fig. 3 implies little random noise in the data, based on the fact that the DSM contains subtle topographic features that have been confirmed by field observations. The results suggest high potential of generating accurate DSMs with UAVs. More tests on post processing are required to eliminate high deviations from dGPS measurements.

In this study, images have been collected in 8-bit JPEG format with minimal compression. For geomorphometrical applications JPEG files were considered suitable. However, more tests are encouraged to analyze the added value of RAW images with respect to the detail and accuracy of derived hillslope geometry. With the current setup, RAW images are limited to > 2.5 cm GSD due to UAV ground speed versus camera processing speed.

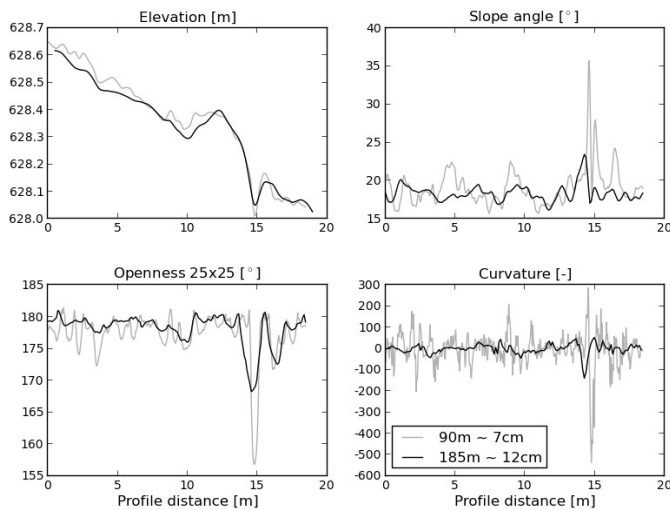


Figure 4: Cross-profiles showing the difference between surface models and derived terrain attributes in smaller and larger rills.

UAV-based DSMs would be valuable for many hydro-geomorphological applications, e.g. in channel connectivity and soil erosion studies. Yet, the amount of data that is produced at smallest DSM resolution may be impractical for large catchment areas with current methods. The 12 cm DSM would likely be suitable for most applications.

Some strengths of fixed-wing UAVs in combination with Structure-from-Motion post-processing are:

- UAVs can be utilized at almost any moment in time, even with (low intensity) rainfall and medium wind speed (< 20 km/h). This makes fixed-wing UAVs flexible for the acquisition of multi-temporal data to study geomorphological processes at fine spatial and temporal scales (e.g. after heavy rainfall events).
- The DSMs contain very high detail for visualizing subtle topographic variation. Narrow and shallow rills are captured which potentially allows detailed modeling of surface flow.
- Continuous developments in making light-weight sensors and increasing UAV payload will allow to equip fixed-wing UAVs with other sensors, such as infrared or thermal cameras and radar. This will enable research in new domains.
- With the exception of marking ground control points, the entire work flow can be automated

In addition, some limitations are addressed:

- GSD is not spatially uniform. The UAV flight lines can be optimized for a single hillslope, but for larger areas in hilly terrain higher parts have considerable smaller GSD

compared to lower situated areas. The final cell size of the DSM is therefore an average of the entire area, but effective resolution is lower in some areas.

- Data quality is highly dependent on the quality and distribution of GCPs. This means that in inaccessible terrain absolute elevation values may be inaccurate.
- When generating points clouds very few ground points are constructed in vegetated areas. This makes it difficult to filter out vegetation points for terrain modeling.
- Processing large areas can be hindered due to large amounts of data. High-end computing or dividing the area into subprojects may be required.

VI. CONCLUSIONS

Fixed-wing UAVs provide a flexible platform for generating multi-temporal surface models. UAVs provide a level of detail that could not have been obtained this easily in the past. Subtle topographic variation is registered so that geomorphological features are visualized in high detail. Yet, more effort is required to better align the surface model to dGPS measurements for more accurate absolute elevation values.

ACKNOWLEDGMENT

This research is part of the Smart Inspectors project funded by the INTERREG IV A program Deutschland-Nederland.

REFERENCES

- [1] Anders, N.S., Seijmonsbergen, A.C. Bouten W., 2011. Segmentation optimization and stratified object-based analysis for semi-automated geomorphological mapping. *Remote Sensing of Environment* 115, 2976-2985.
- [2] Anders, N.S., Seijmonsbergen, A.C., Bouten, W., 2013. Geomorphological change detection using object-based feature extraction of multi-temporal LiDAR data. *IEEE Geoscience and Remote Sensing Letters*, In Press.
- [3] Suomalainen, J., Anders, N.S., Iqbal, S., Franke, J., Wenting, P., Bartholomeus, H., Becker, R., Kooistra, L., 2013. A light-weight hyperspectral mapping system for Unmanned Aerial Vehicles – The first results. *Proceedings of WHISPERS*, 2013.
- [4] Niethammer, U., Rothmund, S., James, M.R., Travelletti, J., Joswig, M. 2010. UAV-based remote sensing of landslides. *International Archive of Photogrammetry and Remote Sensing and Spatial Information Sciences*, Vol. XXXVIII, Part 5. 496-501.
- [5] Fonstad, M.A., Dietrich, J.T., Courville, B.C., Jensen, J.L., Carbonneau, P.E., 2013. Topographic structure from motion: a new development in photogrammetric measurement. *Earth Surface Processes and Landforms* 38-4, 421-430.
- [6] Furukawa, Y.; Ponce, J. Accurate, Dense, and Robust Multi-View Stereopsis. In *Proceedings of the 2007 IEEE Conference on Computer Vision and Pattern Recognition*, Minneapolis, MN, USA, 18–23 June 2007; Volume 1, pp. 1–8.
- [7] Harwin, S., Lucieer, A., 2012. Assessing the Accuracy of Georeferenced Point Clouds Produced via Multi-View Stereopsis from Unmanned Aerial Vehicle (UAV) Imagery. *Remote Sensing*, 4, 1573-1599.

Effects of spatial resolution on slope and aspect derivation for regional-scale analysis

Carlos H. Grohmann
 Institute of Geosciences
 University of São Paulo
 São Paulo, Brazil
 guano@usp.br

Abstract— When performing a regional-scale geomorphometric analysis, one might face a decision on whether to derive morphometric data from a low-resolution DEM or to calculate basic derivatives from a higher resolution dataset and average these data afterwards. This paper investigates differences between morphometric parameters (slope and aspect) derived from a resampled DEM and resampled morphometric data derived from a medium resolution DEM, with examples for three study areas in South America. Using a low resolution DEM for regional scale morphometric analysis is not an optimal choice, since slope attenuation will strongly affect the distribution of calculated values. Unless bounded by computational constraints, one should choose to derive basic morphometric parameters from higher resolution data, and resample it to a coarser resolution as needed.

INTRODUCTION

The widespread availability of medium to high resolution Digital Elevation Models (DEMs) has grown exponentially in the last years. While ASTER GDEM [1] and SRTM [2] provide a global or near-global coverage at medium spatial resolution (30 to 90 m), the forthcoming TanDEM-X will deliver a global dataset with a resolution of 12 m [3] and the Open Topography initiative [4] aim to centralize the distribution of high-resolution (usually less than 5 m) elevation data derived from airborne or ground-based LiDAR.

In the case of a regional-scale analysis, when areas as large as entire continents can be studied [5][6], use of medium/high resolution data may impose computational constraints in processing time, available memory or even software capability to handle large amounts of data.

One common alternative is to use coarser resolution DEMs (such as SRTM30_PLUS [7], with spatial resolution of about 1 kilometer) to derive morphometric data. Another option would be to use medium/high resolution DEMs to derive morphometric

parameters and then resample these parameters to a coarser resolution [8-13].

This paper intends to investigate the differences between morphometric parameters (slope and aspect) derived from a resampled DEM and resampled morphometric data derived from a medium resolution DEM. Examples are presented for three study areas in South America (Fig. 1), one in the Amazon region (gentle, flat topography), one in southeastern Brazil (Minas Gerais State - mixed topography with hills and ranges) and one in the Andes Chain (mountainous relief).

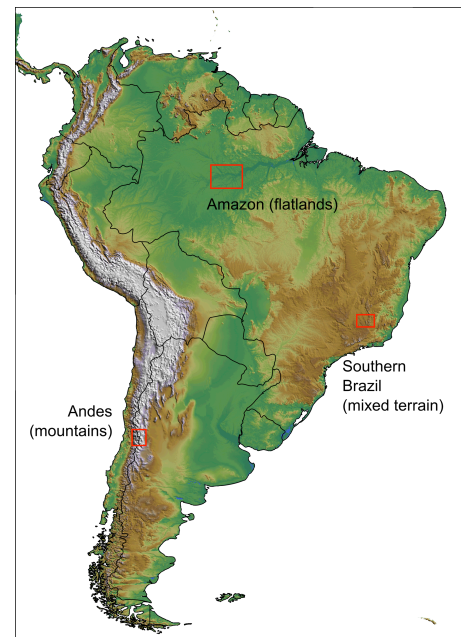


Figure 1. Location of study areas in South America

METHODS

DEM preparation

SRTM V4 elevation data was downloaded from CIAT-CSI website [14] and processed in GRASS-GIS [9]. After merging the data files for each area, a bilinear interpolation was performed at the original resolution of 3 arcsec to avoid artifacts in derived parameters, and slope and aspect were calculated using Horn's formula [16].

Parameters derived from a resampled DEM

For each study area, the base DEM was resampled (averaged) at resolutions of 0°0'10", 0°0'15", 0°0'20", 0°0'25", 0°0'30", 0°0'35", 0°0'40", 0°0'45", 0°0'50" and 0°01'. Slope and aspect were calculated and aspect values were converted from cartesian to azimuth angles [17].

Resampled parameters from a base DEM

In this case, original values of slope and aspect (calculated at 0°0'03" resolution) were resampled at resolutions of 0°0'10", 0°0'15", 0°0'20", 0°0'25", 0°0'30", 0°0'35", 0°0'40", 0°0'45", 0°0'50" and 0°01'. Slope was taken as the average of values and aspect was calculated as a vector mean.

Analysis

The differences between both methods of obtaining aspect and slope values in a coarser resolution was done by comparing: a) density plots [18] of all calculated maps and (Fig. 2) b) plots of the correlation coefficient (R-square) between the original parameter (0°0'03" resolution) and resampled values (Fig. 3).

RESULTS

Fig. 2 shows density plots of the calculated parameters. Shades of green are used for parameters derived from a resampled DEM and shades of blue for resampled morphometric parameters.

Resampling the DEM prior to calculating derivatives will attenuate relief and slope will systematically reduce as the resolution becomes coarser [8,11,12,18]. In all study areas, the density curve's mode shifts towards the y-axis (Fig. 2 A, C) and in the Andes area (mountainous relief), the distribution loses its bimodal character (Fig. 2 E). Resampled slopes do not vary much from the original values, without a significant shift of the mode and maintaining the bimodal character in the Andes area.

Aspect presents a consistent behavior for values calculated from a resampled DEM and for averaged aspect values. In the Amazon area (flat terrain) and in Southeastern Brazil area (mixed terrain), differences between density curves for both methods is

easily noticed, while in mountainous terrain the differences are less distinct.

Correlation plots (Fig. 3) shows that data obtained from averaging the original morphometric parameter (blue lines) has a higher correlation with the original parameter than parameters calculated from an averaged DEM (green lines).

CONCLUSIONS

The data presented in this paper suggests that using a low resolution DEM for regional scale morphometric analysis is not an optimal choice, since slope attenuation will strongly affect the distribution of calculated values.

Unless bounded by computational constraints, one should choose to derive basic morphometric parameters from higher resolution data, and resample it to a coarser resolution as needed.

ACKNOWLEDGMENTS

This study was supported by Brazil's State of São Paulo Research Foundation (FAPESP) grant #09/17675-5. I want to thank John Gallant for the fruitful discussions on the subject and the three reviewers for their criticism and suggestions, which helped to improve this paper.

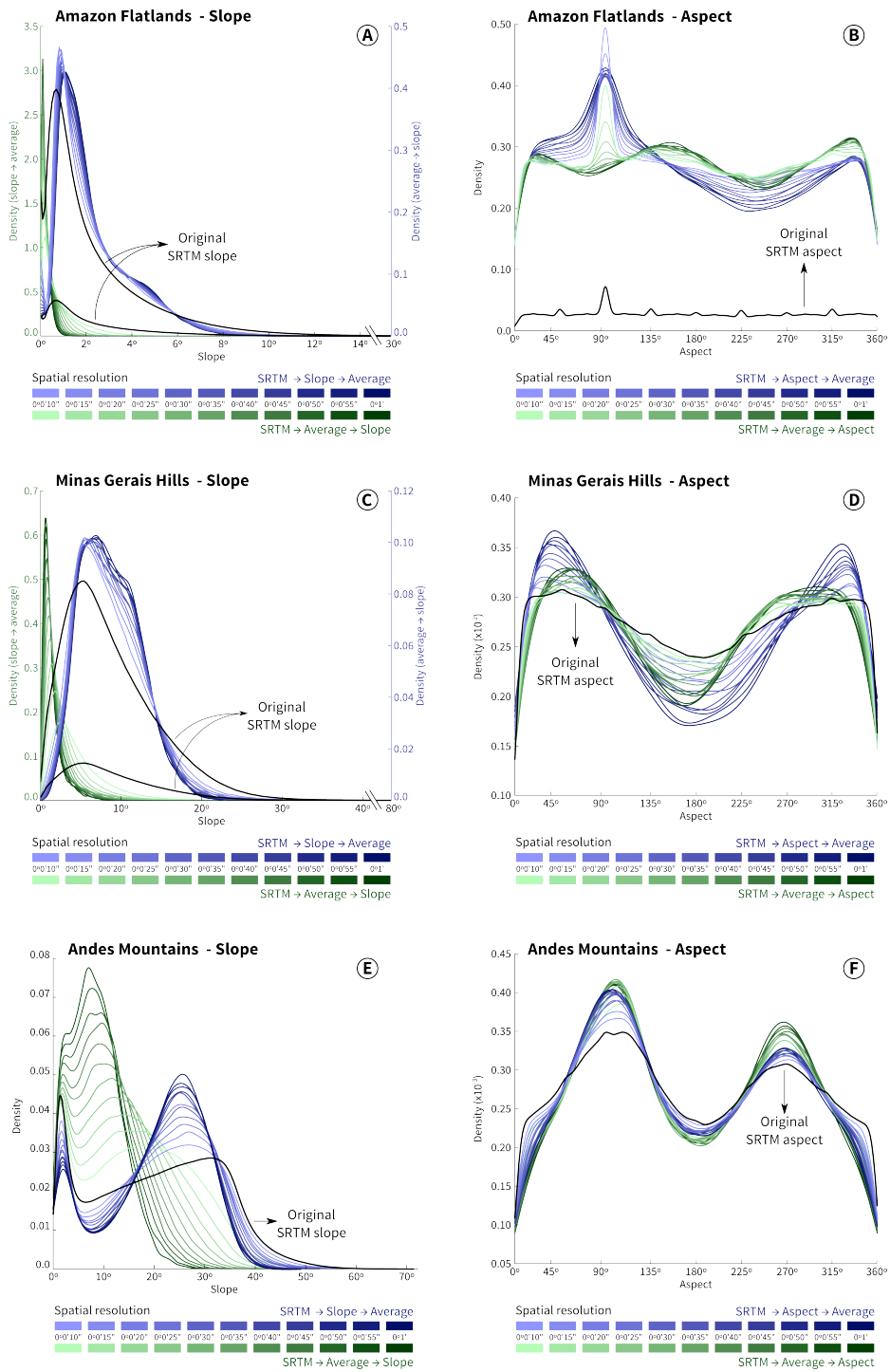


Figure 2. Density plots for slope and aspect derived from a resampled DEM (shades of green) and resampled slope and aspect derived from a base DEM (shades of blue)

REFERENCES

[1] Reuter, H. I., Neison, A., Strobl, P., Mehl, W. & Jarvis, A., 2009. "A first assessment of ASTER GDEM tiles for absolute accuracy, relative accuracy and terrain parameters", *Geoscience and Remote Sensing Symposium, IEEE International, IGARSS 2009*, 5, V-240 -V-243.

[2] Farr, T. G., Rosen, P. A., Caro, E., Crippen, R., Duren, R., Hensley, S., Kobrick, M., Paller, M., Rodriguez, E., et al. 2007. "The Shuttle Radar Topography Mission", *Review of Geophysics*, 45, RG2004.

[3] Krieger, G., Zink, M., Fiedler, H., Hajnsek, I., Younis, M., Huber, S., Bachmann, M., Gonzalez, J., Schulze, D., Boer, J., Werner, M. and Moreira, A., 2009. "The TanDEM-X Mission: Overview and status", *Radar Conference, 2009 IEEE*, 1-5.

[4] Krishnan, S., Crosby, C., Nandigam, V., Phan, M., Cowart, C., Baru, C. and Arrowsmith, R., 2001. "OpenTopography: a services oriented architecture for community access to LIDAR topography", *Proceedings of the 2nd International Conference on Computing for Geospatial Research & Applications, ACM*, 2011, 7:1-7:8. (www.opentopography.org)

[5] Cogley, J. G., 1985. "Hypsometry of the continents", *Zeitschrift für Geomorphologie, Suppl.-Bd.* 53, 48.

[6] Lehner, B., Verdin, K. and Jarvis, A., 2008. "New Global Hydrography Derived From Spaceborne Elevation Data", *Eos, Transactions American Geophysical Union*, 89, 93-94.

[7] Becker, J. J. and Sandwell, D. T., 2007. "SRTM30PLUS: Data fusion of SRTM land topography with measured and estimated seafloor topography" (http://topex.ucsd.edu/WWW_html/srtm30_plus.html).

[8] Zhang, W., and Montgomery, D. R., 1994, "Digital elevation model grid size, landscape representation, and hydrologic simulations", *Water Resources Research*, 30(4), 1019-1028.

[9] Florinsky, I. V., 1998. "Accuracy of local topographic variables derived from digital elevation models". *International Journal of Geographical Information Science*, 12, 47-61.

[10] Kienzle, S., 2004. "The effect of DEM raster resolution on first order, second order and compound terrain derivatives". *Transactions in GIS*, 8, 83-111.

[11] Zhou, Q., Liu, X., 2004. "Analysis of errors of derived slope and aspect related to DEM data properties". *Computers & Geosciences*, 30:369 – 378.

[12] Smith, M. P.; Zhu, A.-X.; Burt, J. E. & Stiles, C., 2006. "The effects of DEM resolution and neighborhood size on digital soil survey". *Geoderma*, 137, 58 – 69.

[13] Li, S.; MacMillan, R.; Lobb, D. A.; McConkey, B. G.; Moulin, A. & Fraser, W. R., 2011. "Lidar DEM error analyses and topographic depression identification in a hummocky landscape in the prairie region of Canada". *Geomorphology*, 129, 263 – 275.

[14] Jarvis A., Reuter, H. I, Nelson, A. and Guevara, E., 2008, "Hole-filled seamless SRTM data V4, International Centre for Tropical Agriculture (CIAT)", available from <http://srtm.csi.cgiar.org>.

[15] Neteler, M., Bowman, M. H., Landa, M. and Metz, M., 2012. "GRASS GIS: A multi-purpose open source GIS", *Environmental Modelling & Software*, 31, 124-130.

[16] Horn, B.K.P., 1981. "Hill Shading and the Reflectance Map", *Proceedings of the IEEE*, 69(1): 14-47.

[17] Grohmann, C. H., 2004. "Morphometric analysis in Geographic Information Systems: applications of free software GRASS and R", *Computers & Geosciences*, 30, 1055-1067.

[18] Cox, N. J., 2007. "Kernel estimation as a basic tool for geomorphological data analysis", *Earth Surface Processes and Landforms*, 32, 1902-1912.

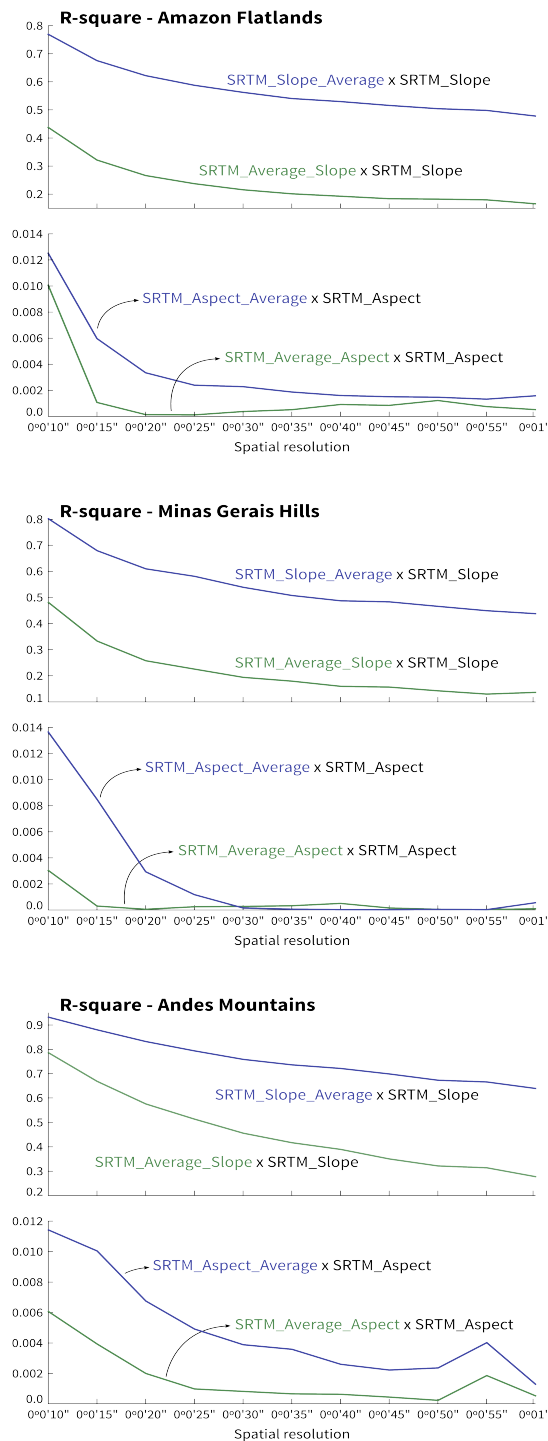


Figure 3. Plots of correlation (R-square) between the original morphometric parameter (0°0'03" resolution) and resampled values

Comparison of several methods for multi-scale DEM generalization in different landform areas

Qiao Wan

School of Resource and Environment Science
Wuhan university
Wuhan, China
wanqiao@whu.edu.cn

Yumin Chen

School of Resource and Environment Science
Wuhan university
Wuhan, China
ymchen@whu.edu.cn

Abstract—There are various landforms in real word and numerous methods proposed previously for DEM generalization. When use different methods to generalize a DEM, the results vary greatly. Therefore, in order to get a most proper method to implement the generalization, we need taking topographic information into consideration. This paper tested four methods widely used in DEM generalization and compared their performances in different landform areas. The results show the compound method delivered the best results among those algorithms. However, the four methods all have its advantages and disadvantages. Thus we can select the most proper one in different practical applications according to their different characteristics.

INTRODUCTION

With the wide use of multi-scale DEMs, it is necessary to study the DEM generalization method further. There are numerous DEM generalization methods proposed before [1,2]. And those can be categorized into three groups, including raster DEM method, restructuring the grid-based DEM using a triangulated irregular network (TIN) method, and generalizing using a drainage-constrained TIN method.

In most generalizations of DEMs, the influence of topography feature is usually ignored. Generally speaking, the most proper method for generalization in different areas which have different topography features and for different practical applications varies greatly. Therefore, how to choose the best method to implement the generalization in different landform areas is a problem should be solved.

This paper classifies landform types into several classes, using a quantitative approach proposed before [3]. The principal objective of this paper is to find the proper method for multi-scale DEM generalization in different landform areas. Therefore this paper tested a lot of samples, and selected some examples from them which belong to the different landform

types. Then implemented DEM generalizations using the selected four methods and compared their performances in different landform tests. The four methods are, the resample method [4], the maximum z-tolerance algorithm [5], the compound method [6], the ANUDEM algorithm [7].

METHODOLGY

There are eight major classes of landforms [3], and those classes of landforms are River Alluvial Plain(RP), Piedmont Plains(PD), Gravelly Fans(GF), Plateaux and Upper Terraces (TR), Hill(H), Mountains(M), Lowlands (LL),Flood Plains(FP). According to their similarity in terrain feature, we merged them into six types. After merging, the results are Plain (P), Gravelly Fans (GF), Plateaux and Upper Terraces (TR), Hill (H), Mountains (M), Lowlands (LL). This paper classified all landforms into six types by their elevation rang and slope(TABLE I).

TABLE I. THE STANDARD OF FIRST CLASSIFICATION

Landform	Slope range (%)	Elevation rang (m) Max-Min elevation
P	0-5%	[0,150)
GF	0-5%	[150,250)
TR	0-12%	[250,500)
H	8-25%	(50,500)
M	Over 25%	[500,1500)
LL	Less than 1	<0

In the paper, the original data are some 30 m DEMs, which was generalized to generate DEMs with different resolutions respectively, including 50, 100, 150, and 250 m spatial resolutions. All the original DEMs were clipped to 1,001×1.001 grid cells, in order to keep their size same.

Therefore, after the classification, we tested the four methods we selected in DEM generalization of different landforms and compared the performances of the selected four methods in different landform types. The resample method is one of the most widely used method for DEM generalization, which requires averaging the neighboring cells of a high-resolution, square-grid DEM into a series of lower-resolution data sets. The maximum z-tolerance algorithm is an example of methods using TIN to generalize DEM, which extracting more points in areas where the terrain are more complicated, so it has superiority in retaining the terrain feature. And the compound method is a drainage-constrained TIN method for DEM generalizations. The difference between the maximum z-tolerance method and the compound method is, the maximum z-tolerance method use only significant points and the compound method take the streamline of DEM into account when structure the TIN. The ANUDEM method is a interpolation method taking the drainage network into consideration.

For the resample method, we chose the nearest neighbor method to carry out the sampling. And for the ANUDEM and the compound method, they used the same significant point and drainage network to get a fair comparison result. For the maximum z-tolerance algorithm, it used the same significant point as the compound method's to restructure a TIN.

When we set the z-tolerance value using the z-tolerance algorithm to extract the significant point, the six landforms can merged into less three types by their similarities in terrain feature (TABLE II).

TABLE II. THE STANDARD OF SECOND CLASSIFICATION

Type	Inclusive landforms
Flats	P, LL, TR
Hills	GF, H
Mountains	M

The USGS DEM data accuracy standard in which a RMSE of one-half contour interval is the maximum permitted guided the specification of z-tolerance values at different scales in different landforms (TABLE III).

TABLE III. THE SPATIAL RESOLUTION AND CORRESPONDING Z-TOLERANCE VALUES IN DIFFERENT LANDFORMS

Resolution(m)		50	100	250	500
Z-tolerance Value (m)	Flats	5	10	25	45
	Hills	15	30	30	90
	Mountains	30	60	125	180

And we use the simple "D8" flow routine algorithms [8] to extract the streamline of the DEM. We set the threshold of this algorithm by taking the grid number of DEMs into consideration, result in a coarser DEM with a smaller threshold value.

This paper classified all landform type areas into those types and tested the four methods we selected and compared their performances. In order to get a credible result of comparison, we used four representative parameters widely used in DEM generalization, including the root mean square errors (RMSE), the mean slope value, the mean roughness value and the streamline matching rate (SMR) [6].

The root mean square errors (RMSE) were compared to measure the accuracy of the original and generalized elevation surfaces. It can be specified as followed:

$$RMSE = \sqrt{\frac{\sum_{i=1}^n (Z'_i - Z_i)^2}{n}} \tag{1}$$

The mean slope (\bar{S}) and surface roughness (K) are good measures to compare the generalized DEMs created at varying scales. Their computational formulas are:

$$\bar{S} = \frac{\sum_{i=1}^n S_i \times A_i}{\sum_{i=1}^n A_i} \tag{2}$$

$$K = \frac{A'}{A} = \frac{\sum_{i=1}^n A_i \sec S_i}{\sum_{i=1}^n A_i} \tag{3}$$

Where S denotes the slope, A denotes the projected area; A' denotes the surface area, i denotes the i th nit; and n denotes the total number of units.

The streamline matching rate (SMR) [6] was computed to test the effectiveness of retaining drainage features. In this paper, the threshold value of 'streamline buffers' is as same as the resolution of the generalized DEM. The computational formula is:

$$SMR = \frac{L'}{L} \times 100 \tag{4}$$

Where L' denotes the length of streamlines that fell into the corresponding stream buffer zones, L is the total length of the streamlines.

RESULT AND DISCUSSION

In this paper, we classified landform types into several classes, and compared the performance of four methods for DEM generalization. The DEMs were all clipped, so composed of the

same 1,001×1.001 grid cells. We take a sample of the Mountains (M) type as an example to show the comparison (Fig. 1).

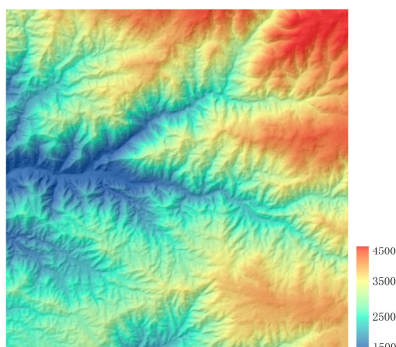


Fig.1 The sample DEM

The basic geographic information of the original DEM is shown in the TABLE IV.

TABLE IV. THE BASIC GROGRAPHIC INFORMATION OF ORIGINAL DEM

Mean Elevation (m)	Maximum elevation (m)	Minimum elevation (m)	Mean slope(°)	Mean roughness
3135.33	4457	1448	21.58	1.0981

The z-tolerance values used in different resolutions (only for the maximum z-tolerance method and the compound method) is shown in TABLE V.

TABLE V. THE Z-TOLERANCE VALUES IN THE SAMPLE GENERALIZATION

Resolution(m)	50	100	250	500
Z-tolerance Value (m)	30	60	125	180

And the threshold values when we extracting the drainage network from the original DEM represent in TABLE VI.

TABLE VI. THE THRESHOLD VALUES FOR EXTRACTING THE DRAINAGE NETWORK

Resolution(m)	50	100	250	500
threshold value	600	1000	1500	2000

The following several tables is the results of the generalization.

TABLE VII. RMSEs (m)

	50m	100m	250m	500m
Compound	22.33	30.47	51.39	113.75
ANUDEM	27.83	34.81	72.60	146.94
Z-tolerance	28.68	35.67	80.94	163.11
Resample	18.86	29.84	53.10	108.47

TABLE VIII. THE MEAN SLOPE VALUES (°)

(21.58)	50	100	250	500
Compound	21.25	18.71	15.99	8.92
ANUDEM	22.25	18.52	14.10	7.64
Z-tolerance	22.61	17.86	14.86	8.01
Resample	21.20	18.52	16.34	8.59

*The 21.58° is the mean slope value of original DEM.

TABLE IX. THE MEAN ROUGHNESS VALUES

(1.0981)	50	100	250	500
Compound	1.0986	1.0751	1.0518	1.0247
ANUDEM	1.1069	1.0610	1.0409	1.0102
Z-tolerance	1.1075	1.0628	1.0412	1.0109
Resample	1.0953	1.0773	1.0539	1.0215

TABLE X. THE SMR VALUES (%)

	50	100	250	500
Compound	60.14	71.92	97.33	85.16
ANUDEM	64.34	65.81	69.10	63.27
Z-tolerance	60.23	68.45	87.22	41.23
Resample	76.99	80.45	87.22	51.34

The results show that the resample method had an effective performance in the generalization, the RMSE, mean slope value, mean roughness values of the resample method are all fine, but it can not keep a excellent streamline than the compound method or ANUDEM method. Compared with the resample method and maximum z-tolerance algorithm, the ANUDEM algorithm and the compound method performed much better in preserving the key morphological and hydrological features. However, the compound method is better than the ANUDEM algorithm in retaining terrain details.

Totally speaking, the compound method delivered the best results among those algorithms. But in practical applications, selecting proper method must take some other factors into account, such as the size of the DEM data after generalized and the priorities of parameters retaining. For example, in a hydrological model, the best method for DEM generalization will be the compound method. But in some applications which demand rapid results and less accuracy, the resample method maybe best choice.

ACKNOWLEDGMENT

This research is supported by the National Nature Science Foundation of China (No: 41171347). We are also grateful for the support provided by School of Resource and Environment Science, Wuhan University.

REFERENCES

[1] Lee, J., 1991. "Comparison of existing methods for building triangular irregular network models of terrain from grid digital elevation models". International Journal of Geographical Information Systems 5(3), 267-285.

- [2] Heckbert, P.S., Garland, M., 1997. "Survey of polygonal surface simplification algorithms". Technical Report. School of Computer Science, Carnegie Mellon University, Pittsburgh.
- [3] Hossein Saadat, Robert Bonnell, 2008. "Landform classification from a digital elevation model and satellite imagery". *Geomorphology* 100 (2008) 453-464.
- [4] Wolock, D.M., Price, C.V., 1994. "Effects of digital elevation model and map scale and data resolution on a topography-based watershed model". *Water Resources Research* 30 (11), 3041-3052.
- [5] Chang, K., 2007. "Introduction to Geographic Information System". 4th ed. McGraw-Hill, New York 450pp.
- [6] Zhou, Q., Chen, Y., 2011. "Generalization of DEM for terrain analysis using a compound method". *ISPRS Journal of Photogrammetry and Remote Sensing* 66(1), 38-45.
- [7] Hutchinson, M.F., 1989. "A new procedure for gridding elevation and streamline data with automatic removal of spurious pits". *Journal of Hydrology* 106, 211-232.
- [8] Mark, D.M., 1984. "Automatic detection of drainage network from digital elevation models". *Journal of Hydrologic Engineering* 4(1), 2-9.
- [9] Li, Z., 2008. Multi-scale digital terrain modeling and analysis. In: Zhou, Q., Lees, B., Tang, G. (Eds). *Advance in Digital Terrain Analysis*. Springer, Berlin, pp. 59-83.
- [10] Kienzle, S., 2004. The Effect of DEM Raster Resolution on First Order, Second Order and Compound Terrain Derivatives. *Transactions in GIS* 8(1), 83-111.

An MPI-CUDA Implementation for the Compression of DEM

Zeng Fei
Wuhan University
61363 Troops
Wuhan, China

Chen Yumin
Wuhan University
Wuhan, China
Tony2fish@163.com

Abstract—A high performance terrain data compression method is proposed based on discrete wavelet transform (DWT) and parallel run-length code. But the implementation of the schemes to solve these models in realistic scenarios imposes huge demands of computing power. Compute Unified Device Architecture (CUDA) programmed, Graphic Processing Units (GPUs) are rapidly becoming a major choice in high performance computing. Hence, the number of applications ported to the CUDA platform is growing high. Message Passing Interface (MPI) has been the choice of high performance computing for more than a decade and it has proven its capability in delivering higher performance in parallel applications. CUDA and MPI use different programming approaches but both of them depend on the inherent parallelism of the application to be effective. In this approach, MPI functions as the data distributing mechanism between the GPU nodes and CUDA as the main computing engine. This allows the programmer to connect GPU nodes via high speed Ethernet without special technologies. We tackle the acceleration of the compression of digital elevation models (DEM) by exploiting the combined power of several CUDA-enabled GPUs in a GPU cluster. This implementation overlaps MPI communication with CPU-GPU memory transfers and GPU computation to increase efficiency. Several numerical experiments, performed on a cluster of modern CUDA-enabled GPUs, show the efficiency of the distributed solver. Our speed-up was over 20 compared to two thread CPU version.

I. INTRODUCTION

With the development of technology of remote sensing, the size and resolution of DEM has quickly increased. Today, spatial resolutions as high as 1m are available for some areas, and data at only slightly lower resolution is currently being acquired for ever larger regions worldwide. The storage and transmission of high-resolution elevation information can consume amounts of resources, and with the increased interest in mapping the earth and having maps for real time navigation, the development of compression techniques to help in these tasks is becoming very important.

At first people use the traditional Fourier transform, although the transform is simple and fast in data compression, but it also loss a lot of information of the data. Therefore, there need fast

lossless compression in order to satisfy application requirement. Different compression schemes have been developed to exploit this property. Wavelet transform have been applied for image lossless compression or at least near-lossless way which can be used for image compression [1]. Since wavelet transform possesses resolution both in space domain and in frequency domain, it is very suitable for dealing with the data with instability, less relativity or less redundancy. DEM data inheres in the characteristics of instability, fragmentation and less relativity, here by discrete wavelet transform is rather suitable for DEM data compression [2, 3, 4]. However, for the huge data, the traditional application of wavelet transform is less considering parallelism, which will cause long time for transform. The GPU is an attractive platform for a broad field of applications, because it still remains a significant high arithmetic processing capability and is often less utilized. Therefore it can be used as a powerful accelerator without extra cost [5]. These platforms make it possible to achieve speedups of an order of magnitude over a standard CPU in many applications and are growing in popularity [6, 7].

Moreover, several programming toolkits such as CUDA [8] have been developed to facilitate the programming of GPUs for general purpose applications. There are previous works to compress data by using a graphics-specific programming language, but currently most of the proposals to compression on a single GPU are based on the CUDA programming model. Although the use of single GPU systems makes it possible to satisfy the performance requirements of several applications, many applications require huge meshes, large numbers of time steps and even real time accurate predictions. These characteristics suggest to combine the power of multiple GPUs.

One approach to use several GPUs is based on programming shared memory multi-GPUs desktop systems. These platforms have been used in fluid dynamic [9] and shallow water [10, 11] simulations by combining shared memory programming primitives to manage threads in CPU and CUDA to program the GPU. However, this cost-effective approach only offer a reduced number of GPUs (2-8 GPUs) and more flexible systems are desirable. A more flexible approach involves the use of clusters

of GPUs-enhanced computers where each node is equipped with a single GPU or with a multi-GPUs system. The computation on GPUs clusters could make it possible to scale the runtime reduction according to the number of GPUs. Thus, this approach is more flexible than using a multi-GPUs desktop system and the memory limitations of a GPUs-enhanced node can be overcome by suitably distributing the data among the nodes, enabling us to simulate significantly larger realistic models and with greater precision. The use of GPUs clusters to accelerate intensive computations is gaining in popularity [12, 13, 14, 15, 16, 17]. Most of the proposals to exploit GPUs clusters use MPI [18] to implement inter process communication and CUDA [19] to program each GPUs. A common way to reduce the remote communication overhead in these systems consists in using non-blocking communication MPI functions to overlap the data transfers between nodes with GPUs computation and CPU-GPU data transfers.

In this work, an implementation of DWT compression to the raster DEM is developed for a GPUs cluster by using MPI and CUDA. The outline of the article is as follows: Section 2 summarizes the background to DWT compression and provides an introduction to MPI-CUDA. In Section 3 we provide the main details of our parallelization strategy for the DWT compression using MPI-CUDA. Experimental results are analyzed in Section 4. Finally, Section 5 summarizes the work and concludes the paper.

II. THE COMPRESSION OF DEM

A. DWT by CUDA

The DWT of image signals produces a non-redundant image representation, which provides better spatial and spectral localization of image information as compared to other multi-resolution representation [20]. For an input represented by a list of $2n$ numbers, the Discrete wavelet transform may be considered to simply pair up input values, storing the difference and passing the sum. This process is repeated recursively, pairing up the sums to provide the next scale: finally resulting in $2n-1$ differences and one final sum. The describe of the DWT is in Eq.1 and Eq. 2. $a_{j-1}(n)$ is the original pending signal data; $a_j(n)$ is the approximation coefficient; $d_j(n)$ is the accurate coefficient; h_0 is the low-frequency filter; h_1 is the high-frequency filter.

$$a_j(n) = \sum_{n=-\infty}^{\infty} a_{j-1}(n)h_0(n - 2k) \quad (1)$$

$$d_j(n) = \sum_{n=-\infty}^{\infty} a_{j-1}(n)h_1(n - 2k) \quad (2)$$

The DWT for an image as a 2D signal will be obtained from 1D DWT. We get the scaling function and wavelet function for 2D by multiplying two 1D functions. This may be represented as a four channel perfect reconstruction filter bank as shown in Fig. 1. Now, each filter is 2D with the subscript indicating the type of filter (HPF or LPF) for separable horizontal and vertical components. By using these filters in one stage, an image is decomposed into four bands. There exist three types of detail

images for each resolution: horizontal (HL), vertical (LH), and diagonal (HH).

The operations can be repeated on the low low (LL) band using the second stage of identical filter bank. Thus, a typical 2D DWT, used in image compression, generates the hierarchical structure shown in Fig. 2.

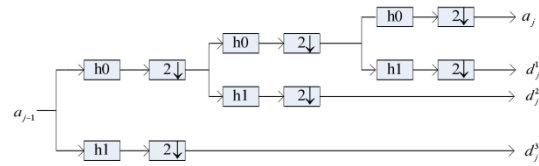


Fig. 1. One Filter Stage in 2D DWT

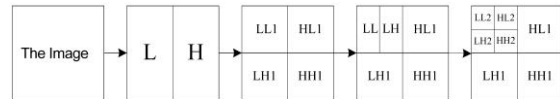


Fig. 2. Structure of wavelet decomposition

B. Parallel Run-length Code by CUDA

This section presents the parallel VLE (Virtual Learning Environment) algorithm for General Purpose GPU with hardware support for atomic operations. The parallel variable-length encoding consists of the following parallel steps: (1) assignment of code words to the source data, (2) calculation of the output bit positions for compressed data (code words), and finally (3) writing (storing) code words to the compressed data array. In the first step, variable-length code words are assigned to the source data. The code words can be either computed using an algorithm such as Huffman, or they can be predefined, e.g. as it is frequently the case in image compression implementations. Without loss of generality, we can assume that the code words are available and stored in a table. This structure will be denoted as the code word look-up table (code word LUT). Each entry in the table contains two values: the binary code for the code word, and code word length in bits, denoted as a (cw, cwlen) pair. Our implementation uses an encoding alphabet of up to 256 symbols, with each symbol representing one byte. During compression, each source data symbol (byte) is replaced with the corresponding variable-length code word.

C. MPI-CUDA

NVIDIA SLI technology can be used to connect multiple GPUs that are in one computer and as of the latest release of the CUDA sdk, all those SLI (Scalable Link Interface) connected GPU cards can only be seen as one single GPU by the programmer. But we can connect GPU cards in different computers using Ethernet and exploit CUDA+MPI model so that it enables the user to see different GPUs in different computers as separate processing engines. Hence the programmer can execute different kernels in one application on different GPUs at the same time.

CUDA is the programming language provided by NVIDIA to run general purpose applications on NVIDIA GPUs. The CUDA incorporates an Application Programmer Interface, a runtime, couple of higher level libraries and a device driver for the underline GPU.

MPI provides a standard set of subprogram definitions which allow parallel programs to be written using a distributed memory programming model to allow more than one process to perform computations on a given set of data copies of this data must be sent to any process which requires it (to be saved on that process’s memory). This is referred to as message passing.

D. System design

We successively overlap computations with inter-node and intra-node data exchanges to better utilize the cluster resources. All the implementations have much in common, with differences in the way data exchanges are implemented. We show that implementation details in the data exchanges have a large impact on performance.

For all implementations, one MPI process is started per GPU. Since we must ensure that each process is assigned a unique GPU identifier, an initial mapping of hosts to GPUs is performed. A master process gathers all the host names, assigns GPU identifiers to each host such that no process on the same host has the same identifier, and scatters the result back. At this point the cuda SetDevice()call is made on each process to map one of the GPUs to the process which assures that no other process on the same node will map to the same GPU.

These kernels implement the computation steps of the solver in the GPU, and do not require any modification for use in the multiple GPU implementation. We added the use of constant memory to support runtime model configuration while maintaining efficient GPU memory accesses to this common data. A temperature kernel was added and the momentum kernel changed to apply the buoyancy effect.

III. RESULTS AND DISCUSSION

A. Experimental Platform

All experiments are done using both CPU and *MPI-CUDA*. The configurations for them are listed in Table 1 and Table 2. The experiment requires some software and tools for programming and documenting purpose: CUDA SDK 4.2\VS 2010\Nsight Visual Studio Edition 2.2.

TABLE I. DEVICE CONFIGURATION AT EXPERIMENT

Feature	Specification
Name	GeForce GT 650M
CUDA Driver Version	4.2
MPI	MPICH2-1.0.1

Feature	Specification
Total Global memory	2048M
#Multiprocessor	2
#Cores	384

TABLE II. TABLE 2: HOST MACHINE CONFIGURATION AT EXPERIMENT

Feature	Specification
System Model	Y480 Notebook
Operating System	Windows xp
Manufacture	Lenovo
Processor	Intel(R) Core(TM) i5-3210M
Memory	4096MB RAM

B. Experimental Data

For test the different performance of the CUDA-based DWT compression, we use *srtm_57_05* images (Fig.3) ranging from 256*256 to 6000*6000.

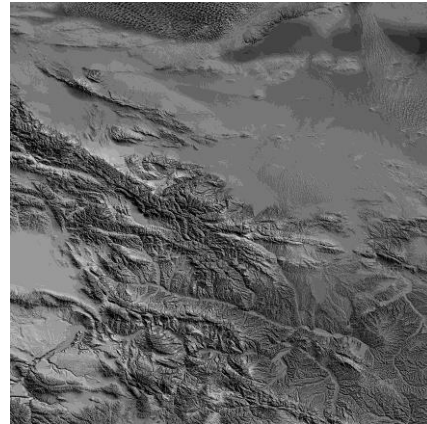


Fig. 3 *srtm_57_05* Image

C. Experimental Result

To evaluate the proposed method, we examined each execution time of the DWT on a CPU and *MPI-CUDA*. The program for the CPU is implemented in C++ language. Every image makes the DWT on a CPU and *MPI-CUDA*. The execution time of the GPU is much less than the time taken on the CPU: we can see that when the image is small (256*256) the time spends on the both devices is almost the same. It is due to the fact that the data transfer overhead (from CPU to *MPI-CUDA* and vice versa) in case of small image size mitigating the parallel execution effects. For larger data sizes, the speedup obtained by the parallel operations take over the data transfer overheads and hence the performance gain becomes more obvious. With resolution’s increase, the *MPI-CUDA*’s accelerator is more obvious (from 1.2 to 20.8). The speed-up ratio increase, when the image size becomes larger. It shows that the larger image the

more efficiency of the *MPI-CUDA* DWT compression. So the experiment has proved the *MPI-CUDA* can be used to improving the speed of DWT compression to dem. By using the GPU for decoding, the CPU is free for other tasks like prefetching and data management. We validated these statements by integrating the compression and decoding schemes into a terrain rendering system, and we showed that high visual quality on high-resolution displays is possible at interactive frame rates.

D. Discussion

In this paper, we present a *MPI-CUDA* accelerated DWT compression for images method using the CUDA and MPI. We realized significant improvement in runtime (speedup to 20.8), with imperceptible degradations of quality. Although this experiment has verified that *MPI-CUDA* parallel computation on GPUs significantly increases the speed of the discrete wavelet transform, much work remains to be done. The DWT method based on CUDA has many places to improve, for example, using the texture memory (it will be fast) to translate the data. Moreover, the DWT compression is only one step of DEM processing, the method should be used in some DEM processing, such as DEM realtime display. By using the GPU for decoding, the CPU is free for other tasks like prefetching and data management. We will validate these statements by integrating the compression and decoding schemes into a terrain rendering system, and show that high visual quality on high-resolution displays is possible at interactive frame rates.

ACKNOWLEDGMENT

The research is supported by the National Nature Science Foundation of China (No: 41171347).

REFERENCES

- [1] Wan Gang, Zhu Changqiang, 1999. "Application of multi-band wavelet on simplifying DEM with lose of feature information". *Acta Geodaetica et Cartographica Sinica*, 28 (1): 36-40p.
- [2] Wu Lun, Liu Yu, Zhang Jing, 2001. "Principle of geographic Information system". Beijing: Science Press, in press.
- [3] Chang Zhanqiang, Wulixin. Montanic, 2004, "grid DEM data compression based on wavelet transform and mixed entropy coding". *Geography and Geo-Information*, 20(1): 24-27p.
- [4] NVIDIA Tutorial at PDP08, "Cuda: A new architecture for computing on the gpu", 2008.
- [5] J.D. Owens, S. Sengupta, and D. Horn, "Assessment of Graphic Processing Units for Department of Defense Digital Signal Processing Applications", Technical Report, ECE-CE-2005-3, Computer Engineering Research Laboratory, University of California, Davis, October 2005.
- [6] M. Rumpf, R. Strzodka, 2005, "Graphics Processor Units: New Prospects for Parallel Computing", in: *Numerical Solution of Partial Differential Equations on Parallel Computers*, Vol.51 of Lecture Notes in Computational Science and Engineering, Springer, 89-134p.
- [7] J. Owens, M. Houston, D. Luebke, S. Green, J. Stone, J. Phillips, 2008, GPU computing, *Proceedings of the IEEE* 96 (5), 879-899p.
- [8] NVIDIA Corporation, *NVIDIA CUDA C Programming Guide 3.2*, 2010.
- [9] W.-Y. Liang, T.-J. Hsieh, M. T. Satria, Y.-L. Chang, J.-P. Fang, C.-C. Chen, C.-C. Han, 2009, "A GPU-Based Simulation of Tsunami Propagation and Inundation", in: *Proceedings of the 9th International Conference on Algorithms and Architectures for Parallel Processing, ICA3PP '09*, Springer-Verlag, Berlin, Heidelberg, 593-603p.
- [10] J. Thibault, I. Senocak, 2010, "Accelerating incompressible flow computations with a Pthreads-CUDA implementation on small-footprint multi-GPU platforms", *The Journal of Supercomputing*, 1-27p.
- [11] M. Geveler, D. Ribbrock, S. Mallach, D. G, 2010, "A Simulation Suite for Lattice-Boltzmann based Real-Time CFD Applications Exploiting Multi-Level Parallelism on modern Multi- and Many-Core Architectures", *Journal of Computational Science In Press*, Accepted Manuscript.
- [12] M. L. Saetra, A. R. Brodtkorb, 2010, "Shallow water simulations on multiple GPUs", *Proceedings of the Para 2010 Conference, Lecture Notes in Computer Science*.
- [13] D. A. Jacobsen, J. C. Thibault, I. Senocak, 2010, "An MPI-CUDA Implementation for Massively Parallel Incompressible Flow Computations on Multi-GPU Clusters", in: *The 2009 High Performance Computing & Simulation- HPCS'09*.
- [14] D. Komatitsch, G. Erlebacher, D. G öddecke, D. Mich éa, 2010, "High-order finite-element seismic wave propagation modeling with MPI on a large GPU cluster", *J. Comput. Phys.* 229, 7692-7714p.
- [15] D. Komatitsch, 2011, "Fluid-solid coupling on a cluster of GPU graphics cards for seismic wave propagation", *High Performance Computing*, 125-135p.
- [16] Z. Fan, F. Qiu, A. Kaufman, S. Yoakum-Stover, 2004, "GPU Cluster for High Performance Computing", in: *Proceedings of the 2004 ACM/IEEE conference on Supercomputing, SC'04*, IEEE Computer Society.
- [17] Y. Zhang, F. Mueller, X. Cui, T. Potok, 2011, "Data-intensive document clustering on graphics processing unit clusters", *J. Parallel Distrib. Comput.* 211-224p.
- [18] R. Abdelkhalik, H. Calendra, O. Coulaud, J. Roman, G. Latu, 2009, "Fast Seismic Modeling and Reverse Time Migration on a GPU Cluster", in: *The 2009 High Performance Computing & Simulation-HPCS'09*, Leipzig Allemagne, Best Paper Award at HPCS'09 Total.
- [19] NVIDIA Corporation, *CUDAZone*, http://www.nvidia.com/object/cudahome_new.html.
- [20] M. Atallah, S. Kosaraju, L. Larmore, G. Miller, S. Teng, 1989, Constructing trees in parallel. In: *Proceedings of the first annual ACM symposium on Parallel algorithms and architectures*, pp. 421-431. ACM, New York.

Land-surface segmentation to delineate elementary forms from Digital Elevation Models

Lucian Drăguț

Department of Geography
West University of Timișoara
Timișoara, Romania
lucian.dragut@cbg.uvt.ro

Ovidiu Csillik

Department of Geography
West University of Timișoara
Timișoara, Romania
cskovi@yahoo.com

Jozef Minár

Department of Physical Geography and Geoecology
Comenius University in Bratislava
Bratislava, Slovakia
minar@nic.fns.uniba.sk

Ian S. Evans

Department of Geography
Durham University
Durham City, England
i.s.evans@durham.ac.uk

Abstract—In this paper, we introduce an algorithm to delineate elementary forms on Digital Elevation Models (DEMs). Elementary forms are defined by constant values of fundamental morphometric properties and limited by discontinuities of these properties. A multiresolution segmentation technique was customized to partition the layers of altitude derivatives into homogeneous divisions through a self-scalable procedure, which reveals the pattern encoded within the data. Layers were segmented successively, following the order of elevation derivatives, i.e. gradient, aspect, profile curvature, and plan curvature. Each segmentation was followed by extraction of elementary forms, thus leaving only heterogeneous surfaces for further segmentation steps. The sequential selection of elementary forms was based on dynamic thresholds of: 1) the inner variance of the respective land-surface variable (LSV); 2) the difference between the mean LSV value of the target segment and the mean LSV values of its adjacent segments; and 3) the shape indices of segments. The results were compared with an existing manually-drawn geomorphological map to evaluate the potential of the algorithm of producing morphologically meaningful land-surface divisions. The evaluation showed that most segments are either directly comparable with manual delineations, or have a clear morphological meaning. We conclude that algorithmic delineation of elementary forms from real DEMs is feasible; more work is needed, however, to design a fully operational process.

INTRODUCTION

Geomorphological maps are fundamental to many applied studies of the Earth's surface [1], yet traditional symbol-oriented geomorphological mapping techniques are not able to meet the current scientific and technical requirements of land management [2]. Geospatial technologies and the ongoing progress in production of high-resolution Digital Ele-

vation Models (DEMs) have revived the interest in geomorphological mapping [1], which is developing in a new form - Digital Geomorphological Mapping (DGM) [3]. Geomorphometry, the science of land-surface quantification [4, 5], is fundamental to quantitative geomorphology and geomorphological mapping [3, 6], potentially enabling manual delimitation to be replaced by automated recognition and delimitation of landforms [6].

In the last decade, land-surface segmentation has demonstrated a great potential to improve geomorphological mapping, it enables better representations of objects from DEMs [7]. Segmentation partitions land-surface into relatively homogeneous areas, bounded by discontinuities in the input variables; multiresolution segmentation (MRS), as implemented into eCognition®, is the most popular segmentation algorithm. Resulting segments are used further as building blocks in classification, based on attributes such as average values of derivatives, shape indexes, and topological relations of segments.

However, DGM to date is dominated by an exploratory or empirical approach, the work being done to conform to different objectives and landform definitions [3]. Robustness and generic applicability of landform mapping have not been evaluated adequately. The most critical aspect is mapping of a whole land surface, which is more difficult than extraction of specific landforms from it [6]. It is acknowledged that scientific progress in DGM has not kept pace with rapidly evolving geospatial technologies [3], therefore a theoretical and operational framework to relate land-surface form to processes would support objective geomorphological

mapping [3]. Such a theoretical framework has recently been proposed by Minár and Evans [8]. Elementary forms have been mapped in the surroundings of Prášilské Lake (Bohemian Forest, the Czech Republic) to analyse patterns of glaciation [9]. While the approach proved successful, elementary forms were delimited manually by means of analysis of contour lines and a DEM. An operational framework to delineate elementary forms is still missing, yet this theoretical framework has a great potential for DGM [3].

The objective of this research was to investigate how and to which degree elementary forms can be delineated on a real DEM, to contribute to an operational framework automating this process. Here we present the preliminary results of the algorithm development, its application on a high-resolution DEM, and a first evaluation of the degree to which the algorithm approximates a manually-drawn map of elementary forms, which had previously been designed for the purpose of geomorphological mapping.

METHODS

I deal elementary forms are defined as ‘landform elements with a constant value of altitude, or two or more readily interpretable morphometric variables, bounded by lines of discontinuity’ [8]. The fundamental morphometric properties are altitude and its derivatives, i.e. gradient, aspect, profile and plan curvatures, which form a coherent system for the local description and analysis of the land surface [5]. Constant values of morphometric properties determine relations among elementary forms in a hierarchy that follows the order of altitude derivatives. Thus, a constant value of elevation corresponds to a zero value of gradient and undefined value of aspect. Constant values of gradient and aspect correspond to zero values of profile curvature and plan curvature respectively. Therefore the importance of constant value decreases from the variables of lower order (altitude) to higher order (curvatures). Spatial transitions between constant values of the five properties are ideally marked by discontinuities.

The above concepts were implemented within an object-oriented approach, which is well-suited to hierarchical analysis. The processing steps (Fig. 1) consist in computation of land-surface variables (LSVs) (Fig. 1, 2) and their pre-processing (Fig. 1, 3) as input layers for object-oriented analysis (Fig 1, 4), which was performed with eCognition®.

MRS, which is a region-growing segmentation algorithm [10], was employed to segment each of the five layers. Characteristics of segments produced by MRS, such as homogeneity, size and shape are controlled by user-defined thresholds called *scale parameters*. To optimize the scale parameters for segmentation (Fig. 1, 4), an automatic procedure devised by Drăguț and Eisank [11] was applied.

This procedure fits the segments to the scales of topographic features with the aid of local variance [12].

Land-surface variables were segmented in a stepwise fashion, starting with the layer of slope and followed by aspect, profile curvature and plan curvature, respectively (Fig. 1). This sequential approach follows the order and importance of the derivatives. While the altitude layer was not directly used in segmentation, it provided the information needed to extract objects constant in altitude, bounded by lines of discontinuity that resulted from segmentation of the gradient layer. Each segmentation was followed by extraction of elementary forms, thus leaving only heterogeneous surfaces for further segmentation steps.

The sequential selection of elementary forms based on dynamic thresholds of: 1) the inner variance of the respective LSV (i.e. variance within a segment); 2) the difference between the mean LSV value of the target segment and the mean LSV values of its adjacent segments; and 3) the shape indices of segments. Two shape indices were used in this study, namely *compactness* and *border index*. *Compactness* is computed as the ratio between the product of the length and width of an image object and the number of pixels within the object, showing how compact an object is [13]. *Border index* is calculated as the ratio between the border length of an object and the smallest rectangle enclosing the object, describing how jagged an object is [13]. These variables were calculated for each object, and the thresholds were given by the means of the scene, except that shape index thresholds were set following a trial-and-error approach. At each segmentation step, segments with variance below the mean, difference above the mean, compactness below 3.5, and border index below 3 qualified as elementary forms.

RESULTS AND DISCUSSION

The algorithm was tested on a DEM at 1 m resolution, interpolated from contour lines (Fig. 2). The DEM covers an elevation range between 145 and 241 m, and an extent of 329 X 323 m. It represents an area located northwest of Bratislava, Slovakia, around the hill of Slovinec and near the highest summit of the Devin Carpathians, Devinska Kobyla (514 m). The general landscape is dominated by two smooth summits situated in the central southwestern and southeastern parts and a large relatively flat area in the north-east.

The algorithm delineated the elementary forms as shown in Fig. 2. It is visible that polygons generally agree with changes in contour lines. In this study, a plausibility assessment was performed based on expert knowledge and comparison with two other manual geomorphological maps available for the study area. The first one was developed by Minár and Mičian [14] from a 1:10 000

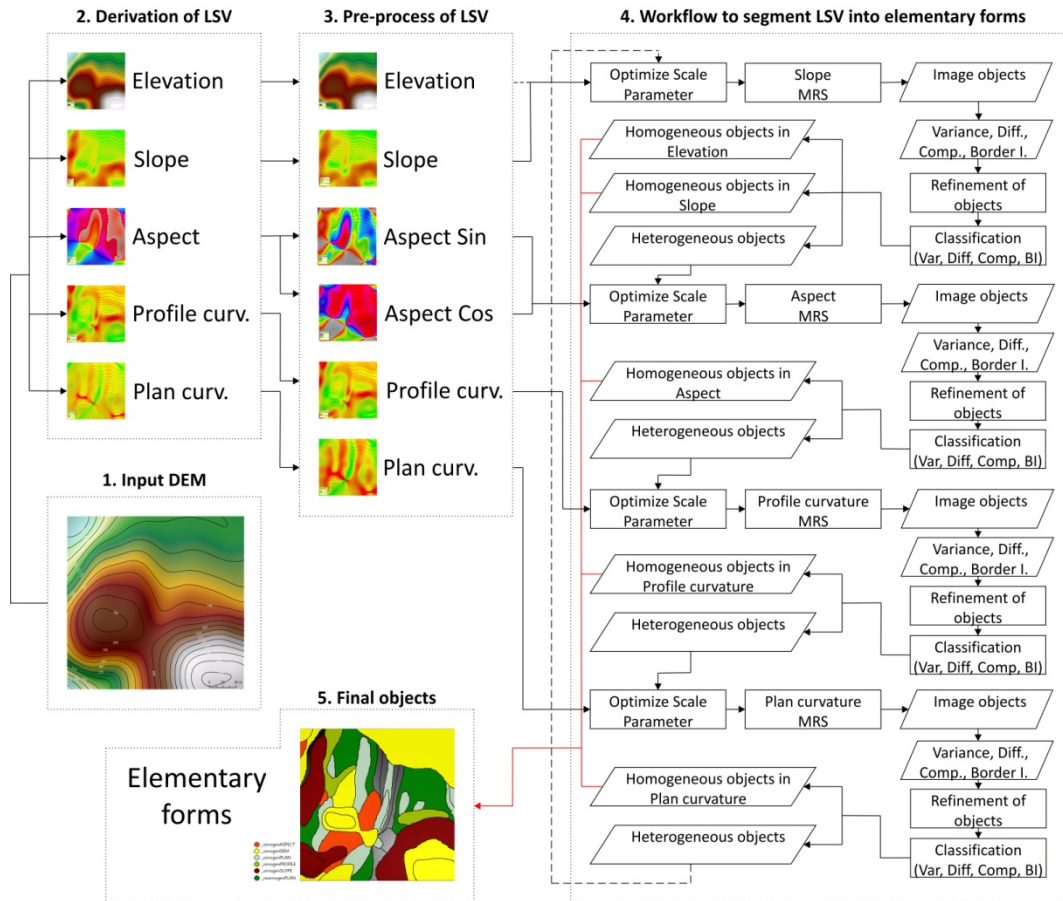


Figure 1. Flow chart showing the main steps in the algorithm development. See text for details.

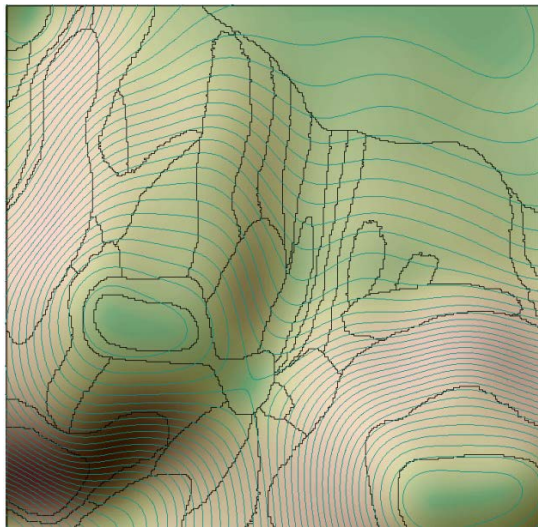


Figure 2. Results of delineation (black polygons), overlaid on a DEM. Contours at 1 m interval are displayed in green.

topographic map (Fig. 3), while the second one (not shown here) added two dells that in the first version were generalized because of the scale. Delimitation of elementary forms on these two maps was made through field research and visual expert analysis [8].

The assessment was conducted by one author of this study (Jozef Minár), by interpreting the geomorphological meaning of each segment against the two maps, based on his long-lasting experience in the geomorphology of the study area and its region. Results are presented on a scale from one (segments with clear geomorphological meaning) to five (elements considered genetically false) (Fig. 4). According to this evaluation, most of the polygons delineated by the algorithm (26 out of the total of 39) represent forms resembling manual delineations well (classes 1 and 2). Classes 3, 4, and 5 include 7, 2, and 4 polygons respectively. These results show that algorithmic delineation of elementary forms from real DEMs is feasible.

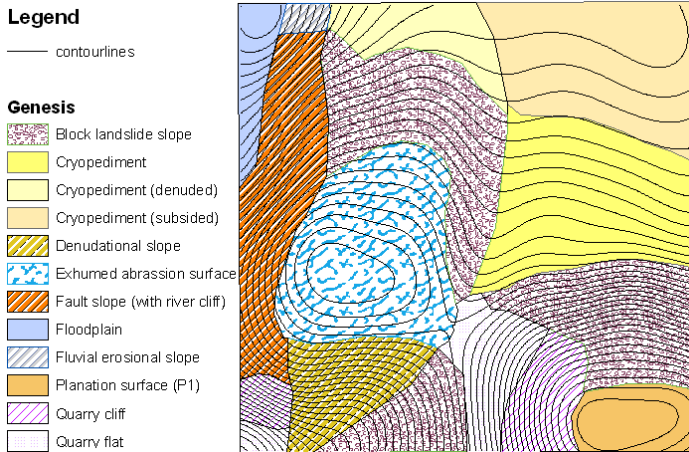


Figure 3. Geomorphological map of the Slovinec area, delineated manually on the basis of the elementary forms concept.

This work was carried out on a small and simple area. It remains to be seen whether comparable results are achievable on larger and more complex areas; tests on these issues are in progress. This study might be particularly important in the context of high-resolution DEMs (LiDAR), which make very fine-scale geomorphological mapping feasible.

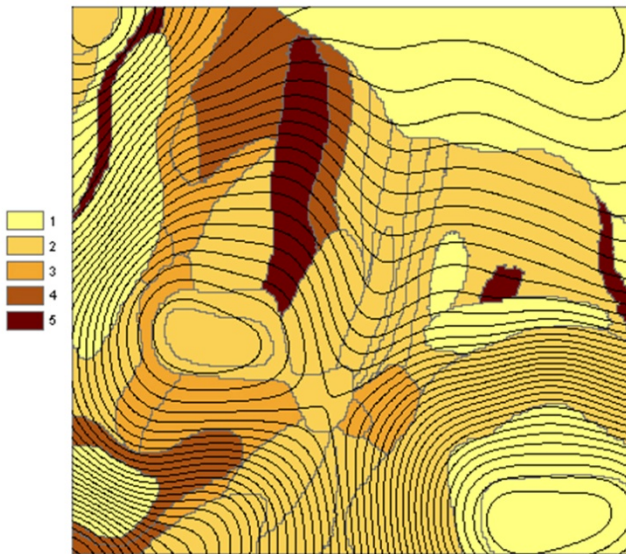


Figure 4. Results of plausibility assessment. Automatically delineated polygons represent: 1) Forms better or equal to manually delineated ones, where whole areas as well as boundaries have clear geomorphological meaning; 2) Forms equal to parts of their correspondent features, where small portions of areas or boundaries have less geomorphological meaning; 3) Approximations of manual forms, where large parts of areas or polygons are questionable; 4) Rough approximations of genetic forms, where majority of areas or boundaries are questionable; and 5) Genetically false elements.

ACKNOWLEDGMENT

This work was supported by a grant of the Romanian National Authority for Scientific Research, CNCS - UEFISCDI, project number PN-II-ID-PCE-2011-3-0499. Comments from three anonymous reviewers were appreciated.

REFERENCES

[1] Smith, M.J., P. Paron, and J.S. Griffiths, Eds., 2011. "Geomorphological Mapping: Methods and Applications". Amsterdam, Boston, Heidelberg, London, New York, Oxford, Paris, San Diego, San Francisco, Singapore, Sydney, Tokyo, Elsevier Science, 612 p.

[2] Dramis, F., D. Guida, and A. Cestari, 2011. "Nature and aims of geomorphological mapping", In Geomorphological Mapping: Methods and Applications, Edited by: Smith, M.J., Paron, P. and Griffiths, J.S., Elsevier Science, Amsterdam, Boston, Heidelberg, London, New York, Oxford, Paris, San Diego, San Francisco, Singapore, Sydney, Tokyo.

[3] Bishop, M.P., L.A. James, J.F. Shroder Jr, and S.J. Walsh, 2012. "Geospatial technologies and digital geomorphological mapping: Concepts, issues and research." Geomorphology, 137: 5-26.

[4] Pike, R.J., 1995. "Geomorphometry-progress, practice, and prospect." Zeitschrift für Geomorphologie, Supplementband 101: 221-238.

[5] Evans, I.S., 1972. "General geomorphometry, derivatives of altitude, and descriptive statistics", In Spatial Analysis in Geomorphology, Edited by: Chorley, R.J., Methuen, London.

[6] Evans, I.S., 2012. "Geomorphometry and landform mapping: What is a landform?" Geomorphology, 137: 94-106.

[7] Drăguț, L., and C. Eisank, 2011. "Object representations at multiple scales from digital elevation models." Geomorphology, 129: 183-189.

[8] Minár, J., and I.S. Evans, 2008. "Elementary forms for land surface segmentation: The theoretical basis of terrain analysis and geomorphological mapping." Geomorphology, 95: 236-259.

[9] Mentlik, P., and M. Novotna, 2010. "Elementary forms and 'scientific reliability' as an innovative approach to geomorphological mapping." Journal of Maps, 2010: 564-583.

[10] Baatz, M., and A. Schäpe, 2000. "Multiresolution Segmentation-an optimization approach for high quality multi-scale image segmentation", In Angewandte Geographische Informationsverarbeitung, Edited by: Strobl, J., Blaschke, T. and Griesebner, G., Wichmann-Verlag, Heidelberg.

[11] Drăguț, L., and C. Eisank, 2012. "Automated object-based classification of topography from SRTM data." Geomorphology, 141-142: 21-33.

[12] Woodcock, C.E., and A.H. Strahler, 1987. "The factor of scale in remote-sensing." Remote Sensing of Environment, 21: 311-332.

[13] Trimble, 2012 *eCognition Reference Book*. Munchen, Germany: Trimble Germany GmbH.

[14] Minár, J., and L. Mičian, 2002. "Complex geomorphological characteristics of the Devínska Kobyla Mt." Landscape Atlas of the Slovak Republic. 1st ed. Bratislava: Ministry of Environment of the Slovak Republic; Banská Bystrica: Slovak Environmental Agency, 92-93.

An automated method to extract typical karst landform entities from contour lines on topographic maps

Fuyuan Liang

Department of Geography
Western Illinois University
Macomb IL, USA
F-Liang@wiu.edu

Yunyan Du

State Key Laboratory of Resources and Environmental Information System
Institute of Geographic Sciences and Natural Resources Research, CAS
Beijing, China
duyy@lreis.ac.cn

Abstract— Mapping specific landform entities in the past is mainly achieved by manually examining contour lines on topographic maps. Automated delimitation of specific landform from digital elevation data remains difficult in geomorphologic mapping. This paper presents a method to automatically identify five common surface features of karst landscapes: isolated karst hill or sinkhole, clustered karst hills or sinkholes, and clustered hills with sinkholes. These landform entities have their own singular geomorphometric characteristics and thus could be identified from digital elevation data. In this study, boundary of individual landform entity is defined by an outmost closed contour line (CCL), which contains at least another CCL but not contained by any other CCLs. The innermost CCL with a local extreme elevation value represents either a peak or a sink of that specific landform. Between the innermost and the outmost CCLs, several intermediate CCLs may exist, depending upon relief of the landform and contour interval of the topographic maps. The aforementioned surface karst landform entities were then delimited and identified by examining the spatial relationships among these CCLs and the change of their elevation values. The method was applied to delimitate these landform entities in Oolitic, IN and Florida, PR. Comparison of the distribution of these surface features in these two areas provides new insights into karst development processes and landscape evolution.

I. INTRODUCTION

The Earth's surface is covered by different types of landforms, which can be recognized and distinguished from their distinct dimensions and the statistical frequency of their geomorphometric attributes [1]. The topography of a specific landform type usually defines its geomorphic form and represents the interactions of climatic, geological, and other surface processes that have acted on it over time [2]. Extraction of different types of landforms and examining their distinct geomorphometric characteristics thus can play an essential role for geomorphologist to understand their origins and evolution processes.

Automated extraction of specific types of landforms from digital elevation data remains a challenge in geomorphologic mapping [3]. One of the possible reasons might be the lack of operational definitions of specific types of landform entities and it is usually hard or even not possible to crisply define their boundaries [3]. This might not be the case for some typical karst landform entities, such as isolated karst hill or sinkhole, clustered karst hills or sinkholes, and clustered hills with sinkholes (Fig. 1). Geometrically, an isolated sinkhole is a small to intermediate enclosed depression which is formed by the dissolution of surface carbonate rocks typically at joint intersections. Sinkholes are actually deemed as the diagnostic karst landform as karst is always developed in the areas where sinkholes are found [4]. As dissolution of surface carbonate continues, isolated sinkholes gradually grow and coalesce with adjacent ones and consequently clustered sinkholes are developed. In many cases, isolated or clustered sinkholes are widely found on temperate plains. Carbonate residual hills are developed when most carbonate has been removed by dissolution processes. These residual hills might be isolated or share a common base (clustered karst hills). The last type of landform entity, clustered hills with sinkholes, is well developed in humid tropical areas and is characterized by occurrence of deep sinkholes within a cluster of karst hills. Obviously these landform entities have their own geomorphologic significance as they are developed in different hydrogeological circumstances [4]. These landform entities are also the representative products of different karst evolution stages [4]. Therefore, mapping these landform entities will help karst geomorphologists better understand their origins and development. Currently these types of specific landforms are mainly identified for a few small areas by visual examining topographic maps and/or remote sensing images [6]. With digital elevation data more accessible today, an automated method thus is needed to map these landform entities at a broad scale.

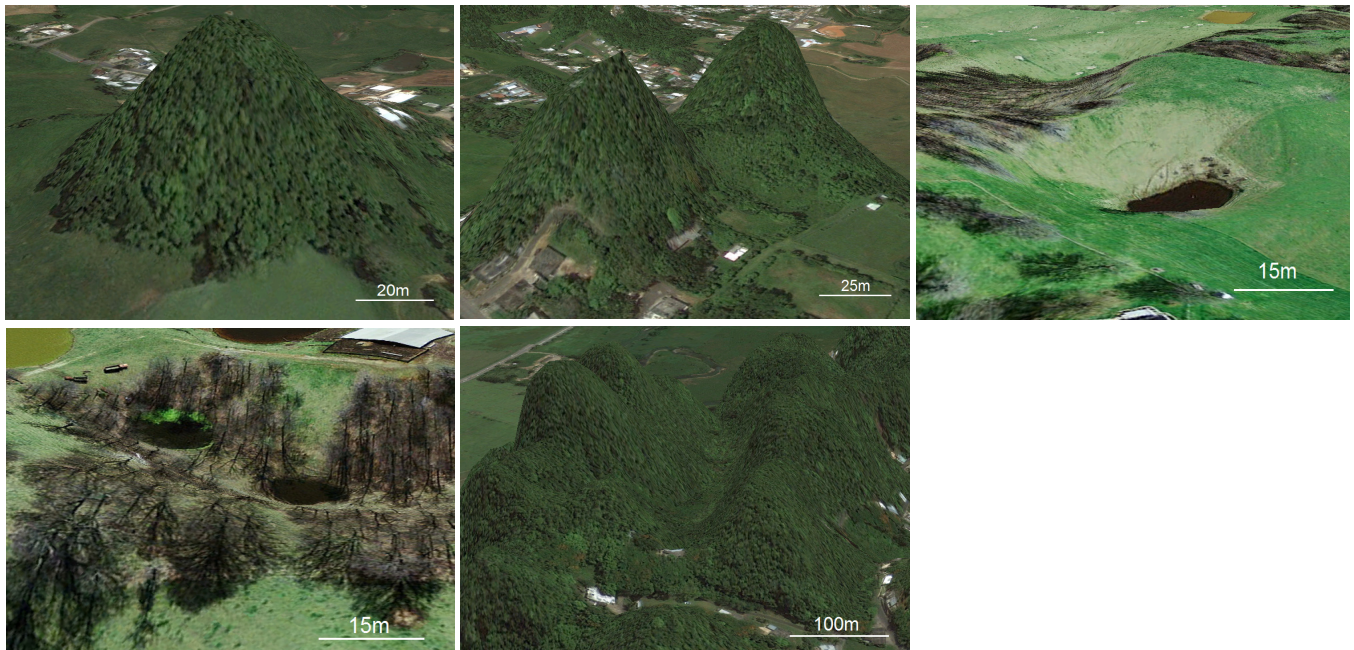


Figure 1. Google Earth screenshots showing A) isolated hill, B) clustered hills, C) isolated sinkhole, D) clustered sinkholes, E) clustered hills with sinkholes. Scales are approximate.

II. STUDY AREA AND DATA

This study examined the typical surface karst landforms in Oolitic, Indiana (38.90N, 86.52W) and Florida, Puerto Rico (18.36N, 66.55W). Landscapes in the first area are mainly characterized by small size isolated and clustered sinkholes scattered on a rolling plain. By contrast, isolated or clustered karst hills and cluster hills with sinkholes are very common in Florid, PR. Landforms in these two areas represent the most typical temperate and humid tropical karst landscapes respectively.

The contour interval is 10 feet and 10 meters on the 7.5 minute Oolitic and Florida quadrangles respectively. Digital Line Graph (DLG) of these 7.5 topographic maps have some contour lines left open due to aesthetic reason in cartography though they should be closed, particularly in the areas with high relief. Therefore, the DLG data were not used in this study. Instead, contour lines were generated from the 30-m USGS DEMs at the same contour intervals as the corresponding topographic maps. The DEM-derived contour lines well match those on the 7.5 minute topographic maps. As this study mainly focuses on surface karst landscapes, geologic maps of these two study areas were also acquired and used to mask out non-karst landscapes.

III. METHODOLOGY

This study delimitates these five types of landform entities by examining the spatial relationships of the closed contour lines (CCLs) that represent each specific landform. The boundary of a landform entity to be delineated is defined by an outmost CCL, which contains at least another CCL but not contained by any other CCLs. Thus a specific landform entity is represented by a cluster of CCLs, including the outmost CCL and all other CCLs within it. The CCL cluster is then converted to an acyclic graph, with a node representing a specific CCL. The outmost CCL is represented by a root node. The innermost CCL, which contains no other CCLs but is contained by at least another CCL, is represented by a leaf node. If a CCL contains at least two other CCLs with same elevation, it is defined as a branch node in the acyclic graph. Any other CCLs within the outmost CCL are represented by middle nodes. Given that, the aforementioned landform entities can be described by following representative scenarios (Fig.2).

Both isolated sinkhole and karst hill have no branch nodes but only one leaf node connecting to the root node. From the root node to the leaf node, elevation gradually increases for the isolated karst hill (Fig.2A) while decreases for the isolated sinkhole (Fig.2C). An acyclic graph with at least one branch node represents a specific landform of clustered hills (Fig.2B) if the elevation gradually increases from the root to the leaf node and

clustered sinkholes (Fig.2D) if the elevation is gradually decreasing. If there are at least one leaf or middle node having elevation higher and another one having elevation lower than the branch, middle, or root node that right connects to them, this scenario defines the clustered hills with sinkhole (Fig. 2E). An algorithm was developed to automatically label these five scenarios and consequently identify these five types of landform entities.

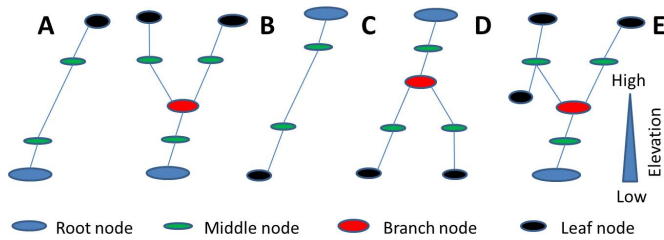


Figure 2 Representative acyclic graphs showing the typical types of surface karst landform entities. A) isolated hill, B) clustered hills, C) isolated sinkhole, D) clustered sinkholes, E) clustered hills with sinkholes

IV. RESULTS AND DISCUSSIONS

Delimitation results are shown atop of hillshaded DEMs of our two study areas (Figs. 3 and 4). Totally 175 and 2079 specific landform entities were delineated in Oolitic, IN and Florida, PR respectively (Table 1). These entities account for 21.9% and 37.8% of the total area of these two regions respectively.

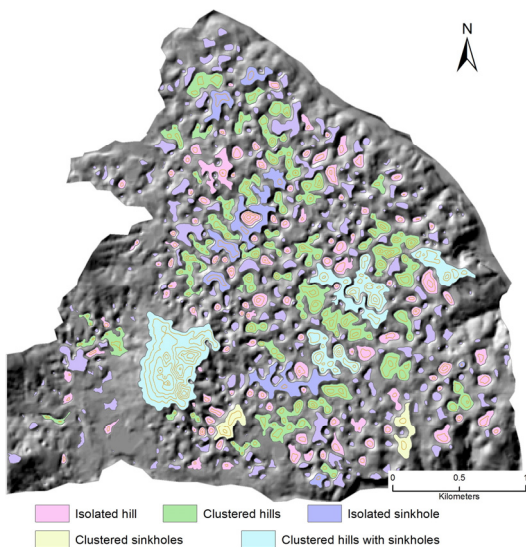


Figure 2. Delimitation results of Oolitic, IN

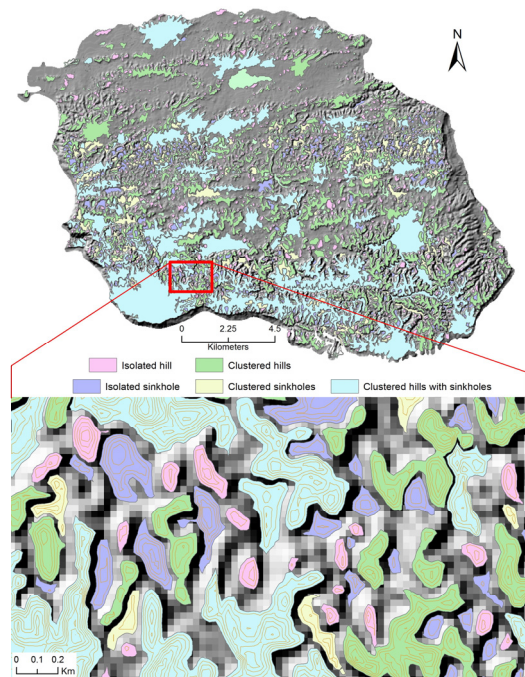


Figure 4. Delimitation results of Florida, PR

Dominant types of landform entities in these two areas are not the same in our two study areas (Tab. 1). The clustered hills with sinkholes type occupies 18.06% of the total area in Florida, PR while the dominant type of landform entities in Oolitic, IN is the clustered sinkholes. Residual hills, either isolated or clustered, are more developed in Florida while isolated or clustered sinkholes outnumber hills in Oolitic in terms of both occurrence frequency and area. Karst geomorphologists have noticed the different dominant karst landforms types in these two areas based on their field observations and subjective interpretation. To our knowledge, this study is the first one to provide an indicator to quantitatively describe the difference. Tectonic uplifting and climate seem to be the main reason that why these two study areas are dominated by different types of landform entities. Both vertical and lateral dissolution of limestone is more intense in the tropical Florida PR than the temperate Oolitic IN. More intense vertical dissolution resulting from tectonic uplifting in Florida PR significantly enhanced the development of deep sinkholes and removed more carbonate formation, producing more isolated and clustered residual hills. By contrast, slower vertical and lateral dissolution processes remove less carbonate and thus mainly produce isolated or clustered sinkholes in Oolitic IN.

TABLE 1. FREQUENCY AND AREA PERCENTAGE OF DIFFERENT TYPES OF LANDFORM ENTITIES DELIMITATED IN OUR TWO STUDY AREAS

Study areas		Oolitic, IN	Florida, PR
<i>Total area (km²)</i>		<i>9.72</i>	<i>278.72</i>
Isolated hill	Number	9	822
	Area (%)	2.29	3.06
Clustered hills	Number	2	524
	Area (%)	0.67	10.82
Isolated sinkhole	Number	114	461
	Area (%)	5.4	2.6
Clustered sink-holes	Number	45	175
	Area (%)	8.23	3.26
Clustered hills with sinkholes	Number	5	97
	Area (%)	5.28	18.06

Number of isolated hill and sinkhole is always more than that of their clustered counterparts in both areas. However, size of isolated hill and sinkhole is much less than the clustered hills or sinkholes respectively. For example, in total 45 clustered sinkholes were delimited in Oolitic and they account for 8.05% of the total study area while the 114 isolated sinkholes occupy only 5.40% of the total area. In Florida, the 822 isolated hills account for only 3.06% while the 524 clustered hills occupy 10.82% of the total area.

These landform entities probably are developed in different stages of karst development though dissolution of carbonate is the dominant driving force. Isolated sinkholes are usually the first surface karst feature that are developed once subsurface conduits were established [4]. Once a sinkhole commences to form, the centripetal focusing of runoff and hence further dissolution of carbonate encourages the enlargement of initial isolated sinkholes. Given enough time, this self-reinforcement process leads to the coalescence of adjacent sinkholes thus clustered sinkholes are developed within a larger enclosed depression.

With more carbonate being removed by the focusing dissolution within sinkholes, original carbonate block is subdivided into smaller chunks. Within these chunks, clustered hills with sinkholes or clustered hills are developed, depending on different hydrogeological settings. New isolated sinkholes may commence to form and existing sinkholes continue to grow in these chunks, from which isolated hills then are developed as the next sequential products. Yet some isolated hills could also be directly derived from the continuous growth and enlargement of isolated or clustered sinkholes [4], [7]. Nevertheless, the isolated residual hills tend to represent the final stage of

karst development as solution activity has removed most of the carbonate formation.

A similar study was conducted to discriminate tower karst and cockpit karst landforms in Guilin, China [5]. The former type includes isolated and clustered karst hills while the latter literally the same as the clustered hills with sinkholes in this study. This study classified karst landscapes from a different perspective, delineating the sequential evolution products of karst development.

V. CONCLUSIONS

Typical types of surface karst landform entities were automatically delimited in Oolitic IN and Florida PR by examining the spatial relationships among closed contour lines on topographic maps. All these five types of landform entities are found in these two areas while they occur at different frequencies and account for significantly different areas. The delimitation results show that isolated or clustered sinkholes are the dominant landforms in Oolitic IN. By contrast, type of clustered hills with depressions accounts for the largest area among all these five types of landform entities in Florida, mainly due to different conditions of climate and hydrogeology in these two areas. Further examination of morphometric characteristics of these specific landforms in these two areas may provide new insights on the development processes of karst landscapes. It would be also of great value if these types of landform entities are identified in more study areas and further comparison definitely helps geomorphologists better understand the controls on karst development. This method, with appropriate modification and improvement, also provide a new approach for landform classification.

REFERENCES

- [1] MacMillan, R. A. and Shary, P. A., 2009. "Landforms and landform elements in geomorphometry," *Developments in Soil Science*, 33: 227–254.
- [2] Bishop, M. P., James, L. A., Shroder, J. F., and Walsh, S. J., 2012. "Geospatial technologies and digital geomorphological mapping: Concepts, issues and research," *Geomorphology*, 137(1): pp. 5–26.
- [3] Evans, I. S., 2012. "Geomorphometry and landform mapping: What is a landform?," *Geomorphology*, 137(1): 94–106.
- [4] Ford, D. C. and Williams, P., 2007. *Karst hydrogeology and geomorphology*. Wiley.
- [5] Liang, F. and Xu, B., 2013. "Discrimination of tower, cockpit and non-karst landforms in Guilin, Southern China, based on morphometric characteristics," *Geomorphology*, <http://dx.doi.org/10.1016/j.geomorph.2013.07.026>.
- [6] Tan, M., 1992. "Mathematical modelling of catchment morphology in the karst of Guizhou, China," *Zeitschrift für Geomorphologie*, 36(1): 37–51.
- [7] Zhu, X., 1988. *Guilin Karst*. Shanghai, China: Shanghai Scientific and Technical Publishers.

Application of supervised landform classification of 9-unit slope model for preliminary rockfall risk analysis in Gunung Kelir, Java

Guruh SAMODRA, Junun SARTOHADI

Environmental Geography Department
University of Gadjah Mada
Yogyakarta, Indonesia
guruh.samodra@gmail.com

Guangqi CHEN, Kiyonobu KASAMA

Department of Civil Engineering
Kyushu University
Fukuoka, Japan

Abstract—Rockfall risk analysis requires assessment of susceptibility and identification of elements at risk. To portray the susceptible area, the opinion of geomorphologists is commonly used to classify landforms through interpretation of aerial photos and field survey. However, the subjectivity of investigators hinders application of this method. Therefore, supervised landform classification is applied in the present study, based on relevant parts of the 9-unit slope model. The main objective is to provide automated landform classification particularly for rockfall analysis. This is achieved in five stages: 1) fieldwork, 2) DEM preprocessing, 3) DEM processing, 4) rockfall modeling, and 5) landform classification based on fuzzy k-means. The result reveals that potentially high risk is located in the transportational middle slope and colluvial footslope. This is useful information on which to base prioritization action for countermeasures, both policy and design. The application of supervised landform classification in Gunung Kelir provides a reasonable result for preliminary rockfall risk assessment.

I. INTRODUCTION

Along with the increasing loss of life and property due to rockfall, awareness toward the need for rockfall risk management has recently greatly increased. Here, geomorphometric analysis can be used as a tool for incorporating disaster risk reduction and transfer measures into development planning. This provides basic ideas for planning priorities in promoting risk management plan and strategy, and evaluating spatial planning policies. Thus, by using geomorphometry as a preliminary tool for risk assessment, the spatial planning manager can make a balance between minimizing risk and promoting some development priorities.

Selection of preventive mitigation measure type, structural protection location and structural protection dimension should be supported by rockfall risk assessment based on geomorphologic analysis. The 9-unit slope model [1] i.e. interfluves, seepage slope, convex creep slope, fall face, transportational midslope, colluvial footslope, alluvial footslope, channel wall and channel bed; can pose important zones of mass movement process where energy and velocity are diverse in places. It can be delineated into a key information for prioritization of mitigation actions. The information is useful to expose the spatial distribution of potentially high damage of elements at risk affected by rockfall.

Traditionally, landform delineation and classification are based on the stereoscopic technique of aerial photo and field investigation. This method is very common in Indonesia. It has been applied for soil mapping, land evaluation analysis, land suitability analysis, spatial planning, and so on. There is also mentioned in Indonesia's National Standard document of Geomorphological Mapping that the technical requirement for geomorphological mapping is an interpretation of remote sensing data combined with field measurement [2]. The standard landform classification in Indonesia is ITC System [3]. However, the traditional method in landform classification requires simultaneous consideration and synthesis of multiple different criteria [4] and the quality depends on the skill of interpreter. Thus, we try to automated classify landform based on the 9-unit slope model which seems more appropriate to rockfall analysis. Even though, the 9-unit slope model is significant for pedogeomorphic process response [5], it is also capable to explain rockfall deposition.

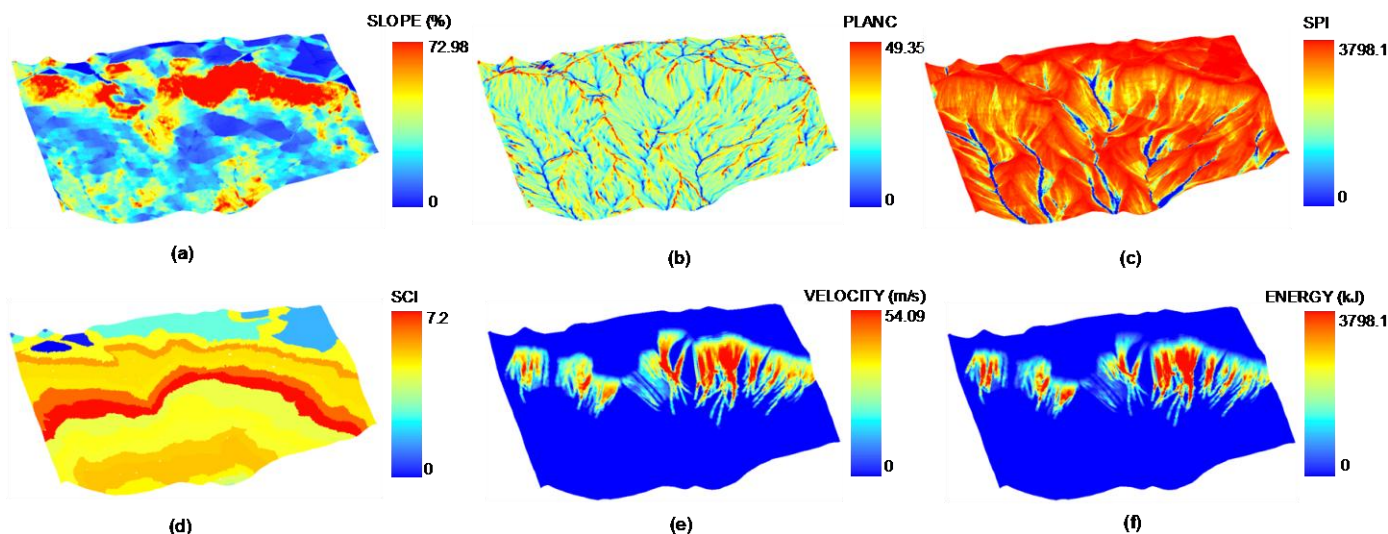


Figure 1. Morphometric variables derived in ILWIS (a) slope, (b) plan curvature (c) stream power index (d) shape complexity index and morphometric variables derived in ArcGIS (e) rockfall velocity (f) rockfall energy

II. STUDY AREA

Gunung Kelir is located in Yogyakarta Province, Indonesia. It lies in the upper part of Menoreh Dome that is located in the central part of Java Island. The area is dominated by Tertiary Miocene Jonggrangan Formation that consists of calcareous sandstone and limestone. Bedded limestone and coralline limestone which form isolated conical hills may also be found in the highest area surrounding the study area. *Gunung* (Mountain) *Kelir*, of Javanese origin, literally means a curtain that is used to perform *wayang* (Javanese traditional puppet). Its toponym describes a 100-200 meter high escarpment that has maximum slope nearly 80°.

Landforms in Gunung Kelir are a product of final uplifting of the Complex West Progo Dome in the Pleistocene [6]. Slope gradient varies between 0° and 80°, meanwhile mean of slope gradient is 23.14° with the standard deviation 13.05°. Altitude ranges from 297.75 to 837.5 m. There are 152 buildings exposed as elements at risk on the lower slope of the escarpment. Some cracks have been found in the upper part of Gunung Kelir after Yogyakarta Earthquake 2006. Nowadays, the local government is still working to anticipate the worst scenario of rockfall hazard in Gunung Kelir area.

III. DATA AND METHODS

Fieldwork activity, DEM preprocessing, DEM processing, rockfall modeling, and landform classification were carried out in this study. Fieldwork was intended to identify rockfall

boulders and elements at risk. A field inventory of fallen rockfall boulders of different size has been done to obtain the spatial distribution and dimension of rockfall deposition. The dimension and potential rockfall source were determined to simulate rockfall trajectory, velocity, and energy. The buildings on the lower slope of the escarpment were also plotted in order to obtain the spatial distribution of elements at risk. Finally, DGPS profiling was conducted to improve performance of DEM.

The objective of DEM preprocessing was to improve the quality of DEM-derived products. We applied DEM preprocessing proposed by Hengl et al. (2004) [7] including reduction of paddy terraces, reduction of outliers, incorporation of water bodies, and reduction of errors by error propagation. DEM was produced by interpolation from a 1:25,000 Topographical Map with contour interval 12.5 and elevation data from the DGPS profiling. DEM processing generated several morphometric and hydrological variables such as slope, plan curvature, SPI (Stream Power Index) and SCI (Shape Complexity Index) (Figure 1). DEM-derived products were processed in ILWIS software with several available scripts in Hengl et al. (2009) [8].

The other morphometric variables were rockfall velocity and energy. There were processed by RockFall Analyst as an extension of ArcGIS [9]. It included modeling of rockfall trajectory by kinematic algorithm and raster neighbourhood analysis to determine velocity and energy of rockfall. Rockfall velocity and energy analysis needed information of slope

geometry and other parameters such as mass, initial velocity, coefficient of restitution, friction angle and minimum velocity offset. Slope parameter was derived from corrected DEM. The other parameters were derived from secondary data and field data. For example, coefficient restitution and friction angle were derived from literature review based on landuse map and geological map, whereas mass was determined from the dimension of boulders derived from field data measurement. The result was validated with the spatial distribution of boulders inventory obtained from fieldwork.

The landform elements were derived, as the 9-unit slope model, by using the supervised fuzzy k-means classification [10] as

$$\mu_{ic} = \frac{[(d_{ic})^2]^{-1/(q-1)}}{\sum_{c'=1}^k [(d_{ic'})^2]^{-1/(q-1)}} \quad (1)$$

where μ is the membership of i th object to the c th cluster, d is the distance function which is used to measure the similarity or dissimilarity between two individual observations, q is the amount of fuzziness or overlap ($q=1.5$). Supervised k-means classification was written and applied in ILWIS script. Modified 9-unit slope model was applied by excluding alluvial toe slope and seepage slope into a final landform classification.

IV. RESULT AND DISCUSSION

Geomorphometry defined as a quantitative landform analysis [11] was initially applied for the assessment and mitigation of natural hazard [12]. Dijke and Westen (1990) [13], for example, introduced rockfall hazard assessment based on geomorphologic analysis. Later, Iwahashi et al. (2001) [14] analyzed slope movements based on the landform analysis. Both utilized DEMs derived from interpolation of 1:25.000 scale contour map to analyze geomorphological hazard. Nowadays, the interpolation of contour map is still powerful to create medium scale mapping when better resolution DEMs are not available. However, reduction of error in interpolation is needed to obtain plausible geomorphological feature.

Reduction of paddy terraces, reduction of outliers, incorporation of water bodies, and reduction of errors by error propagation were applied in this study to improve the performance of DEM. The result shows that paddy terraces still exist where the sampling of elevation data are absent. In addition, “flattening” topography can also be found on slopes less than 2%. Remaining paddy terraces mostly occur in the transportational middle slope and flattening phenomenon mostly occurs in the interfluves. Both errors influence the

plausibility of slope, (Figure 1a) but those do not much influence the final classification of landform elements.

DEM processing was divided into two parts, i.e. morphometric variables derived from ILWIS script and morphometric variables derived from RockFall analyst. Rockfall velocity and energy are second derivative of DEM [9]. The first derivative DEM i.e. slope angle and aspect angle were employed to compute the rockfall trajectory. Then, rockfall trajectory was used to model the rockfall velocity and rockfall energy by using neighborhood and geostatistical analysis. The highest velocity occurs in the fall face and transportational middle slope. Velocity gradually decreases in the colluvial footslope. Since the energy is also calculated from rockfall velocity, the spatial distribution pattern of energy is rather similar to rockfall velocity. Both velocity and energy of rockfall influence the area of fall face, transportational middle slope and colluvial footslope. The first change of a pixel into zero velocity and energy of its neighborhood operation is determined as the end of boulder movements. It means that the rockfall boulders are deposited on this site. Plan curvature and stream power index influence the pattern of the convex creep slope and the channel bed. It forms water divide and stream channel. SCI, sliced using an equal interval 25 m, was measured as the complexity of outline of 2-D object. It predominantly influences the spatial distribution of the interfluves. Its effect on the other landforms is not apparent because the value of SCI in the lower slope is relatively homogeneous e.g. 4-5.

The result of the model is qualitatively evaluated with the boulders inventory obtained from fieldwork activities. The boulder deposit is located on the lower slope of the transportational middle slope and colluvial foot slope. Thus, the most susceptible place for rockfall hazard is fall face, transportational middle slope, and colluvial footslope respectively.

Preliminary rockfall analysis can be delivered by evaluating elements at risk located in the susceptible place for rockfall hazard. There are 3 buildings located on the transportational middle slope and 14 buildings located on the colluvial footslope. This is useful information on which to base prioritization action for countermeasures policy and design. Geomorphologic analysis should be taken into account to locate structural measures (e.g. barriers, embankments, rock sheds) in suitable location. It will improve cost efficiency to optimize budget and design. The information of building located on the landform classified as high hazard can also be an input to the prioritization of evacuation procedure. Therefore, the prioritization of mitigation action based on geomorphometric analysis can meet the technical suitability and the effectiveness of selected mitigation options.

Legend

- : Major Road
- : Elements at Risk
- : Interfluve
- : Convex Creep Slope
- : Fall Face
- : Transportational Middle Slope
- : Colluvial Foot Slope
- : Slope
- : Channel Bed

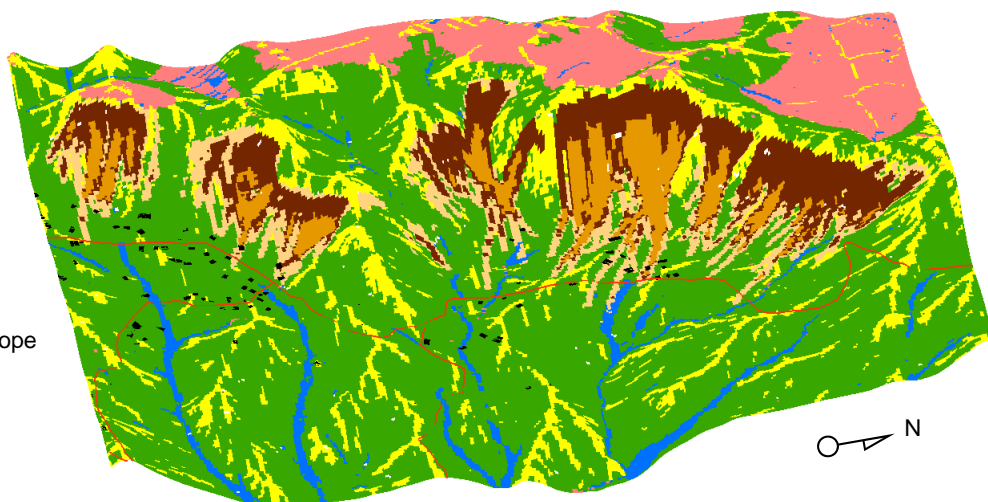


Figure 2 Generic Landforms in Gunung Kelir

However, the classification of 9-unit slope model should be modified if it is applied in different places. The final classification of landform elements i.e. interfluves, convex creep slope, fall face, transportational middle slope, colluvial footslope, slope and channel bed (Figure 2) is different with the original classification of the 9-unit slope model. Alluvial toe slope and seepage slope were excluded from the final landform classification in the present study. Channel wall was also modified as slope. Since the study area is located in the upper part of Kulon Progo Dome, the depositional process of alluvium does not work in that such area. Seepage slope was merged with interfluves slope because interfluves slope and seepage slope landform classification is more related to pedogeomorphic process rather than gravitational process. The considerations to merge and exclude some landforms were based on the experience and the judgement of researchers.

V. CONCLUSION

Geomorphometry application can be an alternative tool to minimize the subjectivity of Indonesia’s standard landform classification applied in disaster risk reduction. Application of supervised landform classification in Gunung Kelir provides reasonable result for preliminary rockfall risk assessment. Landform analysis should be taken into account in disaster risk reduction design and planning. Further studies should explain the effects of scale and spatial dependency on the landform classification.

REFERENCES

[1] Dalrymple, J.B., Blong, R.J., Conacher, A.J., 1968. A hypothetical nine unit landsurface model. *Zeitschrift für Geomorphologie* 12, 60–76.

[2] SNI- Indonesia National Standard (Standar Nasional Indonesia). 2002. *Geomorphology Mapping (Penyusunan Peta Geomorfologi)*. Badan Standarisasi Nasional.

[3] Zuidam van, R.A. 1983. *Guide to Geomorphological Aerial Photographic Interpretation and Mapping*. ITC. Enschede, the Netherlands.

[4] MacMillan, R.A., Shary, P.A., 2009. Landforms and landform elements in geomorphometry. In: Hengl, T., Reuter, H.I. (Eds.), *Geomorphometry: Concepts, Software, Applications. Developments in Soil Science*, vol. 33. Elsevier, Amsterdam, pp. 227-254.

[5] Conacher, A. J. and Dalrymple, J. B. 1977: The nine unit land surface model: an approach to pedogeomorphic research. *Geoderma* 18, 1-154

[6] Bemmelen R.W. van. 1949. *The Geology of Indonesia, Vol II*, Government Printing Office the Hague.

[7] Hengl, T., Gruber, S., Shrestha, D.P., 2004. Reduction of errors in digital terrain parameters used in soil–landscape modelling. *International Journal of Applied Earth Observation and Geoinformation* 5 (2), 97–112.

[8] Hengl, T., Maathuis, B.H.P. and Wang, L. (2009) *Geomorphometry in ILWIS*. In: Hengl, T., Reuter, H.I. (Eds.), *Geomorphometry: Concepts, Software, Applications. Developments in Soil Science*, vol. 33. Elsevier, Amsterdam, pp. 497-525.

[9] Lan, H., Martin, C. D., and Lim, C. H. 2007. RockFall analyst: a GIS extension for three-dimensional and spatially distributed rockfall hazard modelling, *Computer and Geoscience.*, 33, 262–279.

[10] Burrough, P.A., van Gaans, P.F.M., MacMillan, R.A., 2000. High resolution landform classification using fuzzy k-means. *Fuzzy Sets and Systems* 113 (1), 37–52.

[11] Pike, R.J., Evans, I., Hengl, T., 2008. *Geomorphometry: A Brief Guide* In: Hengl, T., Reuter, H.I. (Eds.), *Geomorphometry: Concepts, Software, Applications. Developments in Soil Science*, vol. 33. Elsevier, Amsterdam, pp. 3-30.

[12] Pike, R.J., 1988. The geometric signature: quantifying landslide-terrain types from Digital Elevation Models. *Mathematical Geology* 20, 491–511.

[13] Van Dijke, J. J. and Van Westen, C. J. 1990. Rockfall hazard: a geomorphologic application of neighbourhood analysis with Ilwi, *ITC Journal*, 1, 40–44.

[14] Iwahashi, J., Pike, R.J., 2007. Automated classifications of topography from DEMs by an unsupervised nested-means algorithm and a three-part geometric signature. *Geomorphology* 86 (3–4), 409–440.

Research on the classification of terrain texture from DEMs based on BP neural network

LIU Kai

Nanjing Normal University
Nanjing, P. R. China.
liukaigiser@163.com

TANG Guo'an

Nanjing Normal University
Nanjing, P. R. China.
tangguoan@njnu.edu.cn

JIANG Sheng

Nanjing Normal University
Nanjing, P. R. China.
baobiaojc@163.com

Abstract—Terrain texture is an important natural texture. DEM based terrain texture attracts more and more attention in the research area for its purity in representing surface topography and its derivability in terrain analysis. In this paper, eight sample areas from different landform types of Shaanxi Province in China are selected to make a classification analysis on the terrain texture by Gray level co-occurrence matrix (GLCM) model and BP neural network. First, GLCM was used to extract the feature parameters of the terrain texture from DEMs and its derivative data. Then, the quantitative analysis was conducted by using difference value between the variation coefficient among class and variation coefficient within class in order to find the optimal parameter combination. At last, the BP neural network was applied to classify the terrain texture. The highest recognition rate is 90% which shows a great potential in landform recognition and classification.

INTRODUCTION

Under the inner and outer geological forces, terrain surfaces show the complex morphological characteristics. The research on analysis and quantification of morphology and spatial structure of terrain surface not only play an important role in national economy, but also have actual values in scientific research on landform formation, development and evolution. The existing researches of morphological characteristics of landform mostly discuss landform changes recur to the spatial variable characteristics of topographic factors on micro scale, which can well describe the local morphological characteristics of terrain surface. But the knowledge of morphological characteristics of landform on macro scale is still insufficiency. And recently effective analysis methods of morphological and structural characteristics of landform on macro scale are still in shortage.

As a kind of significant features, texture has been widely used in digital image processing. Haralick (1973) and Ilea (2011) discussed the concept and connotation of the texture. Some texture analysis methods can be adopted such as statistical texture analysis methods, structural methods, methods based on model and frequency domain methods. Recently, Much effort has

been devoted to extracting effective and efficient texture operators from remote sensing images (Wood et al., 2012), and image textural analysis has been the important basis for object identification and classification.

Digital elevation models (DEMs), as the major information source in describing surface morphological characteristics, is widely applied in GIS based digital terrain analysis (DTA). Recently, significant achievements have been made in DEM based digital terrain analysis, such as basic theory of DTA, landform morphological characteristic investigation, landform classification and cartography (Ian S, 2011). Compared with remote sensing images, DEMs are grid cell-based expression of the land surface where buildings and vegetation have been removed, representing bare-ground topography (Anders et al., 2011). Thus, terrain textures from DEMs have purer geomorphological significance than remote sensing images.

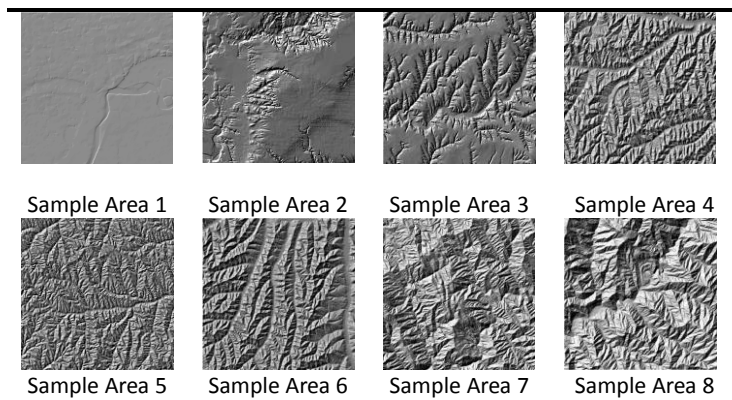
This paper firstly discusses the terrain texture characteristics, then, the Grey Level Co-occurrence Matrix (GLCM), a common textural analysis method, is applied to study the terrain texture from DEMs and its derivatives. At last, the back-propagation (BP) neural network is applied to classify the terrain texture.

MATERIALS AND METHODS

Study areas and data

In this paper, 8 sample areas from different landform types of Shaanxi province in China are selected to make a classification analysis. Each study area is divided into fifteen blocks as test samples with an area of 12 km ×12 km. DEM data in this research is from the contours of 1:50000 topographical maps and produced by the National Geomatics Center of China with a spatial resolution of 25m. The basic morphological characteristics of each sample area are shown in Table 1.

TABLE I. HILLSHADE MAPS OF SAMPLE AREAS



Establishment of GLCM based on DEMs

The Construction of GLCM based on DEMs is on the three-dimension curve described by DEM elevation matrix. It regards XOY-plane as a coordinate plane, and then puts forward a series of hypothesis as follows: pixel size equals to r , pixel numbers of horizontal direction equals to M_x , pixel number of vertical direction equals to M_y , the space domain of horizontal direction is $S_x = \{1, 2, \dots, M_x\}$, the space domain of vertical direction is $S_y = \{1, 2, \dots, M_y\}$, z is the elevation coordinate axis.

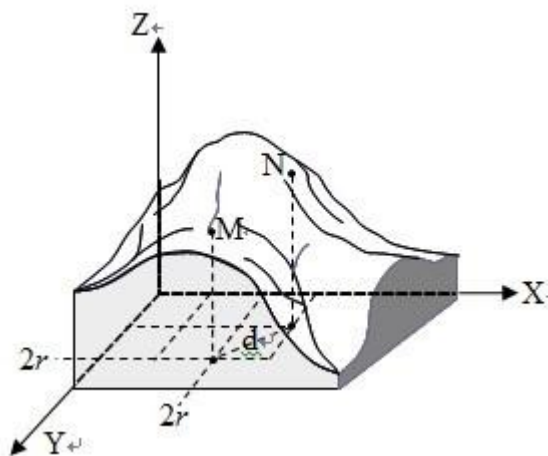


Figure 1. Space expression of dot pair in DEM

Hypothesizing the distance (project distance) between a pair of pixels equals to d , the direction angle of dot pair equals to θ , then when the direction is parallel with X-axis, θ equals to 0 and counterclockwise rotation around z-axis takes the positive direction. Choose a pair of pixels with direction θ and distance d from texture image and then statistics the joint conditional probability density, then a GLCM model $C(d, \theta)$ could be structured. Based on GLCM, Haralick proposed 14 textural

features. According to existing research, this paper select 10 features to analysis the terrain characteristics.

Parameter screening

The parameter should satisfy the requirements of maximizing internal homogeneity while minimizing external homogeneity. In this paper we use the coefficient of variation. The equation is as follows:

$$CV = \frac{\sigma}{\mu} \times 100\%$$

Where σ is standard deviation and μ is the mean value. The smaller the CV value within class is, the more stable the feature will be. The bigger the CV value among class is, the more strong separating capacity the feature will be. Hence, we use the difference value between the CV value among class and the CV value within class to assess the discriminative capacity of each parameter.

Establishment of BP model

BP network is basically a gradient decent algorithm designed to minimize the error function in the weights space. During training of the neural network, weights are adjusted to decrease the total error. In principle, it has been proved that any continuous function can be uniformly approximated by BP network model with only one hidden layer. So a three-layer BP model is employed in our study. It is easy to determine the number of neurons in the input layer and output layer during applications. In this paper, the input neurons number depends on the texture parameters joined in the classification experiments and the output neurons number is eight which depends on the classification categories. However, it is not easy to choose the appropriate number of neurons in the hidden layer and in this paper it is determined by trial-and-error method.

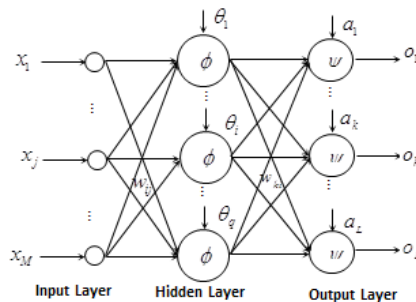


Figure 2. BP neural network structure

RESULT

Table II shows the difference value between the CV value among class and CV value within class, the value varies in different parameters from different data. Some value is negative which means that the CV value with class of such parameter is greater than the CV value among class, and it is unsuited to classification experiments.

TABLE II. DIFFERENCE VALUE BETWEEN CV VALUE AMONG CLASS AND CV VALUE WITHIN CLASS

	DEM	Hillshade	Slope	Curvature
Angular Second Moment	0.168581	1.25958	1.259767	0.229531
Contrast	0.343481	0.29671	0.344383	0.112854
Variance	-0.10602	0.008394	0.361408	-0.05802
Inverse Different Moment	0.0551	0.191398	0.183427	0.051564
Average	-0.05771	0.0135	0.280301	-0.03641
Sum Variance	-0.13523	0.10284	0.368139	-0.05132
Sum Entropy	0.027231	0.283655	0.237616	0.106881
Entropy	0.054366	0.290388	0.27177	0.112752
Different Variance	0.18413	0.65725	0.607766	0.221478
Different Entropy	0.221065	0.260702	0.267087	0.137527

In this paper, BP neural network is applied to classify the terrain texture. Each study region contains 15 samples, 10 samples are selected as the training samples and the rest 5 samples are chosen as the test samples.

Table III shows the classification accuracy by using single data without parameter screening. The accuracy of slope data is the highest, while the accuracy of DEM data is the lowest which indicates that the texture form slope data is more suitable for terrain classification.

TABLE III. CLASSIFICATION ACCURACY BY USING SINGLE DATA

DEM	Hillshade	Slope	Curvature
52.5%	62.5%	77.5%	55%

Figure 3 shows the classification accuracy by using multiple data with parameter screening. According to the difference value in Table one, priority should be given to the parameter with high different value. Classification accuracy varies with parameter number changes but in any case, it is higher than the accuracy by using single data. The accuracy reaches the peak when using seven parameters and it could be regarded as the optimal parameter combination.

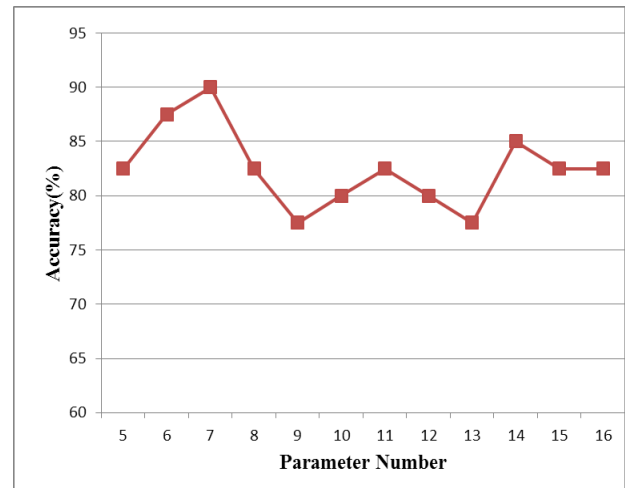


Figure 3. Classification accuracy as change of parameter number

CONCLUSIONS

In order to overcome the shortcoming of describing the terrain characteristics on macro scale, in this paper, the GLCM model and BP neural network are introduced into digital terrain analysis. The results show that texture analysis starts from human vision perceptive mechanism can effectively analyze and quantify the morphological and structural characteristics of terrain surface and such method could be used and improved to reveal the morphological and structural characteristics of landform on macro scale, which can be recognized as a new thinking for the quantification and classification of landform morphological characteristics. In the further, some other complex textural analysis methods and classifiers should be applied, and it could reveal the morphological characteristics of landform in a more painstaking level.

ACKNOWLEDGMENT

This paper was supported by the Natural Science Foundation of China (Key Project No.40930531, No.41171320).The authors gratefully appreciate good suggestions from colleagues in our laboratory for their valuable comments and other helps.

REFERENCES

[1] Anders, N.S., A.C. Seijmonsbergen, and W. Bouten, Segmentation optimization and stratified object-based analysis for semi-automated

geomorphological mapping. *Remote Sensing of Environment*, 2011. 115(12): p. 2976-2985

[2] Haralick, R.M., K. Shanmugam, and I.H. Dinstein, Textural Features for Image Classification. *Systems, Man and Cybernetics, IEEE Transactions on SMC*, 1973. 3(6): p. 610-621.

[3] Ilea, D.E. and P.F. Whelan, Image segmentation based on the integration of colour–texture descriptors—A review. *Pattern Recognition*, 2011. 44(10–11): p. 2479-2501

[4] Panek, T., J. Hradecky, and K. Silhan, Geomorphic evidence of ancient catastrophic flow type landslides in the mid-mountain ridges of the Western Flysch Carpathian Mountains (Czech Republic). *International Journal of Sediment Research*, 2009. 24(1): p. 88-98.

[5] McNamara, J.P., et al., Channel head locations with respect to geomorphologic thresholds derived from a digital elevation model: A case study in northern Thailand. *Forest Ecology and Management*, 2006. 224(1–2): p. 147-156.

[6] Wood, E.M., Pidgeon, A.M., Radeloff, V.C., Keuler, N.S., 2012. Image texture as a remotely sensed measure of vegetation structure. *Remote Sensing of Environment* 121, 516–526.

Research on Terrain Significance Index and Its Quantification Model based on Grid-DEMs

DONG Youfu

College of Geomatics Engineering
Nanjing University of Technology

No.200 North Zhongshan road, Nanjing, Jiangsu, P.R.C. 210009

E-mail: dongyoufu@163.com

Abstract—Representing DEM cell's significance in modeling the true terrain surface, Terrain Significance Index (TSI) which refers to the terrain information capacity for a grid point is presented and discussed in this paper by introducing quantitative model, extracting method and applications. On the basis of hierarchical cognitive models of the information theory, a comprehensive quantitative model of TSI is established by measuring local syntactic and global semantic terrain information contents. Choosing a 70km² area in the loess gully region as test area and 5m-resolution DEM as test data, the paper discussed a series of TSI extraction scheme based on DEMs. In addition, a TSI based application in multi-scale terrain generalization is proposed. Experimental results show that the TSI measurement model proposed is feasible and TSI based multi-scale DEMs construction method is not only easy in implementing but also effective in reducing the terrain distortion. It proves that the multi-scale DEMs constructed by controlling TSI values could meet the demands in different levels of digital terrain modeling. Therefore, the research should be hopeful in deepening our understanding on DEM terrain information characteristics and in building a theoretical foundation and methodological support for multi-scale digital terrain modeling.

KeyWords—Digital Elevation Model (DEM), Terrain Significance Index (TSI), Terrain Modelling, Digital Terrain Analysis

INTRODUCTION

As we know, a grid DEM expresses terrain information by a lattice data with different elevation values. Meanwhile, it is noticeable that the importance of a set of elevation points representing the true terrain surface in local and global area is markedly different. So, how to recognize and assess the importance of elevation points is of theoretical significance and applied value. There are a lot of criteria to evaluate the importance of elevation points. In general, it shows that the assessment of point importance pays attention to elevation difference in local area but ignores the global terrain skeleton.

As a result, it is meaningful to clarify and quantify the importance of elevation points in depth.

METHODS AND PROCEDURES

Methods

The importance of elevation point in modeling the surface is associated with not only elevation variation with the point's grid neighbors but also its topographic position. According to information theory, the importance of elevation point can be expressed by the terrain information of different levels loaded in the point. So, this paper proposes the concept of Terrain Significance Index (TSI) which refers to the importance of elevation points in modeling the terrain surface. And then, TSI is quantified comprehensively from both syntax level and semantic level. The terrain syntax information of elevation point referring to the appearance of terrain variation can be measured by the vector angles of the tangent planes in neighbor grids based on the principle of differential geometry. The terrain semantic information of elevation point referring to the meaning of terrain features is determined by their types and the grades where the point locates in. According to the topographic hierarchy and spatial relationship of terrain features, there are four principles when defining the semantic information of a grid point. The first, each type of terrain features is assigned corresponding semantic information intents; the second, it is independent of the semantic information intents of different terrain features if their spatial locations don't overlay; the third, the semantic information intents of different terrain features such as ridges and peaks are determined further by their geomorphologic characteristics and spatial relations when they coincide in locations; the last, the semantic information intents of the terrain features being the same types and different hierarchies are assigned differentiated weights. The quantification model of terrain significance index is constructed after the measure methods of terrain syntax

information and semantic information for a given grid point being established. For the representation of terrain surfaces, terrain feature elements dominate the whole terrain skeleton and the effect is more and more obvious when terrain structure is complicated. To differentiate the grid point importance in depicting terrain and topography effectively, the comprehensive quantification model of terrain significance index is built by overlaying terrain syntax and semantic information values given proper weights.

Procedures

A basin named Jiu Yuangou drainage located in northern Shaanxi province in the Loess Plateau of China is choosed as test area and 5m-grid DEMs produced by State Bureau of Surveying and Mapping of China are used as test data.

Firstly, the extraction programs of terrain semantic information for channels, ridges, shoulder-lines, toe-lines, peak points, pass points, channel junctions and ridge junctions are determined. Then, its terrain significance information index for a grid point is acquired by summing its terrain syntax information value and terrain semantic information value. The extraction results are shown in TSI's spatial distribution map(Figure 1): (1) the grid points locating in terrain skeleton lines are with marked large TSI values and it shows the different levels of landform features well, i.e. terrain structural points, peaks, passes, ridge junctions, channel junctions, ridge points channel points with different orders are of significant variation reflected in TSI value; (2) the grid points where local elevation change sharply are with high TSI value relatively, such as the grid points locating in the microgrooves and the neighborhood relief points in relative flat areas. (3) the TSI values are very low for most of grid points, including flat points and gentle slope points, which indicate that their roles are not important for the terrain representation.

APPLICATION

A TSI based application in constructing multi-scale DEMs is proposed. As we know, the assessment of grid point importance plays an important role for simplifying terrain based on DEMs. So, terrain significance index (TSI) being a comprehensive quantitative index describing the importance of a grid point in modeling the terrain and topography is more meaningful to construct multi-scale DEMs. The procedure of terrain generalization based on TSI is proposed. Firstly, the TSI for each grid points based on high resolution DEMs is extracted. Secondly, candidate terrain points are selected to construct generalized DEMs by setting a TSI tolerance value; Meanwhile, the candidate points clustering are reduced in

case of the smaller TSI tolerance. Then, the restricted TINs are established with the last candidate points by joining the terrain feature lines. Finally, the result DEMs is generated by interpolating from the restricted TINs. Because of TSI tolerance influencing the details and precisions of the generalized DEMs markedly by controlling the size of candidate points to construct TINs, the determination of TSI tolerance is the most key step in the whole procedure. In order to determine a most appropriate TSI tolerance for constructing a generalized DEMs being of a terrain detail level, a series of DEMs are reconstructed using different TSI values in the first place(Figure 2); Then, taking the standard 25m-grid resolution DEMs produced by State Bureau of Surveying and Mapping of China as a reference target, the reconstructed DEMs performances are evaluated and contrasted by analyzing the values of their root mean square error (RMSE) and the differences of contour structures. Consequently, the TSI value used to reconstruct DEMs with the relatively best performance is identified as the optimal tolerance.

In evaluating the generalization method for grid DEMs based on TSI, the differences are analyzed by comparing the spatial distribution of the candidate points used to reconstruct the result DEMs, elevation statistical parameters and contour structures taking Very Important Points (VIP) and Three-Dimensional Douglas-Peucker (3DD-P) as verify algorithms and 1:50,000 DEMs as a reconstructed target. Experimental results show that the TSI measurement model proposed is feasible and TSI based multi-scale DEMs construction method is not only easy in implementing but also effective in reducing the terrain distortion. It proves that the multi-scale DEMs constructed by controlling TSI values could meet the demands in different levels of digital terrain modeling. Therefore, the research should be hopeful in deepening our understanding on DEM terrain information characteristics and in building a theoretical foundation and methodological support for multi-scale digital terrain modeling.

REFERENCES

- [1] Z.T. Chen and J.A. Guevara,1987, "Systematic selection of very important points (VIP) from digital terrain model for constructing triangular irregular networks," Proceeding of AUTO-CARTO, pp. 50-56.
- [2] J.R. Fowler and J.J. Little, 1979. "A automatic extraction of irregular network digital terrain models," Computer and Graphics, pp. 199-207.
- [3] D. Floriani, 1984. "A hierarchical data structure for surface approximation," Computer and Graphics, pp. 475-484.
- [4] Young, M., 1989. "The Technical Writer's Handbook". Mill Valley, CA: University Science, 325 p.
- [5] L.F. Fei and J. He, 2009. "A three-dimensional Douglas-Peucker algorithm and its application to automated generalization of DEMs," International Journal of Geographical Information Science, pp.703-718.

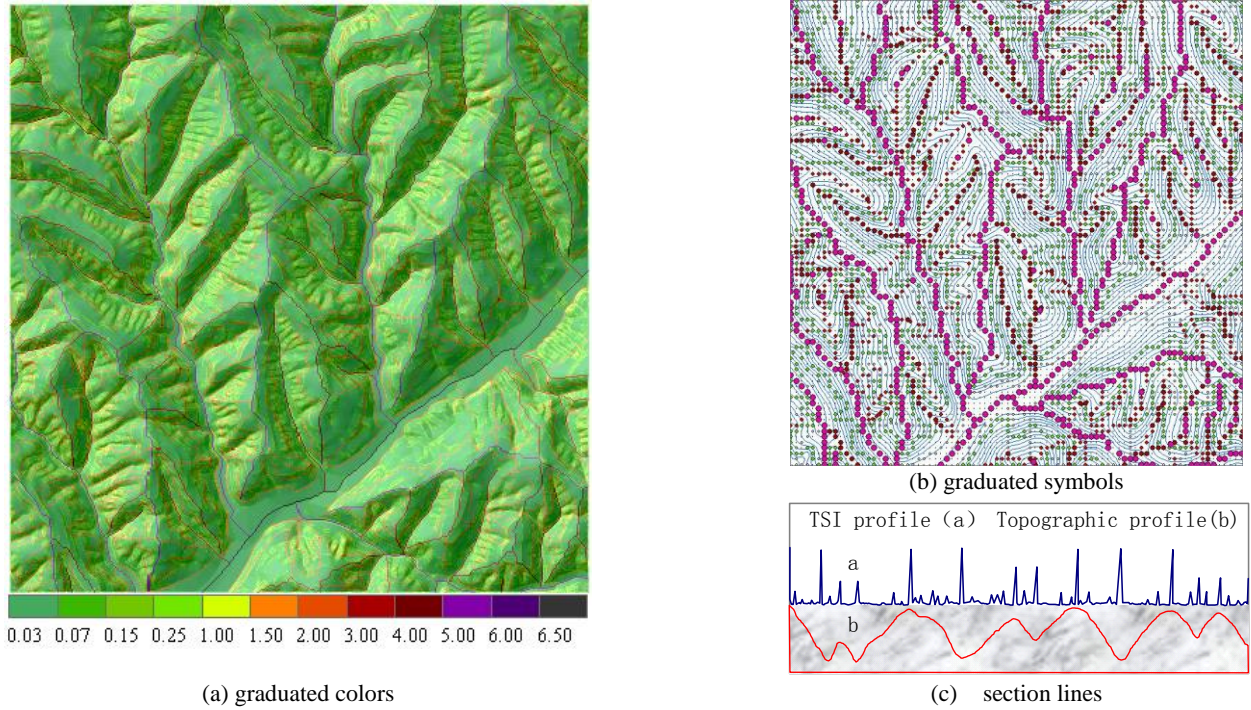


Figure 1. The extraction results of Terrain Significance Information Index

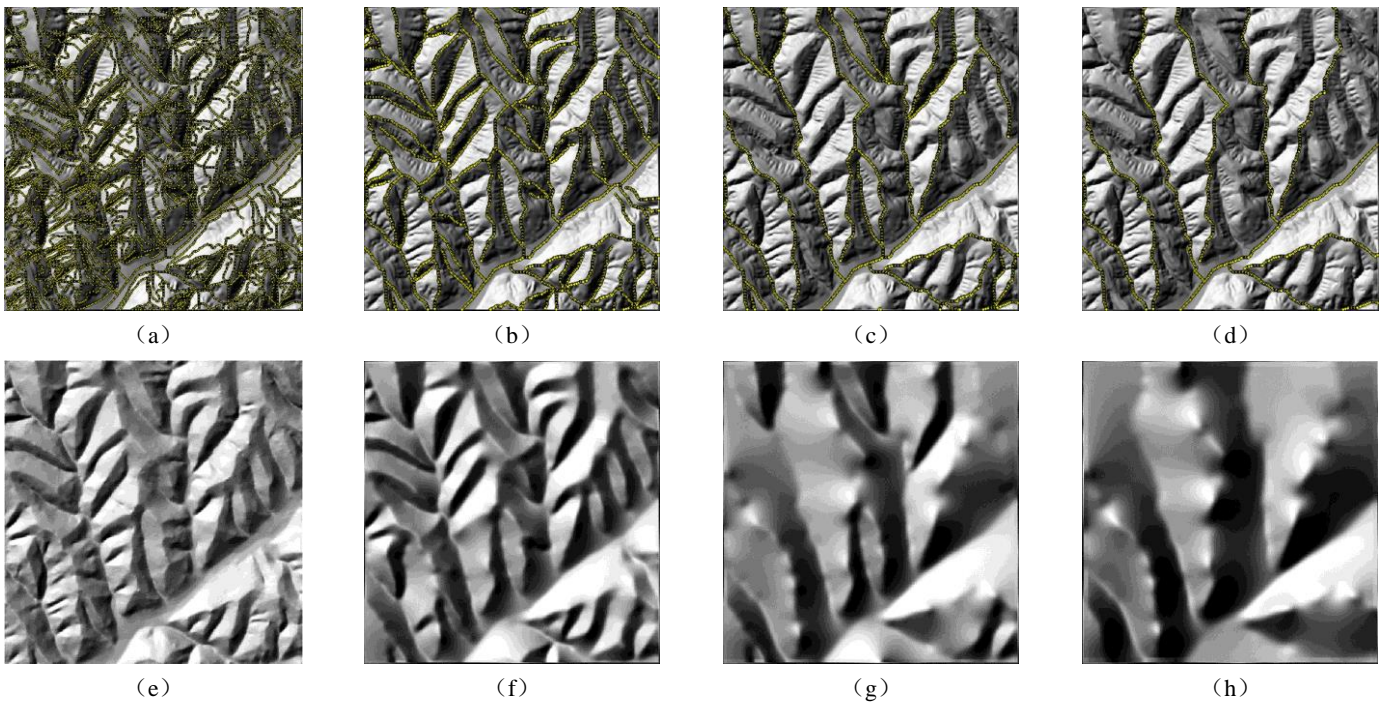


Figure 2. The generalized DEMs with different TSI values. (a,b,c,d: the candidate points with TSI tolerance being 1.0,2.0,3.0,4.0 ; e,f,g,h: the generalized DEMs with TSI tolerance being 1.0,2.0,3.0,4.0 correspondingly)

Mathematical Surfaces for which Specific and Total Contributing Area can be Computed: Testing Contributing Area Algorithms

Scott D. Peckham
University of Colorado
Boulder, Colorado USA
Scott.Peckham@colorado.edu

Abstract—In order to properly evaluate different algorithms for computing the total contributing area (TCA) and specific contributing area (SCA) from DEMs, it is important to have mathematical test surfaces for which these quantities can be computed in closed form. In previous work, the inverted cone and inclined plane have been used for this purpose because they are the only mathematical surfaces for which closed-form results were available. Note that the various algorithms differ most in terms of how well they work on divergent topographic surfaces where streamlines diverge, and several different algorithms based on multiple flow directions have been developed for this case. The purpose of this paper is to show how TCA and SCA can be computed mathematically and to provide several new examples of test surfaces for which results can be given in closed form. These new results are then briefly compared to results from an advanced method for computing TCA and SCA from DEMs called the *mass flux method*. More detailed comparisons to results from this and other methods will be presented later in a full paper.

I. INTRODUCTION

For a divergent, radially-symmetric surface, both the TCA and SCA can be computed in closed form (Gruber and Peckham, 2009). As shown in Figure 1, the TCA of a pixel with $\Delta y = \Delta x$, centered at $(x, y) = (i\Delta x, j\Delta x)$, where i and j are integers and $m = |i| + |j|$, is given by

$$A(i, j) = \begin{cases} \Delta x^2 (m + 1) / 2, & \text{if } i \neq 0 \text{ and } j \neq 0 \\ \Delta x^2 (m + \frac{3}{2}) / 2, & \text{if } i = 0 \text{ xor } j = 0 \\ \Delta x^2, & \text{if } i = 0 \text{ and } j = 0. \end{cases} \quad (1)$$

Even though this expression is exact, the middle case is responsible for an odd-looking “artifact” along the axes. The width of a pixel, as projected toward the origin, is

$$w(x, y) = \Delta x [|\sin(\theta)| + |\cos(\theta)|] \quad (2)$$

$$= \frac{\Delta x (|x| + |y|)}{\sqrt{x^2 + y^2}}, \quad (3)$$

where $\theta(x, y) = \tan^{-1}(y/x)$ and we used the identities $\sin(\tan^{-1}(x)) = x/\sqrt{1+x^2}$ and $\cos(\tan^{-1}(x)) = 1/\sqrt{1+x^2}$. The SCA is therefore given by

$$a(x, y) = \lim_{\Delta x \rightarrow 0} \frac{A(x, y)}{w(x, y)} = \frac{\sqrt{x^2 + y^2}}{2}. \quad (4)$$

It depends only on distance from the origin.

Note: If we instead place the origin/peak at a pixel corner, four pixels will share the peak and we get a single expression for all pixels, $A(i, j) = \Delta x^2 (m + 1) / 2$, where $m = |i + \frac{1}{2}| + |j + \frac{1}{2}|$, $x = (i + \frac{1}{2})\Delta x$, $y = (j + \frac{1}{2})\Delta x$. This change appears to remove the “artifact” associated with the middle case in equation (1).

II. BACKGROUND

A. Orthogonal Curvilinear Coordinate Systems

An orthogonal curvilinear (OC) coordinate system with coordinates u and v can be specified relative to Cartesian coordinates x and y by a transformation $x(u, v)$, $y(u, v)$. The inverse of the transformation is denoted by $u(x, y)$, $v(x, y)$. In order for curves of constant u and constant v to be orthogonal, we must have $x_u x_v + y_u y_v = 0$, where the subscripts denote partial derivatives with respect to u and v . In two dimensions, two functions of u and v

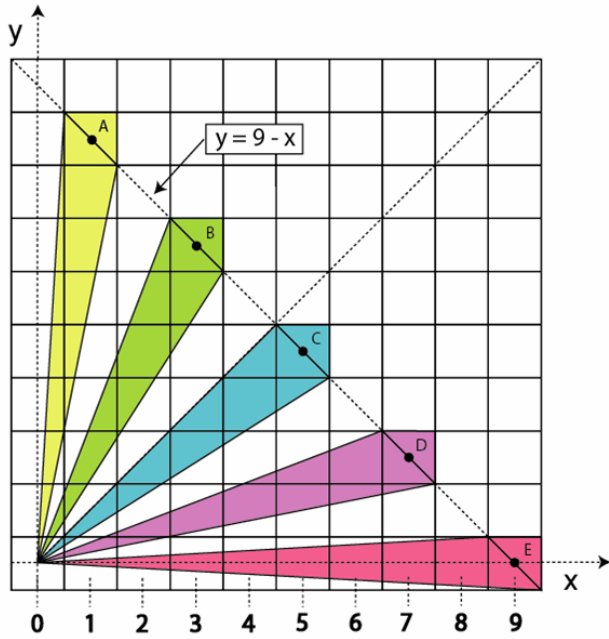


Fig. 1. For a divergent, radially-symmetric surface, such as an inverted cone or a Gaussian hill, the TCA for pixels can be computed analytically. Each *necktie* region shown can be broken into two colored triangles. Triangles below the line $y = m\Delta x - x$ (here $m = 9$) each have base and height given by: $b = \sqrt{2}\Delta x$ and $h = \sqrt{2}m\Delta x/2$, so their area is, $A = m\Delta x^2/2$. Triangles above the line each have an area of $\Delta x^2/2$. This shows that pixels A–D (and those in between) each have $TCA = \Delta x^2(m + 1)/2$. Note, however, that pixel E has $TCA = \Delta x^2(m + \frac{3}{2})/2$.

known as *metric coefficients* determine the local amount of “stretching” associated with the transformation, denoted here by $\rho(u, v)$ and $\sigma(u, v)$. Lengths along curves of constant u and v are obtained by integrating ρ and σ , respectively. The metric coefficients and their product, J , called the *Jacobian* of the transformation are given by

$$\rho(u, v) = \sqrt{x_u^2 + y_u^2} \tag{5}$$

$$\sigma(u, v) = \sqrt{x_v^2 + y_v^2} \tag{6}$$

$$J(u, v) = \rho(u, v) \sigma(u, v). \tag{7}$$

See Peckham (1999) for an application of these concepts to the problem of finding closed-form solutions to a class of nonlinear partial differential equations (PDEs), which includes a PDE for idealized, steady-state landforms.

TABLE I
ORTHOGONAL CURVILINEAR COORDINATE SYSTEMS

	Radial	Parabolic	Elliptic
$x(u, v)$	$u \cos(v)$	$(u^2 - v^2)/2$	$a \cosh(u) \cos(v)$
$y(u, v)$	$u \sin(v)$	uv	$a \sinh(u) \sin(v)$
$\rho(u, v)$	1	$\sqrt{u^2 + v^2}$	$a \sqrt{\sinh^2(u) + \sin^2(v)}$
$\sigma(u, v)$	u	$\rho(u, v)$	$\rho(u, v)$
$u(x, y)$	$\sqrt{x^2 + y^2}$	$-\sqrt{x + r}$	$-\cosh^{-1}[K(x, y)]$
$v(x, y)$	$\tan^{-1}(y/x) + c$	$-y/u(x, y)$	$\sec^{-1}[(a/x)K(x, y)]$

where $r = \sqrt{x^2 + y^2}$, $K(x, y) = \sqrt{G(x/a, y/a)}/2$
and $G(x, y) = 1 + r^2 + \sqrt{1 + 2(r^2 - 2x^2) + r^4}$.

B. General Expressions for TCA and SCA

For any orthogonal curvilinear (OC) coordinate system, the area bounded by two constant- u curves ($u = u_1$ and $u = u_2$) and two constant- v curves ($v = v_1$ and $v = v_2$) is given by the integral

$$A(u_1, u_2, v_1, v_2) = \int_{u_1}^{u_2} \int_{v_1}^{v_2} J(u, v) du dv. \tag{8}$$

The SCA can then be computed (Gallant and Hutchinson, 2011) as

$$a(u_1, u_2, v) = \lim_{\Delta v \rightarrow 0} \frac{A(u_1, u_2, v, v + \Delta v)}{\sigma(u_1, v) \Delta v}. \tag{9}$$

This expression for A can also be used to get approximate values on a rectilinear grid that differ from the exact values by no more than $\Delta x^2/2$. Given closed-form expressions for $u(x, y)$ and $v(x, y)$, the u -value of each grid cell (say u_1) can be computed from the xy coordinates of its center. Similarly, v_1 and v_2 can then be computed from the xy coordinates of two opposite corners of the grid cell. The values u_1, v_1 and v_2 — together with u_2 as the (maximum) u -value of the ridge or peak — can then be inserted into (8) to get the TCA for the given grid cell. SCA can be computed more simply by computing u and v from the xy coordinates of each grid cell’s center and inserting into (9).

III. RADIALLY-SYMMETRIC SURFACES

Any surface with radial symmetry, including a Gaussian hill and an inverted cone, will have its contour lines and streamlines given by a “radial” OC coordinate system (see

Table I, column 1). Contour lines are curves of constant radius, u , and streamlines are curves of constant azimuth angle, v . Elevation is given by $z = H(u)$ for some function, H . Equation (8) then simplifies to

$$A(u_1, v_1; u_2, v_2) = (v_2 - v_1) (u_2^2 - u_1^2) / 2 \quad (10)$$

For a grid cell centered at (x, y) , with sides of length $\Delta y = \Delta x$, and taking $u_2 = 0$, we then have

$$F(x, y) = \tan^{-1}\left(\frac{2y + \Delta x}{2x - \Delta x}\right) - \tan^{-1}\left(\frac{2y - \Delta x}{2x + \Delta x}\right) \quad (11)$$

$$G(x, y) = (x^2 + y^2) / 2 \quad (12)$$

$$A(x, y) = F(x, y) G(x, y). \quad (13)$$

On the diamond-shaped curves where $|x| + |y| = c$, we can eliminate y in $G(x, y)$ and $F(x, y)$. This gives $G(x, y) = (2x^2 - 2c|x| + c^2)/2$, and the first term in a Taylor series of $F(x, y)$ in Δx about 0 gives $F(x, y) \approx c \Delta x / (2x^2 - 2c|x| + c^2)$. As a result, the TCA on these curves is approximately $c \Delta x / 2$, consistent with the exact result obtained in the Introduction. Using (9) to compute the SCA returns us to (4).

IV. SURFACES BASED ON PARABOLIC COORDINATES

The parameters for a *parabolic* OC coordinate system are given in Table I (column 2) where $u \leq 0$ and $v \geq 0$. For any surface with $z = H(u)$, the TCA and SCA can be computed using (8) and (9) as

$$A(u_1, v_1; u_2, v_2) = [(v_2 - v_1) (u_2^3 - u_1^3) + (u_2 - u_1) (v_2^3 - v_1^3)] / 3 \quad (14)$$

$$a(u, v; u_2) = \frac{(u_2^3 - u^3) + 3v^2(u_2 - u)}{3\sqrt{u^2 + v^2}}. \quad (15)$$

For the surface shown in Figure (2), we have $z = u$ with the ridgeline given by the curve $u = u_2 = 0$. SCA can be computed as

$$a(x, y) = \frac{\sqrt{2}}{3} \cdot \frac{[r(2r + x) - x^2]}{\sqrt{r(r + x)}}, \quad (16)$$

where $r = \sqrt{x^2 + y^2}$. Contours of elevation and SCA are shown in Figure (3).

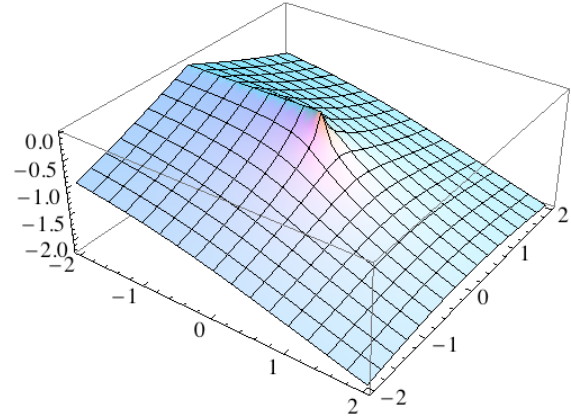


Fig. 2. A divergent surface with contours and streamlines given by a parabolic coordinate system with $z(x, y) = u(x, y)$. The ridgeline is given by $u = 0$ and runs from $x = -\infty$ to $x = 0$ (with $y = 0$).

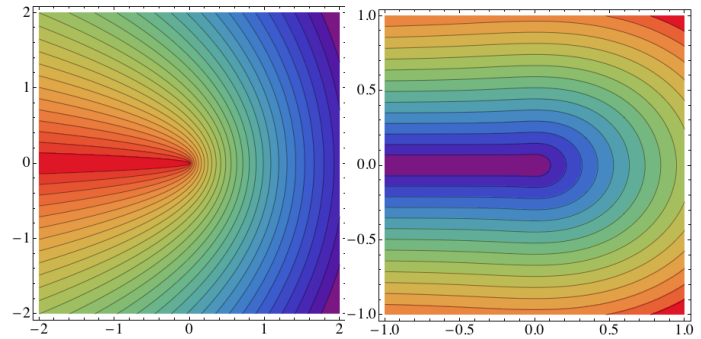


Fig. 3. For the surface in Figure 2: (a) Contours of elevation. Both contour lines and streamlines are given by parabolas. (b) Contours of SCA. SCA is zero on the ridgeline (purple). High values are red and low values are blue.

V. SURFACES BASED ON ELLIPTIC COORDINATES

The parameters for an *elliptic* OC coordinate system are given in Table I (column 3), where $u \leq u_2$ and $v \in [0, 2\pi]$. For any surface with $z = H(u)$, TCA can be computed as

$$A(u_1, v_1; u_2, v_2) = \left(\frac{a}{2}\right)^2 [(u_2 - u_1) F(v_1, v_2) + (v_1 - v_2) G(u_1, u_2)] \quad (17)$$

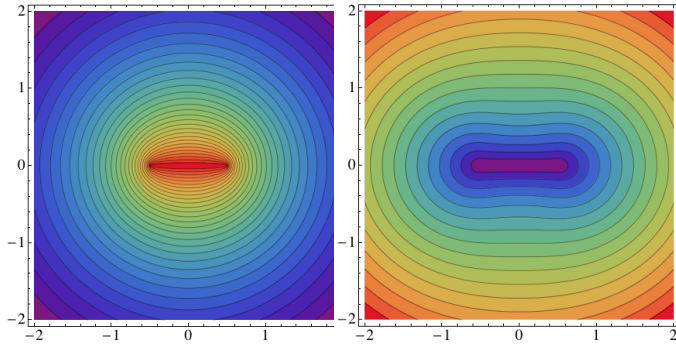


Fig. 4. For the surface based on elliptic coordinates ($z(x, y) = u(x, y)$): (a) Contours of elevation. Contour lines are given by ellipses. Ridgeline is given by $u = 0$, and runs from $x = -a$ to $x = a$ (with $y = 0$). (b) Contours of SCA. SCA is zero on the ridgeline (purple). High values are red and low values are blue.

where

$$F(v_1, v_2) = \sin(2v_1) - \sin(2v_2) \quad (18)$$

$$G(u_1, u_2) = \sinh(2u_1) - \sinh(2u_2). \quad (19)$$

Similarly, the SCA can be computed using (9) as

$$a(u, v; u_2) = \frac{a[B(u_2, v) - B(u, v)]}{4\sqrt{\sin^2(v) + \sinh^2(u)}} \quad (20)$$

$$B(u, v) = \sinh(2u) - 2u \cos(2v). \quad (21)$$

Contours of elevation and SCA are shown in Figure (3) for the case $z = u$, where the ridgeline corresponds to the curve $u = u_2 = 0$.

VI. RESULTS FOR THE MASS FLUX METHOD

Figures (5) and (6) show the SCA as computed using the Mass Flux Method for a radially symmetric surface and for surfaces based on parabolic and elliptic coordinates. Note that the “artifact” that results from the exact TCA calculation is inherited by the SCA figures. The agreement between values computed mathematically and using the Mass Flux Method is quite good. However, work is ongoing to determine how best to remove the artifact. More complete results, including tests of other methods for computing TCA and SCA will be presented in a full paper.

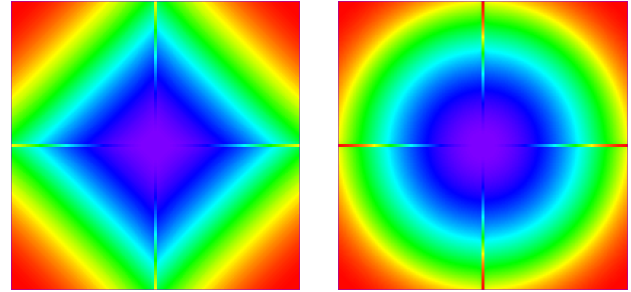


Fig. 5. TCA (a) and SCA (b) for a radially-symmetric surface, as computed with the Mass Flux Method in RiverTools 4.0. High values are red and low values are blue.

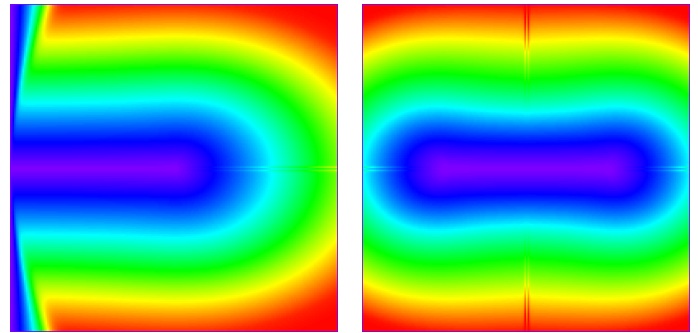


Fig. 6. SCA for surfaces based on parabolic (a) and elliptic (b) coordinates, computed with the Mass Flux Method in RiverTools 4.0. Edge effects are expected in (a). High values are red, low ones are blue.

REFERENCES

- Gallant, J.C. and M.F. Hutchinson (2011) A differential equation for specific catchment area, *Water Resour. Res.*, **47**(5), W05535, doi:10.1029/2009WR008540.
- Gruber, S., and S. Peckham (2009) Land surface parameters and objects in hydrology, In: *Geomorphometry: Concepts, Software, Applications*, edited by T. Hengl and H. I. Reuter, pp. 171–194, Elsevier, Amsterdam.
- Peckham, S.D. (1999) Solutions to nonlinear partial differential equations: A geometric approach, In: *Proceedings of the Conference on Geometry in Present-Day Science*, edited by O.E. Barndorff-Nielsen and E.B. Vedel Jensen, World Scientific, New Jersey, 165–186. (See p. 178.)
- Rivix, LLC (2003) *RiverTools 3.0 User’s Guide*, 218 pp.
- Spiegel, M.R. (1968) *Mathematical Handbook of Formulas and Tables*, 271 pp., Schaum’s Outline Series, McGraw-Hill Book Co.

Simulating Loess with Underlying Bedrock Paleotopographic strata for Landscape Evolution in the Loess Plateau Based on Digital Elevation Models

XIONG LiYang

Key laboratory of Virtual Geographic Environment, Ministry of Education
Nanjing Normal University
Nanjing, China
xiongliyang@163.com

TANG GuoAn

Key laboratory of Virtual Geographic Environment, Ministry of Education
Nanjing Normal University
Nanjing, China
tangguoan@njnu.edu.cn

Abstract—the evolution processes of loess landforms are greatly controlled by the pre-Quaternary underlying bedrock terrain, which is one of the most important aspects to explain the formation mechanism of loess landforms. In this research, on the basis of multiple data sources, 1729 outcropping points of underlying terrain are detected to construct a simulated digital elevation model of the pre-Quaternary underlying paleotopography in a severe soil erosion area of Loess Plateau. The results show that obvious differences could be found between the underlying terrain and modern terrain; the topographic complexity of the underlying terrain appears simpler than that of the modern terrain. In addition, the modern surface has a gentler topographic relief than the topographic relief of the underlying terrain, as well as shows a significant landform inheritance characteristic of loess deposition. All these results deepen the understanding of the formation and evolution of loess landform.

INTRODUCTION

The Loess Plateau is a positive geomorphic unit formed following the transportation and accumulation process of loess deposits on the basis of inheritance of underlying bedrock terrain during the Quaternary period (Liu, 1985). This unique formation mechanism directly determines the current complex and diverse landscapes, which attract world attention with their deep background of global change, thick loess sediments, varied loess landscape types, serious soil erosion and interaction between natural and human activities. Hence, a study of the paleotopography beneath the loess and its controlling impact on the current loess landform is of critical significance in understanding the formation mechanism and the landscape evolution process of the Loess Plateau and loess landforms.

Previous studies have developed many landscape evolution models to numerically represent landscapes and their evolution process over time, like SIBERIA (Willgoose et al., 1991); GOLEM (Tucker and Slingerland, 1994); CASCADE (Braun and Sambridge, 1997); CAESAR (Coulthard et al., 2000); CHILD (Tucker et al., 2000); ULTIMA THULE (Kaufmann and Romanov, 2012); PECUBE (Braun et al., 2012); CASQUS (Maniatis et al., 2009); parallel method (Braun and Willett, 2013); TIN-based method (Refice et al., 2012); phenomenological method (Dymond and Rose, 2011) and global flow path search method (Park, 2012). At the same time, different landscape evolution models have been used in different landforms to test the capability of the model (Ravazzi et al., 2013; Lehmkuhl et al., 2012; Berthling and Etzelmüller, 2011; Ciampalini et al., 2012; Fujioka and Chappell, 2011; Egholm et al., 2012; Bowman et al., 2010; Temme et al., 2011; Perron et al., 2009). Despite the success of these methods and applications in modeling various aspects of landscape evolution, the original underlying surface before landscape evolution process is usually been ignored. Especially for loess landform in the Loess Plateau of China, it is a typical fluvial landform with stable tectonic activity in Ordos platform during Quaternary period (Liu, 1985; Liu et al., 2001). The morphology and distribution of the underlying paleotopography are greatly affecting the process of the landscape formation and evolution. Since the 1950s, much work has been done for loess landforms through geological and geomorphological views. Liu (1985) investigated several intact and complete loess deposit profiles located in the three typical loess landforms, i.e. loess hilly, loess ridge and loess tableland in the Loess Plateau, and found that the sedimentary environment of loess deposit strata including the underlying bedrock paleotopography, closely relate to the climate change, which achieve a deep descriptive understanding of loess deposition and

evolution during the Quaternary period. Other scholars also adopted qualitative and semi-quantitative method to describe the regional variance of soil erosion and geomorphological developmental stage of loess landforms (Cheng et al., 2007; Chen et al., 2010; Liu and Liu, 2010; Chen et al., 2008; Zhu, 2012; Zheng et al., 2008; Xu et al., 2004; Stolte et al., 2003; Fu et al., 2011; Hughes et al., 2010). All these research achievements laid a solid foundation in the further study of loess landforms and their evolution process. However, as Liu et al. (2001) pointed out: ‘loess landscape morphology sequence should strictly correspond to the loess deposition sequence with their geological age’, which means that the underlying strata in the loess landforms, including the Ma-lan, Li-shi, Wu-cheng loess strata and the bedrock strata, should be given priority consideration for the landscape evolution process modeling. These existing underlying strata represent different time nodes during the evolution process, which means that, without these underlying strata, all current proposed landscape evolution models may be useless in representing loess landform evolution process, at least not correctly. Especially for the underlying bedrock strata, an initial landform surface acted as the erosion base level to control the development and evolution process of loess landform.

In this paper, the paleotopography beneath the loess, i.e. the underlying bedrock strata is prior taken into consideration for its controlling effect to landscape evolution process in loess landform. On the basis of geologic maps, RS images, DEMs and loess thickness drilling points, we construct a DEM of the paleotopographic surface through intensive sampling of outcropping paleotopographic points in a severe soil erosion area of the Loess Plateau.

MATERIALS AND METHODS

Materials

The DEMs (digital elevation models) used in this study come from the Shuttle Radar Topography Mission (SRTM) which is an international research effort that obtained digital elevation models on a near-global scale from 56° S to 60° N (Nikolakopoulos et al., 2006; Farr et al., 2007). The cell size of elevation models derived from the SRTM data is approximately 90 m in the Loess Plateau and can be downloaded freely. Geologic maps, with a scale of 1:200,000 composed by the Institute of Geology and Geophysics (Chinese Academy of Sciences), are used as an information source for bedrock outcropping points detected in the loess area. A remote sensing image is applied for the positional correction of bedrock outcropping points mapping. Liu (1985) used 167 loess thickness drilling points to construct a loess thickness distribution map. These point data have exact loess thickness values for different loess underlying terrains. In this paper, the Tertiary Red Clay and the early paleotopographic region are signed in the geologic map.

Hence, the information of loess thickness drilling points could make a further control of the terrain simulation of the Tertiary surface.

Methods

1. Data Preprocessing

The SRTM is globe subdivision elevation data with approximately 90 m cell size, and there exist a systematic deviation on the resolution for each dataset. In order to unify the resolution of DEM data, all of them are resampled, and then, the new DEM data is achieved with the cell size of 100 m and covering the entire study area.

2. Outcropping Bedrock Strata Points Detection

In this experiment, coordinates and elevations for the outcropping bedrock strata points are collected based on the geologic maps, in which definite geologic age and rock type for those points were assigned, such as Tertiary, Cretaceous, Jurassic for geologic age and basalt or limestone for rock type. The method is implemented via the following steps. First, the bedrock outcropping points with the geologic age of Tertiary in channels or valleys are determined based on the geologic maps. Second, image-based positional correction of the bedrock points is done. Finally, an overall outcropping bedrock strata point dataset (Figure 1) is constructed. Because the limited sample points could not provide an overall surface trend for the Tertiary red clay strata, the loess drilling point dataset (Liu, 1985) is used to assist construction of a loess paleotopographic surface model. All sampling points are shown in Figure 1. The main research area is the severe soil erosion zone (Upper and Middle Yellow River Bureau, 2012) on the Loess Plateau, whose north part is a desert area, west part with LIU-PAN Mountains and LONG-XI Basin, east and south are TAI-HANG Mountains and GUAN-ZHONG Basin respectively. The research area is located in the Ordos platform with specific and stable geologic process, where there is a high density of outcropping bedrock strata points.

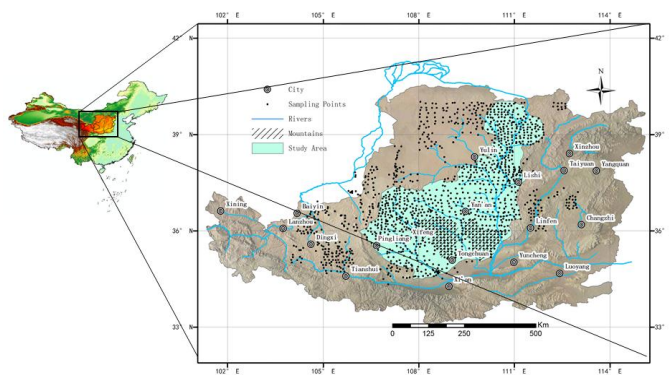


Figure 1. Test area and distribution of sampling points

3. Points Encryption

In the Loess Plateau, there are relatively large mountain ranges (Li and Lu, 2010), such as Ziwu Mountain and Huanglong Mountain etc., it is bedrock strata areas without buried during the Quaternary period and do not need to detect. In this paper, their DEM data are directly added in the elevation modeling of the loess underlying paleotopography.

4. Underlying bedrock strata surface modeling

Based on the outcropping bedrock strata points, the digital elevation model of loess underlying palaeotopography in the experimental area is constructed via interpolation. Through a comparison of all the interpolation methods (Franke, 1982; Mitas and Mitasova, 1988), spline is believed to be the most suitable method in this application for its high accuracy (the RMSE is 36.5 m, relative error is less than 12 percent), as well as relatively low variation. Among all sampling points, 80 percent of the points are prepared for interpolation, the remaining 20 percent ones are for accuracy detection. The simulation result of the loess underlying palaeotopography is shown as the Figure 3b.

The Spline function uses the following formula for the surface interpolation:

$$S(x, y) = T(x, y) + \sum_{j=1}^N \lambda_j R(r_j) \quad (1)$$

where: $j = 1, 2, \dots, N$; N is the number of points. λ_j are coefficients found by the solution of a system of linear equations. r_j is the distance from the point (x, y) to the j th point.

$T(x, y)$ and $R(r)$ are:

$$T(x, y) = a_1 + a_2x + a_3y \quad (2)$$

$$R(r) = \frac{1}{2\pi} \left\{ \frac{r^2}{4} \left[\ln\left(\frac{r}{2\tau}\right) + c - 1 \right] + \tau^2 \left[K_0\left(\frac{r}{\tau}\right) + c + \ln\left(\frac{r}{2\pi}\right) \right] \right\} \quad (3)$$

where: τ^2 and ϕ^2 are the parameters entered at the command line; r is the distance between the point and the sample, K_0 is the modified Bessel function, c is a constant equal to 0.577215, a_i are coefficients found by the solution of a system of linear equations.

RESULTS

By using the above method to model the loess underlying paleotopography, the simulation result is shown in Figure 3(b), and Figure 3(a) shows the modern DEM as a contrast. The result shows that great differences could be found in the spatial distribution between the modern DEM surface and the underlying paleotopographic surface intuitively. At the same time, the basic trend of these two terrains has similarities to some extent. All these differences and similarities reflect the landscape evolution result from the pre-quaternary to now.

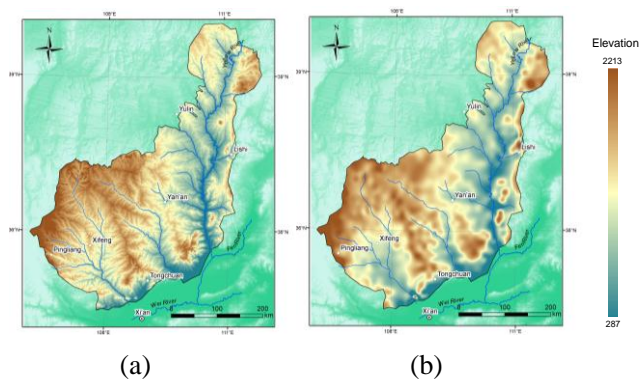


Figure 2. Illustrations of modern DEM and Simulated underlying palaeotopographic DEM

CONCLUSIONS

The Ordos platform in China was once a smoothly bedrock strata terrain in pre-quaternary, while after more than 2 million years of landscape evolution process of the loess deposition, loess accumulation and loess transportation, the morphology of the Ordos platform has been reshaped and thousands of ditches and valleys were formed which result to a more diverse terrain texture features of the platform.

The simulation result of loess palaeotopography can only be a result at macro-level due to the limited sampling methods and density. The development of modern geophysical techniques would provide better condition in the future study of loess landform evolution process investigating and modeling at other spatial scale. The construction of DEMs of Ma-lan, Li-shi and Wu-cheng loess strata should be carried on, which would deepen the understanding of the loess landform genesis and development mechanism.

ACKNOWLEDGMENT

The research is supported by National Natural Science Foundation of China (NO. 40930531, 41171299); Open Foundation of State Key Laboratory of Resources and Environmental Information System (NO. 2010KF0002SA); National High Technology Research and Development Program of China (NO. 2011AA120303). The authors express their great thanks to everyone who have helped in the writing of this article.

REFERENCES

[1] Berthling, I., Etzelmüller, B., 2011. The concept of cryo-conditioning in landscape evolution. *Quaternary Research* 75, 378-384.
 [2] Bowman, D., Svoray, T., Devora, S., Shapira, I., Laronne, J. B., 2010. Extreme rates of channel incision and shape evolution in response to a continuous, rapid base-level fall, the Dead Sea, Israel. *Geomorphology* 114, 227-237.

- [3] Braun, J., Sambridge, M., 1997. Modelling landscape evolution on geological time scales: a new method based on irregular spatial discretization. *Basin Research* 9, 27–52.
- [4] Braun, J., van der Beek, P., Valla, P., Robert, X., Herman, F., Glotzbach, C., Pedersen, V., Perry, C., Simon-Labric, T., Prigent, C., 2012. Quantifying rates of landscape evolution and tectonic processes by thermochronology and numerical modeling of crustal heat transport using PECUBE. *Tectonophysics* 524–525, 1–28.
- [5] Braun, J., Willett, S. D., 2013. A very efficient O(n), implicit and parallel method to solve the stream power equation governing fluvial incision and landscape evolution. *Geomorphology* 180–181, 170–179.
- [6] Chen, H., Shao, M., Li, Y., 2008. The characteristics of soil water cycle and water balance on steep grassland under natural and simulated rainfall conditions in the Loess Plateau of China. *Journal of Hydrology* 360, 242–251.
- [7] Chen, L., Wang, J., Wei, W., Fu, B., Wu, D., 2010. Effects of landscape restoration on soil water storage and water use in the Loess Plateau Region, China. *Forest Ecology and Management* 259, 1291–1298.
- [8] Cheng, H., Zou, X., Wu, Y., Zhang, C., Zheng, Q., Jiang, Z., 2007. Morphology parameters of ephemeral gully in characteristics hillslopes on the Loess Plateau of China. *Soil and Tillage Research* 94, 4–14.
- [9] Ciampalini, R., Follain, S., Le Bissonnais, Y., 2012. LandSoil: A model for analysing the impact of erosion on agricultural landscape evolution. *Geomorphology* 175–176, 25–37.
- [10] Coulthard, T.J., Kirkby, M.J., Macklin, M.J., 2000. Modelling geomorphic response to environmental change in an upland catchment. *Hydrological Processes* 14, 2031–2045.
- [11] Dymond, J. R., Rose, R. D., 2011. Modelling landscape evolution in the Waipaoa catchment, New Zealand — A phenomenological approach. *Geomorphology* 132, 29–34.
- [12] Egholm, D. L., Pedersen, V. K., Knudsen, M. F., Larsen, N. K., 2012. Coupling the flow of ice, water, and sediment in a glacial landscape evolution model. *Geomorphology* 141–142, 47–66.
- [13] Farr, T.G., Rosen, P.A., Caro, E., Crippen, R., Duren, R., Hensley, S., Kobrick, M., Paller, M., Rodriguez, E., Roth, L., Seal, D., Shaffer, S., Shimada, J., Umland, J., Werner, M., Oskin, M., Burbank, D., Alsdorf, D., 2007. The Shuttle Radar Topography Mission. *Reviews of Geophysics* 45, RG2004.
- [14] Franke, R., 1982. Smooth Interpolation of Scattered Data by Local Thin Plate Splines. *Comp. & Maths. with Appls*, 8:237–281.
- [15] Fu, B., Liu, Y., Lü, Y., He, C., Zeng, Y., Wu, B., 2011. Assessing the soil erosion control service of ecosystems change in the Loess Plateau of China. *Ecological Complexity* 8, 284–293.
- [16] Fujioka, T., Chappell, J., 2011. Desert landscape processes on a timescale of millions of years, probed by cosmogenic nuclides. *Aeolian Research* 3, 157–164.
- [17] Hughes, M. W., Almond, P. C., Roering, J. J., Tonkin, P. J., 2010. Late Quaternary loess landscape evolution on an active tectonic margin, Charwell Basin, South Island, New Zealand. *Geomorphology* 122, 294–308.
- [18] Kaufmann, G., Romanov, D., 2012. Landscape evolution and glaciation of the Rwenzori Mountains, Uganda: Insights from numerical modeling. *Geomorphology* 138, 263–275.
- [19] Lehmkuhl, F., Hülle, D., Knippertz, M., 2012. Holocene geomorphic processes and landscape evolution in the lower reaches of the Orkhon River (northern Mongolia). *CATENA* 98, 17–28.
- [20] Li, L.P., Lu, H.Y., 2010. A preliminarily quantitative estimation of the sedimentation and erosion rates of loess deposits in Chinese Loess Plateau over the past 250 ka. *Acta Geographica Sinica*, 1:37–52.
- [21] Liu, L., Liu, X., 2010. Sensitivity Analysis of Soil Erosion in the Northern Loess Plateau. *Procedia Environmental Sciences* 2, 134–148.
- [22] Liu, T., 1985. *Loess and Environment*. Beijing: Science Press. 481
- [23] Liu, T., Sun, J., Wu, W., 2001. Past, present and future of the Chinese loess research: a discussion on the reality of facts and myth. *Quaternary Sciences*, 3:185–207.
- [24] Maniatis, G., Kurfeß, D., Hampel, A., Heidbach, O., 2009. Slip acceleration on normal faults due to erosion and sedimentation — Results from a new three-dimensional numerical model coupling tectonics and landscape evolution. *Earth and Planetary Science Letters* 284, 570–582.
- [25] Mitas, L., Mitasova, H., 1988. General Variational Approach to the Interpolation Problem. *Comput. Math. Applic.*, 16:983–992.
- [26] Nikolakopoulos, K.G., Kamaratakis, E.K., Chrysoulakis, N., 2006. SRTM vs ASTER elevation products. Comparison for two regions in Crete, Greece. *International Journal of Remote Sensing* 27, 4819–4838.
- [27] Paik, K., 2012. Simulation of landscape evolution using a global flow path search method. *Environmental Modelling & Software* 33, 35–47.
- [28] Perron, J. T., Kirchner, J. W., Dietrich, W. E., 2009. Formation of evenly spaced ridges and valleys. *Nature* 460, 502–505.
- [29] Ravazzi, C., Marchetti, M., Zanon, M., Perego, R., Quirino, T., Deaddis, M., De Amicis, M., Margaritora, D., 2013. Lake evolution and landscape history in the lower Mincio River valley, unravelling drainage changes in the central Po Plain (N-Italy) since the Bronze Age. *Quaternary International* 288, 195–205.
- [30] Refice, A., Giachetta, E., Capolongo, D., 2012. SIGNUM: A Matlab, TIN-based landscape evolution model. *Computers & Geosciences* 45, 293–303.
- [31] Stolte, J., Liu, B., Ritsema, C. J., van den Elsen, H. G. M., Hessel, R., 2003. Modelling water flow and sediment processes in a small gully system on the Loess Plateau in China. *CATENA* 54, 117–130.
- [32] Temme, A. J. A. M., Claessens, L., Veldkamp, A., Schoorl, J. M., 2011. Evaluating choices in multi-process landscape evolution models. *Geomorphology* 125, 271–281.
- [33] Tucker, G.E., Lancaster, S.T., Gasparini, N.M., Bras, R.L., Rybarczyk, S.M., 2000. An object-oriented framework for hydrologic and geomorphic modelling using triangulated irregular networks. *Computers and Geoscience* 27, 959–973.
- [34] Tucker, G.E., Slingerland, R.L., 1994. Erosional dynamics, flexural isostasy, and long-lived escarpments: a numerical modelling study. *Journal of Geophysical Research* 99, 12229–12243.
- [35] Willgoose, G., Bras, I., Rodriguez-Iturbe, I., 1991. Results from a new model of river basin evolution. *Earth Surface Processes and Landforms* 16, 237–254.
- [36] Xu, X., Zhang, H., Zhang, O., 2004. Development of check-dam systems in gullies on the Loess Plateau, China. *Environmental Science & Policy* 7, 79–86.
- [37] Zheng, M., Cai, Q., Cheng, Q., 2008. Modelling the runoff-sediment yield relationship using a proportional function in hilly areas of the Loess Plateau, North China. *Geomorphology* 93, 288–301.
- [38] Zhu, T., 2012. Gully and tunnel erosion in the hilly Loess Plateau region, China. *Geomorphology* 153–154, 144–155.

Terrain similarity characterizing approach based on two-dimensional continuous wavelet

Shijiang Yan

School of resource and environment engineering
Anhui university
Anhui, China
anew101@163.com

Jie Wang

School of resource and environment engineering
Anhui university
Anhui, China

Abstract—characterizing and analyzing characteristics of terrain self-similarity, multi-scale and hierarchy structure have been a key point and hard problem. The traditional terrain analysis approaches based on window-shaped filters is hard to overcome the nearsighted and unsteady effects. This paper designs and realizes a new approach to analyze these self-similarity characteristics after a complete analysis of the shortness of the state of art. This paper adopts index to reveal terrain scale similarity by statistics of coefficients of continuous wavelet transformation. It takes Shannxi province as an example to calculate the scale similarity index over the province. The mechanism between the scale issues of terrain landscape and landform geomorphometry is also been analyzed by combination of index derived in the paper and experience in this area. The spatial distribution of the scale similarity index is also used to analysis the loess landscape pattern. The findings of the paper are as following: There is orderly distribution of the scale similarity over Shannxi province. The highest scale similarity appears in the northern areas with wilds and gullies, southeast areas with low hills. The local lowest similarity appears in the in-between areas of sand and loess in the northern area of the province, the Guanzhong Basin et al. The similarity in the belt of Hanzhong Basin and Ankang falls in between these two kinds of areas. The consistency of spatial distribution of the landform morphology and the scale similarity has proved that the two dimensional continuous wavelet based methods fulfill task of characterizing scale similarity in Shannxi province. The frequency domain based approach of characterizing terrain scale similarity is a well supplication of analysis toolsets of digital terrain analysis.

INTRODUCTION

There exists high level of self-similarity characteristic of natural and physical phenomenon. Such as stream channels, shape of watersheds, morphology in the positive and negative terrains, terrain textures and shape of contours with different elevation. Approaches of characterizing, analyzing characteristics of terrain self-similarity, multi-scale and hierarchy structure have been a key point and hard problem in both applications and researches of geosciences in the field of digital terrain analysis.

Researches mainly focus on water flow in stream channels, structure of steam channels and morphology of stream channel in areas with frequency land sliders. There is few researches focus on characterizing scale similarity of terrain properties in a direct way based directly on terrain elevation data.

Frequency domain based methods are increasingly been used for scientific data analyzing, such as the wavelet based digital signal processing (DSP). These researches include three dimensional flow field data analysis (Arneodo et al, 2000; Dong Lin et al, 2004) and applications in image processing et al. Recently, the wavelet based methods are capable of characterizing features embedded in terrain morphology so that the scale issue is clearly investigated.

Generally speaking, the traditional analyzing method is hard to overcome the problem of nearsighted and unsteady effects in a single scale. Not to say finding terrain property of multi-scale issues. The state of the art methods for terrain similarity analyzing are mainly focus on terrain derivatives. Neither is it directly reflect multi-scale property of terrain, nor is it easy to characterizing similarity of multi-scales from local to global, from single to group. What's more, the shortages in acquisition of large-scale and multi-scale terrain data make it problems both in data acquisition and analysis in the aim of characterizing the multi-scale properties of terrain data. The frequency domain based methods starts from the notion of multi-scale. It is helpful of investigating the nature of terrain morphology. The results could be used as reference for terrain landform researches.

PRICIPLES OF 2D CWT

The two-dimensional continuous wavelet transformation is calculated by comprising the mother wavelet with data to be analyzed at each position. By changing the size of the mother wavelet in a continuous way, a series of wavelet coefficients at different scales at each point are collected. The formula of two-dimensional continuous wavelet transformations could be expressed as:

$$Wf(a,b,c) = CWT(a,b,c) = |a|^{-1} \int f(x) \rho\left(\frac{x-b}{a}, \frac{y-c}{a}\right) dx dy \text{ (formula 1)}$$

Characterizing of terrain self-similarity is based on statistics of coefficients of coefficients of the 2d continuous wavelet transform.

EXPERIMENTS

SITES AND DATA SOURCES

Concerning with the representative of the method and result in this paper, test sites should meet with two conditions: 1) The test sites should cover a large area. 2) There should be a variety of landform types. What’s more, the availability and representative of terrain data are also our interests. For the above concerning, we choose the whole Shannxi province as our test site covering with DEM data of 1:50,000 scale to explore the scale behavior of the loess plateau area. The source data is composited with 671 scenes of DEM whose resolution is 25m. It also meets with requirement of data accuracy whereas not too detailed for too detailed data would cause heavy computation.

ANALYSIS AND DISCUSSION

The two-dimensional continuous wavelet transformation is shown in the figure 1(Left), the brightness represents value of scale similarity. The right figure of figure 1 is a hillshade map of the whole Shannxi province, which was derived from the 671 sceneries of DEM. These two maps shows the comparison of terrain morphology and the scale similarity overall the Shannxi province.

The left one of figure 1 is the scale map of the whole Shannxi province. It is easy to see from this map that there is orderly distribution of the scale similarity over the whole province. The value of scale similarity in the northern part is relatively low compared which with the belt between Yulin and Yan’an. For this area is mainly covered by the sandy and loess mass, the repeated landform is of low similarity compared with the Yulin and Yan’an belt. For landscape is the Yulin and Yan’an belt, the highest index may mean that the landform morphology is similar in a wide range of scales, the scale ranges from 25m to 200m. The result is consistence with the existing findings in this area. The similarity concentrates in the Yan’an and Yulin belt. It means in this area, terrain landform units in every scale are of high similarity. The landform morphology in the area is undergoing very intensity interaction between the inner and outer forces and it behaves similarly in wide range of scales. The concentricity lasts to the Baoji and Tongchuan belt. In the southern area of Shannxi province, Guanzhong Basin, terrain scale similarity index is low, this is easy to see from the hillshade map of figure 1 (right). The main reason for is that the low contrast of elevation in this area, the wavelet is hard to characterizing such tiny variations. It may also owed to the accuracy of the low resolution data because there is rare accuracy

data in the plat area. Another high scale similarity spot appears in the hilly area lies in the southern part of the province. It appears apparent in Shangzhou, Hanzhong and Ankang area. There is a descent sort of scale similarity of Shannxi province, namely, the loess plateau in the northern part, the Tongchuan and Baoji belt, the Shangzhou, Ankang and Hanzhong belt, the sandy and loess mixed area in the northern part, the Guanzhong Basin area. The scale similarity represents interaction intensity of the inner and outer force. The distribution of scale similarity is consistent with landform morphology reflected by the hillshade map of figure 1 (right). The consistency notifies correctness of the frequency domain based scale similarity characterizing method.

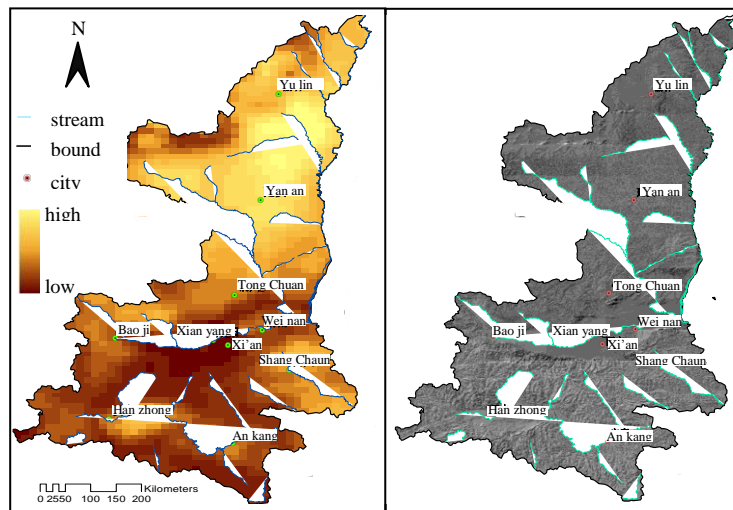


Figure 1. spatial distribution map of 2D cwt terrain self-similarity

REFERENCES

- [1] Arneodo, A., Decoster, N., S.G. Roux. A wavelet-based method for multifractal image analysis. I. Methodology and test applications on isotropic and anisotropic random rough surfaces [J], Eur. Phys. J. B, 2000, 15, 567-600.
- [2] Arneodo, A., F. Argoul, J. Elezgaray, G. Grasseau. Wavelet transforms analysis of fractals: application to nonequilibrium phase transitions [J], Nonlinear dynamics, 1988a.
- [3] Arneodo, A., G. Grasseau & M. Holschneider Wavelet transform of multifractals [J]. Phys. Rev. Lett. 1988b, 61, 2281-2284.
- [4] Dudgeon J.E., Gopalakrishnan R. Fractal-based modeling of 3D terrain surfaces [C], Proceedings of the IEEE Southeastcon 96. Bringing Together Education, Science and Technology, 1996, Tampa, FL, USA: 246 – 252.
- [5] Herzfeld U C, Overbeck C. Analysis and Simulation of Scale-Dependent Fractal Surface with Application to Seafloor Morphology [J]. Computers & Geosciences, 1999, 25: 979-1007.
- [6] Longley P A, Batty M. Fractal Measurement and Line Generalization [J], Computers & Geosciences, 1989, 15(2): 167-183.
- [7] Whalley W B, Orford J D. The Use of Fractals and Pseudo fractals in the Analysis of Two-dimensional Outlines: Review and Further Exploration [J], Computers & Geosciences, 1989, 15(20):185-197.
- [8] Xiangcheng Mi, Haibao Ren, Zisheng Ouyang, Wei Wei et al. The use of the Mexican Hat and the Morlet wavelets for detection of ecological patterns [J], Plant Ecology, 2005, 179: 1-19.

DEM based Extraction of LS factor: integrate channel networks and convergence flow

Hongming Zhang

College of Information and Engineering
Northwest A&F University
Yangling, Shaanxi 712100 China
zhm@nwsuaf.edu.cn

Qinke Yang*

Department of Urbanology and Resource Science
Northwest University
Xi'an, Shaanxi, 710069, China
qkyang@126.com

Shuqin Li

College of Information and Engineering
Northwest A&F University
Yangling, Shaanxi 712100 China
lsq_cie@nwsuaf.edu.cn

Wenting Han

College of Mechanical and Electronic Engineering,
Institute of Water Saving Agriculture in Arid Regions of
China, Northwest A&F University
Yangling, Shaanxi 712100 China
hanwt2000@126.com

Shangshang Yu

College of Information and Engineering
Northwest A&F University
Yangling, Shaanxi 712100 China
yushangshang@nwsuaf.edu.cn

Xiaoyan Zhao

College of Information and Engineering
Northwest A&F University
Yangling, Shaanxi 712100 China
zhaoxiaoyan@nwsuaf.edu.cn

Abstract—LS is a very important factor in erosion evaluation. Slope gradient and slope length is used to calculate LS factor. However a major limitation is the difficulty in extracting the LS factor at regional landscape scales. The geographic information system-based (GIS-based) methods which have been developed for estimating the slope length for USLE and RUSLE model also have limitations. The unit contributing area-based estimation method (UCA) converts slope length to unit contributing area for considering two-dimensional topography, however is not able to predict the different zones of soil erosion and deposition. The flowpath and cumulative cell length-based method (FCL) overcomes this disadvantage but does not consider channel networks, flow convergence and divergence flow in three-dimensional topography. The purpose of this research was to overcome these limitations and extend the FCL method through inclusion of channel networks, convergence and divergence flow. We developed LS-TOOL in Microsoft's .NET environment using C# with a user-friendly interface. Comparing the LS factor calculated with the three methodologies (UCA, FCL and LS-TOOL). LS-TOOL delivers improved results. In particular, LS-TOOL uses breaks in slope identified from the DEM to locate soil erosion and deposition zones, channel networks, convergence and

divergence flow areas. Slope length and LS factor values generated using LS-TOOL correspond more closely with the reality of the Xiannangou catchment than results using UCA or FCL. The LS-TOOL algorithm can automatically calculate slope length, slope steepness, L factor, S factor, and LS factors, providing the results as ASCII files which can be easily used in some GIS software. This study is an important step forward in conducting accurate large-scale erosion evaluation.

INTRODUCTION

Topographic is an important factor in erosion evaluation. Slope gradient and slope length are often used to estimate topographic factor. The Universal Soil Loss Equation (USLE) (Wischmeier and Smith 1978) and Revised Universal Soil Loss Equation (RUSLE) (Renard *et al.* 1997) are the most commonly used equation to estimate soil erosion despite their shortcomings and limitations. In these equations, the slope length factor and slope gradient factor terms of the equation are generally lumped together as "LS" and the effect of topography on erosion is accounted for by the dimensionless LS factor. We often call LS as topographic factor.

Slope length for these equations are defined as “the distance from the point of origin of overland flow to either of the following, whichever is limiting for the major part of the area under consideration: (a) the point where the slope decreases to the extent that deposition begins, or (b) the point where runoff enters a well-defined channel that may be part of a drainage network or a constructed channel such as a terrace or diversion”. Therefore, there are two conditions caused slope length break, one is slope which decreases enough, and the other is channel. (Wischmeier and Smith 1978)

Because of the watershed erosion models are under developing, many researchers applied the USLE and RUSLE to estimate soil loss in watershed estimations for the simple, robust form of the equations to their success in predicting the average, long-term erosion on uniform slopes or field units. Traditionally, the best estimation methods for slope length are obtained from field measurements, but these are not always available or practical, especially at large areas or watersheds.

Moore and Wilson (1992) presented a simplified equation using unit contributing area (UCA) for calculating the LS factor over the three-dimensional terrain. Desmet and Govers (1996) used a multiple-flow direction (MFD) algorithm developed by Quinn *et al.* (1991) to calculate contributing areas, then to calculate the LS factor in segments. Winchell *et al.* (2008) improved Desmet and Govers (1996) method and compared several variations of the GIS approach to come up with a better method. The major limitation of these methods is the absence of an algorithm for predicting topographically-driven zones of soil deposition.

Consequently new models have been developed to overcome this disadvantage. One approach for identifying breaks in slope length involves the evaluation of change in slope based on the concept of slope length as proposed by Dunn and Hickey (1998), Hickey (2000) and Van Remortel *et al.* (2001). The ArcInfo Arc Macro Language (AML) program for creating a USLE/RUSLE-based LS factor grid from an input digital elevation model (DEM) dataset was based on this approach. Later, Van Remortel *et al.* (2004) focused on the mechanisms involved in extracting key flowpath-based and cumulating cell length portions (FCL) of the original AML program.. SFD algorithm allows only parallel and convergence flow, while MFD method can accommodate divergent flow and have a better performance of real terrain than SFD algorithm (Wilson *et al.* 2007). However, it’s a very complex procedure while using MFD algorithm to calculate slope length with cutoff conditions considered, even it’s better than SFD method. Therefore, it is inevitable to cause some inaccuracies by these recent models.

The aim of this paper is to propose an algorithm that extends the FCL method and revise its calculation algorithm for slope length. Using the concept of the MFD algorithm with a focus on the calculation of slope length including slope changes and

channel networks, a calculation process is shown in Figure 1. A comparison of results for slope length and LS factor calculated by the UCA, FCL and LS-TOOL method (this paper) for Xiannangou catchment is presented.

MATERIALS AND METHODS

The model theory

Moore and Burch (1986a, b) recognized that higher erosion or deposition rates occurred at the convergence of a catchment as also postulated in the USLE/RUSLE. These results have implied that sheet flow has the lowest sediment transport capacity and that the topographic convergence or divergence in a catchment can increase or decrease the unit stream power and the sediment transport capacity. Zhang *et al.* (2013) extended the FCL method and revises its calculation algorithm for slope length and flow convergence both based on the UCA algorithm as well as the cutoff conditions for including channel networks. The equations to calculate the slope length are as follows:

$$\lambda_{i,j} = \sum_{x=0,y=0}^{x=i,y=j} \sum_{k=1}^m CSL_{x,y} \tag{1}$$

CSL= cell slope length of coordinates(x,y)

$\lambda_{i,j}$ =the slope length of coordinates (i,j)

k=the code of the surrounding eight cells of coordinates(x,y)

Here we extended the equations of Zhang *et al.* (2013), so we still call slope length as distributed watershed erosion slope length (DWESL). According to the equation, if we use the MFD algorithm, CSL will be decided by slope aspect. For the least sensitive to the DEM data error (Zhou and Liu 2004), the third-order finite difference (3FD) algorithm (Wood 1996) was used to calculate slope aspect and slope gradient. How to calculate CSL and DWESL using MFD algorithm is described in the following section.

The model structure

The methodology for calculating the slope length, slope steepness, L and S factor is illustrated in Figure 1, which shows an overall view of the process:

Step 1: Input data from a DEM data,

Step 2: Analyze the DEM data to determine if suitable data is available to use in the model,

Step 3: If the DEM data is available, fill any spurious single-cell nodata cells and sinks within the source DEM data by using an iterative routine,

Step 4: Use 3FD method for estimation of slope angle and slope aspect,

Step 5: Calculate cell downhill outflow portion (outflow direction) and cutoff direction for the each individual direction by using the MFD algorithm,

Step 6: Calculate the cell slope length (CSL) by using slope aspect,

Step 7: Use a forward-and-reverse traversal method to compute contributing area,

Step 8: Calculate DWESL using outflow portion data, cell slope length data, and contributing area threshold value,

Step 9: Determine L factor by using DWESL, and length-slope exponent,

Step 10: Calculate S factor constituent using the slope angle,

Step 11: Compute the LS factor.

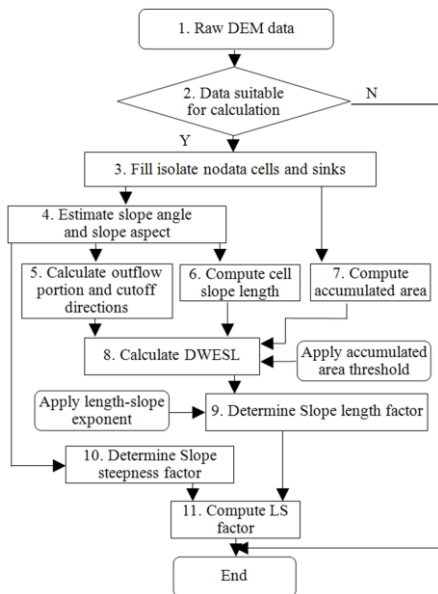


Figure 1. Flowchart illustrating the process of calculating LS factor

Comparison of the model

In order to compare LS-TOOL with existing methods, we applied the three GIS methods in Xiannangou catchment, Shaanxi province, China (Figure 2). The comparison focused on operating of the model.

The three GIS methods, UCA (Moore and Wilson, 1992), FCL (Van Remortel et al., 2004) and LS-TOOL were compared by calculating the slope length and LS values.

With the UCA, because there is an upper bound to the slope length which usually does not exceed 1000 feet (304.8m) (Renard et al., 1997). we chose to use equation (2) (p=0.4, q=1.3) following Jabbar’s approach (2003), with a maximum accumulation of 60 grid cells, and using the spatial analyst tools in ArcGIS.

The FCL method was implemented using C++ program (Van Remortel et al., 2004).

In applying of LS-TOOL, we selected an accumulated area threshold of 40 00m², because this threshold corresponded well to the real channels. LS-TOOL is developed in Microsoft’s .NET environment using C#.

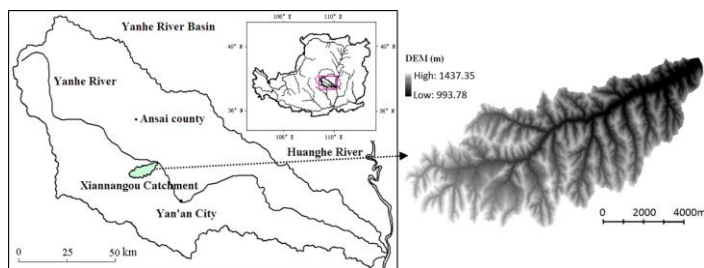


Figure 2. The left main map shows the location of the Xiannangou catchments (light green shading) in the Loess Plateau in the middle reaches of the Yellow River basin. The inset map shows the location of the Loess Plateau in the middle reaches of the Yellow River basin, China. The right map shows the 5 m DEM of the study site.

RESULTS AND DISCUSSION

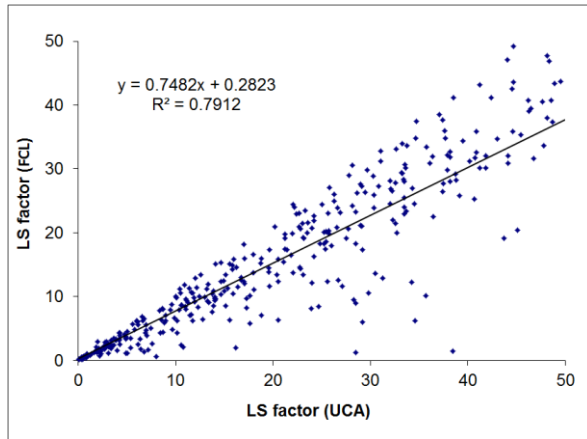
Statistical analysis of slope length and LS factor value

DWESL value calculated by LS-TOOL_{MFD} is a normal distribution, 66.2% of the DWESL is less than 80 meters, 80.5% of the DWESL less than 120 meters, 93.6% of the DWESL less than 300m (Figure 3a). LS factor value is also normal distribution, 99.4% of LS factor value is less than 72, 87.2% LS factor value less than 30, and 52.1% LS value is between 7 and 22 (Figure 3b). These results coincide with the LS factor value in McCool’s findings (McCool et al., 1997).

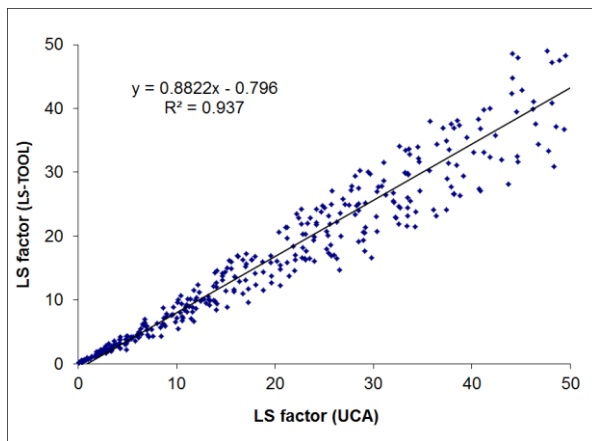
Comparison of LS factor values-correlation to UCA

We compared the calculated LS-values based on the UCA approach to those generated with FCL and LS-TOOL, by using 50 randomly selected cells and the upslope cells to the start of the slope lengths (total 406 cells). The linear regression r² and regression line LS values for this evaluation are shown in Figure 3a (FCL) and 3b (LS-TOOL). An important objective of this study was to gain an understanding of how the existing GIS-based LS-factor values estimation methods compare with LS-TOOL. It can be seen that the distribution of LS-factor values estimated using the LS-TOOL correlates more closely to those approximated by the UCA method. As the slope gradient

increased, the differences of LS factor values also increased. There is clearly a stronger correlation between the UCA method and LS-TOOL at lower slope gradients.



(a) FCL method



(b) LS-TOOL method

Figure 3. Comparison of LS factors with UCA method.

ACKNOWLEDGMENT

The first author would like to express great appreciation to Demie Moore for language edition. Thanks to Lei Wang, Weiling Guo, Chunmei Wang, Jun Li and Lanqin Guo from Institute of Soil and Water Conservation, for providing helpful comments on an earlier draft of this manuscript. Thanks to Chen Yan, Xian Chen, Jie Zhang and Jinxiang Wang from the Northwest A&F University for their useful discussions and suggestions in coding work. This research was supported by the “Five-twelfth” National Key Technology R&D Program (2012BAH29B04), Chinese National Natural Science Foundation (41301283,

41071188) and Fundamental Research Funds (QN2013051, ZD2012018) of Northwest A&F University. Thanks also to the anonymous reviewers and special issue editors who all made valuable comments that improved our paper.

REFERENCES

[1] Desmet, P.J.J., Govers, G., 1996. A GIS procedure for the automated calculation of the USLE LS factor on topographically complex landscape units. *Journal of Soil and Water Conservation* 51), 427-433.

[2] Dunn, M., Hickey, R., 1998. The effect of slope algorithms on slope estimates within a GIS. *Cartography* 27(1), 9-15.

[3] Hickey, R., 2000. Slope Angle and Slope Length Solutions for GIS. *Cartography* 29(1), 1-8.

[4] Moore, I.D., Burch, G.J., 1986a. Modelling Erosion and Deposition: Topographic Effects. *Transactions of the American Society of Agricultural Engineers* 29(6), 1624-1630.

[5] Moore, I.D., Burch, G.J., 1986b. Sediment Transport Capacity of Sheet and Rill Flow: Application of Unit Stream Power Theory. *Water Resources Research* 22(8), 1350-1360.

[6] Moore, I.D., Wilson, J.P., 1992. Length-slope factors for the revised universal soil loss equation: simplified method of estimation. *Journal of Soil & Water Conservation* 47(5), 423-428.

[7] Quinn, P., Beven, K., Chevallier, P., Planchon, O., 1991. The prediction of hillslope flow paths for distributed hydrological modelling using digital terrain models. *HYDROLOGICAL PROCESSES* 5(1), 59-79.

[8] Renard, K.G., Foster, G.R., Weeies, G.A., 1997. Predicting soil erosion by water: A guide to conservation planning with the revised universal soil loss equation(RUSLE). *Agriculture Handbook*, 703, Washington D. C.: U.S. Department of Agriculture

[9] Van Remortel, R.D., Hamilton, M.E., Hickey, R.J., 2001. Estimating the LS factor for RUSLE through iterative slope length processing of digital elevation data. *Cartography* 30(1), 27-35.

[10] Van Remortel, R.D., Maichle, R.W., Hickey, R.J., 2004. Computing the LS factor for the Revised Universal Soil Loss Equation through array-based slope processing of digital elevation data using a C++ executable. *Computers & Geosciences* 30(9-10), 1043-1053.

[11] Wilson, J.P., Lam, C.S., Deng, Y., 2007. Comparison of the performance of flow-routing algorithms used in GIS-based hydrologic analysis. *HYDROLOGICAL PROCESSES* 21(8), 1026-1044.

[12] Winchell, M.F., Jackson, S.H., Wadley, A.M., Srinivasan, R., 2008. Extension and validation of a geographic information system-based method for calculating the revised universal soil loss equation length-slop factor for erosion risk assessments in large watersheds. *Journal of Soil and Water Conservation* 63(3), 105-111.

[13] Wischmeier, W.H., Smith, D.D., 1978. Predicting rainfall erosion losses : A guide to conservation planning with Universal Soil Loss Equation (USLE) *Agriculture Handbook*. Washington,DC: Department of agriculture, No 703.

[14] Wood, J.D., 1996. *The Geomorphological Characterisation of Digital Elevation Models*. University of Leicester, UK.

[15] Zhang, H., Yang, Q., Li, R., Liu, Q., Moore, D., He, P., Ritsema, C.J., Geissen, V., 2013. Extension of a GIS procedure for calculating the RUSLE equation LS factor. *Computers & Geosciences* 52(0), 177-188.

[16] Zhou, Q.M., Liu, X.J., 2004. Error Analysis on Grid-Based Slope and Aspect Algorithms. *Photogrammetric Engineering & Remote Sensing* 70(8), 957-962.

Research on 3D-Openness in urban area based on Urban Digital Elevation Model

He Wenhui

Institute of Geography Sciences and Natural Resources Research
 University of Chinese Academy of Sciences
 11A, Datun Road, Chaoyang District, Beijing, 100101, China
 waixinmaozi@163.com

Abstract—the external space is an important factor contributing to city construction. the openness is often used to measure the external spaces. The original openness models have some limitations such as that the view angles are confined to upward angles or the space under the viewpoint is ignored. This paper developed a new model based on the original 3D-openness model and index set of comprehensive quantification is established. The 3D-openness of main road is also extracted and analyzed. A typical block of 3D-openness parameters are discussed in different ways. The new model could be used in urban landscape design and city planning.

1 INTRODUCTION

The form of external spaces of construction in urban area is closely related to the city physical environment and the city view environment. In cities, narrow streets and high buildings create deep canyons and this 3D external space plays an important role in natural ventilation and long-wave radioactive heat loss. Meanwhile, due to crowded buildings, vision is not open and people are increasingly in bad mood.

Therefore, the external space is an important factor contributing to city construction. Height-to-width ratio and frontal area index had been used to measure the geometry of external spaces. But external space is quite complex and these measures can hardly used in practice. The openness is often used to measure the external spaces. The openness models can divided into two-dimensional models and three-dimensional visual models. In two-dimensional models, the openness has been commonly used to describe the shadow impaction of visualization or sunshine from neighborhood buildings or terrains in urban area. In some other literature, it has been called sky view factor.

By definition in 2D model(Fig. 1), openness is the ratio of the radiation received by a planar surface to the radiation emitted by the entire hemispheric environment. There are two methods to calculate the openness. One is to project every building on the

sky hemisphere and calculate the ratio of projection area to the entire hemispheric area, which is based on urban vector database. The other one is to utilize high resolution raster DEM to compute the openness using shadow casting algorithm. Unger had made a comprehensive literature review of this model.

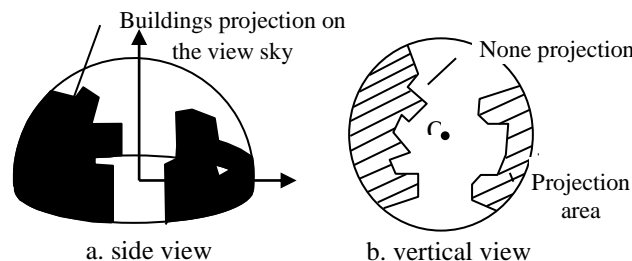


Figure 1. 2D-openness model

Another model presented is 3D-openness model (Fig. 2). It measures the volume of external space potentially seen from a given point .It can simulate the view space and express in terms of 3D visual spatial information.

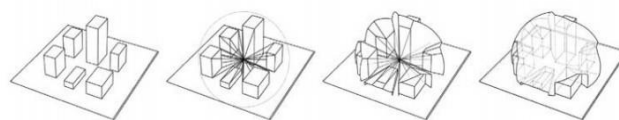


Figure 2. 3D-openness model (Fisher-Gewirtzman,2003)

In previous studies, the view point only in street level can be calculated but multi-level points also need to be discussed. Both models above can support a comparative evaluation of external space but there are still some limitations such as the view angel is confined to upward angles. The space under the view points at levels above streets are not taken into account. What's more, only

one index can hardly describe the external space. Hence, we developed the new model based on the original one, which overcomes the limitation and aims to perfect the theory of openness. The new model could be used in urban landscape design and city planning.

2 METHOOD: NEW 3D-OPENESS MODEL

Concept of new 3D-Openness model is given.

Analysis of the limitation of the original model, the 3D-Openness model is developed. The visual space simulates a sphere instead of a hemispheric(Fig. 3). The space under the view point is also taken into account. The new model is suitable for construction-intensive area.

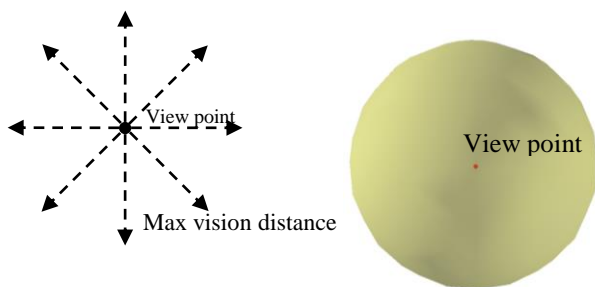


Figure 3. New 3D-Openness model

To give the external space an better description, visible space character are analyzed in detail , which can provide some basic rules for adopting quantified index. The index set of comprehensive quantification is established, considering four aspects of visible space hierarchy(Fig.4), visible space fluctuation(Fig.5), spatial extend direction(Fig. 6) and 3D visible volume.

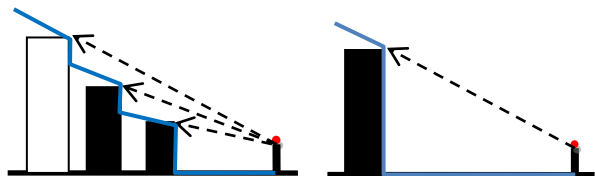


Figure 4. Different visible space hierarchy



Figure 5. Different visible space fluctuation

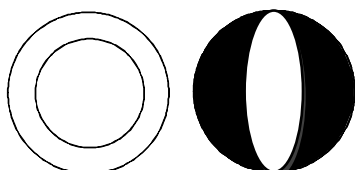


Figure 6. Different spatial extend direction

Among these indexes, the quantity of levels and Height Width Ratio(HWRatio) are about visible space hierarchy. Wave Frequency and Wave Range parameters are about visible space fluctuation, whose calculation methods based on the city skyline. Wave Frequency is defined for measuring the times of the visible space in one direction different from the next direction. Wave Range is defined for measuring the difference between the visible space in two direction. Shape Index, Skewness, Connectivity and Open Direction parameters are about visible space direction, whose calculation methods based on the 2D graphics which are derived from the 3D visible space projection. Shape Index is defined for measuring the complexity of visible space. Skewness is defined for measuring the even degree of visible space. Connectivity is used to describe the patency in one direction and the direction with highest patency is Open Direction. Visible Ratio is defined as the 3D visible volume divided by the volume of view sphere, which is used for measuring the percentage of the visible space that is filled up by the hypothetical spherical view area.

3 URBAN DEM AND STUDY AREA

Urban DEM (Digital elevation model) is widely used visualization analysis of urban landscape and analysis of terrain visibility, for it can properly express the 3-dimentional structures of modern cities. Raster-based data model was used to analysis the openness in this paper.

Nanjing old town is taken as the study area, based on the established Urban DEM. Nanjing is the provincial capital of Jiangsu , and it is the economic , politics and culture center. It is still the comprehensive business center and the assembling place of service trade. Due to the fast development, Nanjing is changed greatly. A lot of tall buildings are built in a decade and population increases greatly. During the same time, some low buildings with great historical significance are preserved.

4 RESULTS AND DISCUSSION

The 3D-openness of main road is extracted and analyzed(Fig. 7). The result shows that Wave Frequency is trending downward while Wave Range is trending upward when the viewpoint is closer to city center. The open space on different side along the road are quite different. The size of open space goes up and down alternately.

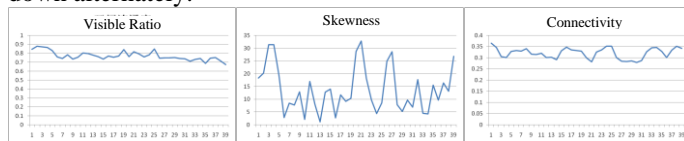


Figure 7. 3D-openness indexes of main road

A typical block of 3D-openness parameters are discussed

The result shows that more landscape levels could be involved in view sight in southwest areas of the block and north areas in Zheng He Park. The open space are larger in the corner and edge than in the other place in this block. The result shows that living on fifth floor or above could get more landscape levels and much larger space than other floors in this building.

The improved openness model has overcome the limitations of the original one and it can describe the open-space in different analysis angles. The new 3D-openness model have actual application value in the selection of sites and the design of houses.

5 ACKNOWLEDGMENT

This research was supported by Ph.D. Programs Foundation of Ministry of Education of China. Helpful comments for DEM research group of Nanjing Normal University.

REFERENCES

- [1] Unger J. Intra-urban relationship between surface geometry and urban heat island: review and new approach. *Climate Res.*2004, 27:253-264.
- [2] Gal T, Lindberg F, Unger J. Computing continuous sky view factors using 3D urban raster and vector databases: comparison and application to urban climate. *Theoretical and Applied Climatology*,2008,10,1007.
- [3] YANG P R, PUTRA S, LI W. View sphere : a GIS-based 3D visibility analysis for urban design evaluation. *Environment and Planning B : Planning and Design*, 2007, 34(6) : 971-992
- [4] FISHER-GEWIRTZMAN D, WAGNER I. Spatial openness as a practical metric for evaluating built-up environments. *Environment and Planning B : Planning and Design*, 2003, 30(1) : 37-49
- [5] FISHER-GEWIRTZMAN D, WAGNER I, TZAMIR Y. A 3-D visual method for comparative evaluation of dense built-up environments. *Environment and Planning B : Planning and Design*, 2003, 30(4) : 575-587
- [6] FISHER-GEWIRTZMAN D, WAGNER I. The spatial openness index : an automated model for three-dimensional visual analysis of urban environment . *Journal of Architectural and Planning Research*, 2006, 23(1) : 78-89
- [7] Oke T.R. *Boundary Layer Climates*, Routledge, New York, 1987. 45-89
- [8] Clark J.A. and Follin G.M. A simple equal area calibration for fish-eye photography. *Agricultural Forest Meteorology*, 1988, 44 : 19-25
- [9] Ratti CF. *Urban analysis for environmental prediction*. Darwin College, University of Cambridge, 2001. 331
- [10] Souza LCL, Rodrigues DS, Mendes JFG. The 3DSkyview extension: an urban geometry acces tool in a geographic information system. In: Klysik K, Oke TR, Fortuniak K, Grimmond CSB, Wibig J(eds) *Proc. Fifth Int. Conf. on Urban Climate*, Vol. 2. University of Lodz, Lodz, Poland, 413-416
- [11] Unger J. Intra-urban relationship between surface geometry and urban heat island : review and new approach. *Climate Res*, 2004, 27 : 253-264

Shoulder-line restricted loess slope segmentation

Fayuan Li

Key Laboratory of Virtual Geographic Environment (Ministry of Education)
Nanjing Normal University
No.1, Wenyuan road, Nanjing, Jiangsu, P.R.C. 210046
E-mail:li_fayuan@sina.com

Abstract — An integrated method combining digital terrain analysis (DTA) and object-oriented image analysis is used to classify loess slope into six types according to surface shape. Firstly, several data layers are extracted from Digital Elevation Models (DEM). Secondly, the data layers are combined into a multi-band image. Thirdly, object-based image analysis is used for slope segmentation and classification based on the multi-band image. Shoulder-line is employed as a thematic element to restrict slope segmentation. It is proved that the methodology is effective, and useful in geomorphological research.

INTRODUCTION

Quantificational analysis of loess terrain is a key subject in the research of the loess plateau^[1-7]. Slope is basic element of geomorphology. Based on slope point of view, Tang et al (2008) proposed slope spectrum to quantitatively describe loess landforms^[8], Zhou et al (2010) discussed the spatial pattern of loess landform based on loess positive and negative terrain^[9], and other researches focus on the extracting of loess landform units, such as gully area, gully bottom area and inter gully area^[10-12]. However, their research cannot properly describe the spatial structure of loess slopes. In this paper, we investigate loess landforms from the landscape ecology point of view based on loess slope segmentation.

MATERIAL AND METHODS

2.1. Study area and data

Jiuyuangou, located in Suide county, Shaanxi province, is selected as the test area (Figure1). This area is one of the key watersheds of soil and water conservation, because of its severe soil and water loss and typical loess hill landform. It covers an area of 100 km².

Test data were the corresponding 5 m-grid resolution DEMs produced according to the national standard of China.

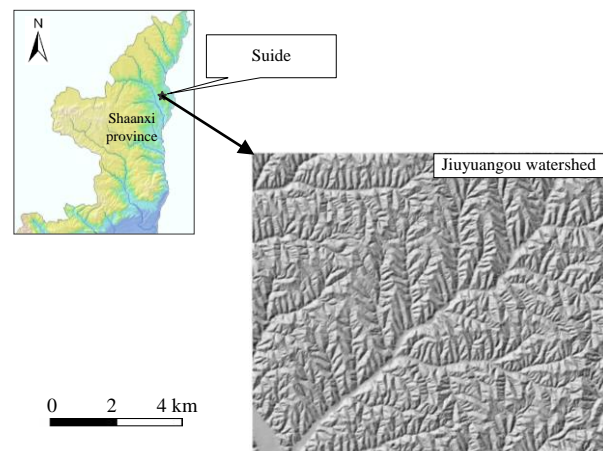


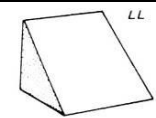
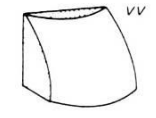
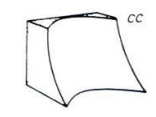
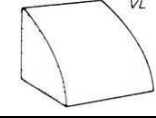
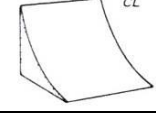
Figure 1 Hillshade Map of test areas

2.2 Classification of slope

Slope classification has long been researched since 1950s. Hammond (1964) gave a manual way based on contoured map^[13]. With the increasing availability of commercial GIS software, Dikau et al (1991) developed GIS technology to automatic slope classification based on Hammond's method^[14]. In this paper, we apply an object-oriented method proposed by Dragut and Blaschke (2006) to loess slope segmentation^[15].

Ruhe (1975) classified slope into nine types according to the surface shape^[16]. In reality, four types of slope form are rare, they are VC, CV, LV, LC type. So our research suggests a classification system including six slope types. Table 1 shows the geometric feature of these types of slope.

TABLE 1 GEOMETRIC FEATURE OF SIX SLOPE TYPES (ND MEANS NO DEFINITION)

Slope form		Geometric feature		
		plane curvature	profile curvature	Slope gradient
LL slope		± 0	± 0	ND
VV slope		> 0	> 0	ND
CC slope		< 0	< 0	ND
VL slope		± 0	> 0	ND
CL slope		± 0	< 0	ND
flat slope		ND	ND	≤ 3

2.3 Classification method

An object-oriented method proposed by Dragut and Blaschke (2006) is adapted to loess slope segmentation. Firstly, several data layers are extracted from Digital Elevation Models (DEM): profile curvature, plan curvature, slope gradient and elevation itself. Secondly, every data layer is taken as a single-band image, and then the four single-band images are combined into a multi-band image. Thirdly, based on the multi-band image, previous rules combining geometric features of the six slope types are used for image segmentation and classification. As we know the shoulder line is one of the most important terrain structure lines in the loess plateau, which can properly decline the loess landform and deeply reflect the mechanism of loess landform evolution^[10-11, 17-18]. So shoulder-line is employed as a thematic element to restrict slope segmentation. Figure 2 shows the test procedure. The entire tests are run on the eCognition software which is developed by Definiens Company. Figure 3 is the result.

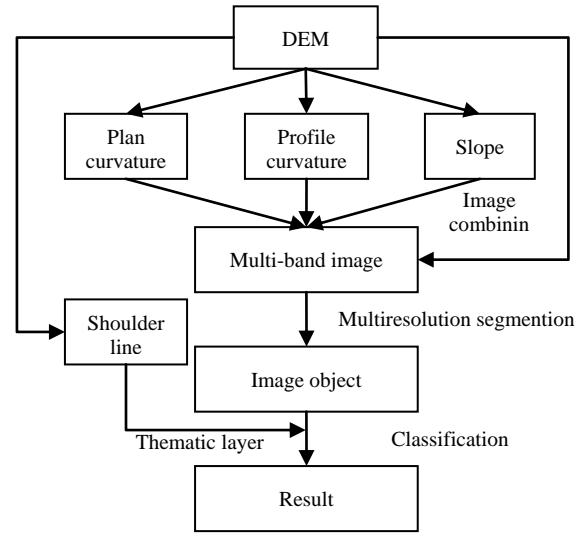


Figure 2 procedure of slope classification

When using the eCognition software, a series of parameters are important to the classification. Any difference of the parameter will change the classification result.

a. Scale parameter

The Scale parameter is an abstract term which determines the maximum allowed heterogeneity for the resulting image objects. For heterogeneous data the resulting objects for a given scale parameter will be smaller than in more homogeneous data. By modifying the value in the Scale parameter value you can vary the size of image objects.

b. Composition of Homogeneity Criterion

The object homogeneity to which the scale parameter refers is defined in the Composition of homogeneity criterion field. In this circumstance, homogeneity is used as a synonym for minimized heterogeneity. Internally three criteria are computed: Color, smoothness, and compactness. These three criteria for heterogeneity may be applied multifariously. For most cases the color criterion is the most important for creating meaningful objects. However, a certain degree of shape homogeneity often improves the quality of object extraction. This is due to the fact that the compactness of spatial objects is associated with the concept of image shape. Thus, the shape criterion is especially helpful in avoiding highly fractured image object results in strongly textured data.

c. Image Layer Weights

This parameter groups allows you to assess image layers differently depending on their importance or suitability for the segmentation result. The higher the weight which is assigned to an image layer, the more important information will be in the

segmentation process. Consequently, image layers that do not contain the information intended for representation by the image objects should be given little or no weight. Along with the image layer weight, the standard deviations of the image layer values for each single image layer over the entire scene are displayed to provide information about the layer dynamics.

In this research, elevation, profile curvature, plan curvature and slope gradient are given the same weight 1 which means in the segmentation the four data layer showing equal importance, and providing same rich information.

The ratio of shape vs. color is set to 0.3: 0.7, which means in the segmentation the color of every image is given higher importance. The ratio of smoothness vs. compactness is set to 0.5: 0.5.

By modifying the value in the scale parameter value you can vary the size of image objects. In this study, we set the scale parameter to 10, 20, 50 and 100 respectively, and calculate the image objects under different scale parameters. After overlaying the resulting image object layers on a hillshade map, we found that the smallest scale parameter (10) gave the best result

CONCLUSION

DEM data availability and image processing technology make it easy to segment slopes. In this paper loess slopes is classified into six types according to surface shape. An integrated method combining digital terrain analysis (DTA) and object-oriented image analysis is used for classification. Results show that the methodology is effective, and useful in respect to providing additional information for geomorphological research.

ACKNOWLEDGMENT

Thanks for financially support from the National Natural Science Foundation of China (No. 40930531, No.41171299).

REFERENCES

- [1] Zhang Z.H. Regional geologic and physiognomy characteristic as well as contemporary erosion process of loess plateau. *Acta geologic sinica*, 1981, 55(4), pp.308 – 319.
- [2] Chen W.N. Statistical analysis of geomorphic conditions effect on loess erosion in loess ridge-hill gully region. *Scientia Geographica Sinica*, 1988, 8(4), pp.323-329.
- [3] Li Q., Lu Z.C., Yuan B.Y. Quantitative study of the stage of geomorphological evolution. *Acta geographica sinica*, 1990, 45(1), pp.110-120.
- [4] Ma X.Z., Lu Z.C., Jin D.S. Evolution and dissipative structure in the drainage-geomorphic system. *Acta geographica sinica*, 1993, 48(4), pp.367-376.
- [5] Jin D.S. Experiment and simulation in geomorphology. Beijing, Earthquake Press, 1995.

- [6] Zhang L.P. and Ma Z.Z. The research on the relation between gully density and cutting depth in different drainage landform evolution periods. *Geographical research*, 1998, 17(3), pp.273-278.
- [7] Xiao X.N., Cui L.Z., Wang C., et al. Analysis of spatial data for simulating the development process of topographic feature of watershed. *Scientia geographica sinica*, 2004, 24(4), pp.439-443.
- [8] Tang G.A., Li F.Y., Liu X.J. et al. Research on the Slope Spectrum of the Loess Plateau. *Science in China Series E: Technological Sciences*, 2008, 51(Supp.1), pp.175-185.
- [9] Zhou Y., Tang G.A., Yang X. et al. Positive and negative terrains on northern Shaanxi Loess Plateau. *Journal of geographical sciences*, 2010, 20(1), pp.64-76.
- [10] Lu G.N., Qian Y.D. and Chen Z.M. Automated extraction of the characteristics of topography from grid digital elevation data. *Acta Geographica Sinica*, 1998, 53(6), pp.562-569.
- [11] Lu G.N., Qian Y.D. and Chen Z.M. Study of automated mapping of channel network in hilly Loess region. *Acta Geodaetica et Cartographica Sinica*, 1998, 27(2), pp.131-137.
- [12] Zhu H.C., Zhang Y.S., Tang G.A., et al. DEM-Based Landform Extraction and Application—A Case Study in the Hilly-gully Areas of the Loess Plateau. *Geo-information science*, 2003(4), pp.110-113.
- [13] MacMillan, R.A., Jones, R.K. and McNabb, D.H. 2004: Defining a hierarchy of spatial entities for environmental analysis and modelling using digital elevation models (DEMs). *Computers, Environment and Urban Systems* 28, 175200.
- [14] MacMillan, R.A., Pettapiece, W.W., Nolan, S.C. and Goddard, T.W. 2000: A generic procedure for automatically segmenting landforms into landform elements using DEMs, heuristic rules and fuzzy logic. *Fuzzy Sets and Systems* 113, 81109.
- [15] Dragut L. and Blaschke T. Automated classification of landform elements using object-based image analysis. *Geomorphology*, 2006, 81, pp.330-344.
- [16] Ruhe, R. V. *Geomorphology*. Houghton Mifflin, Boston, 1975
- [17] L. X. Luo, "A tentative classification of landforms in the Loess Plateau", *Acta Geogr Sin*, 1956, vol. 22(3), pp. 201-222.
- [18] Y. Z. Cheng, "The classification of gully in hilly loess region in the middle reaches of the yellow river", *Acta Geogr Sin*, 1984, vol. 4(4), pp. 321-332.

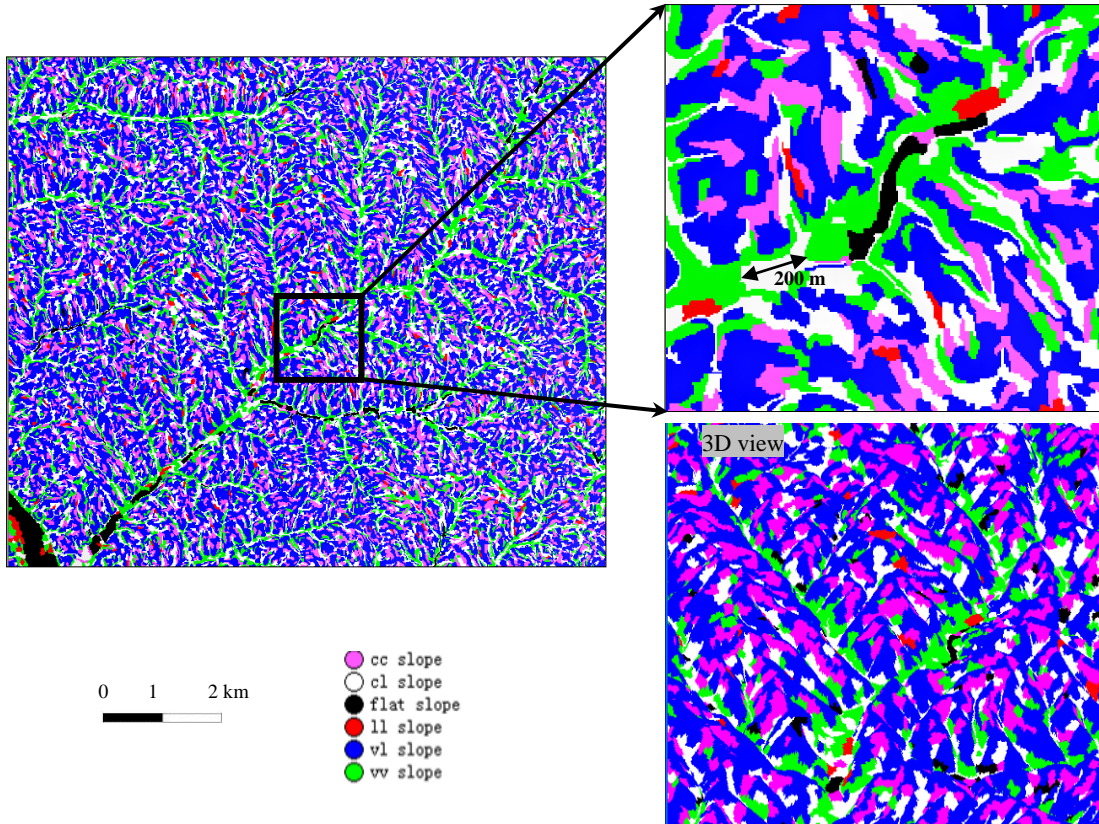


Figure 3 slope classification of Jiuyuangou test area

Land-Surface Segmentation as sampling framework for soil mapping

Lucian Drăguț

Department of Geography
West University of Timișoara
Timișoara, Romania
lucian.dragut@cbg.uvt.ro

Andrei Dornik

Department of Geography
West University of Timișoara
Timișoara, Romania
dornik_andrey@yahoo.com

Abstract—Current sampling methods require a large number of samples to account for spatial variation of environmental covariates, which often conflicts the available financial resources. Thus, efficient sampling strategies are desirable. The aim of this study was to evaluate the potential of land-surface segmentation in stratifying a landscape into homogeneous areas, which can be used as support in optimizing soil sampling. The experiments were carried out in a study area where soil samples were available. Land-surface variables were derived from DEMs and segmented with a multiresolution segmentation (MRS) algorithm, into objects considered as homogeneous soil-landscape divisions. Thus, one sample was randomly selected within each segment, based on which predictions of the A-horizon thickness and soil types, were made. Predictions based on the land-surface segmentation sampling schemes outperformed predictions based on simple random sampling and conditioned Latin hypercube, respectively.

INTRODUCTION

Spatial resolutions of soil maps for about 70 % of the Earth's ice-free land surface are too low to help with practical land management [1]. Conventional survey methods involve too much resources to be cost-effective in high-resolution soil mapping. Digital Soil Mapping (DSM) is an appropriate framework for producing detailed soil maps based on quantitative relationships between soil properties or types and their 'environment' [2]. Efficient sampling designs play an important role in DSM [2], as they have a significant impact on the accuracy of the maps [3].

Classical sampling methods (e.g. simple random sampling, systematic sampling and stratified sampling) as well as the model-based sampling strategy require a large number of samples to account for the spatial variation of environmental variables [4]. As sampling is constrained by financial resources, efficient sampling strategies are desirable [5]. Increasingly available geospatial information (e.g. satellite imagery, geology

maps, Digital Elevation Models (DEMs) can be exploited as environmental covariates to optimize sampling locations [5] within the framework of a soil-landscape model [6]. However, sampling with support of environmental covariates has not been fully developed in DSM [5]. A number of recent papers [e.g. 4, 7, 8] demonstrated the value of purposive mapping based on such covariates in producing more accurate predictions by using fewer, but more representative samples.

Land-surface segmentation (LSS) is a relatively new technique to partition land-surface variables (LSVs) obtained from DEMs into contiguously homogeneous areas in multivariate feature space [9]. The most popular segmentation algorithm is Multiresolution Segmentation (MRS) as implemented in the eCognition® software [10]. The algorithm merges spatially contiguous pixels or cells into segments based on local homogeneity criteria [10]. The resulting land-surface objects incorporate scale, spatial autocorrelation, anisotropy and non-stationarity in their definition of homogeneity [11]. There have been only a few attempts to map soils based on LSS. The only approach of segmentation to optimize soil sampling [12] showed that a segmentation-based sampling (SBS) scheme produced better distribution of sampling locations over the area of interest, as compared to simple random sampling and regular sampling schemes.

It is clear that the potential of LSS to DSM has not been fully employed and the applicability of this technique to optimize soil sampling has only been touched upon. Therefore, we aimed at evaluating the potential of LSS in stratifying a landscape into homogeneous areas, which can be used as support in optimizing soil sampling.

METHODS

The experiments were carried out in the administrative territory of Branisca, which is located in western part of

Romania. The study area extends over 78 km² in a hilly region with altitudes between 165 and 670 m. Over 95 % of the area has slope gradients below 30 degrees. The bedrock consists of limestone, sandstone, igneous and sedimentary rocks. Three soil classes are widely developed, namely cambisols, luvisols and protisols. A 30 m SPOT-based DEM and a spatial database containing 93 records were available.

LSVs were derived from DEMs and segmented with a MRS algorithm, into objects considered as homogeneous soil-landscape divisions. Thus, one sample was randomly selected within each segment, based on which prediction of the dependent variables (thickness of A-horizon and soil classes) were made. Results were compared with predictions based on other sampling schemes, namely simple random sampling (SRS) and conditioned Latin hypercube (cLHS) [5]. The methodology is shown in Fig. 1.

Land-surface variables

Four LSVs, i.e. slope, plan curvature, profile curvature and topographic wetness index (TWI) were selected as potential soil covariates. For slope and curvatures, scale optimization was conducted according to [13]. Regressions between dependent variables and LSVs derived in increasing windows (using LandSerf) were conducted. The scales where the regression peaks emerged were retained for further analyses. The LSVs scaled as above and TWI were used for identification of the best predictors, with linear forward stepwise regression for thickness

of A-horizon and logistic forward stepwise regression for soil class respectively.

Land-surface segmentation

For both dependent variables, six segmentations were performed with the MRS algorithm, in the eCognition 8.8 software. Three of them represent the three segmentation levels obtained from the application of the tool (named PT throughout the paper) presented in [14], using only the elevation layer as input.

The other three schemes were obtained using an improved version of the Estimation of Scale Parameter (ESP) tool [15], based on the best predictors identified as above. Thus, for the A-horizon thickness, segmentation process was based on slope derived in a 5x5 window and TWI. For soil classes, segmentation was performed on profile curvature (9x9 window) and slope (5x5 window).

Sampling schemes

The dataset was divided into two parts: 20 % of samples as control points for validation and 80 % as training points. The SBS schemes resulted by randomly selecting one sample per object out of the training points for each dependent variable and segmentation scheme. The other two sampling schemes, SRS and cLHS, were created using the same number of samples as in the object based-sampling.

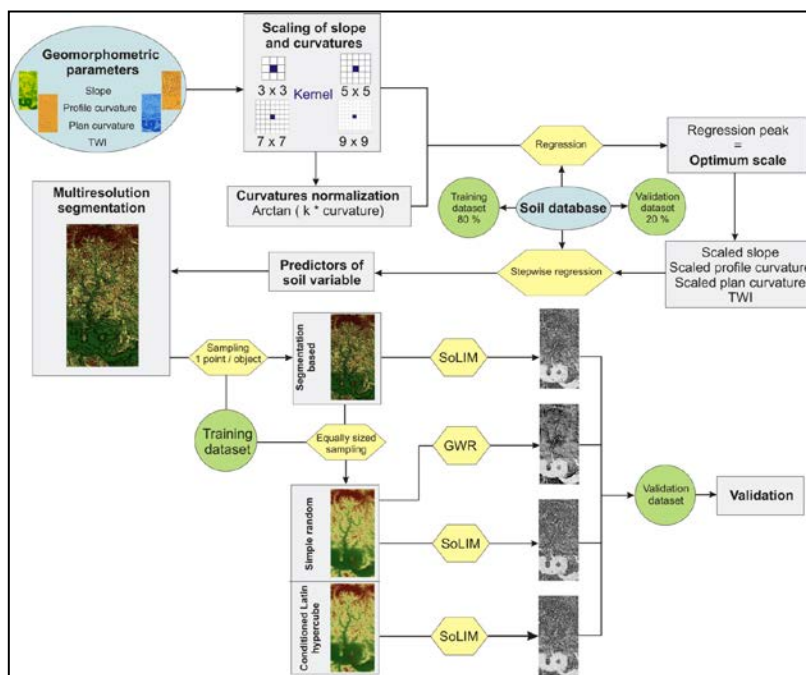


Figure 1. Flow chart showing the main steps of the experiment.

Soil mapping and accuracy assessment

Segmentation schemes were evaluated through their ability of accurately mapping soils. Thus, for each sampling scheme in Tables 1 and 2, maps of soil variables and classes were created using the sample-based inference engine implemented in the SoLIM Solutions 2010 software [16]. The agreement between maps and the reference data were assessed with standard methods: 1) overall accuracy and kappa index of agreement for soil classes; and 2) RMSE, agreement coefficient, mean absolute error and mean error for the A-horizon thickness.

RESULTS AND DISCUSSION

Segmentation produced between 11 and 40 homogeneous areas with the PT tool, and 6 to 22 with the ESP tool (Tables 1 and 2). As expected, accuracies improved with the number of samples for all sampling methods. However, the SBS performed consistently better than SRS and CLHS.

Predictions of the A-horizon thickness with SBS yielded the highest agreement coefficients (AC in Table 1), and the lowest RMSEs (except for PT 1, where cLHS was slightly better) and MAEs (except for PT 1 and 2, where cLHS was better). All SBSs produced results comparable with predictions that used the entire population of training samples. This includes the scheme with 6 samples (about 11 % of total). The other two methods produced less reliable results at the same number of samples, as shown by considerably lower AC values. The best results were achieved with the SBSs at the finest levels (PT3 and ESP3) of the two segmentation methods (Table 1).

Predictions of the soil classes with SBS outperformed SRS and cLHS in all cases but ESP3, where cLHS gave better results (Table 2). PT3 was the only sampling scheme that achieved results similar to those obtained with the entire population of training samples. These results were obtained with about 62 % of training samples. The other two methods produced significantly poorer predictions (kappa of 0.2 and 0.3 respectively). Interestingly, segmentations on the DEM alone (PT1 to 3) produced significantly better results (Table 2) than segmentation on the slope and profile curvature (ESP1 to 3), which predicted well the distribution of cambisols, luvisols and protisols in the study area. This might be due to the conflicts between homogeneity in profile vs. gradient (e.g. convexities/concavities have homogeneous profile, but heterogeneous gradient).

The good performance of SBS in optimizing soil sampling stems from the ability of LSS of delineating objects that maximize internal homogeneity and external difference. Conceptually, SBS can be seen as a particular case of purposive mapping [7], where the appropriate samples can be estimated within areas of homogeneous LSVs, which are delineated with

the aid of segmentation instead of fuzzy c-mean classification. The results presented here agree with previous findings [4, 7] on improving the accuracy of soil mapping with limited samples.

When guided by local variance, LSS self-adapts to the scale of local variability in the LSVs, with additional benefits of accounting for spatial autocorrelation, anisotropy and non-stationarity [11]. To check the impact of non-stationarity on analyses, an additional test was performed with Geographically Weighted Regression (GWR) [17]. The samples obtained with SRS were employed for mapping the A-horizon thickness, using the same covariates as in the other predictions. Results always improved significantly (Table 1), which clearly shows the importance of local models in predicting soil properties.

TABLE I. ACCURACY ASSESSMENT OF THE A-HORIZON PREDICTIONS BASED ON DIFFERENT SAMPLING METHODS

Sampling method						
		No. ^a	RMSE	AC ^b	MAE	ME
PT1 ^c	SRS	11	14.82	0.47	11.38	5.35
	GWR ^d	11	10.64	0.72	9.01	3.99
	SBS	11	11.95	0.75	9.65	0.19
	cLHS	11	11.52	0.63	9.33	- 1.85
PT2	SRS	14	13.92	0.72	11.45	3.41
	GWR	14	10.33	0.77	8.71	- 0.92
	SBS	14	10.41	0.79	9.10	- 3.17
	cLHS	14	11.03	0.74	8.35	3.21
PT3	SRS	31	11.54	0.73	10.27	- 1.36
	GWR	31	9.82	0.77	8.59	- 0.32
	SBS	31	8.84	0.85	6.61	- 2.97
	cLHS	31	10.28	0.84	8.67	3.00
ESP1	SRS	6	15.79	0.37	12.75	2.52
	GWR	6	10.72	0.53	8.60	0.84
	SBS	6	12.65	0.69	10.00	2.37
	cLHS	6	15.88	0.56	11.57	3.27
ESP2	SRS	8	15.67	0.27	11.87	1.76
	GWR	8	12.65	0.61	11.78	- 1.28
	SBS	8	11.25	0.71	9.37	- 1.16
	cLHS	8	12.21	0.69	9.63	- 3.46
ESP3	SRS	15	12.29	0.74	8.70	- 0.65
	GWR	15	8.83	0.79	7.77	- 2.65
	SBS	15	8.73	0.86	7.49	- 1.15
	cLHS	15	10.79	0.82	7.77	5.88
All training samples (80 %)		56	11.11	0.72	9.24	0.38

a. Number of samples. b. Agreement Coefficient. c.PT1 to 3- the three segmentation levels obtained with the PT tool; ESP1 to 3- the three segmentation levels obtained with the ESP tool. d. GWR was used for mapping based on the SRS samples

TABLE II. ACCURACY ASSESSMENT OF THE SOIL CLASSES PREDICTIONS BASED ON THREE SAMPLING METHODS

Sampling method		No.	OA	KIA
PT1	SRS	12	0.25	- 0.05
	SBS	12	0.38	0.09
	cLHS	12	0.25	- 0.01
PT2	SRS	15	0.31	0.05
	SBS	15	0.50	0.23
	cLHS	15	0.38	0.11
PT3	SRS	40	0.44	0.20
	SBS	40	0.63	0.45
	cLHS	40	0.50	0.30
ESP1	SRS	10	0.25	- 0.06
	SBS	10	0.31	0.07
	cLHS	10	0.25	- 0.04
ESP2	SRS	13	0.25	- 0.05
	SBS	13	0.31	0.05
	cLHS	13	0.31	0.01
ESP3	SRS	22	0.38	0.09
	SBS	22	0.38	0.15
	cLHS	22	0.44	0.14
All training samples (80 %)		65	0.63	0.45

In this case, GWR successfully substituted a poor sampling design by accounting for non-stationarity, which is a built-in capability of LSS.

In conclusion, SBS showed a high potential in optimizing soil sampling in the study area. The two SBS methods performed better than SRS and cLHS in predicting the A-horizon thickness and the soil classes. SBS would enable the reduction up to 11 % in the number of samples necessary to predict the A-horizon thickness, and up to 62 % to predict soil classes. This methodology could be effective in reducing costs of soil surveys. The analyses presented here further highlight the importance of considering locally adaptive techniques in optimization of sampling schemes and predictions of soil properties.

ACKNOWLEDGMENT

This work was supported by a grant of the Romanian National Authority for Scientific Research, CNCS - UEFISCDI, project number PN-II-ID-PCE-2011-3-0499. The Romanian dataset was generously provided by OSPA Hunedoara. We thank to three anonymous reviewers for providing comments and suggestions that greatly improved the paper.

REFERENCES

[1] Sanchez, P.A., S. Ahamed, F. Carré, A.E. Hartemink, J. Hempel, J. Huising, P. Lagacherie, A.B. McBratney, N.J. McKenzie, M.d.L. Mendonça-Santos, B. Minasny, L. Montanarella, P. Okoth, C.A. Palm, J.D. Sachs, K.D. Shepherd, T.-G. Vågen, B. Vanlauwe, M.G. Walsh, L.A. Winowiecki, and G.-L. Zhang, 2009. "Digital soil map of the World." *Science*, 325: 680-681.

[2] McBratney, A.B., M.L. Mendonça Santos, and B. Minasny, 2003. "On digital soil mapping." *Geoderma*, 117: 3-52.

[3] Brus, D.J., and J.J. de Gruijter, 1997. "Random sampling or geostatistical modelling? Choosing between design-based and model-based sampling strategies for soil (with discussion)." *Geoderma*, 80: 1-44.

[4] Yang, L., A.X. Zhu, F. Qi, C.-Z. Qin, B. Li, and T. Pei, 2012. "An integrative hierarchical stepwise sampling strategy for spatial sampling and its application in digital soil mapping." *International Journal of Geographical Information Science*, 27: 1-23.

[5] Minasny, B., and A.B. McBratney, 2006. "A conditioned Latin hypercube method for sampling in the presence of ancillary information." *Computers & Geosciences*, 32: 1378-1388.

[6] MacMillan, R.A., A. Torregrosa, D. Moon, R. Coupé, and N. Philips, 2009. "Chapter 24 Automated predictive mapping of ecological entities", In *Geomorphometry-Concepts, Software, Applications. Developments in Soil Science*, vol. 33, Edited by: Hengl, T. and Reuter, H.I., Elsevier, Amsterdam.

[7] Zhu, A.X., L. Yang, B.L. Li, C.Z. Qin, E. English, J.E. Burt, and C.H. Zhou, 2008. "Purposive sampling for digital soil mapping for areas with limited data", In *Digital Soil Mapping with Limited Data*, Edited by, Springer, New York.

[8] Zhu, A.X., F. Qi, A. Moore, and J.E. Burt, 2010. "Prediction of soil properties using fuzzy membership values." *Geoderma*, 158: 199-206.

[9] Drăguț, L., and C. Eisank, 2011. "Object representations at multiple scales from digital elevation models." *Geomorphology*, 129: 183-189.

[10] Baatz, M., and A. Schäpe, 2000. "Multiresolution Segmentation-an optimization approach for high quality multi-scale image segmentation", In *Angewandte Geographische Informationsverarbeitung*, Edited by: Strobl, J., Blaschke, T. and Griesebner, G., Wichmann-Verlag, Heidelberg.

[11] Drăguț, L., C. Eisank, and T. Strasser, 2011. "Local variance for multi-scale analysis in geomorphometry." *Geomorphology*, 130: 162-172.

[12] Häring, T., and B. Schröder, "Sampling optimization using image segmentation," presented at the 4th International Workshop on Digital Soil Mapping, Rome, 2010.

[13] Drăguț, L., T. Schauppenlehner, A. Muhar, J. Strobl, and T. Blaschke, 2009. "Optimization of scale and parametrization for terrain segmentation: An application to soil-landscape modeling." *Computers & Geosciences*, 35: 1875-1883.

[14] Drăguț, L., and C. Eisank, 2012. "Automated object-based classification of topography from SRTM data." *Geomorphology*, 141-142: 21-33.

[15] Drăguț, L., D. Tiede, and S. Levick, 2010. "ESP: a tool to estimate scale parameters for multiresolution image segmentation of remotely sensed data." *International Journal of Geographical Information Science*, 24: 859-871.

[16] Zhu, A.X., L. Band, R. Vertessy, and B. Dutton, 1997. "Derivation of soil properties using a soil land inference model (SoLIM)." *Soil Science Society of America Journal*, 61: 523-533.

[17] Brunsdon, C., A.S. Fotheringham, and M.E. Charlton, 1996. "Geographically weighted regression: A method for exploring spatial nonstationarity." *Geographical Analysis*, 28: 281-298.

Development of gully and its controlling factors in the Loess Plateau of China using high spatial resolution imagery

Li zhen ,Zhang yan, Zhu qingke, He yuanmei, Yao wenjun

Key Laboratory of Soil and Water Conservation and Desertification Combating, Ministry of Education

Beijing Forestry University

Beijing,China

Abstract

Gully erosion damages land resources and is one of the most significant sources of sediment to streams. The purpose of this paper is to investigate the dynamics of gully development and its primary influencing factors on the loess plateau, China. 30 small catchments were selected from Cai jiachuan watershed on the eastern hilly loess plateau in western Shanxi province to compare gully development (changes of the area and perimeter of the valley region from 2003 to 2010), based on high-resolution remote sensing data (QuickBird image) and GIS. Pearson correlation coefficient was employed to analyze the influence of catchment area, ratio of drainage area to catchment area, slope gradient, vegetation coverage on gully development. The results showed that the area of the valley region increased 0.83%~10.57% and perimeter of the valley region changed -14.16%~11.07% from 2003 to 2010. Gully develop ratio was significantly related to catchment area, ratio of drainage area to catchment area, slope gradient of drainage area and change of area with coverage larger than 60% in the inter-valley region. Gullies developed more quickly in catchments covered partly with farmland than those covered mainly with grassland or with forestland.

1. Introduction

Gullies have been defined as channels whose width and depth do not allow for normal tillage (FAO, 1965). Gullies have also been defined as large rills with a cross-sectional area more than 1 ft² (0.0929 m²) (Poesen, 1993). Gully processes have a three-dimensional nature affected by a wide array of factors and processes. Gully erosion represents an important sediment source in drylands, contributing on average 50–80% of sediment production by water erosion (Poesen et al., 2002). However, gully erosion rates are difficult to assess, particularly at the catchment scale. The major contribution of remote sensing to gully erosion assessment has been the visual

interpretation of aerial photography. Gully limits are delineated from aerial photographs and gully retreat rates are assessed using multi-temporal comparison (e.g. Daba et al. 2003; Vandekerckhove et al. 2003). Studies suggested that high resolution remote sensing can be used to derive gully headcut development rate quickly and accurately at middle spatial and time scales. Vrieling et al. (2007) used a panchromatic QuickBird image to validate permanent erosion gullies obtained from optical ASTER imagery. Li, et al. (2012) used QuickBird images in 2003 and 2010 to compare changes of the area and perimeter of the gully region and the headcut development rate of gully on the eastern hilly loess plateau, China and the results showed that gully expanded mainly on side branches with the rate of 0.36~0.44 m/a. This paper aimed to using multi-temporal comparison of QuickBird images (Li et al., 2003) to investigate the dynamics of gully development and the primary influencing factors of gully retreat on the loess plateau, China.

2. Study area, data and methods

The study area, Cai jiachuan watershed (38 km²) is located on the eastern Loess Plateau (E 110°40'~ 110°48', N 36°14'~ 36°18'), ranging from 905 to 1580 m and an annual rainfall above 517 mm. 30 small catchments were selected to analyze the development of gullies and its main influencing factors (Fig. 1).

QuickBird images acquired on Oct.21,2003 and Oct.11, 2010 (blue, green, red and NIR of 2.44 m resolution, and PAN data of 0.61m resolution) were used for extracting the spectral and spatial information of study area. DEM of 5m resolution was used to extract slope gradient information. Valley edge is the division between valley area and inter-valley are. Its movement denotes the development of gullies. Valley edges were delineated from QuickBird images by the methods of visual interpretation, taking the DEM as reference. Vegetation

coverage was extracted based on the method of NDVI using the formulation (1)

$$fc = \frac{NDVI - NDVI_{soil}}{NDVI_{veg} - NDVI_{soil}}$$

(1)

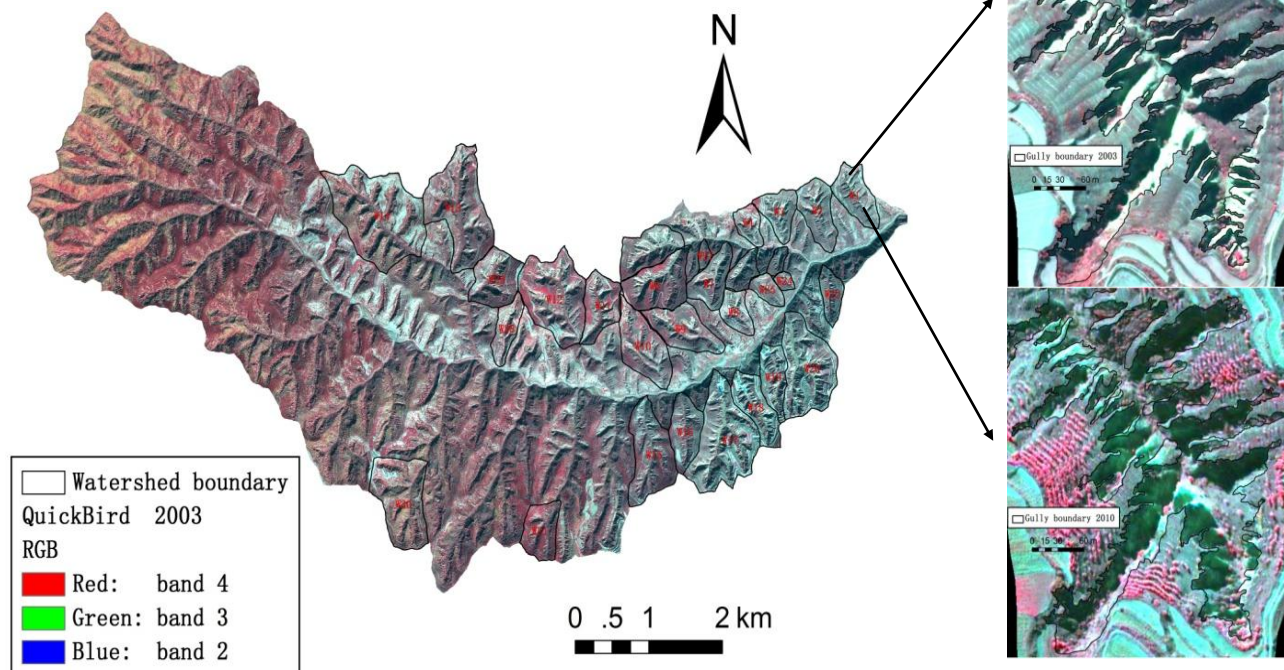


Fig.1. Location and QuickBird image of study area

3. RESULTS

Area and perimeter of the Valley region changed by 0.83% ~ 10.57% and -14.16% ~ 11.07% respectively from 2003 to 2010. Valley area of more than 60% of the 30 catchments increased by 0~4% while valley perimeter of 40% of the 30 catchments decreased by -14.16% ~ -0.33% (figure 2). The disappearance of some narrow intervalley area near valley, which was obvious on the images, accounted for the decrease of valley perimeter.

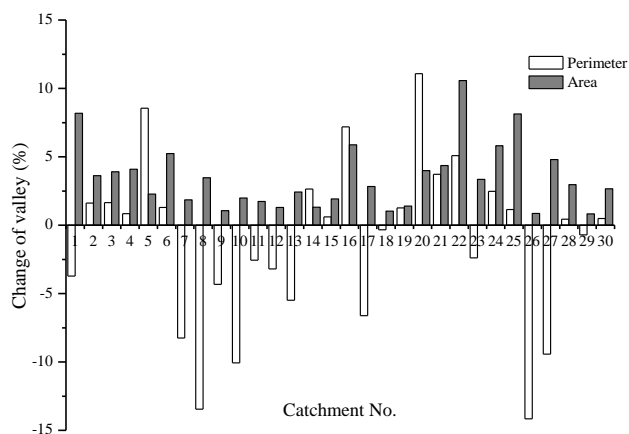


Fig.2. The change of valley areas and perimeters from 2003 to 2010

in which, fc is vegetation coverage, $NDVI$ is the $NDVI$ value in pixel, $NDVI_{soil}$ is the $NDVI$ value of bare soil, and $NDVI_{veg}$ is the $NDVI$ value of pure vegetation. Landuse types were classified by visual interpretation into Farmland, grassland, forestland and other.

Increase of Valley area was influenced significantly by catchment area (A), ratio of valley area to catchment area (A_{int}/A_g) and slope of inter-valley (S_{int}) at the level of 0.05 and by change of area with coverage larger than 60% (C_c-w) on inter-valley (C_c-g) at the level of 0.1 (table 1).

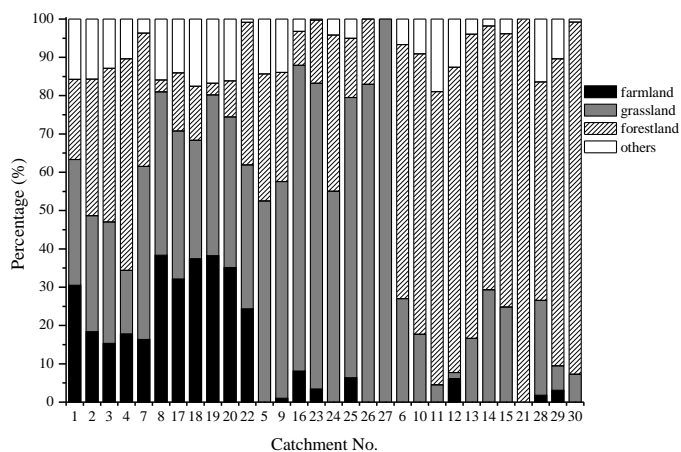


Fig.3. The percentage of landuse in the catchments in 2003

30 small catchments were classified to 3 types according to landuse types. Gullies developed more quickly in catchments with mosaic types of Farmland, grassland and forestland (4.02%) than those of grassland (3.75%) and forestland (2.43%). For mosaic catchments, the gully development related significantly with A_{int}/A_g and S_{int} . For

grassland catchments, the gully development ratios were influenced on only by A_{int}/A_g . Significant negative correlation was found between the gully development ratios in forestland catchments and C_{c-g} . It suggested that forests with dense canopy were not helpful to gully erosion control.

Table1 Correlation coefficients between the change of valley area (A_c) and the influencing factors for different types of catchments

Catchment types	A (hm^2)	A_{int}/A_g (m^2/m^2)	S_{int} (%)	C_{c-w}	C_{c-g}
All 30 catchments	-0.371**	0.599***	0.532***	-0.341*	-0.353*
Catchments with Farmland,grassland and forestland (n=11)	-0.225	0.633**	0.610**	-0.234	-0.239
Grassland catchments (n=8)	-0.495	0.944***	0.545	-0.386	-0.591
Forestland catchments (n=11)	-0.362	-0.358	-0.097	0.484	0.656**

* $p < 0.10$, ** $p < 0.05$; *** $p < 0.01$.

A: watershed area ; A_{int} : inter-valley area; A_g :valley area; S:watershed slope gradient ; S_{int} :intervalley slope gradient ; C_{c-w} : change of watershed area with coverage larger than 60%; C_{c-g} : change of intervalley area with coverage larger than 60%.

4. Conclusions

In all the 30 investigated catchments, the area of the valley region increased from 2003 to 2010; while perimeter of the valley region in 60% catchments increased and the others decreased because of some narrow inter-valley area near valley disappeared. Significant positive correlations were observed between increase of valley area and catchment area, ratio of valley area to catchment area, slope of inter-valley and change of area with coverage larger than 60% inter-valley. Gullies developed more quickly in catchments with mosaic types of farmland, grassland and forestland than those of grassland and forestland. The results suggest that an increase in grassland and forestland could reduce the rate of gully development. For catchments of different types of landuses, the main influencing factors were different. Significant negative correlation was found between the gully development rates in forestland catchments and change of area with coverage larger than 60%, suggesting that forests with dense canopy were not helpful to gully erosion control.

REFERENCES

[1] Daba,S.,Rieger, W.,Strauss,P.,2003.Assessment of gully erosion in eastern Ethiopia using photogrammetric techniques.Catena,50,273-291
[2] Leprieur,C.,Verstraete,M.M.,Pinty,B.,1994, Evaluation of the performance of various vegetation indices to retrieve vegetation cover from AVHRR data. Remote Sensing Review, 52,265—284.
[3] Li,Y.,Poesen,J.,Yang,J.C.,Fu,B.,Zhang,J.H.,2003.Evaluating gully erosion using ^{137}Cs and $^{210}Pb/^{137}Cs$ ratio in a reservoir catchment. Soil and

Tillage Research,69(1-2),107-115.
[4] Li,Z., Zhang,Y., YaoW.J., Zhu,Q.K.,2012, Estimating gully development rates in Hilly Loess Region of Westem Shanxi province based on QuickBird images. Transactions of the Chinese Society of Agricultural Engineering. 28,141-148. (in Chinese)
[5] Martinez-Casasnovas,J.A.,Anton-Fernandez,C.,Ramos,M.C. .2003.Sediment production in large gullies of the Mediterranean area (NE Spain) from high-resolution digital elevation models and geographical information systems analysis. Earth Surface Processes and Landforms, 285,443—456.
[6] Martinez-Casasnovas,J.A.,Ramos,M.C., Poesen, J.,2004. Assessment of sidewall erosion in large gullies using multi-temporal DEMs and logistic regression analysis. Geomorphology,58,305—321.
[7] Valentin,C., Poesen,J., Li,Y.,2005. Gully erosion: Impact, factors and control. Catena, 63, 132—153.
[8] Vandekerckhove,L.,Poesen,J.,Govers,G.,2003.Medium-term gully headcut retreat rates in Southeast Spain determined from aerial photographs and ground measurements.Catena,50,329-352.
[9] Vrieling,A.,Rodrigues,S.C.,Bartholomeus,H.,etal.,2007.Automatic identification of erosion gullies with ASTER imagery in the Brazilian Cerrados. International Journal of Remote Sensing, 28,2723—2738.
[10] Whitford,J.A., Newham,L.T.H., Vigiak,O., et al,2010. Rapid assessment of gully sidewall erosion rates in data-poor catchments: A case study in Australia. Geomorphology, 2010, 118, 330—338.
[11]Wu,Y.,Q.,Cheng,H., 2005. Monitoring of Gully Erosion on the Loess Plateau of China Using a Global Positioning System.Catena,63,154—166.

From rills to gullies: how do we measure them?

Sheng Li

Agriculture and Agri-Food Canada
Fredericton, New Brunswick, Canada
Sheng.Li@agr.gc.ca

Rene Wackrow

Loughborough University
Loughborough, Leicestershire, United Kingdom

Fangzhou Zheng, Zisheng Xing, Fanrui Meng

University of New Brunswick
Fredericton, New Brunswick, Canada

David Lobb

University of Manitoba
Winnipeg, Manitoba, Canada

Abstract—*Water erosion can take the forms of inter-rill (sheet), rill and gully erosion. Although gully erosion has been recognized as a major form of water erosion in many agricultural lands, studies on water erosion have focused on inter-rill and rill erosion. There is a gap in knowledge about how gullies are formed and how this process can impact surface runoff, sediment yield and nutrient losses from the landscape. In this study, we propose to conduct a plot study to examine the initiation of channels and the development of channels from rills to gullies.*

The study was carried out on six plots in the research farm of the Potato Research Centre in Fredericton, Canada. Three management treatments were applied to the plots: cropped and up-down-slope tillage, cropped and contour tillage, and fallow and up-down-slope tillage (serving as the control). The formation and development of channels are monitored using three methods: 1) manual measurement, 2) a total station scanner, and 3) photogrammetry. Preliminary results showed that the resolution and accuracy of data obtained using the total station scanner varied substantially, depending on the view angle and the distance of the measurements whereas the photogrammetry method was capable of detecting fine elevation changes across the plots.

INTRODUCTION

In many regions, accelerated soil erosion is a major cause of soil degradation on agricultural landscapes (Lobb et al., 2010). Major forms of soil erosion on cultivated lands are water, wind and tillage erosion, categorized based on the force involved in the erosion processes (e.g., Li et al., 2008). Among these three major forms of soil erosion process, water erosion is most intensively studied. Many of the early studies on water erosion are within the framework of the Universal Soil Loss Equation (USLE), which focuses almost entirely on sheet and rill erosion at the plot-scale, while not accounting for erosion that occurs in large channels, especially in classical gullies (Renard et al., 1997). Channels occupy only a small portion of the land area and were often considered only as pathways for water and sediments transportation. Since then, many BMPs developed to reduce sediment and nutrient loadings in receiving waterbodies (e.g., rivers, lakes and wetlands) were aimed at controlling water erosion in agricultural fields (Chow, 2010). However, studies

have shown that as water flows along channels, it may interact with channels and these interactions may have profound impacts on hydrology, soil erosion and the transportation of sediments and nutrients. For example, previous studies have found that gully erosion is an important form of water erosion and can contribute up to 94% of the total sediment yield due to water erosion (Poesen et al., 2003).

Our literature review suggests that there is a lack of knowledge on how the channels are formed and evolved, especially those lower-order channels at the plot- and field-scale, in agricultural landscapes. Therefore, we propose a plot study to investigate the initiation and development of channels and the effects of channels on hydrology, soil erosion and nutrient losses in agricultural land.

MATERIALS AND METHODS

Study site and plot layout

A field located in the farm of the Potato Research Centre (PRC) in Fredericton, New Brunswick, Canada was used in this experiment. The field is situated on an east-north facing slope with a slope gradient of about 10% and a slope length of about 100 m (Fig. 1). A 110 m wide and 80 m long area in this field was used to establish 6 plots. Each plot was approximately 78 m long and 6 m wide (the width of a typical potato seeder) with 5 m wide space between plots for machine operations. Three management treatments were applied to the plots: cropped and up-down-slope tillage, cropped and contour tillage, and fallow and up-down-slope tillage (serving as the control). The three treatments, each with two repeats, were randomly assigned to the 6 plots. Lidar topographic data (point density of about 2 m² per point with accuracy at the level of ~0.3 m) were obtained for the study site and were used to determine the plot orientation. The up-down-slope tillage plots were oriented along the direction of the steepest slope. The contour tillage plots were oriented at the direction of ~3 degree included angles to the contour lines. This created a slope for the plots to shed water away, which is a common setup for contour tilled fields in this region. A set of reference points was established around the plot area. These

reference points were permanently marked with 1 m long iron sticks buried into the ground and their absolute coordinates were surveyed using a Trimble GeoXH GPS system with a real-time accuracy at the level of 0.1 m.

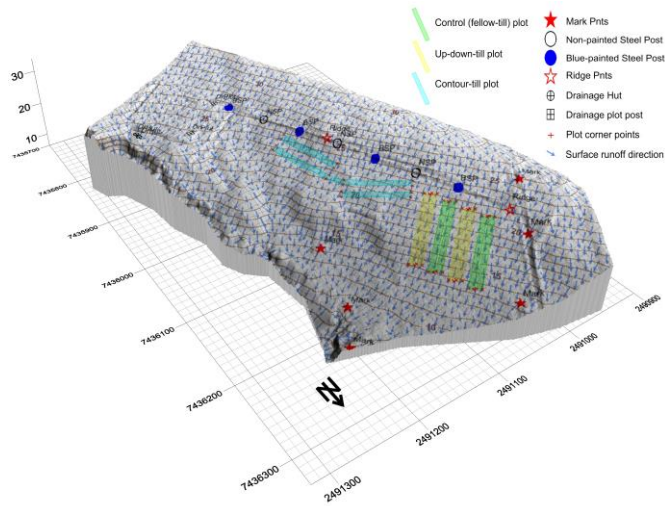


Figure 1. Maps of the study site and the plot layout.

Monitoring of channel initiation and development

Channel initiation and development are determined morphometrically in this study, using three methods. The first method (M0) is to measure the density and geometry of channels manually. To facilitate the measurement, a platform of ~6 m wide is built. The platform is put on wheels and going across the plot at about 1 m height from the ground. The measurement is done by standing on the platform so that the plot is not disturbed. The measurement is conducted along eight transects across each plot. The transects are 10 m apart, located using permanent markers as references. The channels along the transects will be counted and numbered systematically. The location, depth and width of each channel will be recorded. This manual measurement will be carried out after every major rainfall or snowmelt event. Although crude, M0 is applicable year round. The other two methods described below use remote sensing technologies and will not work during periods of snow coverage and crop canopy. The first remote sensing method (M1) is to use a total station scanner (Fig. 2). Total station is easy to operate and can scan the entire plot area within a few hours. However, the accuracy (< 1 cm) is not ideal for capturing small changes after every erosion event. So the entire study area will be scanned for only four times per year: after snowmelt but before cultivation (T1), after seeding (T2), before 10% crop canopy coverage (T3) and after fall tillage (T4). Comparison between T2 and T3 will be used to characterize the effect of rainfall erosion and the comparison between T4 and T1 in the following year will be used to characterize snowmelt erosion.

Another remote sensing method is photogrammetry (M2). A pair of cameras is installed on top of two poles welded to the platform (Fig. 3). Pairs of overlapping images of the plot surface are taken while the platform is moving along the plot. Overlapped pictures are imported into a photogrammetry

software (Photomodeler Scanner 2012) to generate a three dimensional image of the soil surface. Data collection using photogrammetry is fast, efficient and cost effective and can be seen as an advantage of this method. Collected data will be compared with data acquired in methods M1. The timing for taking the photos will match those for the total station scanning.

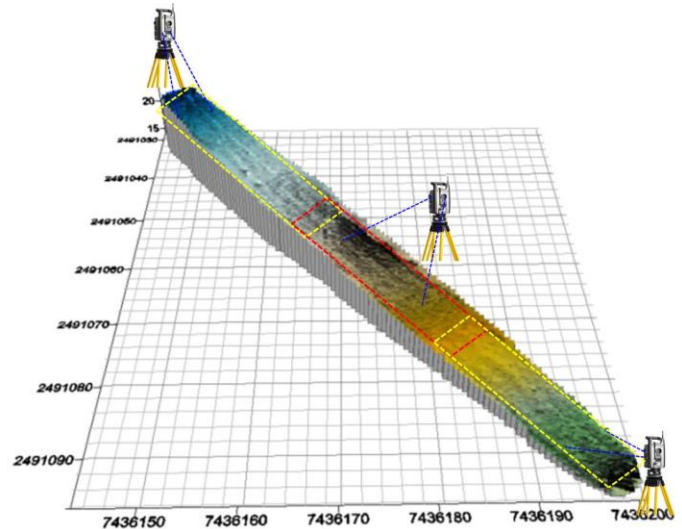


Figure 2. Illustration of the total station scanning method (M1). The total station is set up at multiple locations for scanning. The coordinate systems for the scanning are based on the same reference points so that the data can be merged and used to generate the 3D map for the entire plot. Raw data points obtained from the scanning are shown as black dots on the map.

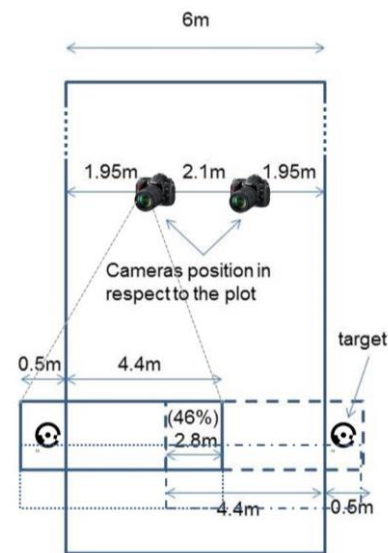


Figure 3. Illustration of the photogrammetry method (M2). The pair of cameras are mounted on top of poles (welded on a platform) at positions ~5 m above the ground. There are overlaps between the pair of pictures in the same row. Along the plot, pictures are taken every two meter to ensure sufficient overlaps between adjacent rows of pictures. The overlapped pictures are used to generate the 3D surface of the ground using a photogrammetry software. Targets are installed along both sides of the plot and are used as reference points to bring together pictures taken at different time periods.

Monitoring runoff water

A 6 m wide flume will be installed at the bottom of each plot to collect surface runoff. Flow rate and discharge will be monitored and recorded in a datalogger. An auto-sampler will be connected to the datalogger and water sampling will be triggered by the initial rise of water level (> 1 cm) in the flume. Hourly samples will be taken after the first sample until the water level is lower than 1 cm. Additional samples will be taken whenever the water level change from the last sampling is > 5 cm. All water samples collected will be analyzed in the hydrological lab in PRC for total sediment (TS), particulate nitrogen (PN), nitrate and nitrite (NO_x), ammonium (NH₃), total dissolved nitrogen (TDN), total nitrogen (TN), particulate phosphorus (PP), total dissolved phosphorus (TDP) and total phosphorus (TP). A weather station located about 700 m south-east of the plot will provide hourly or more detailed data on precipitation, air temperature, evaporation, wind direction and speed, solar radiation and soil temperature.

PRELIMINARY RESULTS

The plots were prepared in the spring of 2012. The GPS reference points were surveyed and marked. A first set of total station scanning were conducted in the fall of 2012 after harvesting. A grid DEM was generated for each plot based on the total station scan data (Fig. 2). Tillage furrows can be identified on these DEMs so that it was expected that large channels/gullies should be identifiable using this method. However, it was found that the resolution and accuracy of the data obtained using the total station scanner varied substantially, depending on the view angle and the distance of the measurements. Point cloud was extremely dense near the total station and was becoming increasingly sparse at further distances. Beyond ~20 m, the points were too sparse to reflect the shape of ridges and furrows. Also, when the total station was set up at the side of the plot, there were blind areas behind the ridges. This created errors for the elevation data, especially for those high ridges or deep furrows.

The photogrammetry photos were taken at about the same time as the total station scanning. Firstly, the camera geometry was determined following a calibration procedure. The photo image block of each plot was imported into the PhotoModeller software, which uses these camera parameters in a bundle adjustment for image restitution. When the exterior orientation parameters of all images are determined, PhotoModeller can measure a vast number of 3D points on the surface which can then be used to generate a digital elevation model (Fig. 4). With the number of data points provided by the photogrammetry method, subtle changes in elevation can be detected. Therefore, the shapes of ridges and furrows in the plots can be precisely determined.

FUTURE PLANS

In this coming spring, another set of total station scanning will be conducted, as well as another set of photos will be taken. The generated DEMs will be compared against the ones obtained in last fall to determine the shape and volume of channels. Also, a flow monitoring station will be established at the bottom of each plot to monitor the runoff and sediment and nutrient yields during critical periods of water erosion. Weather data will also be

collected at a nearby weather station. The effects of topographic, climatic and hydrologic factors and the interactions between these factors will be investigated.

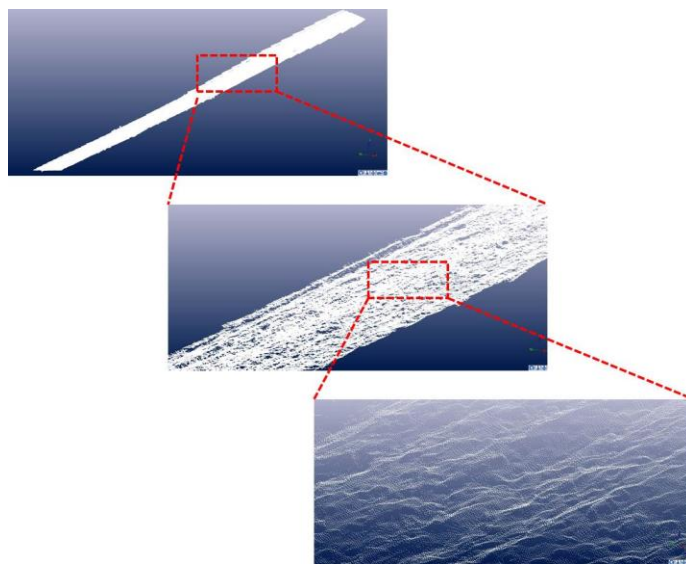


Figure 4. Illustration of the DEM generated using the PhotoModeller scanner software.

ACKNOWLEDGMENT

This study is funded by the Agriculture and Agri-Food Canada through its AgriFlex program. The authors would like to thank John Monteith, Lionel Stevens and the crew of the farm service from the AAFC-PRC for assisting with the field work.

REFERENCES

- [1] Chow, L. 2010. Black Brook Watershed, New Brunswick, p. 108-114, In V. Stuart, et al., eds. Watershed Evaluation of Beneficial Management Practices (WEBs) : Towards Enhanced Agricultural Landscape Planning - Four- Year Review (2004/5-2007/8).
- [2] Li, S., D.A. Lobb, M.J. Lindstrom and A. Farenhorst. 2008. Patterns of tillage and water erosion on topographically complex landscapes in the North America Great Plains. *J. Soil Water Conservation* 63 (1):37-46.
- [3] Lobb, D.A., S. Li, and B.G. McConkey. 2010. Soil Erosion. In Eilers, W., R. MacKay, L. Graham and A. Lefebvre (eds). 2010. Environmental Sustainability of Canadian Agriculture: Agri-Environmental Indicator Report Series — Report #3. Agriculture and Agri-Food Canada, Ottawa, Ontario.
- [4] Poesen, J., J. Nachtergaele, G. Verstraeten, and C. Valentin. 2003. Gully erosion and environmental change: importance and research needs. *Cantena* 50:91-133
- [5] Renard, K.G., G.R. Foster, G.A. Weesies, D.K. McCool, and D.C. Yoder. 1997. Predicting Soil Erosion by Water: A Guide to Conservation Planning with the Revised Universal Soil Loss Equation (RUSLE). USDA, Agricultural Handbook 703, 404 pp.

Method for extraction continuous shoulder line in Loess watershed

Yi Zhou

Collage of Tourism and Environment
Shaanxi Normal University
Xi'an, China
zhouyilucky@gmail.com

Jian Tian

College of Resources and Environmental Engineering
Hefei University of Technology
Hefei, China

Abstract—A method for automatic connection of Loess shoulder line is designed in this paper. Firstly, according to the morphological characteristics of loess hillslope, raster points on the position of shoulder-lines are detected based on high resolution DEM data. Then buffer curve of divide line sets as the initial curve. Thirdly, initial curve is forced to creep to shoulder-line points under the guidance of the hillslope flow direction matrix to make a continuous shoulder line. Experiments in the loess hilly-gully area show the continuity and precision of results meet our need and have good agreement with the real topography.

Efficiency and accuracy are two key aspects should be concerned for extraction of shoulder line by using of digital productions of earth surface. However, extraction method based on remote sensing images can not satisfy the two aspects mentioned above simultaneously. Manually digitalizing shoulder line method based on high-resolution aerial remote sensing photographs has relatively high precision but low efficiency. Meanwhile, automatic interpretation algorithm has problem because of shadow always exists at the shoulder line area, and this interference affects the precision of extraction results greatly.

INTRODUCTION

The Loess Plateau is famous for the typical dual structure landform, namely, the upper smooth inter-gully area and the lower cliffy gully area. This is unique landform types in the world. The loess Shoulder line, which is the dividing line of the gully area and the inter-gully area, can be found widely developed on Loess Plateau.

Due to vertical cleavage characteristics of loess, the soil materials on both sides of loess gullies will be eroded after heavy rainfall in monsoon and precipitous loess gully cliff formed. Contrasting to the upper relatively flat inter-gully area, there is obviously slope turning line between the gully area and inter-gully area^[1]. This line is called shoulder line.

Existing achievements show that there are significant differences in erosion types, confluence mode, terrain slope, land use types as well as vegetation cover between the upper and lower regions of shoulder line. Meanwhile, the shoulder line plays significant role not only in controlling the loess terrain structure but also in constructing soil erosion model^[2]. Therefore, basing on National GIS database and GIS spatial analysis, automatic recognition of loess shoulder line becomes a central issue research in this area.

Fortunately, automatic extraction method based on high resolution Digital Elevation Model (DEM) and series of slope information data derived from it has been proved has both greater advantage in efficiency and accuracy recently. Overall, methods for extraction shoulder line based on DEMs can be summarized in three kinds. The first is to recognize shoulder line raster by using of local terrain characteristic identification method^[1-4], the second is identifying inflection points on the profile of slope flow line^[5], and the third is the great occlusion difference between the upper area and the lower area of shoulder line^[6]. However, because of the complexity of loess terrain, discontinuous shoulder line always exists when using above-mentioned algorithm, which makes the extraction result a great constrain in modeling applications.

In this paper, an automatic loess shoulder line extraction method based on 5-meter resolution DEM data was designed. Main advantage of this method is greatly improvement in the continuity of shoulder line.

METHODOLOGY

2.1 Identification of shoulder line raster

The morphological characteristic of shoulder-lines is the slope gradient difference between the locations up and down. Fig.1 is a typical loess gully model represented by DEM

combined with DOM surface layer. The dark line, which is the traverse profile line of gully, shows the structure of the hill slope

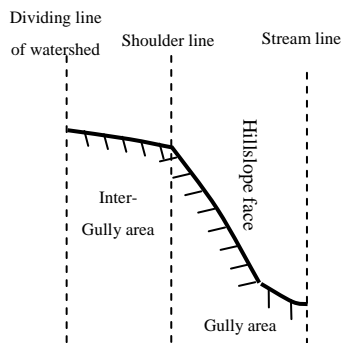


Fig.1 profile structure of hillslope in hilly-gully area

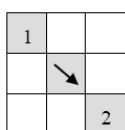


Fig.2 structure of operator

and the slope position of the shoulder-line. From which we know that the shoulder-line is the location have the biggest slope gradient variance on the direction of hillslope aspect. This is the emblematical configuration of the shoulder-line and is the theoretic foundation for automatic detection of shoulder line grid cells.

In order to identify structure of hillslope, an operator is designed for the detection. Two kind of topographic criterions are needed including the aspect matrix and slope gradient matrix which are the first derivations of the DEM data. The structure of the operator is shown in fig.2. This method is made up of following steps:

1. Detecting the hill slope direction of the central cell by aspect matrix. For example, if the aspect value of the target cell is 135°, then the cell number 1 and 2 which on the direction from northwest to southeast should be chosen for next processing.

2. Comparing slope variance (Sv) between cells detected above. Thresholds are needed in this step. Only when the Sv values exceed 20°, and the slope gradient of downstream cells should larger than the upstream cells, can the central cell be marked as the shoulder-line cells. In this example, slope of grid cell No.1 should larger than that of the cell No. 2. Then the adjacent cell would be regarded as the target cell until the whole DEM matrix was scanned over, Fig.3 shows shoulder line raster detected by this proceeding.

3. Noisy identified shoulder line cells can be removed by characteristic of cluster number less than 6.

2.2 Shoulder line raster connection under guidance of hillslope flow direction

1. Choosing Initialized connecting curve(ICC). There are two principles for choosing the location of the connecting curve in watershed. Firstly, the curve should as closed to dividing line of watershed as possible. Secondly, all of the gully area should be surrounded by the curve. Thus the boundary line buffer 2 grid to inner watershed should be the location of the ICC.

2. Hillslope flow direction matrix(HFDM), which is the guidance for creep direction of raster on ICC, can be derived from DEM data by D8 algorithm^[7]. in fig.4.

3. Successively Moving rasters on the ICC by guidance of HFDM until all rasters locate on shoulder line raster identified above and gully lines. As shown in fig.5.

4. Connecting the broken shoulder line raster by order of the

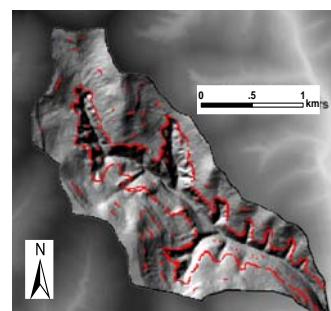


Fig.3 Shoulder line rasters

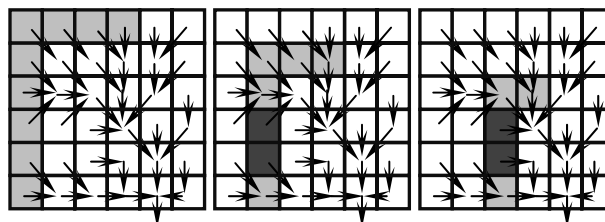


Fig.4 Locomotive processing of points on ICC

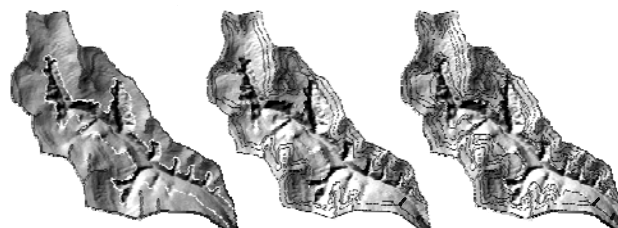


Fig. 5 Locomotive processing of ICC (white points are raster points on Shoulder-line, real-time location of snake curve is marked by black solid line, location of snake curve has been derived is marked by dash line)

ICC raster.

RESULT ANALYSIS

Accuracy assessment of method in this paper has been evaluated by a comparison with the manual extraction results from the 1-m resolution DOMs (Digital Ortho-image Maps).

TABLE I. PARAMETERS COMPARISON BETWEEN EXTRACTION AND STANDARD RESULTS

Location of watershed	Landform type	area (km ²)	Percentage of rasters with offset distance less than 10m	Max offset distance (m)
Suide county	Hilly-gully area	3.68	91.6 %	20.3

Tables 1 give the statistic results, in which max detection offset 20.3m is achieved. This offset is equal to 4–5 grid pixels in 5-m resolution DEMs, showing a satisfied accuracy.

ACKNOWLEDGMENT

This research is supported by the National Natural Science Foundation of China (NO. 41201464,41171299) and the Central Universities Fundamental Research projects (NO. GK201102012).The authors express their great thanks to everyone who have helped in the writing of this article.

REFERENCES

[1] Zhou Y, Tang G.A, Yang X, et al. 2010, "Positive and negative terrains on northern Shaanxi Loess Plateau", *Journal of Geographical Sciences*. 20(1): 64-76.

[2] Lv G N, Qian Y D, 1998. "Study of automated extraction of shoulder line of valley from grid digital elevation data". *Scientia Geographica Sinica*, 18(6): 567-573. (in Chinese)

[3] Zhou Y, Tang G.A, Wang C. 2010,"Automatic Segmentation of Loess Positive and Negative Terrains Based on High Resolution Grid DEMs", *SCIENTIA GEOGRAPHICA SINICA*, 30 (2) , 261-266. (in Chinese)

[4] Song X.D, Tang G.A, Li F.Y et al. 2013, "Extraction of loess shoulder-line based on the parallel GVF snake model in the loess hilly area of China" , *Computers & Geosciences*,52:11-20.

[5] Liu P J, Zhu, Q K; Wu D L et al. 2006. "Automated extraction of shoulder line of valleys based on flow paths from grid Digital Elevation Model (DEM) data". *Journal of Beijing Forestry University*, 28(4): 72-76. (in Chinese)

[6] Chen Y.G, Tang G.A, and Y Zhou.2012, "The Positive and Negative Terrain of Loess Plateau Extraction Based on the Multi-azimuth DEM Shaded Relief", *SCIENTIA GEOGRAPHICA SINICA*,23(1):104-109.

[7] O'Callaghan JF, Mark DM. 1984. "The extraction of drainage networks from digital elevation data". *Computer Vision, Graphics, and Image Processing* 28: 323-344.

Vegetation mapping using discrete-return and full-waveform airborne LiDAR data

Chen Dong^{a,b}, Zhang Liqiang^{b,*}, Xu Xiang^b, Wang Zhen^b

^aNanjing Forestry University

^bState Key Laboratory of Remote Sensing Science

Beijing Normal University

Beijing, China

chendong@njfu.edu.cn

Abstract—Vegetation mapping is a significant issue in city modeling and estimating vegetation properties. This paper aims to accurately extract vegetation point clouds from urban and mountainous areas using discrete-return and full-waveform airborne Light Detection and Ranging (LiDAR) data. For the full-waveform LiDAR data, the full-waveform decomposition and modeling technique based on kernel function is proposed to generate dense 3D point clouds. Then, the pre-segmentation algorithm based on probability density analysis is employed to generate homogenous segments for a supervised, segment-based SVM classifier, which uses more relevant features derived from geometric, radiometric, multi-echo and full-waveform attributes. Finally, Our approach is experimentally validated on the datasets from the Helsinki University of Technology, Finland and Dayekou, Zhangye City, Gansu Province, China.

I. INTRODUCTION

To acquire the accurate 3D point clouds for vegetation mapping, in this paper, the object-based vegetation extraction method is proposed using airborne LiDAR data from discrete-return TopEye sensor and full-waveform RIEGL LMS-Q560 scanner. We address the following objects. (i) Decomposition and modeling of waveform profiles by extensible kernel library using optimization technique; (ii) A pre-segmentation by the probability density clustering for the subsequent segment-based SVM classifier; (iii) Extraction of relevant features from both full-waveform backscattered amplitude profiles and discrete point clouds for segment

features calculation and (iv) Hierarchical object-based classification framework to extract vegetation point clouds using these relevant segment features.

II. MATERIALS

A. Study areas

Two airborne LiDAR datasets of Helsinki (Fig. 1a) and Dayekou (Fig. 1b) were used to evaluate the robustness of the proposed approach.

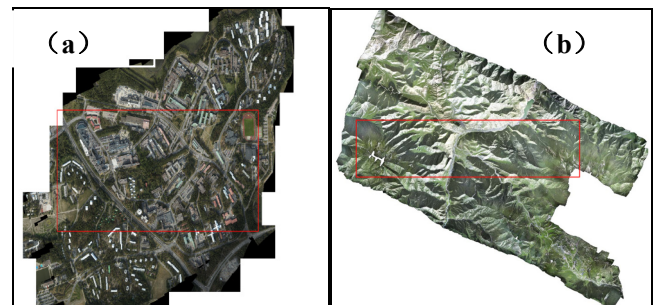


Fig1. Aerial image of the study area in (a) Helsinki and (b) Dayekou

B. Data sets

The discrete-return TopEye instrument system was used to conduct the Laser campaigns of Helsinki University of Technology in September 2002. It can only simultaneously acquire the first and last pulse point clouds and the helicopter-borne TopEye system (wavelength of 1064 nm, maximum scan angle $\pm 20^\circ$) was used to collect laser data at flying altitudes of 200 m and 550 m.

For the other study area of Dayekou, the full-waveform data with the coordinate system of the UTM/WGS 84 at the zone of 32 was used in this paper. It were captured by Y-12 airplane, which carried the LiteMapper 5600 full-waveform airborne LiDAR system at 1GHz frequently sampling rate in June 2008. The LiteMapper system adopted in this paper used a RIEGL LMS-Q560 laser scanner with near-infrared (1550 nm) laser pulses and a transmitted pulse width of 4 ns. It has a laser beam divergence angle of 0.5 mrd, which produces a footprint diameter of approximately 0.38 m on the target at nadir. The laser scanning pulse rate was 50 KHz and the maximum scan angle for data set was $\pm 22.5^\circ$ from nadir.

III. METHODOLOGY

A. Full-waveform decomposition and modeling techniques

(1) Savitzky-Golay filtering

As shown in Fig. 2, the raw backscattered profile includes actual signal and noise. To uncover the regular pattern and provide the reliable signal for calculating robust initial parameters in full-waveform decomposition and modeling process, the Savitzky-Golay (SG) smoothing filter (Savitzky *et al.*, 1964) is selected to smooth the equally time spaced full-waveform signals.

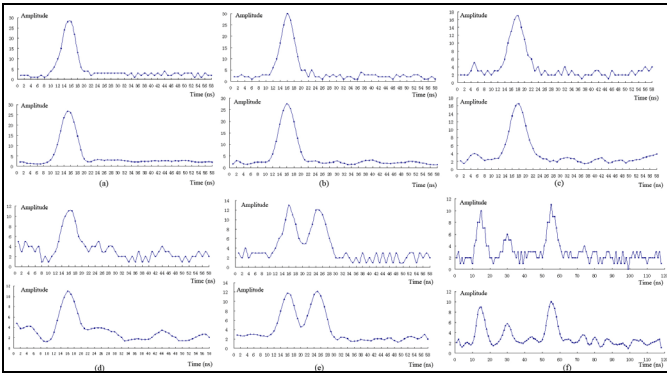


Fig. 2 Savitzky-Golay (SG) smoothing for some typical full-waveform backscattering pulses.

(2) Full-waveform decomposition and modeling

The waveform airborne backscatter signal is composed of points uniformly spaced $(x_i, y_i)_{i=1, \dots, N}$ sampled at 1 GHz for our Riegl LMS-Q560 point clouds, and the energy function is

described as:

$$\theta^* = \arg \min_{\theta} \frac{1}{N-p} \sum_{i=1}^N (y_i - \sum_{j=1}^n P_j(x_i, \theta) - \varepsilon) \quad (1)$$

where N is the number of samples; n is the number of components, representing the targets located within the travel path; p is the number of parameters of the fitting functions, and $P_j(x_i, \theta)$ represents the given kernel function. Three

kernel functions are used in this paper: (i) the Gaussian and general Gaussian kernels are used to process symmetrical backscattered echoes; (ii) the Nakagami kernels are employed to process left-skewed or right-skewed echoes.

Since the composition of kernels is varied, the traditional Gaussian-Newton or Levenberg-Marquardt algorithm cannot solve the above non-convex energy function. To deal with this problem, the reversible jump Markov chain Monte Carlo (MCMC) sampler (Hastings, 1970) coupled with simulated annealing are used to find the global minimum. As shown in Fig. 3, The typical full-waveform backscattering pulses are modeled by the above proposed method.

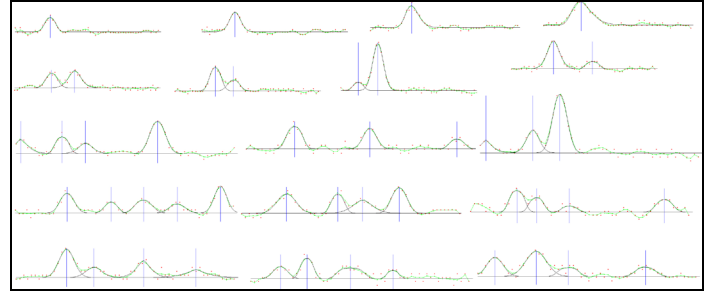


Fig. 3 Results of typical full-waveform fitting on Dayekou airborne LiDAR pulses. The red points denote the raw digitalized backscatter signals; The green and black profiles indicate the smoothed signals and the modeled backscattered signals, respectively.

(3) Generation of three-dimensional point clouds

When the optimal location of each backscattered echo T_j is obtained, the corresponding discrete point clouds X_j are analyzed by:

$$X_j = X_{start} + C(T_j - T_{start})d_{start} \quad (j = 1, \dots, n) \quad (2)$$

where X_{start} , d_{start} and T_{start} are the first sample of start pulse waveform, the emitted laser pulse direction, and the start

time of the waveform, respectively; n is the number of detected targets or components per emitter laser pulse; C is the speed of light.

B. Pre-segmentation

Object-based classification approach has already proven to be a high suitability for pixel classification. In this section, the pre-segmentation method (Poullis *et al.*, 2009) based on probability density clustering is proposed to segment discrete point clouds, and the pre-segmentation results are prepared for the subsequent segment-based SVM classifier. The pre-segmentation result is shown in Fig. 4.

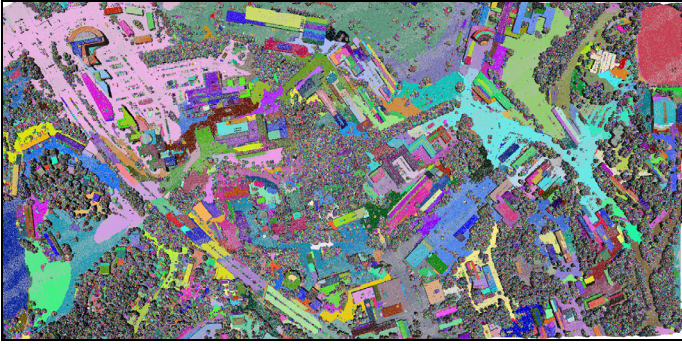


Fig. 4. Pre-segmentation results based on probability density clustering. Note that the colors are reused and may appear in different regions.

C. Extraction attributes from full-waveform profiles

Through the Eq. (1), the optimal T_j , A_j and σ_j of each backscatter echo j are obtained. The parameter A_j should be corrected to eliminate the fluctuation effects of the emitted power E , the incidence angle α and the range R . The corrected procedure is described as:

$$A_j' = \frac{A_j}{\alpha} \frac{A_{mean}}{A_{current}} \frac{R^2}{R_s^2} \quad (3)$$

where A_{mean} is the average amplitude value of all emitted pulses and $A_{current}$ is the amplitude of the emitted pulse of the current peak. R , R_s and α are the range between the current target and the sensor, a standard range for the whole survey area and the incident angle between the laser beam and the estimated local plane, respectively. The full width at half maximum (FWHM) echo W_j can be inferred by:

$$W_j = 2\sqrt{2 \ln 2} \sigma_j \quad (4)$$

Based on the radar equation, the “apparent” cross-section σ^j of each detected backscatter echo j derived by Wagner *et al.* (2006), which is defined as:

$$\sigma^j = C_{cal} R^4 A_j \sigma_j \quad (5)$$

where C_{cal} is the calibration constant, which is calculated by the process of Lehner and Briese (2010) where a portable reflectometer and spectralon targets are used to estimate calibration constant of in situ radiometric reference targets (*e.g.*, asphalt areas close to nadir view for each LiDAR strips). R is the range from the sensor to the target.

Furthermore, σ^0 is the cross-section normalized by the illuminated area s_j [$m^2 m^{-2}$], which is described as:

$$\sigma^0 = \frac{\sigma^j}{s_j} \quad (6)$$

The used of σ^0 has advantages that measures of radar system with different spatial resolution can be easily compared, when σ^j increases in general with s_j . However, when α is changed, the corresponding illuminated area s_j is also changed, so the cross-section σ^j is also related to the incoming beam. The backscatter coefficient γ is the cross-section normalized by the incoming beam and described as:

$$\gamma = \frac{4\sigma^j}{\pi R^2 \beta^2} \quad (7)$$

When the reflected target is an area-extend targets, *i.e.*, the size is larger than the footprint size of the sensor, the γ is also equal to Eq. (8), which can be considered as σ^0 corrected by incidence angle α .

$$\gamma = \frac{\sigma^j}{s_j \cos \alpha} \quad (8)$$

The four full-waveform attributes (*i.e.*, echo width W , backscatter cross-section σ , backscatter cross-section per illuminated area σ^0 and backscatter coefficient γ) derived from the full-waveform airborne LiDAR data are referred to as radiometric information.

D. Extraction features from discrete point clouds

In this section, the radiometric, Height-based, Plane-based,

Eigenvalue-based and multi-echo features are extracted from discrete airborne LiDAR point clouds. For more details of feature definition, please refer to the related paper (Mallet *et al.*, 2011).

IV. CLASSIFICATION

In this section, non-parametric method, *i.e.*, SVM classifier is employed to classify the segments. It performs a robust non-linear classification of samples using the diversity kernel functions with a small number of parameters, and can effectively avoid over-fitting and under-fitting problems during learning from samples. As shown in Figs. 5 and 6, the accurate vegetation points are extracted from Finland and Dayekou data sets.

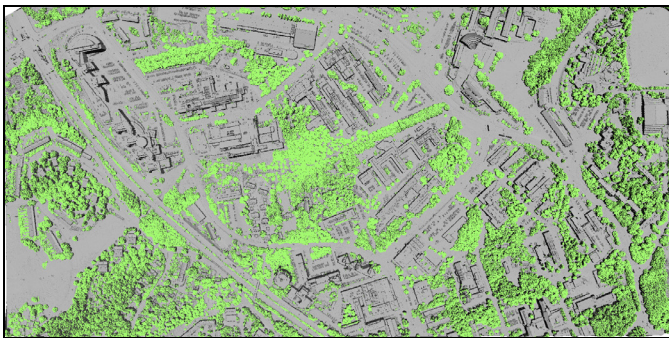


Fig. 5. The classification results of the Helsinki dataset.

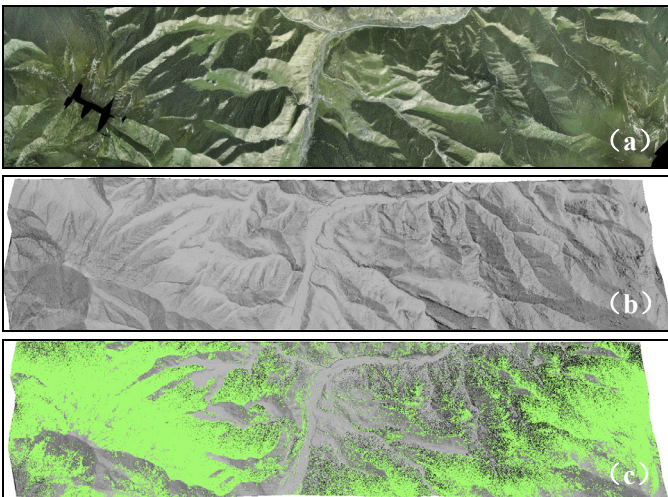


Fig. 6. The classification results of the Dayekou dataset. (a) The multispectral ortho-image. (b) The generated DEM. (c) The extracted vegetation points (light green color) are overlaid on their digital surface model.

V. CONCLUSION

The segment-based classification algorithm exhibits more significant features and robust classification than point-wise or pixel-wise classification. The combination of full-waveform attributes and geometrical features derived from discrete point clouds can significantly improve the accurate vegetation mapping. In our further research, the full-waveform, LiDAR data will be employed to acquire more plentiful information that is based on a radiation mechanism. Additionally, for high density point clouds, vegetation structure models will be integrated into our future work for better vegetation extraction.

ACKNOWLEDGEMENT

We are grateful to the editors and reviewers for their valuable comments and suggestions which have helped us improve the context and presentation of the paper. The study is supported by National Natural Science Foundation of China (No. 41301521).

REFERENCES

- [1] Savitzky, A., Golay, M.J.E., 1964. Smoothing and differentiation of data by simplified least squares procedures. *Analytical chemistry*, 36(8):1627-1639.
- [2] Hastings, W. K., 1970. Monte Carlo sampling methods using Markov chains and their applications, *Biometrika*, 57(1):97-109.
- [3] Poullis, Charalambos You, Suya, 2009. Automatic reconstruction of cities from remote sensor data. *IEEE Conference on Computer Vision and Pattern Recognition*, 2775-2782.
- [4] Wagner, W., Ullrich, A., Ducic, V., Melzer, T., Studnicka, N., 2006. Gaussian decomposition and calibration of a novel small-footprint full-waveform digitising airborne laser scanner. *ISPRS Journal of Photogrammetry and Remote Sensing*, 60(2):100-112.
- [5] Lehner, H., Brese, C., 2010. Radiometric calibration of full-waveform airborne laser scanning data based on natural surfaces. *International Archives of Photogrammetry Remote Sensing and Spatial Information Sciences*. XXXVIII, part7B, 360-365.
- [6] Mallet, C., Bretar, F., Roux, M., Soergel, U., Heipke, C., 2011. Relevance assessment of full-waveform lidar data for urban area classification. *ISPRS Journal of Photogrammetry and Remote Sensing*, 66(6): 71-84.

Extraction and Analysis of Slope, Slope Length, and LS for National Soil Erosion Inventory in China

Yang, Q. K.^{1,2}, Wang, C. M.¹, Guo, M. H.², Zhao, M. D.¹,
Wang, L.¹, Liu, Y. M.¹, Li, R.²

Sciences and Ministry of Water Resources,
Yangling, Shaanx, China)

(1. College of Urban and Environment, Northwest University, Xi'an, Shaanxi, China; 2. Institute of Soil and Water Conservation, Chinese Academy of

Abstract—In order to meet the demand of topographic parameters for national soil erosion inventory and mapping, hydrologically correct DEMs (Hc-DEMs in short) with 25m resolution for China have been generated with more than 21000 map sheets of 1:50,000 topographic maps (using contours, spot heights, and part of the streams), primary topographic parameters, including slope, slope length (distributed watershed slope length), and aspect, have been extracted, then a compound parameter, slope length factor (LS), has been calculated based on the fundamental principles of soil erosion and geomorphometry. All the parameters have been analysis, and the results showed that: (1) DEMs representing the terrain shape accurately and correctly, with some preprocessing, and following certain procedures, are base and prerequisite for the extracting of slope, distributed watershed slope length, aspect and calculating of LS (figure 1). (2) Hc-DEMs with 25m resolution generated in this project represent the topographical features of the country, and the parameters, including slope degree, distributed watershed slope length, and aspect, are consistent with general principles and regular understanding of erosional geomorphology (figure 2). (3) It is possible for all the parameters to be extracted and calculated based on the DEM with standard quadrangle DEM datasets (1.5°×1.0° of 1:250,000). But the DEM must be extended the boundary out for some distance for extracting of distributed watershed slope length; the distances at least are 3.8 km and 2.8 km for gentle and steep terrain area respectively. (4) Some local scale characteristics and also large scale differentiation laws for themes of slope and distributed watershed slope length can be identified in China. The slope degree is steeper in the mountainous area, hilly areas (especially in loess hill of northwestern China, red earth hills of southern China), and transitional areas among three terrain ladders. The distributed watershed slope length is longer in gentle hills, mountains in Hengduan mountain area of southwest China, and centre area of Qinghai-Tibet Plateau (figure 3 and figure 4, and table 1). (5) Generally speaking, the calculation result of LS factor is influenced by the slope and distributed watershed slope length synchronously. But it is much more influenced by the slope degree. As result, LS is basically consistent with the slope, and similar to slope, in the geo-spatial pattern and distribution in China (figure 5, figure 6). This paper also proposes some problems to be further researched, including: resolution of DEMs of representative areas, analysis and assessment of the quality of the

slope and distributed watershed slope length datasets, scaling effects of slope, distributed watershed slope length and LS factor, analysis of factors influencing on extraction and calculation of LS factor, applicability of the parameters in soil erosion assessment and mapping, methodologies for making thematic maps for slope, distributed watershed slope length, aspect and LS factor for Chin at small map scale (1:4 million).

Key words—soil erosion; slope degree; slope length; LS factor; geomorphometry

1 INTRODUCTION

The fourth national soil erosion survey is now ongoing. The Chinese Soil Loess Equation (CSLE)^[1] is used in the water erosion assessment, in which the LS factor is needed. There are series of researches on LS factor^[2-5]. However, there is few researches on LS factor in large extent (larger watershed or national scale) and with relatively high resolution source data. In this paper, the authors talked about some questions in the extraction and analysis on LS factor in Chinese soil erosion survey.

2 METHOD

2.1 Base data

In this paper the base data included DEMs all over China which was built based on 1:50000 topographic maps. And the layers of contours, spot heights, and streams were used in the DEM generations. There were more than 22000 map-sheets in total. And the topographic maps had been checked before building DEMs.

2.2 Calculation of terrain parameters

Slope degree and aspect were calculated in ARCGIS9.3 using slope and aspect functions. Slope length was calculated

based on runoff cumulative method proposed by Hickey^[7] and the software developed by the authors^[8-9]. The LS factor was calculated based on functions proposed by Liu baoyuan^[10-12].

2.3 Mapping and analysis

Mapping about slope degree, slope length and LS factor were designed and mapped based on 25m resolution data talked above.

3 RESULTS AND ANALYSIS

3.1 Presentation of erode terrain surface

DEMs were built using the software ANUDEM^[13-14] in this paper. The technical route is as Fig.1. DEMs built using this method are able to present varied types of terrain in China scientifically and accurately. The DEMs presentation of terrain is accordance with field survey and reported by references^[15] (Fig.2).

(Fig.1 and Fig.2 near here)

3.2 Micro characteristics of terrain parameters

The microcosmic characteristics of slope degree, slope length and LS factor were analyzed and the result shows that: Slope degree is smaller in undulated hills in the northeast of China, and greater in hilly red soil region of south-east of China and purple soil hilly area of Sichuan Basin. In Loess hilly areas, it's steeper below the gully edge line and flatter in the upward areas of the line (Fig.3 and Tab.1).

(Fig.3 and Tab.1 near here)

Slope length increased from local high point downward along flow path. In the view of small watershed, slope length increased from waterline downward, which is accordance with the extraction principle of slope length (Fig.4 and Tab.1).

(Fig.4 near here)

The surface of LS factor is influenced both by slope degree and slope length, but the influence of slope degree is greater than slope length (Fig.5).

3.3 Macro characteristics of terrain parameters

There was obvious macro characteristics of terrain parameters (including slope degree, slope length and LS factor), which were shown by small scale maps of terrain parameters (Fig.6).

(Fig.5 and Fig.6 near here)

The steep areas in China distribute in Hengduan Mountains, Qinling Mountains, mountains in east of Sichuan Province, Northern Rock Mountains, Liaodong Peninsula, Hilly Red Soil Region of South-east of China and Loess Hilly areas. These

areas are mainly located in the transition region of the Three Gradient Terrain of China.

The slope length was shown to be longer in the areas following: the undulated hills in the northeast of China, the Southwest Mountainous region (Hengduan Mountains) and the hinterland of the Qinghai-Tibet Plateau. In most of the hilly areas, such as Loess hilly areas, north hilly areas of China, purple soil hilly area of Sichuan Basin and hilly red soil region of south-east of China, the slope length is shorter.

In the areas of Southwest Mountains, hilly red soil region, Loess hilly areas and northeast of China, LS factor was relatively large. There were two kinds of reason for the large LS factor value, one is steep slope (mainly in hilly areas), and the other one is steep slope and long slope length (for example in Southwest Mountainous region).

4 CONCLUSION AND DISCUSSION

We can conclude as follows: 1) a certain processing route should be followed and pre-processing should be taken in the processes of Hydrologically correct DEMs building. 2) Hc-DEM with resolution of 25m could be used to present terrain characteristics all over China and in typical terrain areas. 3) There were both macro and micro characteristics in slope degree and slope length surface. At the national scale, slopes are steeply in the transition region of the Three Gradient Terrain of China and in hilly areas. And slope length was large in gentle hilly areas, Southwest Mountainous region and the hinterland of the Qinghai-Tibet Plateau. 4) Generally speaking, LS factor was influenced both by slope degree and slope length, but the influence of slope degree was greater, thus the national spatial pattern of LS factor was basically accordance with slope degree.

5 DISCUSSION

Some questions still needs to be answered, such as, what is the appropriate resolution in different terrain areas, some questions about the data quality assessment of slope degree and slope length, influence of scaling effect of slope degree and slope length on LS factor, slope degree and slope length maps at small scales and influence factors of LS calculation.

ACKNOWLEDGMENT (HEADING 5)

This research is supported by Natural Science Foundation of China project (Estimating Spatially Distributed Slope Length at Watershed for Soil Erosion Assessment41071188; Re-scaling of Slopes Derived from Lower Resolution DEMs for Regional Soil Erosion Modeling, 40971173), and Project of Ministry of Water Resources (SBZX-SBPC-1005)

REFERENCES

[1] Liu, B. Y., Zhang, K. L., Xie, Y. An empirical soil loss equation [M]. In: Proc of 12th ISCO [M] Beijing: Tsinghua press, 2002. 143-149.

[2] Moore, I. D., Burch, G.J. Physical basis of the length-slope factor in the Universal Soil Loss Equation [J]. Soil Science Society of America Journal, 1986, 50(5): 1294-1298.

[3] Wilson, J. P. Estimating the topographic factor in the universal soil loss equation for watersheds [J]. Journal of Soil and Water Conservation, 1986, 41(3): 179-184.

[4] Moore, I. D., Wilson, J.P. Length-slope factors for the Revised Universal Soil Loss Equation: Simplified method of estimation [J]. Journal of Soil and Water Conservation, 1992(47): 423-428.

[5] Gallant, J. Terrain scaling for the Continental Scale Soil Erosion Modeling [C]. In: Proceedings of MODSIM 2001: International Congress on Modelling and Simulation. Canberra, Australia: Modelling and Simulation Society of Australia and New Zealand: 925-930. Canberra. 2001.

[6] Yang, Q. K., McVicar, T. R., Van Niel T G, Hutchinson M F, Li L T, Zhang X P. Improving a digital elevation model by reducing source data errors and optimising interpolation algorithm parameters: an example in the Loess Plateau, China. [J]. International Journal of Applied Earth Observation and Geoinformation (JAG), 2007, 9(3): 235-246.

[7] Hickey, R., Smith, A., Jankowski, P. Slope Length Calculations from a DEM Within ARC/INFO GRID [J]. Computers, Environment and Urban Systems, 1994, 18(5): 365-380.

[8] Yang, Q. K., Guo, W. L., Zhang, H. M., et al. Method of Extracting LS Factor at Watershed Scale Based on DEM [J]. Bulletin of Soil and Water Conservation, 2010. 30(2): 203-206.

[9] Zhang, H. M., Yang, Q. K., Li, R., Research on the estimation of slope length in distributed watershed erosion, Journal of Hydraulic Engineering. 2012. 43(4): 437-443.

[10] Liu, B. Y., Nearing, M. A., Risse, L. M. Slope gradient effects on soil loss for steep slopes. [J]. 37, 1994, 6(Transactions of the ASAE): 1835-1840.

[11] Liu, B. Y., Nearing, M. A., Shi, P. J., Jia, Z. W. Slope Length Effects on Soil Loss for Steep Slopes [J]. Soil Science Society of America Journal, 2000(64): 1759-1763.

[12] Ministry of Water Resources, Guide for Soil Erosion Inventory. 2010.11, Beijing: China WaterPower Press (in Chinese)

[13] Hutchinson, M. F. A new procedure for gridding elevation and stream line data with automatic removal of spurious pits [J]. Journal of Hydrology, 1989(106): 211-232.

[14] Hutchinson, M. F. ANUDEM Version 5.2 [M]. Canberra: The Australian National University, Centre for Resource and Environmental Studies, 2010.

[15] Chinese Academy of Sciences., Regionalization of Geomorphology of China [M]. Beijing: Science Press, 1965.

Fig.1 workflow of LS extraction

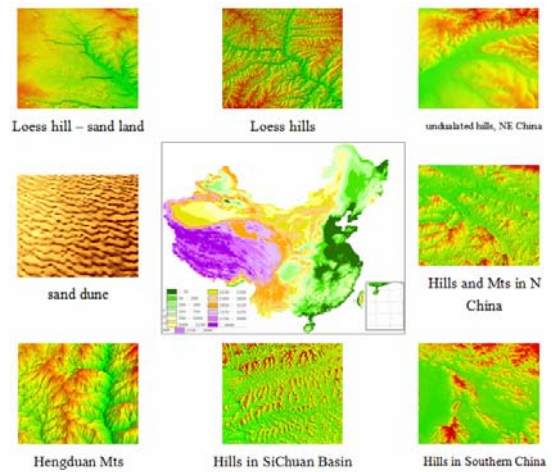


Fig.2 DEMs of China and representative areas

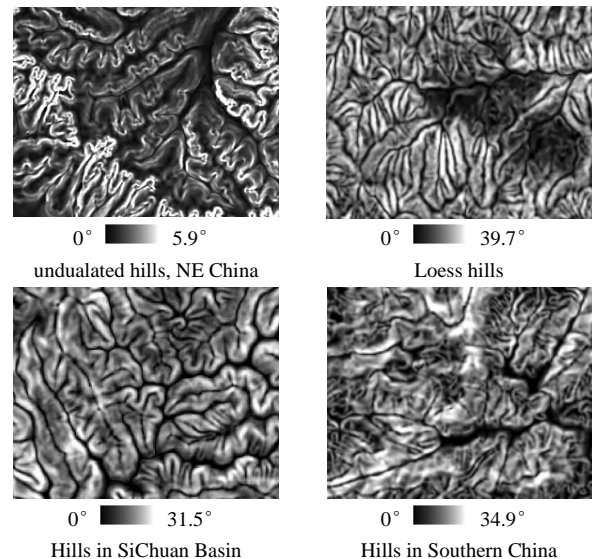
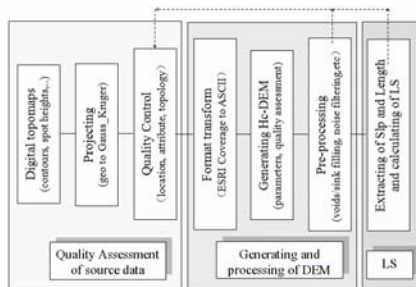


Fig. 3 microscopic characteristics of slope in main erosion area of China

Figures and Tables



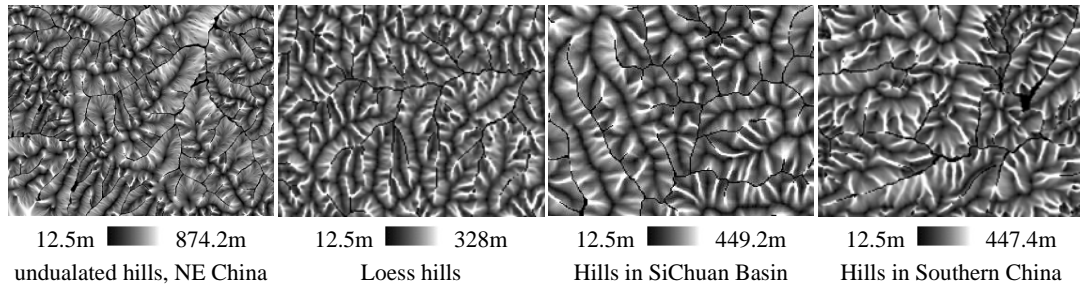


Fig. 4 microscopic characteristics of distributed slope length in main erosion area of China

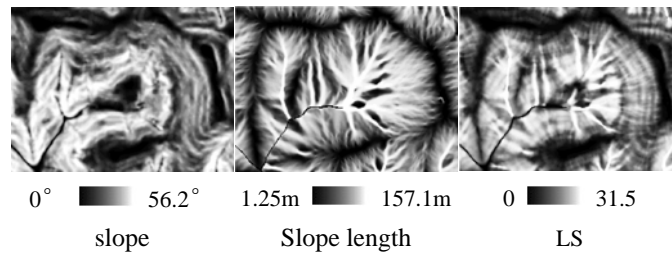


Fig. 5 spatial pattern of slope, slope length, and LS

Tab. 1 statistics of slope, slope length and LS for main erosion area of China

sites	mean	medium	max	std	mean	medium	max	std	mean	medium	max	std
	slope/degree				slope length/m				LS			
undulated hills	2.02	1.7	5.9	1.26	208.18	150	874.2	191.31	1.17	0.9	4.2	0.98
Hills in Sichuan	18.53	19.2	31.5	6.74	123.12	100	449.2	98.20	13.69	13.6	32.6	7.86
Hill in South	18.46	18.9	34.9	7.69	103.72	70.7	447.4	94.02	12.51	11.3	34.2	8.32
Loess hills	21.46	22	39.7	9.14	82.84	67.6	328	67.90	13.87	13.1	35.1	8.60

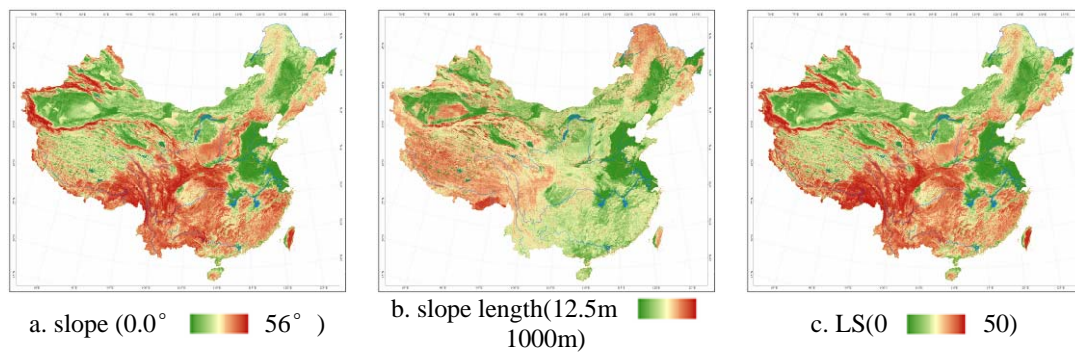


Fig. 6 Maps of topographic parameters, China

Landscape planning of route-based visibility analysis

Song Xiaodong

Key Laboratory of Virtual Geographic Environment (Nanjing Normal University), Ministry of Education
Nanjing, China
E-mail: xdsong@issas.ac.cn

Zhang Gang

Key Laboratory of Virtual Geographic Environment (Nanjing Normal University), Ministry of Education
Nanjing, China
E-mail: zhanggang_625@qq.com

Abstract—Landscape scenery is an extremely important resource not only for tourism but also for the quality of life. Hence there is a need to classify and manage landscapes. This paper shows how viewshed analysis based on the mobile viewer can be used to evaluate a route and provides a method for assessing the landscape planning of highway. Bresenham algorithm is adopted to select the candidate points to calculate the visibility. This research represents a new method toward the development of geographic information system tools which could provide visual information for making decisions for route-based visibility analysis.

Keywords—Visual resources; Viewshed; Spatial analysis; Digital Elevation Model

I. INTRODUCTION

As an essential function in GIS systems, visibility analysis provides the ability to analysis the visible areas or judges the intervisibility between two points. There are plenty of applications in various fields such as optimal path planning^[1,2], determining visual impact of quarries^[3], analyzing slow-moving landslide-affected areas^[4], wind turbine placement^[5, 6] and archaeological landscape research^[7, 8].

Landscape design of highway has been abstracted widely attentions in recent years. It is deemed that landscapes are considerably more than just what is seen and perceived. Objective visual analysis could be achieved by viewshed approach which is a widely used technique in the Geographic Information System (GIS)^[9].

By means of the quantitative analysis of inter-visibility, Montis and Caschili study the Nuraghes and landscape planning integrating viewshed and complex network analysis^[10]. Results show a hierarchical organization and not a random structure in the inter-visibility network, and the inter-visibility among these towers is plausibly connected. Previous work by Castro et al.^[11] analyzes the distance visible to a driver on the highway for the highways design and presents a corresponding procedure supported by a GIS. The preliminary experimental results show that sight distance estimation based on GIS has viability which could be similar distances compared with highway design

software. In order to link a visibility evaluation to aspects of vision and perception, Chamberlaina et al. recently adopt visual magnitude to calculate the amount of visibility by quantifying the effect of slope, aspect and distance of an area^[12]. This composite derivative could be used for route-based applications so that planners can better understand how what is visible may relate to an individual's judgment and response. Based on this work, we proposed a new description of visibility analysis of mobile viewer and take the Mount Lu as study area.

In general, as one moves away from the viewpoint a point is visible only if its elevation angle is larger than the largest elevation angle already found between the point and the viewpoint. We adopt the Xdraw algorithm to computer the viewshed^[13].

II. METHODS

A. Study area

For these considerations of specific location of Mount Lu and current traffic, this paper selects four routes as linear features for the viewshed analysis of moving points and evaluates the visible landscape on the basis of the distance between routes and the core regions of Lushan. As can be seen in Fig. 1, there are two non-motorized routes and two motorized routes.

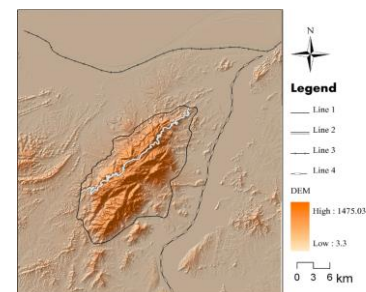


Figure 1. Four routes of Lushan area for the viewshed analysis of moving points

In order to achieve the evaluation of landscape in road planning, this section selected Mount Lu area highway as line 1 for visibility analysis. As one only route between Xiufeng Scenic Spot and Jiujiang Jiujiang City, Line 1 is located at the border of Xingzi County, Jiujiang County and Lushan District, and its length is 56.2 km. Line 2 is a mountain road through many important scenic spots of Mount Lu. For the evaluation of close landscape by visibility analysis, this road is located in the Mount Lu. Line 3 is a segment shipping line of Yangtze River route from Wuhan City to Anqing City with about 50 km length, where people could visit the northbound Mount Lu landscape over long distances. Analogously, line 4 is another segment shipping line from Poyang Lake to the confluence of Yangtze River and Poyang Lake, where the water slowly moves and the natural scenery is beautiful. The details of these four lines are shown in Tab. 1. In this table, the average distance is measured from points on each line to Great Hanyang Peak.

TABLE I. DETAILS OF FOUR ROUTES

Route	Name	Length (km)	Average distance (km)	Speed (km/h)
Line 1	circling highway of Mount Lu	80.7	21.7	50
Line 2	sightseeing route	43.2	10.8	30
Line 3	Yangtze River shipping line	50.9	31.7	25
Line 4	Poyang Lake shipping line	53.8	25.6	15

B. Notation

The moving-point visibility is defined as the viewshed computation from a viewer-point along specific path. After the calculation, we would get all the visible area from the path, which could be served as a reference to some decision support, such as traffic management, environmental planning and visual navigation.

We suppose the complexity of moving viewer is a simple point of DEM, target area is the whole Mount Lu and around areas. The moving-point visibility issue could be represented as follows:

$$f(OSh, OSt, OM, PS, PEf, CTy) \tag{1}$$

$$\begin{cases}
 OSh = \sum_{i=1}^{k1} fl + \sum_{j=1}^{k2} fb \\
 OSt = 1 \\
 s.t. \begin{cases}
 OM = \frac{f_{top}(fl)}{n} \\
 PS = ax + b \\
 PEf = 2 \\
 CTy = f_{vsh}(OM, PS)
 \end{cases}
 \end{cases} \tag{2}$$

where Osh denotes the geometrical shape, OSt is the status of movement, OM is the number mapping of viewer and target points, PS is the shape of LOS, PEf is the visual effect and the CTy is the output mode of current analysis. Because the Landscape planning does not require high-precision visibility, here the value of PEf ($PEf=2$) identified low visibility precision.

C. Viewshed calculation

The route of visibility analysis will be transformed in to a visibility set by the Bresenham Algorithm (Fig. 2). A problem should be considered is the selection of viewer-points. If the application adopts many viewer-points so as to obtain an approximate simulation of real word, the calculation time of viewshed analysis will be increased rapidly, and vice versa. Hence, an appropriate threshold should be selected to get visibility points. The candidate points should satisfy two conditions:

- (1) The Euclidean distance between candidate point and last point should be greater than $CellSize * CellSize/10$, where $CellSize$ is the resolution of DEM.
- (2) If there are at least 3 point in the 3×3 neighborhood, this point might be a turning point of the projection line of route.

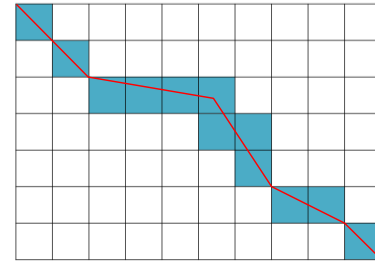


Figure 2. Selection of viewshed points

III. RESULTS

The analysis results of this method discussed above are shown in Fig. 3. The details of the visibility analysis of these four routes are summarized in Tab. 2.

TABLE II. DETAILS OF VISIBILITY ANALYSIS OF FOUR ROUTES

Route	Total visible area (km ²)	Visible area of Mount Lu (km ²)	Average elevation (m)
Line 1	1145.5	151.2	95.3
Line 2	1656.6	102.0	594.4
Line 3	306.3	87.4	10.4
Line 4	615.3	97.2	11.4

The viewshed of Line 1 covers the area around this route and some hillside of Mount Lu. In the viewshed analysis result of Line 2, it covers almost all the area of Mount Lu and the around

area, as the elevations of this route are high enough. The coverage area of Line 3 is the northern slope of Mount Lu and the coverage area of Line 4 is mainly the eastern slope.

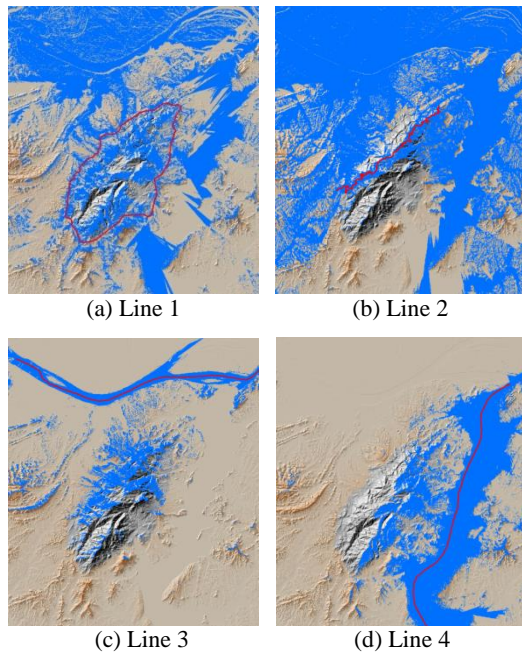


Figure 3. Viewshed analysis of four routes

In order to investigate the variation of the visible area upon Mount Lu, this paper selects fifteen points of these four routes equally (Fig. 4). The visible areas of these points are shown in Fig. 5.

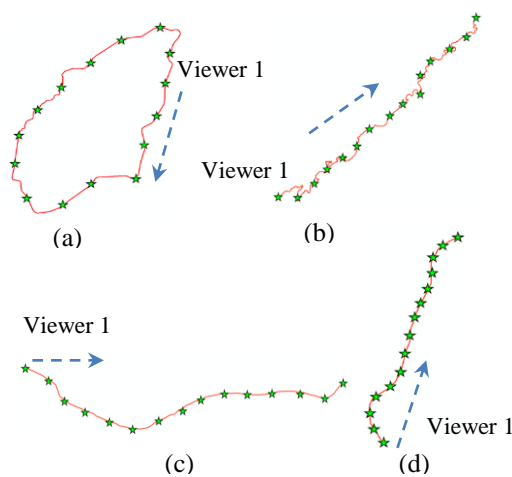


Figure 4. Fifteen viewpoints of four routes

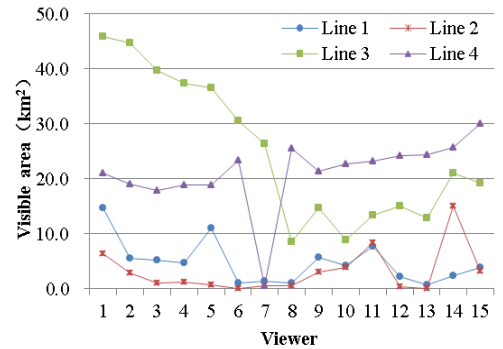


Figure 5. Line chart of fifteen mobile points

IV. CONCLUSIONS

Viewshed analysis provides a quantitative method for the visibility applications, such as landscape design and forestry. This paper proposed a new method to analysis the total visible area of routes and this method could be used in the highway design and tourism planning.

ACKNOWLEDGMENT

This work has been substantially supported by the National Natural Science Foundation of China (No. 41171298), National High Technology Research and Development Program of China (863 Program, NO. 2011AA120303) and the Foundation of Graduate Innovation Training Plan of Jiangsu Province (NO. CXZZ12_0393).

REFERENCES

- [1] Li X., He J., Liu X., "Ant intelligence for solving optimal path-covering problems with multi-objectives". *International Journal of Geographical Information Science*, 2009, 23(7): 839-857.
- [2] Choi Y., Park H. D., Sunwoo C., et al, "Multi-criteria evaluation and least-cost path analysis for optimal haulage routing of dump trucks in large scale open-pit mines". *International Journal of Geographical Information Science*, 2009, 23(12): 1541-1567.
- [3] Mouflis G. D., Gitas I. Z., Iliadou S., et al, "Assessment of the visual impact of marble quarry expansion (1984-2000) on the landscape of Thasos island, NE Greece". *Landscape and Urban Planning*, 2008, 86(1): 92-102.
- [4] Cascini L., Fornaro G., Peduto D., "Analysis at medium scale of low-resolution DInSAR data in slow-moving landslide-affected areas". *Journal of Photogrammetry and Remote Sensing*, 2009, 64(6): 598-611.
- [5] Kidner D. B., Railings P. J., Ware J. A., "Parallel processing for terrain analysis in GIS: visibility as a case study". *Geoinformatica*, 1997, 1(2): 183-207.
- [6] Devereux, C. L., Denny, M. J. H., et al., "Minimal effects of wind turbines on the distribution of wintering farmland birds". *Journal of Applied Ecology* 2008, 45, 1689-1694.
- [7] Jones E. E., "An analysis of factors influencing sixteenth and seventeenth century Haudenosaunee (Iroquois) settlement locations". *Journal of Anthropological Archaeology*, 2010, 29(1): 1-14.

- [8] Bongers J., Arkush E., Harrower M., "Landscapes of death: GIS-based analyses of chullpas in the western Lake Titicaca basin". *Journal of Archaeological Science*, 2012, 39(6): 1687-1693.
- [9] Kim Y., Rana S., Wise S., "Exploring multiple viewshed analysis using terrain features and optimization techniques". *Computers & Geosciences*, 2004, 30(9-10):1019-1032.
- [10] Montis A. De, Caschili S., "Nuraghes and landscape planning: Coupling viewshed with complex network analysis". *Landscape and Urban Planning*, 2012, 105(3): 315-324.
- [11] Castroa M., Iglesiasb L., Sánchez J. A., et al. "Sight distance analysis of highways using GIS tools". *Transportation Research Part C: Emerging Technologies*, 2011, 19(6): 997-1005.
- [12] Chamberlaina B. C. and Meitner M. J., "A route-based visibility analysis for landscape management". *Landscape and Urban Planning*, 2013 (111): 13-24.
- [13] Franklin, W. R., RAY, C.K. MEHTA, S., 1994, Geometric algorithms for siting of air defense missile batteries. Research Project for Battelle, Columbus Division, Contract Number DAAL03-86-D-0001, Delivery Order No.2756.

Extraction of drainage network from grid terrain datasets using parallel computing

Ling JIANG
Nanjing Normal
University
Nanjing, China
jinagling_xs@163.com

Guo-an TANG
Nanjing Normal
University
Nanjing, China
tangguoan@njnu.edu.cn

Kai LIU
Nanjing Normal
University
Nanjing, China
liukaigiser@163.com

Jian-yi YANG
Nanjing Normal
University
Nanjing, China
yang_gis@163.com

Abstract—Drainage-network extraction from grid terrain datasets is the essential content for hydrologic analysis, soil erosion and geomorphology. However, drainage-network extraction is normally very time-consuming using the sequential program, especially for grid terrain datasets with high resolution and large scope. This paper proposed a set of parallel algorithms to preprocess DEM, determine flow routing and delineate drainage network using cluster computers in an MPI programming model. Both depressions and flat areas could be processed by the DEM preprocessing algorithm. For using the number of upslope-dependence neighbors of a cell, the flow-routing algorithm makes flow accumulation calculation similar to a local algorithm. The experiment results shows that the proposed parallel approach to extract drainage-network performs much better than sequential algorithms and has the better parallel efficiency.

I. INTRODUCTION

As one of the most significant spatial data, digital elevation models (DEMs) are data structures representing rectangular grids of terrain data composed of cells arranged as a raster, where the value of each cell denotes the elevation of that geographic point above some base value [1]. Based on DEMs, it could mine much useful information about the morphology of a terrain surface via the technology of digital terrain analysis (DTA). The drainage network derived from DEMs is one of the key contents in DTA and has a marked influence on many fields, such as hydrologic analysis, soil erosion and geomorphology [2, 3]. Commonly, drainage-network delineation from DEMs is based on a model for representation of flow routing across the surface and between grid cells [4]. To achieve flow routing, it need to firstly determine a flow direction to each grid cell, and then calculate flow accumulations. According to the flow allocation ratio from a cell when it drains into the neighboring cells, existing flow-direction algorithms can be classified into two main types: single-flow-direction (SFD) algorithms [4, 5] and multiple-flow-direction (MFD) algorithms [6, 7]. Among all the flow-direction algorithms, the D8 algorithm proposed by O'Callaghan and Mark (1984) is widely applied for its simplicity and efficiency [8,9].

From the flow direction grid, a flow accumulation grid can be achieved, and then drainage network can be extracted by means of a threshold [4].

During drainage-network extraction for real DEMs, a DEM preprocessing algorithm is normally applied to fill in the depressions and remove the flat areas in the DEMs before calculating the flow direction [2]. These depressions and flat areas which are both from real topographic features and errors introduced during the DEM production process would cause to fail to obtain correct result for flow direction. Over the last twenty years, many DEM preprocessing algorithms have been develop to obtain a smooth DEM without any depression and flat area [10, 11]. The algorithm proposed in [11] has generally been recognized to perform better from the perspective of algorithm efficiency [12].

At present, along with the development of spatial data capture technology, DEMs have increasingly been big datasets for large scopes and high resolutions [13]. Meanwhile, drainage-network extraction is normally very time-consuming caused not only from the recursive routing algorithm, but also from the iterative DEM preprocessing algorithm. As a result, the traditional serial algorithm for calculating drainage basin is usually hard to meet users' demand of time responding for its long execution time. To speed up the execution time, some researchers have proposed parallel solution for drainage-network extraction [14-16]. These researches focused on the segment of drainage-network extraction, however, DEM preprocessing phase, by far the correction procedure and time consuming, was not processed in parallel. Wallis [17] and Song [18] proposed a parallel DEM preprocessing algorithm from the method of Planchon and Darboux, respectively. However, these parallel algorithms could only fill the sinks to flat areas, and could not remove the flat areas with a very small slope gradient.

This paper presents a design and implementation of parallelized drainage-network extraction. In this work, it adopts Planchon and Darboux's method for DEM preprocessing and the

D8 approach for flow routing to parallelize algorithms using MPI. The remainder of this paper is organized as follows. In section 2, we introduce the implementations of both serial algorithms and parallel ones. In section 3, the performance results from parallel computing are compared with sequential computing on a small cluster, and in Section 4, the main conclusions are drawn.

II. COMPUTATION ALGORITHMS FOR EXTRACTING DRAINAGE NETWORK

The drainage network is a basic feature of terrain surface. Extracting drainage network from DEMs commonly contains three steps: (1) DEM preprocessing, which fills dispersions and removes flat areas, (2) flow routing, which determines the flow direction and flow accumulation for each grid cell, and (3) drainage-network delineating, which identifies a grid cell as being part of a channel using a fixed threshold. Among them, the steps of DEM preprocessing and flow routing are main parts for drainage-network extraction. They are usually the iteration processes and very time consuming. When the first two steps implemented, a common approach for the last step is to decide a cell if its flow accumulation is greater than a fixed threshold [4].

A. DEM preprocessing

The DEM preprocessing algorithm proposed by Planchon and Darboux (called P&D algorithm for short) includes two stages: (1) the water-covering stage, which inundates a thick layer of water over the entire DEM except for the boundary, namely cells on boundary initialized values of the original DEM and the remain initialized an infinite height, and (2) the water-removing stage, which drains the excess water to ensure that for each cell, there is a path that leads to the boundary [11]. Algorithm 1 is the pseudocode of the P&D algorithm. Line 1 implements the water-covering stage and the intensive computing part of the algorithm is the water-removal stage, an iterative process (lines 2-18).

Algorithm 1 Pseudo code of sequential P&D DEM preprocessing algorithm. (zDEM and wDEM are the input DEM and the output result respectively, gap is the very small slope gradient.)

```

viod sDEMProcessing(zDEM, wDEM, gap)
1:  wDEM = Watercovering(zDEM)
2:  do
3:    finished = true
4:    for each c in wDEM do
5:      if wDEM(c) > zDEM(c) then
6:        min_neighbor ← minimum value of neighbors of c
7:        if zDEM(c) >= min_neighbor + gap then
8:          wDEM(c) = zDEM(c)
9:          finished = false
10:       else
11:         if wDEM(c) > min_neighbor + gap then
12:           wDEM(c) = min_neighbor + gap
13:           finished = false
14:       end if

```

```

15:     end if
16:   end if
17: end for
18: loop while not finished

```

B. Flow routing

The D8 (deterministic eight-node) algorithm, proposed by O’Callaghan and Mark, directs flow from each grid cell to one of eight neighbors based on slope gradient [4]. The simplest method of calculating flow direction is to determine the slope (Si) to each neighbor and set it to the direction for which Si is the greatest [3]. For each cell, there are two steps to complete the calculation: computing the maximum gradient of eight neighbors and encoding the flow direction to the cell as Figure 1.

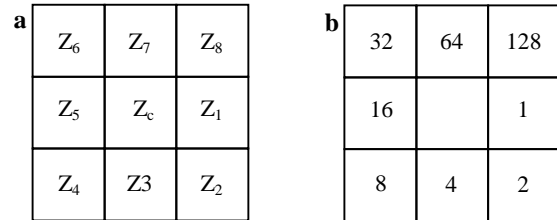


Figure 1. Three-by-three subgrid for the D8 algorithm calculation: (a) Node numbering convention. (b) Flow direction encoding convention.

Once the flow direction is achieved, it could be applied to calculate flow accumulation for each cell. For a cell, the flow accumulation means the flow of all upstream cells which flow into the cell. Assuming each cell has one unit of water, its flow accumulation is the water of all neighbors which drain into it plus their own water (i.e., one multiplies their number):

$$A(c) = n + \sum_D A(D) \quad (1)$$

where c denotes any grid cell, n is the number of neighbors flowing into c and D is each neighbor of c whose flow direction is towards c . To calculate the flow accumulation of a cell c , all cells in the region that drain into c must first be calculated [17]. It is means that a cell could achieve its flow accumulation only after all the neighbors which drain into the cell implement their calculation. Assuming m is the number of neighbors that drain into cell c , the flow accumulation of c could be calculated when m equals to 0. Along with m of each cell gradually increased to 0, the flow-accumulation calculation would be done.

The sequential flow-routing algorithm is shown in Algorithm 2. Lines 1-8 serve to achieve the flow-direction grid. In lines 9-20, an iteration process is used for flow accumulation calculation. It is no doubt that the time consuming of flow

accumulation computation is much more than that of flow direction.

Algorithm 2 Pseudo code of serial flow-routing algorithm. (wDEM is the input DEM after preprocessing, FDIR and FACC are the output flow direction and flow accumulation.)

```

viod sFlowRouting(wDEM, FDIR, FACC)
1:   for each c in wDEM do
2:     if c is not boundary of wDEM then
3:       i ← the greatest slope between c and neighbor i
4:       FDIR(c) = 2 ^ (i-1)
5:     else
6:       FDIR(c) = NODATA
7:     end if
8:   end for
9:   do
10:    finished = true
11:    for each c in FDIR do
12:      if flow accumulation of c is not calculated then
13:        m ← number of neighbors that drain into cell c
14:        if m == 0 then
15:          FACC(c) ← accumulation calculation by Eq. 1
16:          finished = false
17:        end if
18:      end if
19:    end for
20:  loop while not finished

```

C. Parallel computation

The first requirement to extract drainage network in parallel is to partition the data among processors. The paper uses a method proposed by Wallis [17], namely, striped partitioning scheme. In this approach, the input dataset is divided horizontally into *size* equal partitions to *size* processors, with any extra portion remaining being attached to the last subdomain. Each process reads in its assigned partition from a grid file, along with an attached buffer which consists of a row of cells as overlapping area from adjacent partitions above and below it. The buffers could be easily updated by obtaining information from adjoining partitions. From these buffers, each processor has access to neighboring partitions with little communication.

According to the above analysis, the parallel algorithms that integrate single program, multiple data (SPMD) are developed. Algorithm 3 and Algorithm 4 are the parallel programs for drainage-network extraction step1 and step 2 respectively, along with Algorithm 5 for step 3. In these parallel algorithms, the function *ShareBuffers()* serves to update the buffers of each partition - the last row of processor P_i is copied to the top buffer of processor P_{i+1} and the top row of processor P_{i+1} is copied to the bottom buffer of processor P_i . In the function *RingTermination()*, the final signal gets 0 if any processor is 0, in addition, the final signal gets 1 while all processors are 1, here, 0 denotes an incompleteness status. For Algorithm 3, the function *Waterremoving()* could find its implementation in lines 3-17 of

Algorithm 1. And in line 4 of Algorithm 4, the function *Flowaccumulation()* is completed as lines 10-19 in Algorithm 2.

Algorithm 3 Pseudo code of parallel P&D DEM preprocessing algorithm. (zDEM and wDEM are the input DEM and the output result respectively, gap is the very small slope gradient.)

```

viod pDEMProcessing(zDEM, wDEM, gap)
1:   wDEM = Watercovering(zDEM)
2:   do
3:     ShareBuffers(wDEM)
4:     finished = Waterremoving(zDEM, wDEM, gap)
5:     finished = RingTermination(finished)
6:   loop while not finished

```

Algorithm 4 Pseudo code of parallel flow-routing algorithm. (wDEM is the input DEM after preprocessing, FDIR and FACC are the output flow direction and flow accumulation.)

```

viod pFlowRouting(wDEM, FDIR, FACC)
1:   FDIR = Flowdirection(wDEM)
2:   do
3:     ShareBuffers(FACC)
4:     finished = Flowaccumulation(FDIR, FACC)
5:     finished = RingTermination(finished)
6:   loop while not finished

```

Algorithm 5 Pseudo code of parallel network-delineating algorithm. (FACC and DNET are the output flow accumulation and drainage network, respectively.)

```

viod pNetwork Delineating(FACC, DNET, threshold)
1:   for each c in FACC do
2:     if FACC(c) > threshold then
3:       DNET(c) = 1
4:     else
5:       DNET(c) = 0
6:     end if
7:   end for

```

III. EXPERIMENTS AND RESULTS

The parallel algorithms proposed in this paper has been implemented in C++ using MPI library and tested on a 10-node cluster linked with a Gigabit Ethernet network. These nodes have the same hardware configuration with Intel Core Quad-Core i3-2350 2.3GHz with 4 GB Memory and operating system. For comparison, the sequential algorithms were executed on a single processor within the cluster. Two datasets on a hilly area of Loess Plateau are chosen as study area, the first one consists of a large grid with size 4589 by 6832, and the second dataset consists of a small grid with size 688 by 1025. The time taken to complete the extraction task was measured using the serial algorithms for each dataset. For the parallel algorithms, the time taken to complete the task was measured using a varying number of processors. Figure 2 shows the total execution time of different processors for drainage-network extraction for the small dataset,

while Figure 3 provides the total execution time for the large dataset.

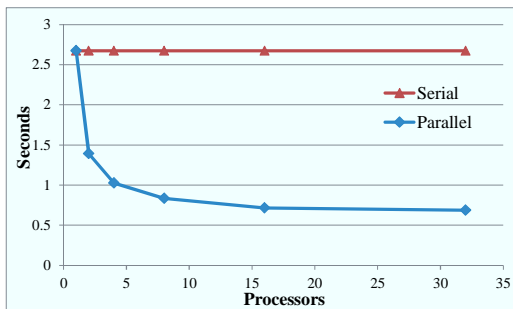


Figure 2. Time taken to complete drainage-network extraction on the small DEM

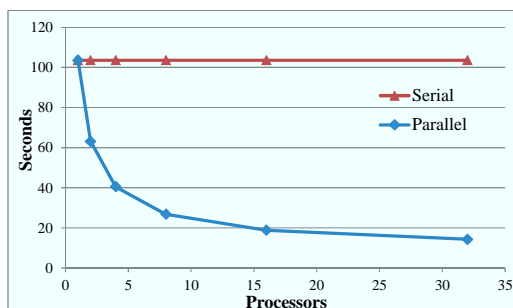


Figure 3. Time taken to complete drainage-network extraction on the large DEM

As seen in Figure 2 and Figure 3, the advantage of parallelization for drainage-network extraction is apparent with the crossover at two processors. The computing time within the two processors is obviously shorter than that of the sequential algorithm. Compared with the serial mode, the parallel results of the large and small datasets are almost identical in terms of increased performance speed, even though the data volumes of the large and small datasets are significantly different from each other. With the increase of processor number, the computational time of the parallel implementation decreases greatly with the crossover at eight processors as the increasing of communication time. Fortunately, the proportion of communication is small and the phase scaled well. The parallel algorithm of drainage-network extraction with a large dataset can achieve good performance acceleration. However, the parallel performance does not increase further when the dataset volume achieves a certain size.

IV. CONCLUSIONS

In this paper, we present a set of parallel algorithms for drainage-network extraction from grid terrain datasets. Compared with the existed algorithms, the parallel DEM preprocessing

algorithm proposed in the paper could not only fill the depressions, but also remove the flat areas. And the parallel flow routing algorithm makes flow accumulation calculation similar to a local algorithm as using the number of upslope-dependence neighbors of a cell. Furthermore, the parallel strategy is relatively simple and can be easily augmented for other similar terrain analysis parameters.

Although this research deals specifically with drainage-network extraction, the drainage-basin delineation is a directly extensional concept for further study, and could be easily implemented based on this paper.

ACKNOWLEDGMENT

This work was supported by the National High Technology Research and Development Program of China (2011AA120303), the National Natural Science Foundation of China (40930531, 41171298) and the Foundation of Graduate Innovation Plan of Jiangsu Province under Grant (CXZZ12_0391).

REFERENCES

- [1] Wilson, J.P., and Gallant, J.C., 2000. *Terrain Analysis: Principles and Applications*. John Wiley and Sons, New York.
- [2] Hengl, T., and Reuter, H.I., 2008. Developments in soil science, In: *Geomorphometry: Concepts, Software, Application*, vol.33. Elsevier, Amsterdam, Netherlands, 707pp.
- [3] Wilson, J.P., and Gallant, J.C., 2000. *Terrain Analysis: Principles and Applications*. Wiley, New York, pp. 52-55.
- [4] O'Callaghan, J.F., and Mark, D.M., 1984. The extraction of drainage networks from digital elevation data. *Computer Vision, Graphics, and Image Processing*, 28(3):323-344.
- [5] Fairfield, J., and Leymarie, P., 1991. Drainage networks from grid elevation models. *Water Resources Research*, 27(5):709-717.
- [6] Freeman, T.G., 1991. Calculating catchment area with divergent flow based on a regular grid. *Computers & Geosciences*, 17(3):413-422.
- [7] Qin, C.Z., Zhu, A.-X., Pei, T., Li, B.L., Zhou, C., and Yang, L., 2007. An adaptive approach to selecting a flow-partition exponent for a multiple-flow-direction algorithm. *International Journal of Geographical Information Science*, 21(4):443-458.
- [8] Moore, I.D., *Hydrologic Modeling and GIS*, In Gooldchild, M.F., Steyaert, L.T., Parks, B.O., Crane, M.P., Maidment, D.R., and Glendinning, S. (Eds.), 1996. *GIS and Environmental modeling: Progress and Research Issue*, GIS World Books, Fort Collins, pp.143-148.
- [9] Tarboton, D.G., Schreuders, K.A.T., Watson, D.W., and Baker, M.E., 2009. Generalized terrain-based flow analysis of digital elevation models. In: *Proceedings of the 18th World IMACS Congress and MODSIM09 International Congress on Modelling and Simulation*, Cairns, Australia, pp. 2000-2006.
- [10] Jenson, S.K., and Domingue, J.O., 1988. Extracting topographic structure from digital elevation data for geographical information system analysis. *Photogrammetric Engineering and Remote Sensing*, 4(11):1593-1600.
- [11] Planchon, O., and Darboux, F.A., 2001. fast, simple, and versatile algorithm to fill the depressions of digital elevation models. *Catena*, 46(2-3):159-176.
- [12] Wang, L., and Liu, H., 2007. An efficient method for identifying and filling surface depressions in digital elevation models for hydrologic

- analysis and modelling. *International Journal of Geographical Information Science*, 20(2):193-213.
- [13] Hengl, T., and Reuter, H.I., 2009. Geomorphometry concepts, software, applications. In: A.E. Hartemink and A.B. McBratney (Eds.), *Developments in Soil Science*, first ed. Elsevier, Amsterdam, p.765.
- [14] Gong, J., and Xie, J., 2009. Extraction of drainage networks from large terrain datasets using high throughput computing. *Computers & Geosciences*, 35(2):337-346.
- [15] Ortega, L., and Rueda, A., 2010. Parallel drainage network computation on CUDA. *Computers & Geosciences*, 36(2):171-178.
- [16] Mower, J.E., 1993. Implementing GIS procedures on parallel computers: a case study. In: *Proceedings of the Eleventh International Symposium on Computer-Assisted Cartography*, Minneapolis, MN, USA, pp.424-43.
- [17] Wallis, C., Wallace, R., Tarboton, D.G., Watson, D.W., Schreuders, K.A.T., and Tesfa, T.K., 2009. Hydrologic Terrain Processing Using Parallel Computing, 18th World IMACS/MODSIM Congress, Cairns, Australia, 13-17 July.
- [18] Song, X.D., Tang, G.A., Jiang, L., Zhang, G., and Qian, K.J., 2012. A Novel Parallel Depression Removing Algorithm for Hydrology Analysis in Digital Elevation Models, 20th International Conference on Geoinformatics, Hong Kong, China, 15-17 June.

Mass elevation effect: Concept and quantification

Baiping Zhang
Institute of Geographical Sciences
and Natural Resources Research,
Chinese Academy of Sciences
Beijing, China
zhangbp@reis.ac.cn

Abstract—Mass elevation effect (massenerhebungseffect, short as MEE in the following) was introduced more than 100 years ago by A. de Quervain to account for the observed tendency for temperature-related parameters such as tree line and snowline to occur at higher elevations in the central Alps than on their outer margins. It is a significant factor shaping the three-dimensional pattern of climate, vegetation and soil globally. But in the past, it is mostly neglected in exploring the mechanism of terrestrial complex ecosystems. We have shown that MEE contribute greatly to the actual altitudinal position of snowline and alpine timberline. It should be quantified so as to explain more clearly the geographical and ecological pattern and mechanism of the terrestrial sphere. Two approaches are put forward to quantify MEE, namely indirect and direct quantification.

I. WHAT IS MEE?

Larger mountain massifs serve as a heating surface absorbing solar radiation and transforming it to long-wave energy. In other words, the climate becomes increasingly continental from the rim to the central parts of the mountain areas, with lower precipitation and higher percentages of sunshine in the inner parts compared to the outer mountain ranges. Consequently, temperature is higher than in the free atmosphere at any given elevation, which makes the identical altitudinal belt at higher position in the interior than in the outer margins of mountain massifs. This is the so-called “Massenerhebungseffect” or “mass elevation effect” [1], sometimes called “Mountain mass effect”. This can effectively explain the large difference in elevation of altitudinal belts in similar latitudes. Some extremely high timberlines (in the central Andes and the Tibetan Plateau) are mainly the result of mass elevation effect. Without MEE, the highest timberline should not surpass 3500m above sea level in any mountains. The magnitude of MEE was considered to be closely related with the mean elevation of a mountain massif; however, what is really significant is the base elevation of the local basins or valleys in the inner parts of the massif. To a large extent, the local base elevation could represent MEE, and it has been proved to contribute a lot to the elevation of snowline and timberline [2,3].

By using the concept of MEE, many outstanding geoecological phenomena could be explained more scientifically. For example, the timberline only go upwards to about 3200m in Mt. Kilimanjaro nearly on the equator, only to about 4000m in the southern flank

of the Himalayas, while to 4600-4900m in the southeastern Tibetan Plateau. The reason is simple: the mountain base elevation (namely MEE to a large extent) is relatively low (about several hundreds of meters) in Mt. Kilimanjaro and in the southern flank of the Himalayas.

II. HOW MUCH MEE CONTRIBUTES TO THE ALTITUDINAL DISTRIBUTION OF SNOWLINE AND TIMBERLINE?

Snowline elevation is related to longitude, latitude, and mountain base elevation (MBE). According to multivariate linear regression analysis, these three factors could explain 83.5% of snowline elevation’s variation in the Tibetan plateau and its surrounding areas. Longitude, latitude, and MBE (representing MEE to some extent) contribute 16.14%, 51.64%, and 32.22%, respectively, to the variability of snowline elevation [2]. If latitude, continentality and MEE are considered the factors determining the elevation of timberline, the coefficient of determination (R^2) of the linear model is as high as 0.904, and the contribution rate of latitude, continentality and MEE to timberline elevation is 45.02% ($p = 0.000$), 6.04% ($p = 0.000$) and 48.94% ($p = 0.000$), respectively. This revealed that MEE is the primary factor in determining the elevation of timberline on continental and hemispherical scale [4]. These researches indicate that MEE has a great contribution to the altitudinal distribution of timberline and snowline. However, the contribution mentioned above is the general relative average on a macro-scale. As a significant factor shaping the ecological and geographical pattern, MEE should be quantified so as to put it into the models explaining the altitudinal distribution of mountain ecosystems [5].

III. QUANTIFICATION OF MEE

The present manuscript intends to use MEE index to represent the magnitude of MEE. We have considered two approaches to realize the quantification of MEE.

1. Indirect quantification. We suppose that the actual altitudinal position of a given altitudinal belt or ecotone (e.g., alpine timberline) is the sum of its ideal elevation and MEE index. If we know the actual

elevation and the ideal position of an altitudinal belt, then we get the MEE index at the given place or mountain slope. So, the key step is to develop an ideal distribution (MEE-free) model for altitudinal belts. It should be such: the altitudinal limits go upwards from high to low latitude, from border to central parts of highland massifs, and from shady to sunny slopes. This way we acquire MEE index from a number of locals. Then, we can expand MEE index to larger areas through appropriate interpolating and extrapolating.

Without MEE, the highest alpine timberline should not surpass 3500m above sea level, no matter in tropical or subtropical regions. This is the ceiling of any ideal models for timberline distribution. This must be taken into account when developing ideal models for global timberline distribution. We also find that warm index, hottest month mean temperature, continentality and annual mean precipitation are the four most significant factors controlling the altitudinal distribution of timberline. They must be considered in developing ideal distribution models of altitudinal belts.

2. Direct quantification. Generally, the magnitude of MEE has been considered to be related with the area, average height, inner base elevation and even the absolute height of a mountain massif. So, if we want to quantify MEE, these geomorphological factors must be involved. Our recent studies have shown that the actual magnitude is closely related with local mountain base elevation (MBE). We have shown in the study of the impact of MEE on timberline altitude that, when the MBE goes upwards of 1000m, the timberline climbs by 600-800m. Of course, MEE may vary greatly from mountain to mountain. The magnitude of MEE may show quite different for two mountains with completely same geometry but in different latitudes, for two massifs with same elevation and different volume, and for two sites at different distance from the border of the same highland [6].

A very important issue is the warmer climate in the inner parts than in the outer parts of highlands [7]. This is the real mechanism of MEE. The quantification of MEE involves the heating effect of inner highland. Fortunately, this effect could be studied with remote sensing data, especially MODIS ground surface temperature data [8], combined with measured data. The final step of quantifying MEE is to explore the relationship between MBE, inner temperature and vertical shift of altitudinal belts (mainly alpine timberline and snowline).

REFERENCES

- [1] Quervain, A. D. 1904. "Die Hebung der atmosphärischen Isothermen in der Schweizer Alpen und ihre Beziehung zu deren Höhengrenzen. Gerlands Beitr". *Geophys*, 6: 481-533.
- [2] Han, F.; Zhang, B.; Yao, Y.; Zhu, Y.; and Pang, Y.

"Mass Elevation Effect and Its Contribution to the Altitude of Snowline in the Tibetan Plateau and Surrounding Areas". *Arct. Antarct. Alp. Res.*, 2011, 43(2), 207-212.

- [3] Han, F.; Yao, Y.; Dai, S.; Wang, C.; Sun R.; Zhang, B. "Mass elevation effect and its forcing on timberline altitude". *Journal of Geographical Sciences*, 2012, 22(4), 609-616.
- [4] Zhao, F., Zhang, B., Pang, Y., Yao, Y., Han, F., Zhang, S., Qi, W. 2012. "Mass Elevation Effect and Its Contribution to the Altitude of Timberline in the Northern Hemisphere". *Acta Geographica Sinica*, 67(11): 1556-1564.
- [5] Koerner, J. P., 1998. A re-assessment of high elevation treeline positions and their explanation. *Oecologia*, 115(4): 445-459.
- [6] Zhang, B. P., Wu, H. Z., Xiao, F., Xu, J., and Zhu, Y. H., 2006. Integration of data on Chinese Mountains into a digital altitudinal belt system. *Mountain Research and Development*, 26(2): 163-171.
- [7] Barry, R. G. 2008. *Mountain Weather and Climate*. Boulder, U.S.A. University of Colorado, 65 pp.
- [8] Yao, Y. and Zhang, B. 2012. MODIS-based air temperature estimation in the southeastern Tibetan Plateau and neighboring areas. *J. Geogr. Sci.* 22(1): 1-15.

A Browser/Server-based Prototype of Heuristic Modelling Environment for Digital Terrain Analysis

Cheng-Zhi Qin¹, Jing-Chao Jiang¹, Li-Jun Zhan¹, Yan-Jun Lu¹, A-Xing Zhu^{1,2}

¹State Key Laboratory of Resources and Environmental Information System,
Institute of Geographic Sciences and Natural Resources Research, CAS
Beijing, China
qincz@lreis.ac.cn

²Department of Geography, University of Wisconsin-Madison
Madison, Wisconsin, USA

Abstract—To narrow the “digital divide” in Digital Terrain Analysis (DTA) modelling and application, we proposed a Browser/Server (B/S)-based prototype of heuristic DTA modelling environment. In this prototype, formalized DTA knowledge was used to support heuristic and visualized modelling of user’s application-specific DTA workflow. B/S structure can provide DTA users with high accessibility to DTA algorithms. Parallel DTA algorithms of computing not only local topographic attributes but also regional topographic attributes were implemented based on Message Passing Interface (MPI) to speed up the execution time of user-built DTA workflow. A case study of calculating topographic wetness index (TWI) for a low-relief catchment at fine resolution shows that employing the proposed DTA modelling environment, user can build an application-specific TWI-calculating workflow for his/her application context in a much easier way than existing DTA-assisted tools. There is less requirement of user’s DTA knowledge during the modelling process. The TWI-calculating workflow can get reasonable TWI result when the execution time of the workflow was distinctly speeded up.

INTRODUCTION

Similar to many other complex geo-spatial analyses, the practical application of Digital Terrain Analysis (DTA) is typically a non-trivial workflow-building process for users (especially for non-expert users) [1-2]. In this process, knowledge in DTA domain is necessary not only to properly organize different DTA tasks, but also to specify the algorithm with parameter-settings for each task to match the application context. However, current DTA-assisted tools often leave this to users.

Furthermore, current DTA-assisted tools are often implemented as standalone software with a serial DTA algorithm base. This makes the new-developed DTA algorithms difficult to reach the real application. And the execution of user-built DTA

workflow is often too time-consuming to support real applications, especially those with large area and fine scale.

These inconveniences in current DTA-assisted tools make a so-called “digital divide” challenge [3] in DTA modelling and application. To narrow this digital divide, we proposed an attempt on web-based heuristic modelling environment for DTA.

BASIC IDEA

Heuristic and visualized DTA modelling

A graphical user interface (GUI) similar to that of ArcGIS ModelBuilder can support users’ visualized modelling of DTA workflow. When DTA knowledge on such as the organization among tasks, the data flows, selection of algorithm for a specific task, etc. could be formalized and be saved in knowledge base, the formalized DTA knowledge could be used by an inference engine combining with the GUI to aid the non-expert users to model DTA workflow in a much easier way [4]. By this means when an initial target task is requested by user, the corresponding DTA workflow will be interactively expanded until all input data are ready. This heuristic and visualized modelling process of automatically expanding the application-specific DTA workflow from the last task to the first task is different to the traditional modelling process of user-assigning from the first task to the last task by most existing DTA-assisted tools. We believe that the heuristic and visualized modelling for DTA is more natural for non-expert users.

Browser/Server structure

Browser/Server (B/S) structure can provide DTA users with high accessibility to all kinds of DTA algorithms which are saved in algorithm base in server or are published as web services [5-6]. Even mobile terminal will be available for DTA modelling. Not

only DTA algorithms but also open DEM dataset are increasingly being released as web services. These resources could enhance the functionality of web-based DTA modelling environment.

Parallel computing of DTA algorithms

Parallel computing is widely used to speed up the execution time for time-consuming geo-computation. More and more DTA algorithms are parallelized. They can take advantage of the high parallel computation capacity of server for faster execution of user-built DTA models.

A PROTOTYPE

Currently, we prototyped a B/S-based heuristic modelling environment for DTA (<http://159.226.110.183:8080/egc/>). Two views, i.e. Google map view and modelling GUI, were provided through browser for users to view geographic information and conduct modelling process, respectively. Different types of DTA knowledge can be formalized based on semantic network or case, and then saved in the knowledge base in the server. An inference engine we developed before [4,7] uses the knowledge base to support heuristic DTA modelling process which is visualized in browser.

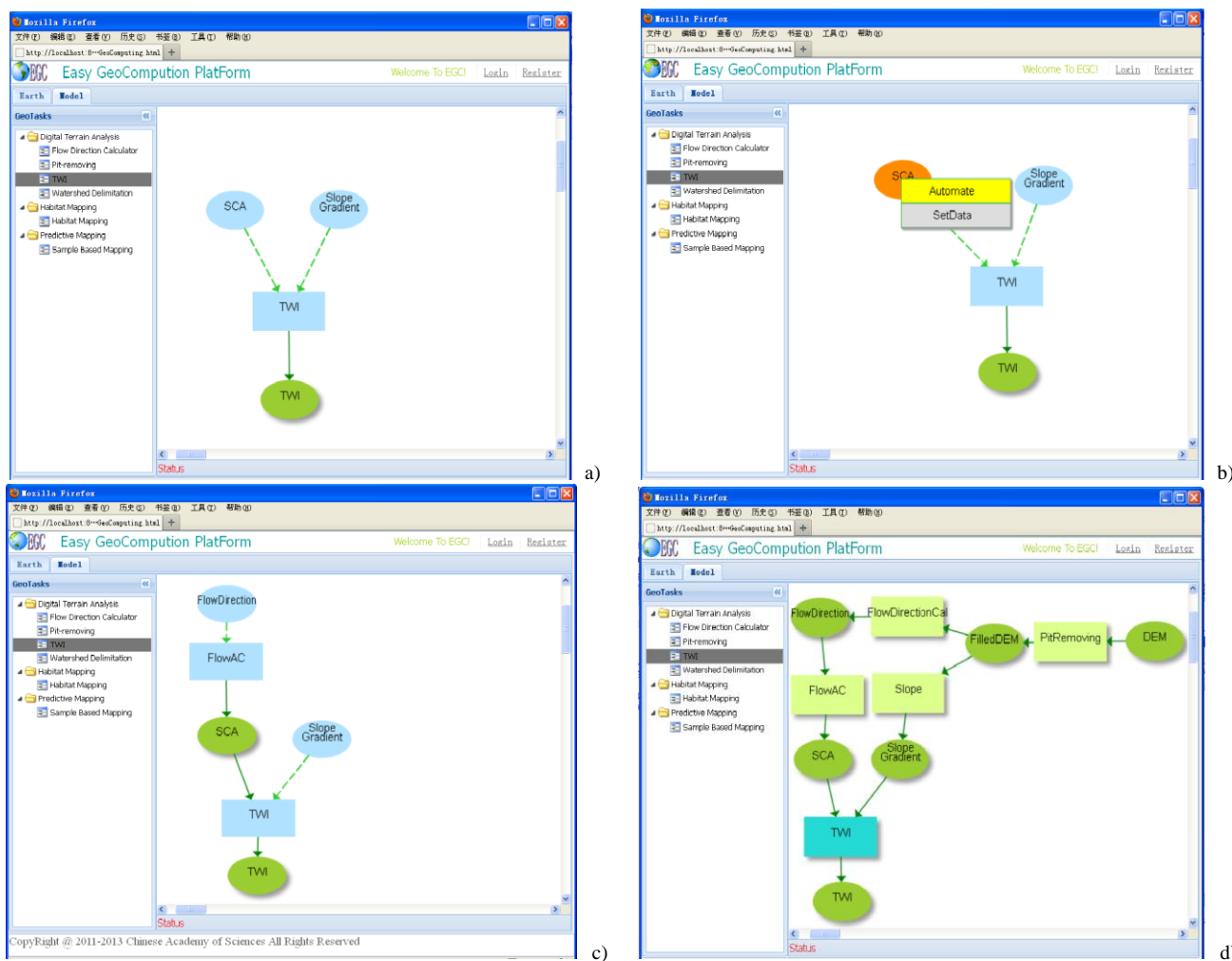


Figure 1. The heuristic and visualized modelling process of user’s TWI-calculating task with the proposed DTA modelling environment. a) Drag a TWI-calculating task into canvas panel of the modelling GUI (Light blue ellipse and dotted line means that the data source is not specified yet); b) Interaction on whether the current workflow should be extended (the ‘Automate’ option means to automatically extend current workflow by joining a task of computing the data for current data icon); c) New task is automatically added in current DTA workflow; d) A complete TWI-calculating workflow after modeling process.

Within this modelling environment, user can further manually adjust the automatically-built DTA workflow, such as adjusting the parameter value for an algorithm, or assigning another specific algorithm for a task in this DTA workflow. The resulted application-specific DTA workflow can be stored as a file with XML format, which in the future can be loaded in this modelling environment. This file also plays the role of meta data to describe how the result is produced.

Through browser, user can submit an application-specific DTA workflow to the server for execution. Currently the DTA workflow built in this modelling environment is executed in a cluster owned by our laboratory. DTA algorithm base includes not only serial algorithms implemented before, but also parallel algorithms we implemented based on Message Passing Interface (MPI). The iterative DEM-preprocessing algorithm for removing pits and flat areas in original DEM was parallelized with a new efficient parallelization strategy [8].

After execution of an application-specific DTA workflow, the executed result will be published as WMS (Web Mapping Service) with MapServer to be shown in the Google map view. User can also download the result data through the browser.

APPLICATION

Application context

For example, a user needs calculate topographic wetness index (TWI) for a low-relief catchment (about 60 km²) in northeastern China. In database only a DEM at 1-m resolution is available for this area.

Heuristic and visualized modelling process

When the user entry the prototyped B/S-based heuristic modelling environment for DTA through the browser, he/she can view both existing geographic information and consequent DTA results from a Google map view. In the other view (modelling GUI), he/she drags the TWI-calculating task into the canvas panel of the modelling GUI, not only a TWI task but also its links to the output data (TWI) and input data (two topographic attributes, i.e. slope gradient and SCA) are visualized (Fig. 1a). Because the necessary input data are not available, the inference engine instruct the current DTA workflow to be automatically expanded by adding additional tasks of calculating slope gradient and SCA (Fig. 1b, c). The similar process will be repeated until the finish of modelling user's TWI-calculating workflow, i.e. all input data needed in this workflow can be found in database or be calculated (Fig. 1d).

During this modelling process, for each task in workflow a specific algorithm with proper parameter-settings is chosen by the inference engine based on the knowledge base. For example, in this TWI-calculating application the MFD-md algorithm [9] instead of other flow direction algorithms was chosen for SCA-

calculating task for low-relief area with 1-m resolution DEM, according to the formalized knowledge (Fig. 2).

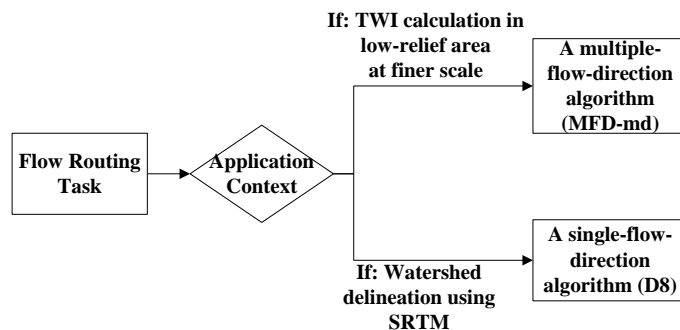


Figure 2. Selection of flow direction algorithm based on the DTA knowledge.

Execution process and result

After above modelling process, the resulted application-specific DTA workflow is ready to be submitted to the server for execution. The MPI-based parallel programs of specific DTA algorithms in this workflow were executed in cluster. The TWI result is shown in the map view, and the data is also ready for download by user (Fig. 3).

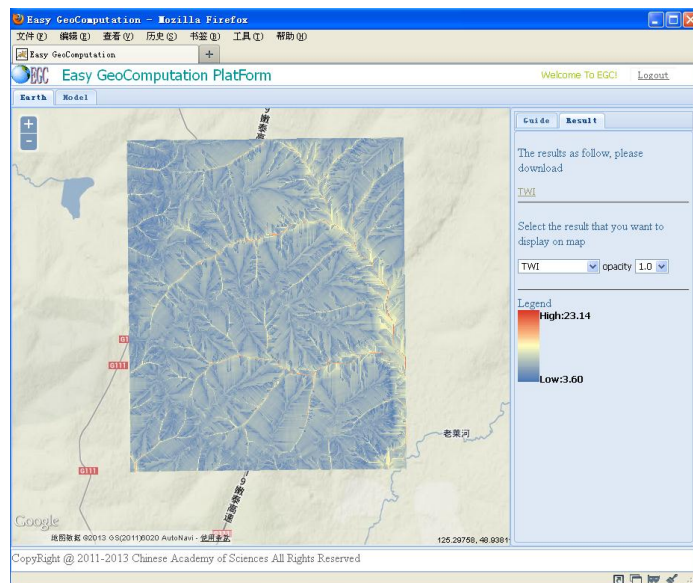


Figure 3. TWI result shown in the map view.

Discussion

By this B/S heuristic modelling environment for DTA, user can build an application-specific TWI-calculating workflow for his/her application context in a much easier way. There is less requirement of user's DTA knowledge during the modelling

process. The resulted TWI-calculating workflow can get reasonable TWI result. With the aid of parallel computing, the run time of the workflow was distinctly speeded up (measured as the speedup, i.e. (time for serial algorithm) / (time for parallel algorithm with p processes), Fig. 4).

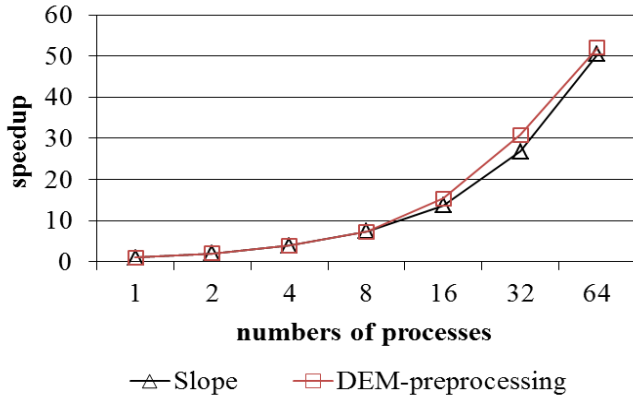


Figure 4. Speedup of the MPI-based parallel algorithms in the application-specific TWI-calculating workflow built with the proposed DTA modelling environment when were executed on an IBM SMP cluster. The cluster has 134 calculation nodes through Infiniband parallel network interconnection. Each node has 2 Intel Xeon (E5650 2.0 GHz) 6-core CPU and 24 GB DDRIII memory. The dimension of DEM is 11130 × 9320 cells. Run time (not including I/O time) for serial programs of slope gradient and DEM-preprocessing is 5.4 s and 40110 s, respectively.

ACKNOWLEDGMENTS

This study was supported by the Institute of Geographic Sciences and Natural Resources Research, CAS (No. 2011RC203), and the National High-Tech Research and Development Program of China (No. 2011AA120302).

REFERENCES

[1] Wilson, J. P., and J. C. Gallant, 2000. "Terrain Analysis: Principles and Applications", Wiley, 479 p.
 [2] Hengl, T., and H.I. Reuter (Eds), 2008. "Geomorphometry: Concepts, Software, Application", Developments in Soil Science - Volume 33, Elsevier, 765 p.
 [3] Zhu, A.-X., C.-Z. Qin, and Y.-J. Lu, 2011. "High performance computing, CyberGIS and digital divide", In 19th International Conference on Geoinformatics, June 24-26, Shanghai, China.
 [4] Qin, C.-Z., Y.-J. Lu, A.-X. Zhu, and W.-L. Qiu, 2011. "Software prototyping of a heuristic and visualized modelling environment for digital terrain analysis", In 11th International Conference on GeoComputation, July 20-22, University College London, UK.
 [5] Yue, P., L. Di, W. Yang, G. Yu, and P. Zhao, 2007. "Semantics-based automatic composition of geospatial Web service chains", Computers & Geosciences, 33(5), 649-665.

[6] Zhao, P., T. Foerster, and P. Yue, 2012. "The geoprocessing web", Computers & Geosciences, 47, 3-12.
 [7] Lu, Y.-J., C.-Z. Qin, A.-X. Zhu, and W.-L. Qiu, 2012. "Application-matching knowledge based engine for a modelling environment for digital terrain analysis", In 20th International Conference on Geoinformatics, June 15-17, Chinese University of Hong Kong, China.
 [8] Qin, C.-Z., and L. Zhan, 2012. "Parallelizing flow-accumulation calculations on Graphics Processing Units—from iterative DEM preprocessing algorithm to recursive multiple-flow-direction algorithm", Computers & Geosciences, 43, 7-16.
 [9] Qin, C.-Z., L.-L. Bao, A.-X. Zhu, X.-M. Hu, and B. Qin, 2013. "Artificial surfaces simulating complex terrain types for evaluating grid-based flow direction algorithms", International Journal of Geographical Information Science, 27, 1055-1072.

Classification and formation environment of glacial valleys based on morphometric analyses

Kosuke Naruse

Graduate School of Frontier Sciences
The University of Tokyo
Kashiwa, Japan

Takashi Oguchi

Center for Spatial Information Science
The University of Tokyo
Kashiwa, Japan
oguchi@csis.u-tokyo.ac.jp

Abstract—This paper analyzes glacial valleys in the Swiss Alps, the Himalayan Range, Yosemite, the New Zealand Southern Alps, and Patagonia using DEMs. Transverse and longitudinal profiles of four to six valleys in each region were obtained and the aspect/form ratio (*FR*) and slope of each small segment of a transverse profile were calculated. Forms of glacial valleys were evaluated using *FR* and the kurtosis, skewness, and standard deviation of slope. *FR* tends to converge into 0.28 with increasing valley size, which may correspond to the balance of vertical and lateral glacial erosion as well as a threshold slope angle for slope failure after deglaciation. The transverse profiles were classified into four types based on their geomorphometric properties: 1) U-shaped, 2) V-shaped, 3) plain, and 4) others. The most common type, other than “others” that include various forms, is U-shaped in New Zealand and Patagonia, V-shaped in the Himalayas, and plain in Yosemite and the Swiss Alps. These differences may reflect regional characteristics of snowfall, mass wasting, tectonics, and the history of glacier advances. *FR* may also indicate the past location of the glacial equilibrium line.

profiles; and 3) to discuss environmental factors affecting glacial-valley forms.

STUDY AREAS AND METHODS

The study areas are typical glaciated mountains in the Swiss Alps, the Himalayan Range, Yosemite, the New Zealand Southern Alps, and Patagonia. Four to six deep and wide glacial valleys without large existing glaciers were selected from each area for detailed morphometric analysis. Valleys that underwent glaciation during MIS2 (Last Glacial Maximum) were selected to minimize the effect of postglacial erosion. The names of the selected valleys are shown in Table I. Fig. 1 shows maps illustrating the distribution of the four glacial valleys in Patagonia, adjacent to the Hielo Patagonico Norte Icefield. Like this case, the selected valleys tend to be located near large existing glaciers.

INTRODUCTION

Glacial valleys or troughs are a major type of glacial landforms, and their transverse sections are widely known as U-shaped [1]. Although some researchers investigated the form of transverse profiles of glacial valleys, they typically focus on theoretical interpretation of U-shaped form [2, 3] or net volume of erosion [4]. Detailed studies on the actual shape of glacial valleys, including discussion on whether they are really U-shaped, have been limited to a few case studies [5, 6]. The objectives of this paper are: 1) to analyze the detailed morphometric characteristics of glacial valleys in various regions of the world using digital elevation models (DEMs); 2) to classify glacial valleys based on the statistical analysis of the shape of transverse

TABLE I. SELECTED GLACIAL VALLEYS.

Area	Valleys
Swiss Alps	Burgli, Heimritz, Kandersteg, Lauterbrunnen, Leukerbad, Schwanden
Himalaya	Lachung, Mangan, Pandim, Sikkim
Yosemite	Long Mountain, Lyell A, Lyell B, Lyell C, Tower, Yosemite
NZ Southern Alps	Dechen, Fettes, Fiordland, Manapouri, Sefton
Patagonia	San Rafael, San Valentin, Teresa, Tortel

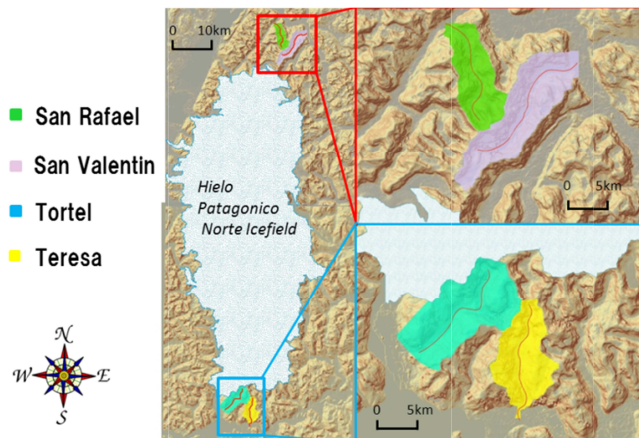


Figure 1. Maps showing the location of the four selected glacial valleys in Patagonia.

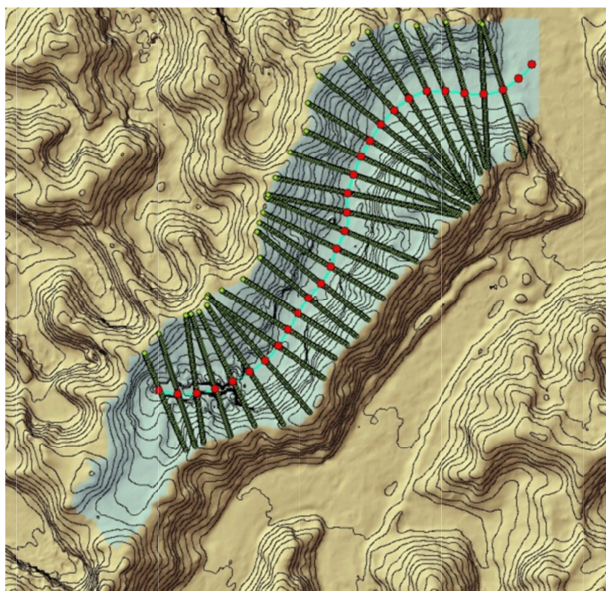


Figure 2. Morphometric measurements of the San Valentín glacial valley in Patagonia. Red points show the bottom of the valley (1 km interval). Green lines through the points show the location of obtained transverse profiles.

Longitudinal and transverse profiles of each glacial valley were obtained from the ASTER-G DEM, based on the method of Lin and Oguchi [7] (Fig. 2). Although the accuracy of the DEM is limited, it allows us to analyze the general characteristics of large and deep valleys like those we studied. Both ends of a transverse profile basically follow the drainage divide as shown in Fig. 2. However, if there is a marked break of slope below the divide, the break is used as the end. If significant topographic

modification such as the entrance of a tributary is observed along a transverse profile, the profile is not used for further analysis.

We computed the aspect/form ratio (FR ; total height/total width [4]) of each transverse profile and slope of each small segment of the profile (30 m interval in horizontal length). From the frequency distribution of the slope values, statistical moments including kurtosis (Kr), skewness (Sk), and standard deviation (Sd) were computed for each profile. Because of large valley sizes and the 30-m sampling interval, the number of data for each profile was sufficient for computing the statistical moments. Forms of glacial valleys were evaluated using these moments as well as FR . We did not deal with areas covered with existing glaciers. As noted, the selected valleys do not contain any large glaciers.

RESULTS AND DISCUSSION

Correlations between any two of the four parameters (FR , Kr , Sd and Sk) were investigated. Considering the correlations and observing the actual form of the transverse sections, we classified the sections into four types according to the combinations of the parameter values: 1) U-shaped, 2) V-shaped, 3) plain (valley width is much larger than depth), and 4) others (Table II). The “large” and “small” parameter values in Table II correspond to upper and lower 30% values of each parameter, respectively, as illustrated in Fig. 3. One valley often meets more than one conditions shown in Table II. In such a case, the type with the largest number of conditions met is regarded as the type of the valley. If none of the conditions in Table II is met, the type of the valley is “others”. In addition, if two types share the same largest number of conditions met, the type of the valley is also “others”. Fig. 4 shows typical examples of the U-shaped, V-shaped and plain types.

TABLE II. TYPES OF TRANSVERSE SECTIONS AND CORRESPONDING COMBINATIONS OF PARAMETERS.

U-shaped	V-shaped	Plain
large FR , small Kr	large FR , large Kr	small FR , large Kr
large FR , large Sk	large FR , small Sd	small FR , large Sk
large FR , large Sd	large Kr , small Sd	small FR , small Sd
small Sk , large Sd	large Kr , small Sk	large Kr , large Sk
	small Sk , small Sd	large Sk , small Sd

FR : form ratio, Kr : kurtosis of slope, Sd : standard deviation of slope, Sk : skewness of slope. large = values belonging to upper 30% of the total population. small = values belonging to lower 30%.

The classification results for all transverse profiles in the five regions revealed that the most common valley-form type other than “others”, is U-shaped in New Zealand and Patagonia, V-shaped in the Himalayas, and plain in Yosemite and the Swiss Alps (Table III). These observations may be interpreted as follows. In New Zealand, highly abundant snowfall let glaciers create typical U-shaped valleys. In the Himalayas both V-shaped and U-shaped valleys are abundant and they have high *FR* values, indicating that active glacial erosion, mass movements after deglaciation, and rapid tectonic uplift contributed to valley formation. The high proportion of the plain type in Yosemite and the Swiss Alps may reflect smaller precipitation in both regions, a low uplift rate in Yosemite, and marked glacial re-advances in the Swiss Alps that led to stepped valley-side slopes. *FR* of valleys in Patagonia tends to be small because of active lateral erosion by ice sheets; therefore U-shaped valleys there differ from those in the Himalayas and can be referred to as elongated box-shaped. The above discussion indicates that glacial valleys are not necessarily U-shaped, and the variety of their forms is due to the regional characteristics of precipitation, tectonics, glaciation histories, and post-glacial erosion. Therefore, it is important to examine the shape of valleys in relation to the effects of various factors even in glaciated areas [4].

As a common trend for all glacial valleys investigated, *FR* tends to converge into about 0.28 with increasing valley size (Fig. 5). The value may correspond to the balance of vertical and lateral glacial erosion. The value also roughly corresponds to the threshold slope angle of V-shaped valleys with frequent slope failure (ca. 35° [8]), suggesting that erosion after deglaciation also plays a role in determining the convergent value of *FR*.

TABLE III. PERCENTAGE OF THE TYPES OF TRANSVERSE SECTIONS IN EACH AREA. THE REST IS CLASSIFIED AS “OTHERS”.

	U-shaped	V-shaped	Plain
Swiss Alps	25.7% (45/174)	12.6% (22/174)	23.4% (41/174)
Himalayas	27.1% (32/117)	28.8% (34/117)	17.8% (21/117)
Yosemite	22.1% (45/203)	9.3% (19/203)	30.9% (63/203)
NZ S Alps	31.9% (45/140)	18.4% (26/140)	9.9% (14/140)
Patagonia	26.4% (23/86)	16.1% (14/86)	11.5% (10/86)

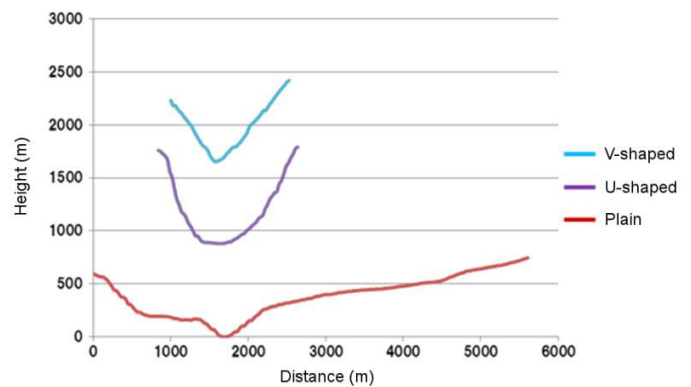


Figure 4. Typical examples of three types of valley transverse profiles.

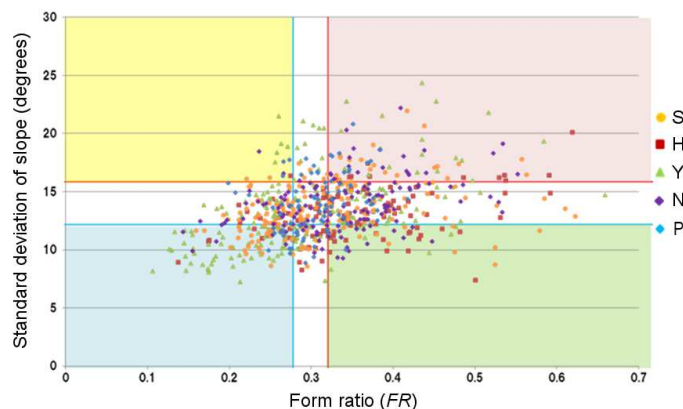


Figure 3. Relationship between the form ratio (*FR*) and standard deviation of slope (*Sd*) for all transverse sections analyzed. S: Swiss Alps. H: Himalayas. Y: Yosemite. N: New Zealand Southern Alps. P: Patagonia. Color zones are based on upper 30%, intermediate 40%, and lower 30% of each parameter values. Yellow zone: large *Sd*, small *FR*. Pink zone: large *Sd*, large *FR*. Blue zone: small *Sd*, small *FR*. Yellow-green zone: small *Sd*, large *FR*. White zone: intermediate *Sd*, intermediate *FR*.

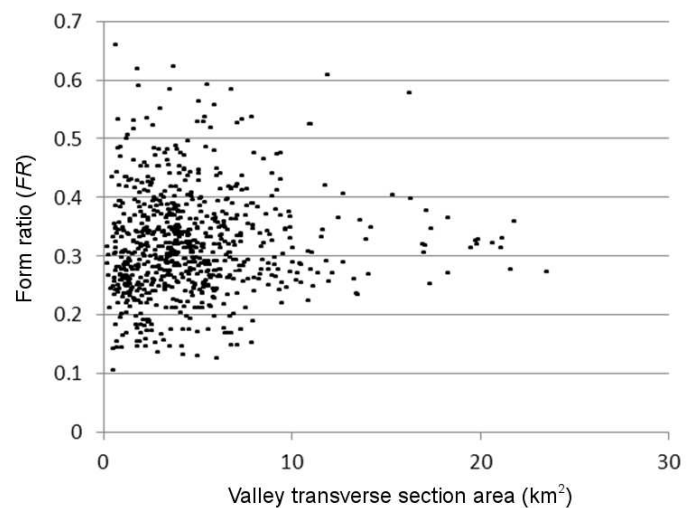


Figure 5. Relationship between the area of the valley transverse section and the form ratio (*FR*) for all transverse sections analyzed. *FR* tends to converge into ca.0.28 with increasing section area.

The correlation between the area of each transverse section and the equilibrium line altitude was also investigated. In each region, *FR* tends to change according to elevation, and reaches the maximum in an intermediate elevation in the Swiss Alps and areas around Mt. Cook in New Zealand (Fig. 6). The elevation approximately corresponds to the estimated equilibrium line altitude during the Last Glacial Maximum, suggesting a possibility of estimating the past equilibrium line from morphometric analysis of glacial valleys.

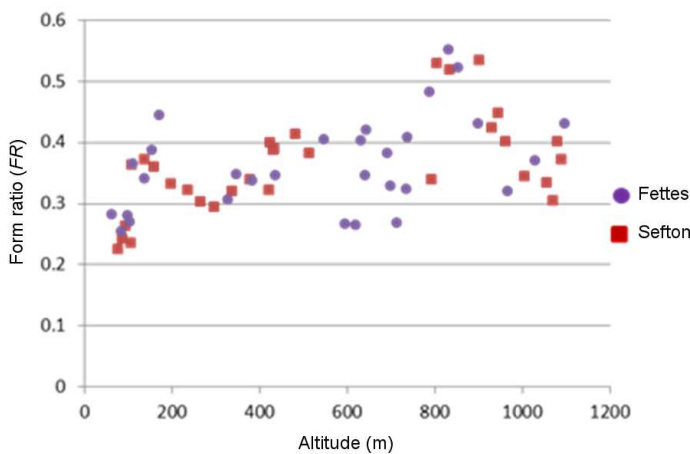


Figure 6. Relationship between altitude of the lowest point of each transverse section and the form ratio (*FR*) for the Fettes and Sefton glacial valleys near Mt. Cook, New Zealand. *FR* tends to be the highest at elevations around 900 m, which corresponds to the estimated equilibrium line altitude during the Last Glacial Maximum.

Future studies are needed to confirm the results of this paper and improve the quality of research. For example, whether a valley bottom consists of mostly bedrock or a valley fill may affect the determination of valley types, although this paper does not take it into account because of the lack of detailed information. Sampling of data also deserves future investigation. In this paper we sampled abundant transverse profiles from each valley, but it is also possible to sample less profiles per valley but from more valleys. The latter strategy may be suitable to discuss local- to meso-scale diversity of glacial valley forms.

ACKNOWLEDGMENT

We appreciate Ian Evans and Peter Guth for their constructive comments on an early draft of this paper.

REFERENCES

[1] Evans, I., 2013. "Major scale forms". In Encyclopedia of Quaternary Science, edited by S. A. Elias, Elsevier, Amsterdam, 847-864.

[2] Hirano, M., and M. Aniya, 1988. "A rational explanation of cross-profile morphology for glacial valleys and of glacial valley development". Earth Surface Processes and Landforms, 13, 707-716.

[3] Harbor, J. M., 1992. "Numerical modeling of the development of U-shaped valleys by glacial erosion". Geological Society of America Bulletin, 104, 1364-1375.

[4] Montgomery, D. R., 2002. "Valley formation by fluvial and glacial erosion". Geology, 30, 1047-1050.

[5] Li, Y., G. Liu, and Z. Cui, 2001. "Longitudinal variations in cross-section morphology along a glacier valley: a case-study from the Tien Shan, China". Journal of Glaciology, 47, 234-250

[6] Brook, M. S., M. P. Kirkbride, and B. W. Brock, 2004. "Rock strength and development of glacial valley morphology in the Scottish Highlands and Northwest Iceland". Geografiska Annaler, 86A, 225-234.

[7] Lin, Z., and T. Oguchi, 2006. "DEM analysis on longitudinal and transverse profiles of steep mountainous watersheds". Geomorphology, 78, 77-89.

[8] Oguchi, T., Z. Lin, K. Katsube, and Y.-G. Chen, 2011. "Characteristic slope angle of V-shaped valleys in humid steep mountains with frequent slope failure" In Geomorphometry 2011, edited by T. Hengl, I. S. Evans, J. P. Wilson and M. Gould, Redlands, CA, 93-96.

Floodplain delineation using cluster analysis of geomorphometric variables and class spectral statistics

Mihai Niculiță

Department of Geography
University „Alexandru Ioan Cuza” from Iași
Iași, Romania

mihai.niculita@uaic.ro

Abstract—Floodplain delineation is very important in geomorphology and hydrology. Nowadays DEMs are the most used representations of terrain and landforms. We present a method of morphological floodplain delineation from DEMs based on cluster analysis of geomorphometric variables and class spectral statistics. The method is easy to be implemented in most GIS packages and perform well on different scales and DEM sources. The precision of the delineation depends on the DEM resolution.

I. INTRODUCTION

Floodplains are morphologic sectors of a valley, flat area adjacent to the river [1], [2]. The extension of the floodplain can be hydrologically argued, as the area which is flooded [1], but in a geomorphologic morphologic interpretation, the floodplain extent is limited by the valley walls [1].

Floodplain delineation is an important aspect for river geomorphology and hydrology. The range of methods for floodplain delineation varies from the use of relative altitude [3], water inundation modelling [4], hydraulic modelling [5] or object based image analysis [6]. The floodplain delineation criteria is either pure morphologic, or associated with hydraulic thresholds. In the present case we use a morphologic approach, and not a hydrologic one, by searching for the steep change between the floodplain and the valley wall.

Our approach is to use cluster analysis, for separating landform geomorphometric clusters, for different numbers of classes, and the spectral statistic of the classes, to find the areas where, irrespective of the number of classes, the clusters are stable.

II. DATA

A. DEMs

DEM are used for the representation of terrain and landforms, becoming the de facto source for landform analysis. Some DEM data can be hydrological pre-processed in various settings [7], [8], while other has some influence of vegetation or man made features (the case of SAR DEMs).

B. Study area

We have chosen three study areas, and two DEMs. Entire Romania SRTM3-DEM at 90 m resolution, Iași county SRTM1-DEM resampled from 90 m to 30 m, and Bălțați-Sârca region 30 m DEM, interpolated using kriging from 1:25 000 topographic contours.

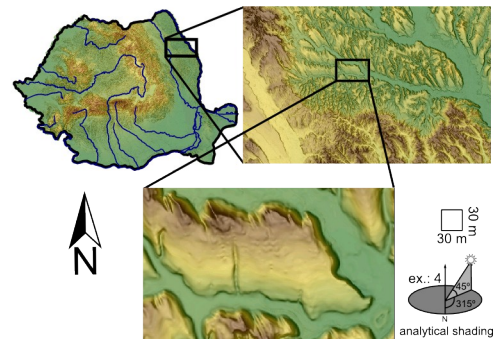


Fig. 1 Study areas

III. METHODS

A. Cluster analysis

We have used for the simplicity of the computation, a cluster analysis method implemented in SAGA GIS. This is the Hill climbing cluster algorithm [9]. The algorithm was applied for the three areas, with 5 step classes between 5 and 35 classes. The used geomorphometric variables were absolute altitude, range of altitude and the vector ruggedness measure [10] in 3x3 pixels kernel window.

B. Class spectral statistics

For the assessment of cluster stability, we have used a spectral variation measure, implemented in SAGA GIS, after the idea of [11]. This measure is the distance in the feature space, to the centroid for all cells in a specified neighborhood (3x3 pixel kernel window).

IV. RESULTS

A. Discussions

Cluster analysis methods are widely used in landform classification based on DEMs [12], [13], [14]. The cluster analysis results are specific to the study area, but the results from different extents, and data sources, can show that the clusters are morphologically stable, reflecting real landform features, as others stated [15]. While the clusters are stable, their threshold limit can vary (Fig. 2). In the present case we use the spectral distance of this variation to find the areas which does not change the cluster centroid on big feature space distances. These areas are the flat or gentle sloping areas, in which the floodplain areas appears. The delineation of the floodplains will result from the tracing of the spectral distance spikes around the small values areas.

B. Validation

Because reference data about the floodplain limit is not available, we have used cross-sections (Fig. 3) to test the validity of the method. The results (Fig. 4) show that in general the step altitude change of the valley wall bottom part is well depicted, giving spikes of big spectral distances, but there are areas where due to the gentle change, the method fail to find the change (the low terraces from the Fig. 4). This problem can be resolved in the delineation, by extrapolating the limits where the method apply.

Because of the DEM resolution, the floodplain can be depicted only for rivers with floodplain width bigger than 3 pixels.

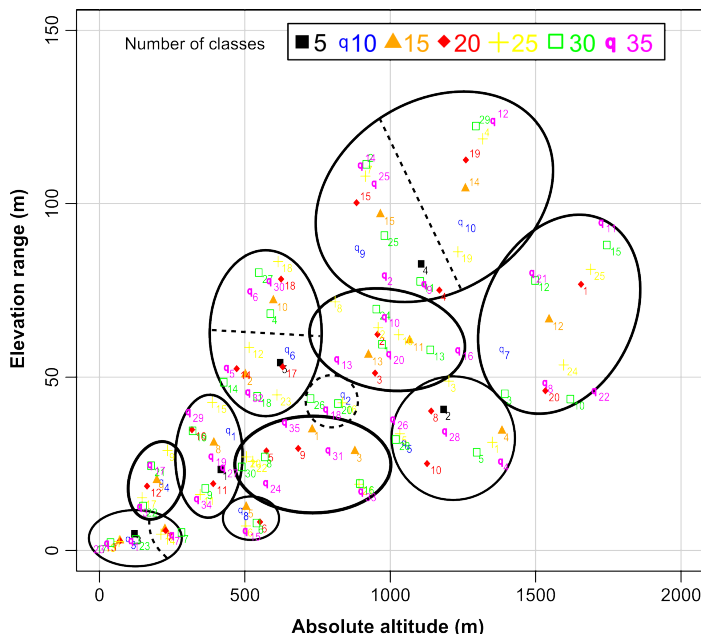


Fig. 2 Positions of the resulted clusters in a 2D feature space

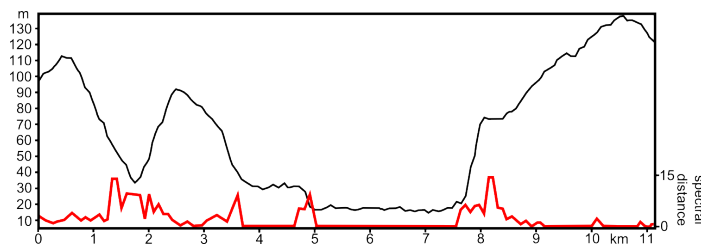


Fig. 3 Topographic cross-section on a typical floodplain site (same area from Fig. 4)

V. CONCLUSIONS

In the technical problem of morphological floodplain delineation from DEMs, we use the results of a cluster analysis of geomorphometric variables and their class spectral statistics. The strong part of the method is that is easy to be implemented in most GIS packages. The partial validation show that the method perform well on different scales and DEM sources, but this must be further evaluated with truth data, other areas, and other elevation sources.

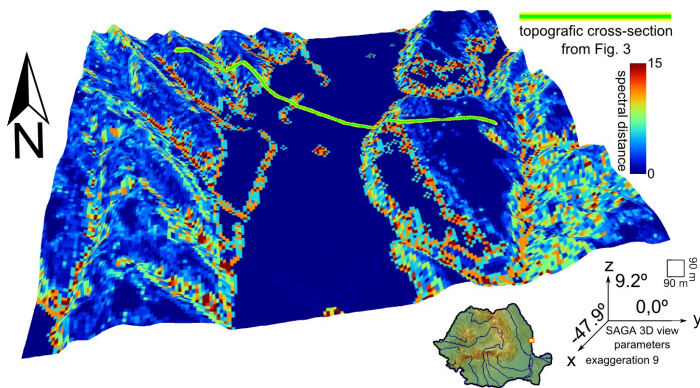


Fig. 4 Depiction of floodplain and lower terraces in Prut river valley

REFERENCES

[1] Charlton, R., 2008. "Fundamentals of fluvial geomorphology", Routledge, 234 p.

[2] Dury, G.H., 1971. "Relation of morphometry to runoff frequency", in "Introduction to fluvial processes", ed. R.J. Chorley, Methuen & Co Ltd, p. 177-188.

[3] Hartvich, F and J. Jedlicka, 2008. "Progressive increase of inputs in floodplain delineation based on the DEM: application and evaluation of the model in the catchment of the Opava River", Acta Universitatis Carolinae, Geographica, 1-2:87-104.

[4] Dodov, B.A., and E. Foufoula-Georgiou, 2006. "Floodplain morphometry extraction from a high-resolution digital elevation model: a simple algorithm for regional analysis studies" Geoscience and Remote Sensing Letters, IEEE, 3(3):410-413.

[5] Yang, J., R.D. Townsend and B. Daneshfar, 2006. "Applying the HEC-RAS model and GIS techniques in river network floodplain delineation", Canadian Journal of Civil Engineering, 33(1):19-28.

[6] Alfaya, F.A.V.S., T.G. Florenzano, and C.C.F. Barbosa, 2012. "Mapping Amazon river floodplain reach with SRTM-DE using the hand descriptor and object based image analysis", Proceedings of the 4th GEOBIA, May 7-9, 2012, Rio de Janeiro, Brazil, p. 137-140.

[7] Tate, E.C., D.R. Maidment, F. Olivera and D.J. Anderson, 2002. "Creating a terrain model for floodplain mapping", Journal of Hydrologic Engineering, 7(2):100-108.

[8] Getirana, A.C.V., M-P Bonnet, O.C. Rotunno Filho and W.J. Mansur, 2009. "Improving hydrological information acquisition from DEM processing in floodplains", Hydrological Processes, 23:502-514.

[9] Rubin, J., 1965. "Optimal classification into groups: an approach for solving the taxonomy problem", Journal of Theoretical Biology, 15(1):103-144.

[10] Sappington, J.M., K.M. Longshore, and D.B. Thoompson, 2007. "Quantifying landscape ruggedness for animal habitat analysis: a case study using bighorn sheep in the Mojave desert", Journal of Wildlife Management, 71(5):1419-1426.

[11] Palmer, M.W., P.G. Earls, B.W. Hoagland, P.S. White and T. Wohlgenuth, 2002. "Quantitative tools for perfecting species lists", Environmetrics, 13:121-137.

[12] Lagacherie, P., D.R. Cazemier, P.F.M. Van Gaans, and P.A. Burroughs, 1997. "Fuzzy k-means clustering of fields in an elementary catchment and extrapolation to a larger area", Geoderma, 77(2-4):197-216.

[13] Burroughs, P.A., P.F.M. Van Gaans and R.A. MacMillan, 2000. "High-resolution landform classification using fuzzy k-means", Fuzzy Sets and Systems, 113(1):37-52.

[14] Biosca, J.M., and J.L. Lerma, 2008. "Unsupervised robust planar segmentation of terrestrial laser scanner point clouds based on fuzzy clustering methods", ISPRS Journal of Photogrammetry and Remote Sensing, 63(1):84-98.

[15] Vilalta, R., T.F. Stepinski and M. Achari, 2007. "An efficient approach to external cluster assessment with an application to martian topography", Data Mining and Knowledge Discovery, 14(1):1-23.

Modeling hourly solar radiation over rugged terrains, based on DEM

Jie Wang, Shijiang Yan

School of Resources and Environmental Engineering
Anhui University
Hefei, China
wangjie09@lzb.ac.cn

Yuhuan Cui

School of Sciences
Anhui Agriculture University
Hefei, China
cuiyh@lzb.ac.cn

Abstract—Solar radiation is the principal energy source of the Earth's surface, it provides important data for runoff simulation and forecasting, and ecological evaluation. In this paper, a distributed hourly solar radiation model is built by combining Yang Kun clear-sky solar radiation model and digital elevation model. This model introduced the shadows - sun factor firstly, which characterizes the effect from the slope itself and the surrounding topography, then added topographic correction parameters, which make received direct solar radiation closer to the actual value to slope, and lastly introduced the sky view factor to calculate the possible scattering value from the surroundings in calculating diffuse radiation. The model was successfully used to simulate hourly instantaneous solar irradiance by a spatial resolution of 30 m, at the head of Ürümqi river, and the result suggest that: 1) the model has the high accuracy, and the determination coefficients (R^2) between simulated and measured radiation in Daxigou and Kongbingdou are 0.94 and 0.83, respectively; 2) the model is highly depend on sunshine hours, and the accuracy of simulation at Kongbingdou is less than that at Daxigou in cloudy day; 3) the model has good accuracy of simulation in clear day except the sunrise and sunset hours, and the determination coefficients between the simulated radiation values with the measured values are 0.96 and 0.89, respectively.

Keywords —rugged terrain; solar radiation; sky view factor; terrain shading

INTRODUCTION

Solar radiation provides the primary energy resources to the earth, which distribution is the basic power of the physical processes in nature, such as snow/ice melting, photosynthesis and evaporate-transpiration. Thus, it is extremely necessary to explore the solar radiation variation in the researches on hydrological and thermal regimes, land surface geographical

processes and the use of solar energy. With the rugged terrain in the mountain regions on basis of current conditions, the terrain factors of slope, aspect and hill shade by surrounding terrain varies, and the received solar energy on the land surface varies with different conditions, which causes the complex spatial distribution of solar radiation.

Taking the influence of topographical factor on the solar radiation distribution into consideration, the distributed solar radiation models based on terrain analysis were built to simulate the total solar radiation over rugged terrains since 1980s(Fu, 1983; Bonan, 1989; Dozier, 1990; Dubayah et al, 1990). Latter, the impact of surrounding terrain and weather condition on the received solar radiation considered, several methods such as amending sunshine hours (Li et al, 1999), introducing transform indexes (Zeng et al, 2008; Gu et al, 2010), sky view factor (Chen et al, 2007; Manners et al, 2011) and topographic correction index (Helbig et al, 2010), were used to improve the simulated values of distributed solar radiation models. Nevertheless, the calculated values of hillshade in the current researches exists the certain bias, due to the spatial scale of DEM and the accuracy of the measured meteorological data, and the accuracy and temporal resolution of solar radiation model needed to be improved.

DATA AND METHOD

A new hourly distributed solar radiation model over mountains is built in this paper, making use of ASTER GDEM data to amend the current Yang-Kun solar radiation model at single point under clear weather conditions. The total solar radiation is divided into the direct solar radiation and diffuse solar radiation. Shade-sunshine judgment factor is introduced into the calculation of direct solar radiation, as well as topographic correction parameter, with aim to quantify the hillshade effects of slope itself and its surrounding terrains.

Meanwhile, the parameter of sky view factor is also introduced to simulate the values of possible diffuse solar radiation which comes from nearby eight directions.

Then the meteorological variables of atmospheric pressure, air temperature, air relative humidity and sunshine hours provided by two automatic weather stations (AWS) named Daxigou and Kongbingdou (Figure 1), as well as ASTER GDEM, are collected as the input parameters of the model, and the model is used to simulate hourly instantaneous solar radiation with the resolution of 30 meters at the head of Ürümqi river basin in Xinjiang province. Lastly, the simulated values of solar radiation at AWS positions are validated against the measurements of solar radiation to assess the applicability of the model.

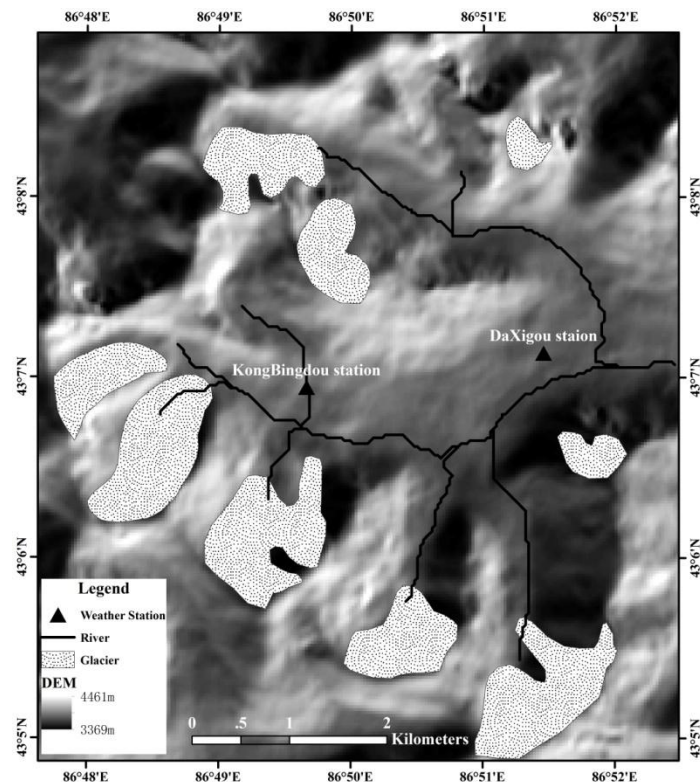


Figure 1. Locations of DaXigou station and KongBingdou station at the head of Ürümqi river basin in Xinjiang province

RESULTS

The results in this research can be shown as following: 1) the model built has the high accuracy, and the determination coefficients (R^2) between the simulated and measured values of solar radiation at Daxigou and Kongbingdou weather stations are 0.94 and 0.83, respectively, shown in Figure 2; 2) for the lack of the measured sunshine hours at Kongbingdou station, the accuracy of solar radiation simulation at this station appears less than that at Daxigou station in cloudy day, which implies that this

model is highly depend on the sunshine hours; 3) the model proves the perfect accuracy of simulation in the clear day except for the sunrise and sunset hours, with the determination coefficients(R^2) between the simulated values and the measurements at Daxigou and Kongbingdou stations are 0.96 and 0.89, the mean relative error of 2.6% and 0.8%, respectively (Shown in Figure 3). While the model performs the poor simulated values of solar radiation in the cloudy day, with the determination coefficients (R^2) between the simulations and the measurements at Daxigou and Kongbingdou stations are only 0.43 and 0.56, the mean relative error of 34.5% and 25.9%, respectively, which implies that the simulated values of the model built are strongly dependent on solar radiation in clear day and topographic correction indexes.

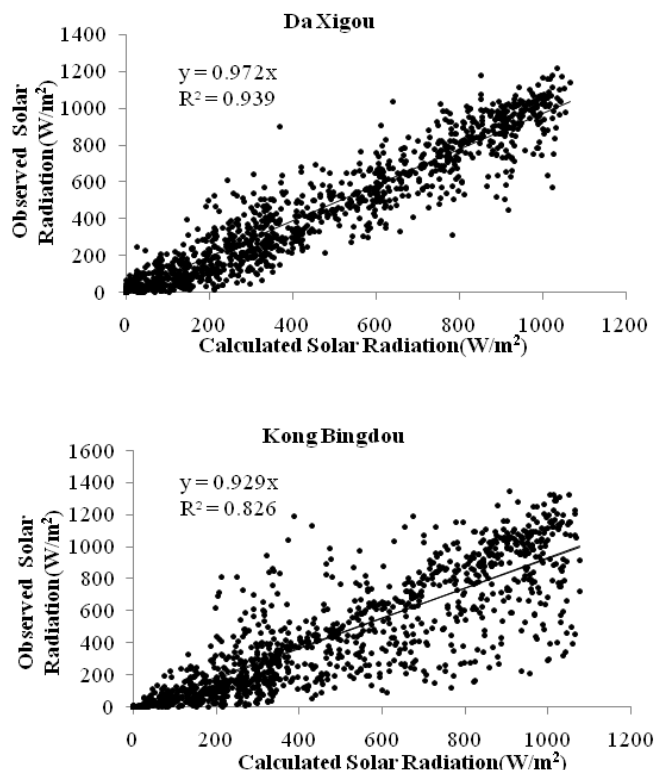


Figure 2. Relationship between the observed hourly solar radiation and the calculated series under the actual weather conditions

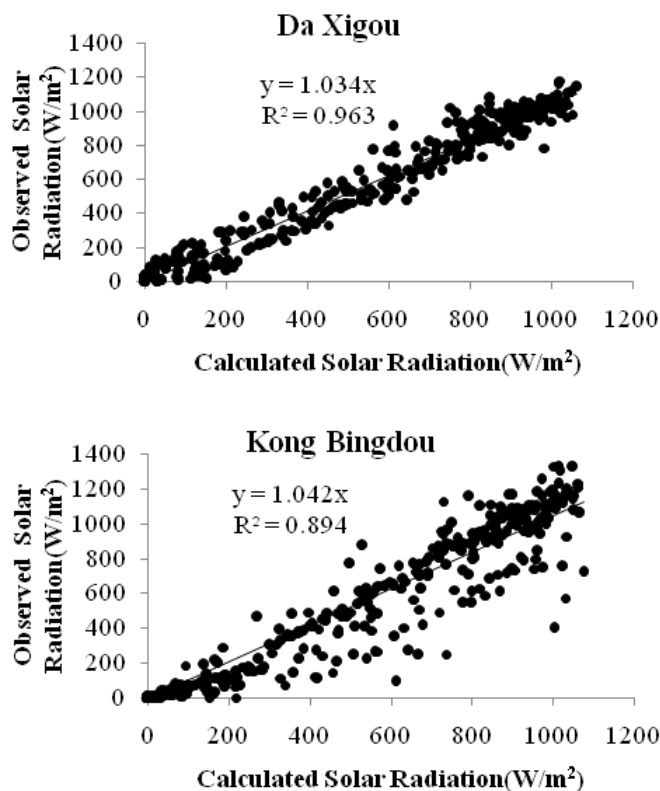


Figure 3. Relationship between the observed hourly solar radiation and the calculated series under the sunny weather conditions

PROSPECTS

Generally speaking, the distributed solar radiation model built in this paper, considering the influence of topographic factors on the received solar energy over rugged terrains, proves the high simulation of solar radiation, especially under the clear conditions. This implies that the quantification of terrain characteristic will be helpful to improve the accuracy the simulation of the physical parameters near the land surface.

ACKNOWLEDGMENT

This research is sponsored by the China National Natural Science Foundation (No.41030527) and Doctoral Research Start-up Funds Projects of Anhui University (No.32030068).

REFERENCES

[1] Bonan G B, 1989. "A computer model of the solar radiation, soil moisture, and soil thermal regime in boreal forests". *Ecological modeling*, 45: 275- 306.

[2] Chen R S, Kang E S, Ji X B, et al, 2007. "An hourly solar radiation model under actual weather and terrain conditions: A case study in Heihe river basin". *Energy*, 32: 1148-1157(In Chinese).

[3] Dozier J, Frew J, 1990. "Rapid Calculation of Terrain Parameters for Radiation Modeling from Digital Elevation Data". *IEEE, Transaction on Geoscience and Remote Sensing*, 28(5): 387-393.

[4] Dubayah R, Dozier J, Davis F W, 1990. "Topographic distribution of clear- sky radiation over the Konza Prairie, Kansas". *Water Resource Research*, 26(4): 629- 690.

[5] Gu X P, Yuan S J, Shi L, et al, 2010. "The elaborate spatial distribution of global solar radiation over complex terrains in Guizhou Plateau". *Journal of mountain science*, 28(1): 96-102(In Chinese).

[6] Helbig N, Löwe H, Mayer B, et al, 2010. "Explicit validation of a surface shortwave radiation balance model over snow-covered complex terrain". *Journal of geophysical research*, 115.

[7] Li X, Cheng G D, Chen X Z, et al, 1999. "The amelioration of solar radiation model in discretional condition". *Chinese Science Bulletin*, 44 (9): 993-998(In Chinese).

[8] Manners J, Vosper S B, Robers N, 2011. "Radiation transfer over resolved topographic features for high-resolution weather prediction". *Quarterly journal of the royal meteorological society*: 956-967.

[9] Zeng Y, Qiu X F, He Y J, et al, 2008. "Distributed modeling of diffuse solar radiation over rugged terrain of the Yellow river basin". *Chinese J. Geo phys*, 51(4): 991-998(In Chinese).

Modeling of Topographic Spatial Structures Using Geo-statistical Method

Chunmei Wang¹, Qinke Yang^{1,2*}, David Jupp³, Lei Wang¹,
Rui Li²

1. College of Urban and Environment, Northwest University, Xi'an, Shaanxi, 710127, China; 2. Institute of Soil and Water

Conservation Chinese Academy of Sciences Ministry of Water Resources, Yangling, Shaanxi, 712100, 3.CSIRO Division of Marine and Atmospheric Research, GPO Box 3023, Canberra A CT 260

Abstract: Terrain is one of the most important factors in many areas such as hydrology, geomorphology, soil erosion, and so on. Terrain factors, (such as slope, aspect, et al.) are mainly extracted from coarser resolution DEMs at regional and global scales. And terrain factors are influenced by resolution obviously. Researchers studied the relationship between terrain factors and resolution. However, most of these researches are about the relationship between statistics of terrain (for example ‘mean slope’) and resolution, and there is a lack on the mechanistic explanations about this. As we know, terrain is a combination of several scales of structures. If we want to know the mechanistic explanations about scaling effect of terrain factors, one of the most important thing is to separate these structures and then we can know which structures are most influenced by resolution. This study is mainly about this topic. In this research, the spatial structures of terrain surface is analyzed based on DEM with resolution of 10m, and the spatial frequency (lower frequency and higher frequency) is linked to the spatial structures of terrain surface. Geo-statistics method (especially semi-variogram) is used, and a model named Independent Structures Model (ISM for short) is given to model the variance of different terrain structures with different spatial frequency. The model is applied in Loess Hilly area. This result shows that: ISM is useful in the modeling of topographic spatial structures. The key parameters of the model are: number sub models, range and sill of each sub model.

Key words: DEM, Geo-statistic, semi-variogram, resolution

Terrain variables are sensitive to the resolution of DEM based. The effect of resolution on terrain variables and the models which based on terrain variables has been one of the most intensively studies [1-8]. However, it is more important to take steps back and ask “why the topographic variables are effected by resolution?”, “what kind of information have lost in the up scaling process?” If we want to answer these questions, we should absolutely know “what are the terrain spatial structures in a certain area?” then we can explore “which special frequencies were lost with resolution change?” In this paper, the authors tried to answer these questions using geostatistical analysis.

Variogram is a basic tool in geostatistical analysis. It has been used as a primary tool in many spatial studies such as Land cover [9-11], soil moisture [12] et al.

It is clear that landscape processes have a range of characteristic scales and that it is not easy to estimate (or possible) them by a single commonly defined variogram model. The different scales are important features of the landscape and need to be understood to characterize regions for purposes such as hydrology and erosion. [13]. This is also discussed by Oliver [14]. In this paper, variograms were used to explore the topographic structures represented by DEMs with two different resolutions (10m and 50m). In this paper, an “Independent Structures Model” was used to quantitatively analyze of topographic structures.

METHOD

The study area and base data

The study area locates in the Loess Hilly-Gully Region in the Loess Plateau. It is a square with side of 8.1km or an area. There is a significant watershed named JiuYuan watershed crossing this study area in a northeast-southwest direction. It is a typical Loess-hilly area with complex terrain surface and intensively soil erosion.

Hc-DEM^[15-16] (Hydrological-correct DEM) with resolution of 10m were built based on 1:50000 topomaps. The projection is Gauss_Kruger based on the Krasovsky 1940 Datum. Fig.1 shows the basic topographic of the study area.



Fig. 1 Terrain of study areas

Variograms and modeling

In this research variograms are used to measure the spatial variation in DEMs. Normally the formula for calculating semivariance γ , at a given distance h is:

$$\gamma(h) = \frac{1}{2N(h)} \sum_{i=1}^{N(h)} [Z(x_i) - Z(x_i + h)]^2$$

Where $\gamma(h)$ is the semi variance; x_i is the location of a certain point; $Z(x_i)$ and $Z(x_i + h)$ are the observed values of Z at locations x_i and $x_i + h$; h is a vector in both direction and distance, known as lag; $N(h)$ is the number of points paired with a separation distance (or lag) of h . A set of values is obtained by changing h , and this is the experimental variogram.

We used ISM (Independed Structure Model) to model the nested variation. The original field $Z(x)$ is considered to be composed of N “independent” fields in ISM; the covariance between the N fields is assumed to be zero. Total variance of $Z(x)$ can be written as sum of variance in each component.

$$Z(x) = \sum_{j=1}^n \sigma_j Y_j(x)$$

$$\sigma_z^2 = \sum_{j=1}^n \sigma_j^2$$

In this case, the covariance function and semi-variogram function for $Z(x)$ is given by:

$$C_z(h) = \sum_{j=1}^N \sigma_j^2 c_j(h)$$

$$\gamma_z(h) = \sum_{j=1}^N \sigma_j^2 \gamma_j(R_j; h) = \sum_{j=1}^N \sigma_j^2 (1 - c_j(h))$$

We assumed that range values R of each component were ordered by:

$$0 < R_1 < R_2 < R_3 \dots \dots < R_N$$

The first component is the one with most “detail” or high spatial frequency information and the last component is the one with greatest low frequency or regional information.

By ISM, we can model terrain by several “scale” components $Y_1 Y_2 Y_3 \dots \dots Y_N$, and the change of each component with resolution can be modeled.

Model efficiency coefficient

The model efficiency coefficient (ME) was used to evaluate Independent Structures model. ME was calculated by formula following.

$$ME = 1 - \frac{\sum (Y_{obs} - Y_{pred})^2}{\sum (Y_{obs} - Y_{mean})^2}$$

ME refers to the model efficiency coefficient, Y_{obs} refers to the observed values, Y_{pred} refers to the predicted values, Y_{mean} refers to mean value of the observed values. The values for ME range from $-\infty$ to 1. The model is better if ME is close to 1.

RESULTS AND ANALYSIS

Semivariograms based on the DEMs with different resolutions were modeled using Independent Structure Model. The graphic modeling results were shown in Fig.2. The parameters for the models were shown in Tab.1.

Four independent components (Y1, Y2, Y3 and Y4) were used to model DEMs surfaces. The range values for the four componets were numbered as R1, R2, R3 and R4. The sill values for the four components were numbered as S1, S2, S3 and S4.

For Hc-DEM_10m, range values for components Y1, Y2, Y3 and Y4 are R4 are about 174, 439, 1440 and 13712 meters. S1, S2, S3 and S4 are about 508, 532, 414 and 6258 square meters (Fig.2 and Tab.1). The range value for the fourth component is larger than the size of the study area. It is a trend comparing with the size of study area. So the main components are Y1, Y2 and Y3. The ME value is 0.9999 which shows it’s a good model.

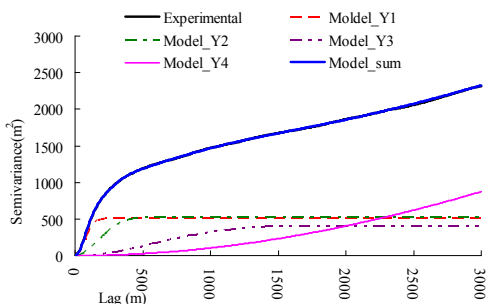


Fig.2 ISM results (resolution: 10

TABLE 1. PARAMETERS OF ISM

	DEM type	Range(m)	sill(m ²)
Y1	Hc-DEM_10m	173.6	507.8
Y2	Hc-DEM_10m	438.8	532.3
Y3	Hc-DEM_10m	1440.1	414.2
Y4	Hc-DEM_10m	13711.8	6258.2
ME	Hc-DEM_10m	0.9999	

CONCLUSIONS

With the analyses above, we can conclude that:

Semi variance is a useful tool to characterize topographic spatial structures. There are different wave length information contained in terrain, and they can be modeled by ISM model.

DISCUSSIONS

In the future, the geostatistical comparison between DEMs with varied resolution may makes people clear about the differences in scale presentation when using DEMs with different resolutions. Further more, the means of identifying certain spatial scales make it clear that which component is most different with resolution reduction. And the analyses on differences of terrain structures in different terrain types is needed to gives a good way to tell why there is distinct scaling effects in varied terrain types.

ACKNOWLEDGMENT (HEADING 5)

This study has been financially supported through the projects Estimating Spatially Distributed Slope Length at Watershed for Soil Erosion Assessment (NSFC Project, 41071188) and Spatial Structures Research of Erosional terrain surface based on GIS (North West University Project, J01938).

REFERENCES

[1] Wolock, D. M., McCabe G J. Differences in topographic characteristics computed from 100- and 1000-m resolution digital elevation model data [J]. Hydrological processes, 2000, 14(6): 987-1002.

[2] Wu, S., Li, J., and Huang, G. A study on DEM-derived primary topographic attributes for hydrologic applications: Sensitivity to elevation data resolution [J]. Applied Geography, 2008, 28(3): 210-223.

[3] Yang Q, Jupp D, Li R, et al. Re-scaling lower resolution slope by histogram matching [M]. In: Advances in Digital Terrain Analysis (Lecture Notes in Geoinformation and Cartography) [M], Zhou, Q., Lees, B.G. and Tang, GA., (eds), Editor 2008. 193-210.

[4] Zhang, X. Y., Drake, N. A., Wainwright, J., et al. Comparison of slope estimates from low resolution DEMs: Scaling issues and a fractal method for their solution [J]. Earth Surface Processes and Landforms, 1999, 24(9): 763-779.

[5] Wang, X. and Yin, Z. A comparison of drainage networks derived from digital elevation models at two scales [J]. Journal of Hydrology, 1998, 210(1-4): 221-241.

[6] Yin, Z. and Wang, X. A cross-scale comparison of drainage basin characteristics derived from digital elevation models [J]. Earth surface processes and landforms, 1999, 24(6): 557-562.

[7] Wolock, D. and Price, C. Effects of digital elevation model map scale and data resolution on a topography-based watershed model [J]. Water Resources Research, 1994, 30(11).

[8] Vaze, J., Teng, J., and Spencer, G. Impact of DEM accuracy and resolution on topographic indices [J]. Environmental Modelling & Software, 2010.

[9] Woodcock, C. E. The use of Variograms in Remote Sencing; I. Sence Models and Simulated Images [J]. Remote Sensing of environment, 1988, 25: 323-348.

[10] Oliver, M. A., Shine, J. A., and Slocum, K. R. Using the variogram to explore imagery of two different spatial resolutions [J]. International Journal of Remote Sensing, 2005, 26(15): 3225-3240.

[11] Woodcock, C. E. The use of Variograms in Remote Sencing; II. Real Digital Images [J]. Remote Sensing of environment, 1988, 25: 349-379.

[12] Western, A. W. and Bloschl, G. On the spatial scaling of soil moisture [J]. Journal of Hydrology, 1999, 217: 203-224.

[13] Jupp, D., Note on using a "filter bank" for variogram modelling, 2011.

[14] Oliver, M. A., Webster, R., and k.Slocum. Filtering SPOT imagery by kriginganalysis [J]. Remote Sensing, 2000, 21(4): 735-752.

[15] Hutchinson, M. F. New procedure for gridding elevation and stream line data with automatic removal of spurious pits [J]. Journal of Hydrology, 1989, 106(3): 211-232.

[16] Hutchinson, M. F. ANUDEM version 5.1 user guide [M]. Canberra: The Australian National University, 2004.

Monitoring topographical changes of island in the outlet of the Dongting Lake from 2000 to 2010 using time series of Landsat images

Yan Yi

University of Chinese Academy of Sciences
Institute of Geodesy and Geophysics, Chinese Academy of Sciences
Wuhan, China
yanyi@asch.whigg.ac.cn

Xiao Fei

Institute of Geodesy and Geophysics, Chinese Academy of Sciences
Wuhan, China
xiaof@whigg.ac.cn

Abstract—Natural evolution and anthropogenic disturbance have influenced the river-lake relationship in the middle Yangtze River and the impact is deeper and deeper during the last ten years with the Three Gorges Dam putting into use. An analysis of the island located at the outlet spillway of the Dongting Lake draining into Yangtze River topography change between pre-dam and post-dam period was conducted based on twelve Landsat TM and ETM+ images acquired during the last ten years. Remote sensing data and in-situ water level data are combined for analysis. Results of this study show that the island has experienced a little erosion process after post-dam period. Different direction of the island has different topography change trend. Along transect 1 the gradient slope was getting flatter, and along transect 2 and transect 4 the gradient slope was getting steeper, while along transect 3 there was little change occurred.

INTRODUCTION

The Three Gorges Project (TGP) is the largest water conservancy project ever undertaken in China, and indeed the world. The TGP is expected to control flooding not only in the area along the Yangtze river mainstream but also in the area surrounding Dongting Lake, which connects directly with the Yangtze river[1]. The Three Gorge Project intercepts a large volume of silt and regulated the runoff of the Yangtze River[2], which will result ecological environment changes in the Yangtze river area. People are more and more concerning about the relationship between the river and lakes under the influence of the Three Gorges Project impacts. Recently, a project on Chenglingji sluice construction goes on to propose, while the

lake ecological environment was more vulnerable affected by increasingly natural and human activities.

The lake bottom topography has changed greatly in the middle Yangtze River under various natural and anthropogenic activities. In this research, an island located at the outlet spillway of Dongting Lake to Yangtze River near chenglingji chose as an example. The island morphology change can reflect topography changes in the outlet spillway area of Dongting Lake. Various methods getting the topography change have been developed, Sedimentology[3,4,5], sonar measuring technique[6], underwater survey, and geophysical methods[7]. However, these methods tend to be long and costly, and sometimes impossible for high disturbance area like the outlet spillway of Dongting Lake. Remotely sensed satellite data can provide valuable information of highly frequent change environment, and it has been widely used in lake researches. M.Ma et al. observed Ebinur lake area change between 1998 and 2005 applying the remote sensing based technique[8], Lian Feng et al. derived Poyang lake bottom topography using MODIS data[9].

Water level can indirectly reflect the lake bottom topography. In this research, water level and island area and water/land boundary change distance are joined up to reflect morphology changes of the island, which will contribute to outlet spillway management and protection.

STUDY AREA

The island in this research is located at the outlet spillway of Dongting Lake draining to Yangtze River(113.03° E-113.08° E, 29.2° N-29.5° N)(Fig.1). It is located in north-

east part of the Dongting Lake, where there is water and sediment exchange bond between Dongting Lake and Yangtze river and experiences frequent and complex hydrologic change process. In dry season, water come from Dongting Lake drain to Yangtze river through there, while in flooded season, water come from Yangtze river may backflow into Dongting Lake also through there.



Figure 1. Location of the study area

DATA AND METHODS

Twelve Landsat Thematic Mapper(TM) and Enhanced Thematic Mapper(ETM+) images (Tab. 1) between 2000 and 2010 were acquired from USGS website [http://earthexplorer.usgs.gov/]. All the images were rectified using image to image rectification with more than 30 ground control points (GCPs) in each image ensuring that root mean square error (RMS) less than 0.5 pixels. The water/land boundary was got through unsupervised classification and human-computer interactive interpretation. Then the classification result was converted to vector format in ARCGIS software. The Digital Shoreline Analysis System (DSAS) was employed to calculate the rate of island boundary line change.

DSAS computes rate-of-change statistics for a time series of shoreline vector data initially applied to the seashore change research. DSAS generates transects that are cast perpendicular to the baseline at a user-specified spacing alongshore[10]. The transect and shoreline intersections along this baseline are then used to calculate the rate-of-change statistics. In this study, baseline was constructed landward in elliptical shape with a point never submerged in water in the center of the island as ellipse center. Then shoreline change envelope (SCE) was calculated, which is the distance between the shoreline farthest from and closet to the baseline at each transect. The calculated change distance was comparative analyzed with the in-situ water level data from nearby chenglingji hydrologic station which is the representative and control station of Dongting Lake.

Table 1. Date of the remote sensing data used and water level at Chenglingji station

Date	Water level(m)
2000-02-26	21.06
2001-01-11	21.88
2001-12-29	20.98
2002-03-19	23.79
2003-01-17	22
2003-02-02	22.23
2006-12-19	21.07
2007-05-20	23.2
2007-10-27	23.48
2007-12-14	20.74
2009-10-24	21.74
2010-03-09	21.88

RESULTS

This paper takes the operation of the Three Gorges Dam as a transition point and illustrate the island, lying at the outlet of the Dongting Lake, topography change in pre-dam and post-dam periods based on twelve LANDSAT TM/ETM+ images from 2000 to 2010, six before the Three Gorges Dam operation and six after that. All the results below are based on the assumption that there is a same gradient around the island.

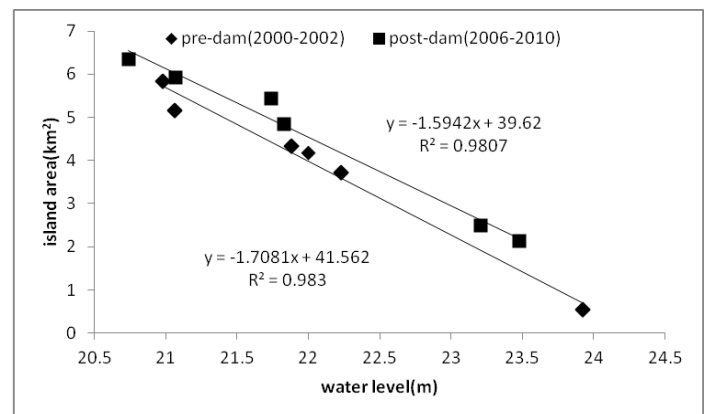


Figure 2. Relationship between exposure area of the island and chenglingji hydrologic station water level before and after the Three Gorges Dam putting into use.

Results of this research show that the emerged island area has strong correlation with water level of the nearby chenglingji hydrological station (Fig.2). During the period 2000-2002, there was 1.7km² or more land area expected to be submerged as each meter rise in water level, while after the Three Gorges Dam went into operation for three years, from 2006 to 2010, as water level rise 1 meter, the submerged land area was approximately 1.6km². The different submerged area change indicates that island topography have changed after the Three Gorges Dam put into use. It revealed that a little erosion was occurred in the island area at the elevation between 20.5 meter and 24 meter.

To assess the spatial change of the island topography, four representative transects were selected to quantify pre-dam and post-dam change rate differences (Fig.3). The distance island boundary and the baseline during each period was calculated in DSAS, and then be correlated analyzed with water level measured from nearby chenglingji hydrologic station.

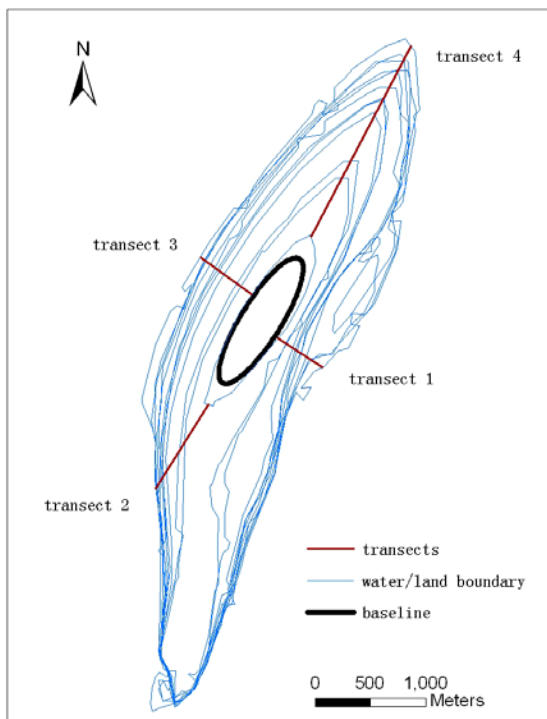
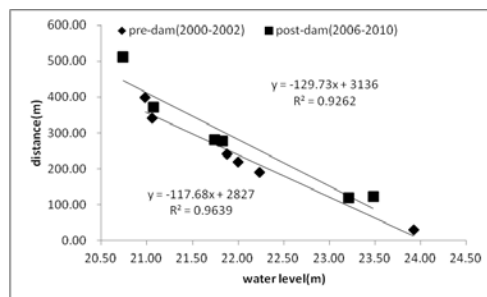


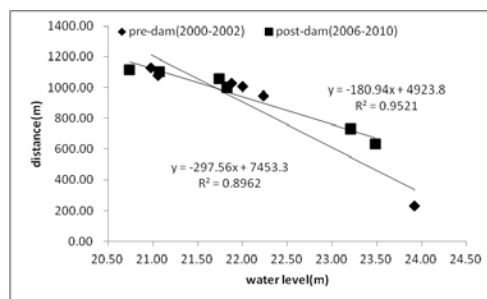
Figure 3. The island boundary position derived from remote sensing data. Four representative transects were generated to intersect all boundaries and the proposed baseline based on DSAS soft ware.

The figure (Fig.4) shows the topography change varied with different direction of the island. In general, the larger change in distance between the island boundary and baseline over a certain range of water level, the relatively flatter island topography there is. Among the four transects, there is the steepest gradient along transect 1, steeper are along transect 3, transect2, and along transect 4 the topography is the flattest. When it comes to the change along the four transects following the Three Gorges Dam construction, along the transect 1 direction the topography became flatter in the post-dam period, along the transect 2 and transect 4 direction the topography became steeper, along the transect 3 the topography barely changed.

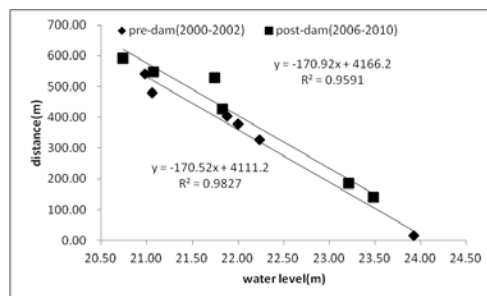
(A)



(B)



(C)



(D)

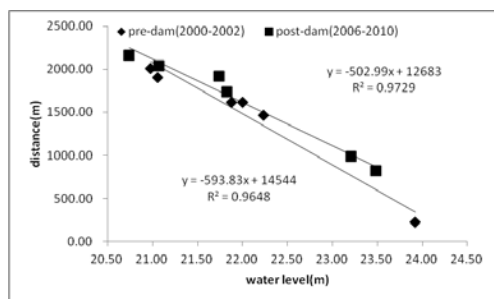


Figure 4. The correlation between island boundary change deriving from the remote sensing data and in-situ water level change of chenglingji along four transects. (A) Transect 1, (B) Transect 2, (C) Transect 3, (D) Transect 4. Note that the distance is each period island boundary to the baseline along the transect.

CONCLUSIONS

The results of this research demonstrate that it is possible to detect the island topography change with remote sensing data and in-situ water level data. The combination use of remote sensing and ARCGIS software provide a strong tool for assessing spatial and temporal change of the island topography in a frequent change environment.

Further studies are needed to applying this method in lake bottom topography change mapping and quantifying changes in different section of island beach but not a transect. Besides, many other remote sensing data can be used to get more period images for more detailed topography change

ACKNOWLEDGMENT

The study was supported by National Program on Key Basic Research Project of China (2012CB417001) and National Natural Science Foundation of China (41271125).

REFERENCES

[1] XIE, Y.h., CHEN, X.s., 2008, Effects of Three-Gorge Project on Succession of Wetland Vegetation in Dongting Lake [J]: Research of Agricultural Modernization, v. 6, p. 013.

[2] LI, J., CHANG, J., LU, D., ZHU, X., LU, C., ZHOU, Y., and DENG, C., 2009, The Hydrological Effect between Jingjiang River and Dongting Lake during Initial Period of Three Gorges Project Operation [J]: Acta Geographica Sinica, v. 11, p. 010.

[3] Dell, C., 1976, Sediment distribution and bottom topography of southeastern Lake Superior: Journal of Great Lakes Research, v. 2, no. 1, p. 164-176.

[4] Flood, R. D., 1989, Submersible studies of current-modified bottom topography in Lake Superior: Journal of Great Lakes Research, v. 15, no. 1, p. 3-14.

[5] Livingstone, D. A., 1965, Sedimentation and the history of water level change in Lake Tanganyika: Limnology and Oceanography, p. 607-610.

[6] Whetten, J. T., 1967, Lake Chelan, Washington: bottom and sub-bottom topography: Limnology and Oceanography, p. 253-259.

[7] Studinger, M., Bell, R. E., and Tikku, A. A., 2004, Estimating the depth and shape of subglacial Lake Vostok's water cavity from aerogravity data: Geophysical Research Letters, v. 31, no. 12, p. L12401.

[8] Feng, L., Hu, C., Chen, X., Li, R., Tian, L., and Murch, B., 2011, MODIS observations of the bottom topography and its inter-annual variability of Poyang Lake: Remote Sensing of Environment.

[9] Ma, M., Wang, X., Veroustraete, F., and Dong, L., 2007, Change in area of Ebinur Lake during the 1998-2005 period: International Journal of Remote Sensing, v. 28, no. 24, p. 5523-5533.

[10] Thieler, E.R., Himmelstoss, E.A., Zichichi, J.L., and Ergul, Ayhan, 2009. Digital Shoreline Analysis System (DSAS) version 4.0 — An ArcGIS extension for calculating shoreline change: U.S. Geological Survey Open-File Report 2008-1278. *current version 4.3

Soil erosion and rill system evolution based on field observations in Kongshan Hill, South-west Jiangsu Province, China

Zhenke Zhang

School of Geographic and Oceanographic Sciences
Nanjing University, Nanjing, China
E-mail: zhangzk@nju.edu.cn

Fayuan Li

School of Geographic Sciences
Nanjing Normal University, Nanjing, China
fayuanli@nnu.edu.cn

Yuexin Fu

School of Geographic and Oceanographic Sciences
Nanjing University, Nanjing, China
fuyuexin0722@163.com

Yingying Chen

School of Geographic and Oceanographic Sciences
Nanjing University, Nanjing, China
chenyy@nju.edu.cn

Shengfen Li

School of Geographic and Oceanographic Sciences
Nanjing University, Nanjing, China
E-mail: lisf@nju.edu.cn

Linghua Zhang

School of Geographic and Oceanographic Sciences
Nanjing University, Nanjing, China
zhanglinghua86@sina.com

Abstract—Water erosion is the main type of soil erosion in hills of south-west Jiangsu Province, China where the severe soil erosion happened in the hill slope covered by brown-yellow or red earth during the summer monsoon season. In this study the authors selected a man-made bare slope as the study site which was divided into 4 sub-watersheds in the northern slope of Kongshan Hill, South-west Jiangsu Province. Based on a five-year rill system and slope soil erosion observations in the study area, the rill system evolution and the soil erosion was observed and discussed. The study indicates that the human activities in the hill slope playing important role for the severe soil erosion. The natural vegetation recovery process was usually after the stage of severe soil erosion and the vegetation recovery started with decline of the intensity of slope morphological processes.

INTRODUCTION

Rills are created when water erodes the topsoil on hillsides, and so are significantly affected by seasonal weather patterns. They tend to appear more often in rainier months [1]. Although rills are small, they transport significant amounts of soil each year. Some estimates claim rill flow has a carrying capacity of nearly ten times that of non-rill, or interrill areas. In a moderate rainfall, rill flow can carry rock fragments up to 9 cm in diameter down slope. In 1987, scientist J. Poesen conducted an experiment

on the Huldenberg field in Belgium which revealed that during a moderate rainfall, rill erosion removed as much as 200 kg (in submerged weight) of rock [2]. Unfortunately, the considerable effect rills have on landscapes often negatively impact human activity. Rills have been observed washing away the surface soils. They are also very common in agricultural areas because sustained agriculture depletes the soil of much of its organic content, increasing the erodibility of the soil

Soil erosion is the fundamental earth surface process and has an important significance in the fields of morphological study and farmland management. Recently investigation revealed almost 40 percent of China's territory, or 3,569,200 square kilometers of land, suffers from soil erosion, and 1.6 million square kilometers scoured by water and 2 million square kilometers by wind were the official data in China. Soil erosion has become the severe environmental problem in China and every year the total erosion volume was estimated about 4.52 billion tons[3]. The soil erosion caused the reservoir sedimentation, farmland soil layer thinning, and the nutrients declining. In south-west China, there are almost 100 million people will lose the land they live on within 35 years if soil erosion continues at its current rate, a nationwide survey found and the Crops and water supplies are suffering serious damage as

earth is washed and blown away across a third of the country [4]. Water erosion is the main way of soil erosion in eastern China, where the severe soil erosion happened in the hill slope covered by brown-yellow or red earth during the summer monsoon season. Soil erosion in China has been interested by many foreign and domestic researchers in the past century [5-6]. In the past decades, many papers and books related to soil erosion in China were published. In North China, the dust wind erosion and the soil erosion in the Loess Plateau are the main study contents. In the farming lands, soil erosion and tillage controls was the main topic of different researches [7]. The Cesium-137 measuring method has been widely used to evaluate the soil erosion in China in the past decades [8]. Apart from the field observations and laboratory experiments, the GIS and modeling were widely used in regional soil erosion analysis [9-10].

In China few studies were about rill system and soil erosion in small field survey based on year to year land surface morphological observation and discussion on rill system evolution in a small scale settings. In this paper, a no more than 100 square meters area and five-year observations data (from 1990 to 1995) demonstrate the process of soil erosion and rill system evolution initiated by the slope runoffs after the human excavating parts of the top soil in the study area.

GEOGRAPHICAL SETTINGS OF STUDY AREA AND METHOD

The study area is located in the eastern suburb of Nanjing city. The geographical site is located on the bottom of the slope of Kongsha Hill, South-west Jiangu Province, China (Figure 1).

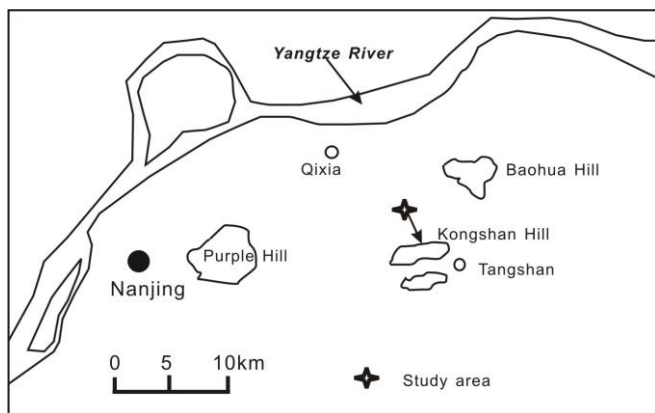


Figure 1 Location of the study area

The Climate environment in the study area is the typical subtropical monsoon. During the summer season, warmer and wetter period is usually with heavy rain storms. The Dongshan station is close to the study area and monthly rainfall in 2007 was shown in Figure 2.

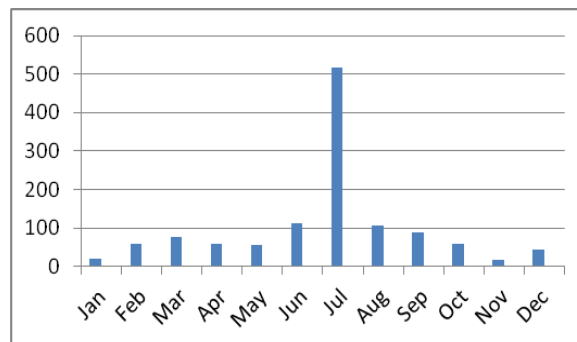


Figure 2. Monthly rainfalls distribution in 2007 (mm)

Human activities strongly influenced the landscape of the Kongsha Hills, such as the limestone mining and the road construction. For the purpose to study the soil erosion and rill system changes, we selected an area in the bottom of the hill slope. The study area was covered with deep earth and the upper 20 cm surface soil was eliminated by human excavating in the first year of spring season. The study area covered an area of 80.0 square meters including four small watersheds named A, B, C, and D. The study area was not disturbed from 1990 to 1995, so the natural processes including the soil erosion, the rill system evolution, the vegetation recovery were observed in the later a few years. The five-year observations were carried out in each September after the summer heavy rain seasons. The rill system changes, the surface erosion and the vegetation changes (plant types and land cover percentage) were measured annually in the field. In the first year, the four watersheds (A, B, C and D) features shown in table 1. The A and B were observed detailed in the later a few years. The upper parts of the slopes of the watershed were corresponded with the landforms of steep scarps.

TABLE 1. FEATURES OF THE WATERSHEDS IN THE FIRST YEAR

Water sheds	Area (m ²)	Upper slope	Middle slope	Lower slope	Rill number Level-1	Rill number Level-2	Rill number Level-3	Rill number Level-4
A	25.0	30-50°	13-20°	8-13°	3	6	8	20
B	25.0	30-50°	15-30°	10-15°	2	7	15	29
C	14.0	30-50°	15-20°	15-20°	2	7	8	/
D	14.0	30-50°	5-10°	5-10°	2	6	10	/

RESULTS

Rill system evolution

Rills formation is intrinsically connected to the steepness of the hillside slope. Gravity determines the force of the water, which provides the power required to start the erosional environment necessary to create rills. Therefore, the formation of rills is primarily controlled by the slope of the hillside. Slope controls the depth of the rills, while the length of the slope and

the soil’s permeability control the number of incisions in an area. Each type of soil has a threshold value, a slope angle below which water velocity cannot produce sufficient force to dislodge enough soil particles for rills to form [11].

In the study area, the rill system was appeared in summer season of the first year after the slope surface soil excavated and the rain season. With the slope surface changed and the soil erosion, rill systems developed in the small watershed A and B with one main channel (level-1) and more small rills of level-2, level-3 and level-4. In Table 1 there were 3 and 2 level-1 rills respectively, except one main rill (level-1), the others were the small rills with the outlets directly out of the watershed. Most parts of the small watershed A and B had the rill system respectively. The five-year observation demonstrated on the evolution of the rill system. An example was watershed B, its rill systems development was shown in table 2. From the first to the third year, the rill system was quickly developed with the severe soil erosion in the upper part of the small watershed. The rills of level-3, level-4 and level-5 disappeared in the later time of the five-year observation. The field observation indicated that in the small scale the rill system experienced the evolution processes from complex to simple.

TABLE 2. RILL SYSTEM EVOLUTION PROCESS FROM SMALL WATERSHED B

Year	Rill system: rill number and cutting depth(cm)				
	Level-1	Level-2	Level-3	Level-4	Level-5
First	2/16cm	7/22cm	15/18cm	29/12cm	Abundant ^a
Second	2/10cm	7/18cm	10/13cm	16/8cm	Abundant ^a
Third	2/8cm	7/12cm	6/7cm	0	Few
Forth	2/6cm	7/9cm	0	0	None
Fifth	2/5cm	7/5cm	0	0	None

a. refers to very small rills

Soil erosion

In the study area, soil erosion was very severe in the first few years. Because of human excavating parts of the top soil, there were no vegetation at the beginning. Slope overflow induced by gravity was the main power for the formation of rill system and soil erosion. According to the five-year observations dada, the soil erosion on the man-made bare slope in Kongshan Hill was experienced a very quick processes especially in the first 3 years. The maximum erosion site was located the divide parts between the small watershed edges (watershed A, B and watershed C, D) with the average cutting rate of 50 cm/a in the first 3 years. In the small watershed A and B, the average surface cutting rates were about 10-20cm/a in the same period. So the soil erosion rate was much higher than the estimated value before the observations. In the watershed divide, the slope was steeper. So the slope mass movement was active especially in the rain storm

period, which caused the quickly decline of elevation of the watershed divide (Figure 3)..

Slope evolution of the small watershed

Based on the field observations in the watershed B, the slope evolution of the small watershed was reconstructed and shown in the Figure 3. In the diagram the lines with numbers indicates the slopes of different year since the beginning. The thickness of the layer with yellowish brown soils was about 2.0 meters at the first year. Below the yellowish brown soil layer was the layer of deluvium gravels.

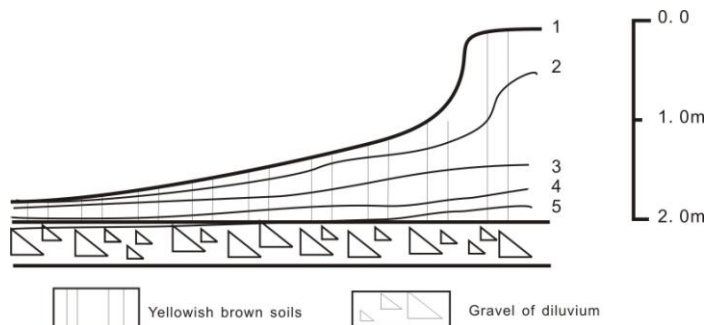


FIGURE 3. SLOPE EVOLUTION OF THE WATERSHED B

In the earlier 3 years the profiles of the slope of the watershed changed rapidly (Figure 3). The initiate upper part of the slope was more steeper and with the landform of the scarp. So the slope mass movement accelerated the soil erosion, which caused the decline of the watershed divide. In the earlier 3 years the decline of the divide was about 1.5 meters. The profile of the slope became more gentle. There was a tendency of soil erosion in the study area: the more gentler the profile of the slope, the more fewer soil erosion.

It was a interesting finding that the layer of deluvium gravels had the function prevent the erosion of surface cutting. When the upper layer of yellowish brown soil was vanished. The surface of the watershed was partly composed of gravels. The gravels protected the slope surface and slowed down the slope water erosion.

Vegetation recovery process

Vegetation coverage plays an important role in the prevention of soil erosion [12]. The natural process of vegetation recovery was also surveyed during the five-year observations [13]. With the development of the slope of the small watersheds in the study area, the slope became gentler. The grass seeds in the adjacent area were blown to the study watershed. The five-year observation also found the changes of natural vegetation

recovery processes in the small scale. The following table 3 showed the changes of vegetation recovery in the watershed A and watershed B.

TABLE I. YEARLY VEGETATION RECOVERY PROCESS IN WATERSHED A AND B

Year	Vegetation recovery process (percentage of vegetation cover)	
	Watershed A	Watershed B
First	0	0
Second	10%	15-20%
Third	50%	60-70%
Forth	70-80%	80-90%
Fifth	90%	100%

According to the survey of the vegetation species, the plant main quickly occupied the man made bare slope was the flowing vegetation species: *Artemisia arigyi* Levl. et Vant., *Artemisia Japonica* Thunb, *Kummerowia Striata* Schindl., *Lespedeza tomentosa* Seib., *Carex, sp., Cleistogenes chinensis* Keng. The pecies of *Atemisia sp.* was the pilot species occupied the bare land in the first time and also the main plant covering the small watersheds.

The vegetation covered land was protected by the plant, which was benefit to the reduction of soil erosion. The observation found in the watershed B, there was a small scarp in nor more than one centimeter scale between the vegetation covered land and bare land.

CONCLUSION

Based on five-year observations of rill system, soil erosion and the vegetation recovery in the study area, the rill system evolution, soil erosion, slope evolution and vegetation recovery were discussed in a small scale settings. That study revealed some interesting results in this study.

- (1) Rill system evolution demonstrated that the rill system in the small scale settings had the grades of five levels. With the soil erosion process and the profile changes of the slope, rill system changed from more complex to simple. The lower level rills vanished.
- (2) Soil erosion was much intensive in the study area. The maximum erosion rate in the watershed divide reached to 50 cm per year during the first 3 years. and most part of the watershed experienced the strong soil erosion in the study area with the erosion rate of 10-20 cm per year in the first 3 years. The composition of the watershed strata included the layer of diluvium gravels. When the depletion of the upper soil, the diluvium gravels had the function to prevent the soil erosion. It suggested that the earlier controlling the erosion, the better results for preventing the soil erosion in a small scale.

- (3) The watershed of the rill system had specific morphological profile from the head to the mouth of the rill system. The general tendency of the slope evolution was controlled by the erosion baseline. The slope became gentler with the process of soil erosion.
- (4) The natural vegetation recovery in the small bare slope was finished in 3 to 4 years. *Atemisia sp.* was the pilot species occupied the bare slope in the first time during the process of soil erosion and slope evolution. The grass vegetation prevented the soil erosion in the scale of centimeter level.

Acknowledgment

This study was supported by Key Projects in the National Science & Technology(No 2012BAC07B01) and the NSFC project (No.41371024 and No. 41230751)

REFERENCES

- [1] Fullen, M.A. and Reed, A.H., 1987. Rill Erosion on Arable Loamy Sands in the West Midlands of England. Bryan, R.B. (ed). Rill Erosion: Processes and Significance. Catena Supplement 8. W. Germany: Catena Verlag. 85-96.
- [2] Poesen, J. 1987. Transport of Rock Fragments by Rill Flow—A Field Study. Catena Supplement 8. W. Germany: Catena Verlag. 35-54.
- [3] Ministry of Environmental Protection of China, 2009. Bulletin of the Environment of China (2008). Issued on Jan 4, 2009, Beijing. 87 pp
- [4] Branigan, T.,2013. Soil erosion threatens land of 100m Chinese, survey finds. Available from: <http://www.guardian.co.uk/world/2008/nov/21/china-soil-erosion-population>. Last access on 2013-03-10
- [5] Tie, H. T. M., 1941. Soil erosion in China. Geographical Review, 31(4): 570-590
- [6] Morgan R. P. C., 2005. Soil erosion and conservation (Third Edition). Blackwell Publisheng, USA, p304
- [7] Liu, X.B., Zhang SL, Zhang XY et al, 2011. Soil erosion control practices in Northeast China: a mini-review. Soil and Tillage research, 117(2):44-48
- [8] Yang M.Y. Tian J.L. Liu P.L., 2006. Investigating the spatial distribution of soil erosion and deposition in a small catchment on the Loess Plateau of China, using 137Cs. Soil and Tillage Research, 87(2):186-193
- [9] Zhou ZC, Shuangguan ZP, Zhao D, 2006. Modelling vegetation coverage and soil erosion in the Loess Plateau Area of China. Ecological Modelling, 198 (3):263-268.
- [10]Fu B.J., Liu Y, Lu Y.H. et al.2011. Assessing the soil erosion control service of ecosystems change in the Loess Plateau of China. Ecological Complexity, 8(4): 284-293
- [11] Planchon, O., E. Fritsch & C. Valentin. 1987. Rill Development in a Wet Savannah Environment. Bryan, R.B. (ed). Rill Erosion: Processes and Significance. Catena Supplement 8. W. Germany:Catena Verlag. 55-70
- [12] Huang M.B, Gallich and Shao M. A, 2012. Optimization of plant coverage in relation to water balance in the Loess Plateau of China. Geoderma, 173-174(1):134-144
- [13] Zhang Zhenke, 1998. Study on Natural Recovery of Vegetation on Man-made Bare Slope. Bulletin of Soil and Water Conservation. 1:26-28

Use of SRTM data for a quick recognition of active tectonic signatures

Biju John, K.S. Divyalakshmi
 Dept of Engineering Seismology
 National Institute of Rock Mechanics
 Kolar Gold Fields
 Karnataka India

Yogendra Singh and C. Srinivasan
 Dept of Engineering Seismology
 National Institute of Rock Mechanics
 Kolar Gold Fields
 Karnataka India

Abstract Peninsular India is considered tectonically stable even though a few damaging earthquakes occurred here. However, region around Wadakkancheri has been a site of microseismic activity since 1989. Studies, subsequent to 1994 M= 4.3 earthquake, had identified a prominent NW–SE structure overprinting the E–W trending lineaments associated with Palghat–Cauvery shear zone. The right angled turn of Bharathapuzha River at Desamangalam and a waterfall near this structure shows the influence of the structure to the drainage system which is identified as a south dipping reverse fault. The hanging wall side of the fault is characterized by abandoned river courses due to the river shift. The network of paleochannels was identified through SRTM data. Distance elevation profiles were also drawn from SRTM data to observe the influence of fault on the drainage system of the area. Near the coast both paleochannels and the river is flowing approximately at the same elevation. The data generated in the present study indicates, that a marked correlation between channel morphology and the proximity of the fault in the Bharathapuzha river basin.

INTRODUCTION

Cratonic areas in continental interiors in general are characterized by low rates of stress accumulation and smaller slip rates. Recognizing active structures from such plate interiors is not easy. However, various studies in the cratonic hinterland show that the damaging earthquakes occur on pre-existing faults with a recurrence period of tens of thousands of year [1]. Such faults generally do not develop any dramatic fault scarps. In addition to this, weathering and erosion would neutralize any remnant of physiographic evidence of faulting. Even after these difficulties, various studies have however established that the deformation related with active tectonism can be identified from

careful geomorphological studies using topographic maps, aerial photographs, and satellite images and by field investigation and repeat leveling [2] [3] [4].

For several decades, the morphometric analysis of relief is being widely applied for problem solving in various areas of geology and geomorphology [5] [6] [7]. Since SRTM data became widely available, many studies have utilized them for applications in topography, geomorphology, vegetation cover studies, tsunami impact assessment, and urban studies [8]. Using SRTM data and GIS techniques is a, precise, fast and inexpensive way for morphometric analysis [9] [10] [11] [12]. The present study is an attempt to find out whether SRTM data can be used to detect active faults from the slow deforming plate interiors.

STUDY AREA

The region around Wadakkancheri is a part of intraplate region of peninsular India. It lies in the vicinity of Palghat Gap, a major physiographic break in western Ghats. The E-W trending Palghat Gap also coincides with this Gap. Even though no major earthquakes have occurred in this area in the historic past, a few earthquakes are reported in the vicinity of Palghat Gap. Since 1989 this area has been experiencing repeated slight earthquake events. Among them the 1994 Wadakkancheri earthquake of M=4.3 is the biggest one recorded, which is followed by a number of aftershocks.

The E-W trending Bharathapuzha and its tributaries constitute the drainage network of the Palghat Gap. The lineaments within the gap generally trends in E-W direction where as in the southwestern end, NW-SE trending lineaments dominate. The studies subsequent to the 1994 earthquake identified an abrupt change in Bharathapuzha river course near Desamangalam and a

NW-SE trending structure that influences the course of the river down stream from that point [13]. Further studies identified the NW-SE trending structure as a reverse, south-dipping fault, which moved episodically in the present stress regime [14]. Through ESR dating techniques of fault gouge the last movement along this fault is determined as about 430 ka bp [15]

Geomorphic studies based on the topographic maps and satellite images suggest anomalies related with the fault movements. South of Bharathapuzha, signatures of drainage adjustments were picked up from these studies. The width of the present valley of Bharathapuzha ranges from 400-700 m. The occurrence of paleochannels south of Bharathapuzha is another anomalous feature in this area. They are interlinked and abut against the coast parallel sand bars. Presently small drainages occupy these wide paleochannel valleys. Trench studies reveal that the deposits in the paleochannels are of fluvio-lacustrine origin. The studies further reveal that these channels were formed when sufficient water was flowing through it to make the valley wide. Due to lack of running water in the channels at present, which might have supplied by Bharathapuzha earlier, it is unable to cut the coast parallel sandbars across it.

METHODOLOGY

In order to check whether these signatures can be identified from topography, Shuttle Radar Topography Mission (SRTM) data is used, which have a spatial resolution of 90/90 m. The data has been cropped for the study area using ERDAS. Contours are generated for an interval of 20m using ARC GIS. Triangular Irregular Network (TIN) has been created from the contours using the 3D analyst tool of Arc GIS. The mapped faults are projected in the DEM and distance-elevation profiles are drawn across it. For the identification of paleochannels as well as present channel hydrogeological modeling, (Hydrology Tool) of ARC GIS software has been used.

Analysis

Paleochannels are demarcated in the southern side of the river. They occur at an elevation close to the present active channels. From the colour coded map (Fig.1) it can be observed that the central segment of the fault does not have appreciable elevation changes. However, for evaluating the subtle topographic features of the study area, 21 N-S trending profiles were extracted across the river at an interval of 2km. These are numbered from left to right. Two more profiles were drawn

parallel to the coast and one profile has been drawn along the river. The profile i has been taken nearly 11 km from the coast. On profile i, the lowest elevation is zero wherever it goes over the paleochannels in the southern side of the river. This situation continues up to the profile no vii (marked as profile 1 in fig. 1) where the paleochannels are located at an elevation close to the present active channels. From profiles viii to xiv the river is controlled by the fault. Profile xiii (marked as profile no 2 in fig. 1) shows the maximum separation between fault and the river within the influenced zone. The paleochannel immediately south of the fault in the hanging wall occupied is at a higher elevation than the ones further south. Profile xiv (marked as profile no 3 in fig. 1) runs close to the N-S turn of the river. The profile xvii (marked as profile no 4 in fig. 1) is passing through the river where fault does not have any influence on it. The profiles further show that the valley through which Bharathapuzha is flowing in the vicinity of Desamangalam fault is very wide. Once it crosses the area of influence of the fault the river flows through a narrow zone or the river cuts down further, compared to the upstream side. The profiles across the fault indicate a sudden increase in elevation in the southern side compared to a relatively flat valley in the northern side.

The analysis shows an interlinking nature of paleochannels with valleys in N-S, NE-SW and NW-SE directions, where remote sensing studies shows that NE-SW trending channels are wide in comparison to other directions.

CONCLUSION

SRTM data can be used for a quick evaluation of active faults. Bharathapuzha river is controlled by the faults in the study area. Paleochannels of the drainage network in the area are located at the same elevation as the present active channels. Along the vicinity of the fault the drainage flows through a wider valley compared to the region where the faults do not have any influence. The data generated in the present study indicates a marked correlation between channel morphology and the proximity of the fault in the Bharathapuzha river basin and it can be useful in active fault studies if properly employed.

ACKNOWLEDGMENT

The SRTM data is downloaded from <http://srtm.csi.cgiar.org/>. The authors are thankful to the Director, National Institute of Rock Mechanics for his encouragement and support. We thank Prof. Kusala Rajendren for offering comments. BJ and YS thank DST for funding for the present study (No SR/S4/ES-434/2009).

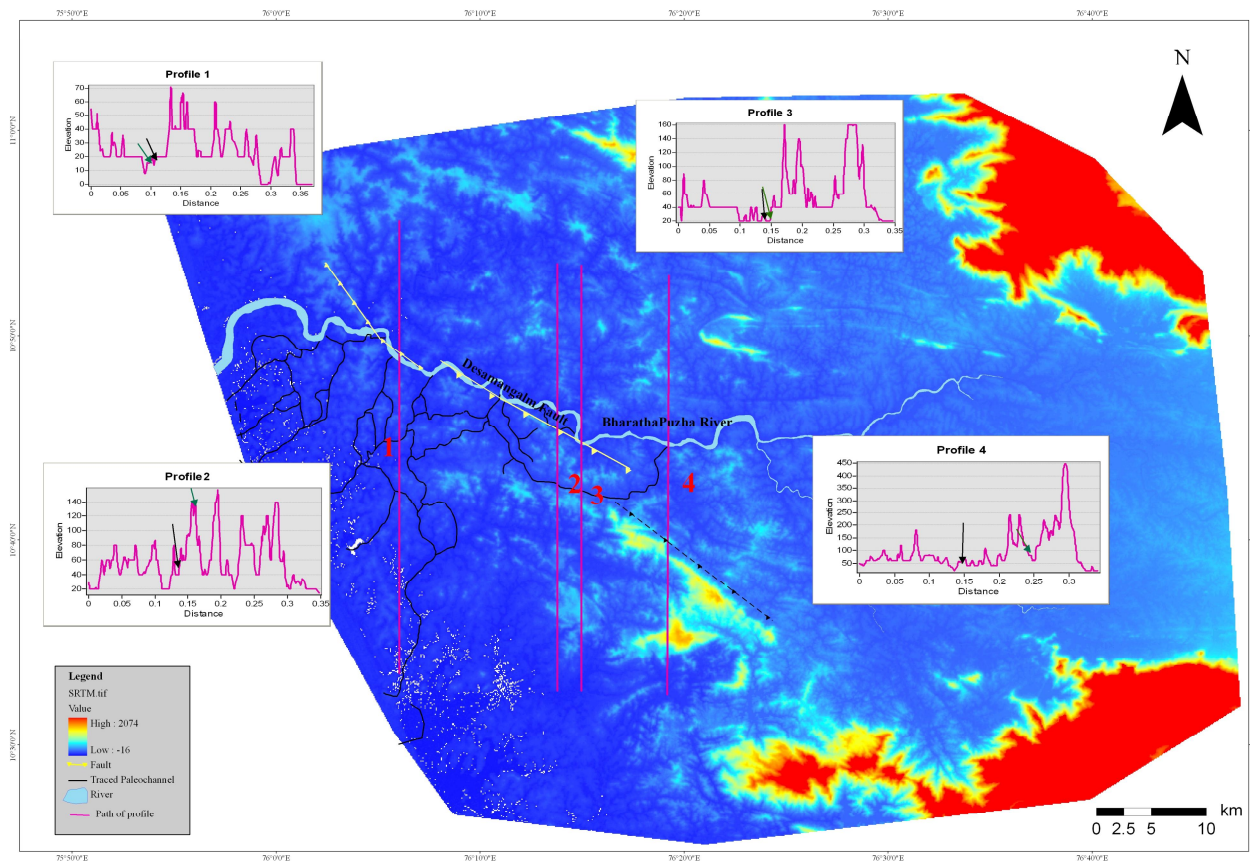


Fig. 1 Colour coded DEM generated from the SRTM data. The faults identified in the area are marked and profiles are drawn across it. The green arrow indicates the location of the fault where as the black arrow indicates the location of the river.

REFERENCES

[1] Crone, A.J., Machette, M.N., Bowman, J.R., 1992. Geologic investigations of the 1988 Tennant Creek, Australia, Earthquakes-implications for paleoseismicity III stable continental regions. U.S. Geol. Surv. Bull. 2032-A, 51.

[2] Quennel, A.M., 1958. The structural and geomorphic evolution of Dead sea Rift. Q. F. Geol. Soc. 11: 1-24.

[3] Nakata, T., 1989. Active faults of Himalaya of India and Nepal. Geol. Soc. Am. Sp. Pap. No. 232: 243-264.

[4] Vita-Finzi, C., 1986. Recent Earth Movements an introduction to neotectonics. Academic pres, 18-43.

[5] Strahler A. N., 1957. Quantitative Analysis of Watershed Geomorphology. Transactions of the American Geophysical Union 8(6): 913-920.

[6] Beasom, S. L., Wiggers E. P., Giordano R. J., 1983. A technique for assessing land surface ruggedness. Journal of Wildlife Management 47: 1163-1166.

[7] Riley, S. J., DeGloria S. D., Elliot R., 1999. A terrain ruggedness index that quantifies topographic heterogeneity. Intermountain Journal of Sciences 5: 164.

[8] Gorokhovich, Y., Voustantiouk, A., 2006. Accuracy assessment of the processed SRTM-based elevation data by CGIAR using field data from USA and Thailand and its relation to the terrain characteristics. Remote Sensing of Environment 104: 409-415

[9] Farr, T.G., Kobrick, M., 2000. Shuttle radar topography mission produces a wealth of data. American Geophys. Union, EOS 81: 583-585.

[10] Smith, B., Sandwell, D., 2003. Accuracy and resolution of shuttle radar topography mission data. Geophys. Res. Lett. 30 (9): 20-21.

[11] Grohmann, C.H., 2004. Morphometric analysis in geographic information systems applications of free software GRASS and R. Computers & GeoSciences 30: 1055-1067

[12] Grohmann, C.H., Riccomini, C., Alves, F.M., 2007. SRTM based morphotectonic analysis of the Pocos de caldas alkaline massif Southeastern Brazil. Computers & GeoSciences 33: 10-19.

[13] John, B., Rajendran, C.P., 2008. Geomorphic indicators of Neotectonism from the Precambrian terrain of Peninsular India: a

- study from the Bharathapuzha Basin, Kerala.ö J. Geol. Soc. India 71: 827-840.
- [14] John, B., Rajendran, C.P., 2009. öEvidence of episodic brittle faulting in the cratonic part of the Peninsular India and its implications for seismic hazard in slow deforming regions.ö Tectonophysics 2: 139-154
- [15] Rao, T.K.G., Rajendran, C.P., Mathew, G., John, B., 2002. öElectron spin resonance dating of fault gouge from Desamangalam, Kerala: Evidence for Quaternary movement in Palghat gap shear zone.ö Proc. Indian Acad. Sci. (Earth and Planet. Sci.) 111: 103-113.

Estimating shortwave radiation based on DEM and MODIS atmospheric products in rugged terrain

Zhang Yanli

Cold and Arid Regions Environmental and Engineering
 Research Institute, Chinese Academy of Sciences
 Lanzhou, 730000, China
 zyl0322@nwnu.edu.cn

Li xin

Cold and Arid Regions Environmental and Engineering
 Research Institute, Chinese Academy of Sciences
 Lanzhou, 730000, China
 lixin@lzb.ac.cn

Abstract—A method was proposed to estimate shortwave irradiance in rugged terrain, which was integrated to accurately consider the terrain and atmospheric key factors based on fine resolution DEM and MODIS atmospheric products. Experiments showed that the relative radiation deviation between the measured and the estimated data was 9.2% in Guantan Forest Observatory, Qilian Mountains.

INTRODUCTION

Accurate estimation of Surface Shortwave Radiation (SSR) is essential in various disciplines, including climate monitoring, biomass estimation, solar energy applications, and topographic normalization. Various algorithms have been proposed to simulate it. The parametric approach retains the same physical principles from radiative transfer models, but with a set of simplified key atmospheric parameters, which may be readily available on the flat surface. But estimating the SSR in the rugged terrain remains a significant challenge. Some models had serious limitations due to incorrect transmittance equations or simplistic assumptions (Ruiz-Arias *et al.*, 2010).

The difference in terrain orientation and atmospheric environment often leads to significant difference in radiances of pixels in the steep mountainous. Complex terrain introduces significant variations, and influence of terrain features was already described by many authors (Dozier and Frew, 1990; Li *et al.*, 2002; Wen *et al.*, 2009) with the aid of DEM, which accounted for some terrain parameters such as slope and illumination angle. However, these models use simplified atmospheric parametrizations and require ground measurements, and some even assume that the transmittance is a constant.

In this paper, we will explore a method to estimate surface shortwave radiation based on DEM and MODIS atmospheric products in complex mountains.

DATA AND METHODS

A. Data

The selected study area is located in Dayekou watershed (DYK) in the upper stream of the Heihe river basin, Qilian Mountains, China. It is a hilly terrain, and the altitude varies from 1804 m to 4613 m above sea level. The dataset for this study consisted of high resolution ASTER GDEM (30m), Landsat TM images, MODIS water and aerosol productions, which were obtained from the United States Geological Survey (USGS) Earth Resources Observation System (EROS) Data Center. Also, Guantan Forest Observatory ground measurements (Li *et al.*, 2009) were selected for the model validation.

B. Methods

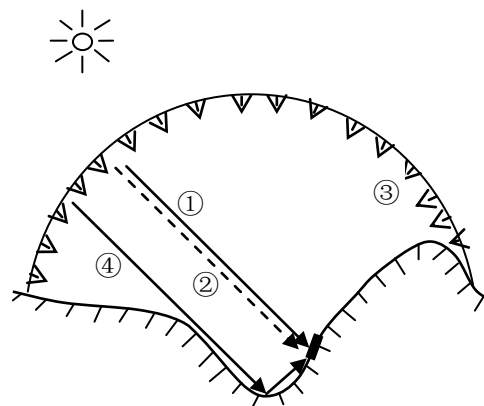


Figure 1. Global irradiance on the slope surface : ①direct, ② anisotropic diffuse, ③isotropic diffuse, ④surrounding-reflected.

In mountains, global irradiance at the surface consists of the direct, isotropic diffuse, anisotropic diffuse and surrounding-reflected irradiance, as shown in fig. 1. The amount of isotropic diffuse irradiance obscured by the mountain is estimated by considering the sky-view factor. The reflected radiation from the

around terrain can be sometimes important, which is affected by the shape factor between two mutually seen pixels and its reflectance (Li *et al.*, 2002).

On the other hand, a major portion of solar radiation transmits through the atmosphere and ultimately interacts with the Earth's surface. Thus surface solar radiation flux is mainly affected by atmospheric properties in addition to topographical variables. The factors contributing to atmospheric attenuation of solar radiation include five types: Rayleigh scattering, aerosol extinction, ozone absorption, water vapor and permanent gas absorption (Yang *et al.*, 2001). The atmospheric transmittance model is obtained as the sum of the contributions of these components. But, downward radiative fluxes are more sensitive to the aerosol, followed by the water vapor, which are strongly influenced by their spatial and temporal distribution.

The study estimated the complex surface solar radiation by making comprehensive use of Li (2002) mountainous radiation scheme and Yang (2001) atmospheric transmittance model, and MODIS aerosol and water vapor atmospheric products as input parameters. A detailed description and discussion of the algorithms were given in the above-mentioned two articles.

RESULTS AND ANALYSIS

In order to prove the effectiveness of this method, we choose this time period at 11:30 on August 14, 2010 to simulate solar radiation of the study area. Fig. 2 showed the same day of MODIS aerosol and water vapor atmospheric products.

The global irradiance and each component were obtained, and the results of total radiation and surface-reflected radiation were shown as Fig. 3. It is easy to see radiation estimated seriously influenced by terrain.

The total irradiance difference between the measured and the estimated data was 89.2 W m⁻², and the relative radiation deviation was 9.2% in Guantan Forest Observatory.

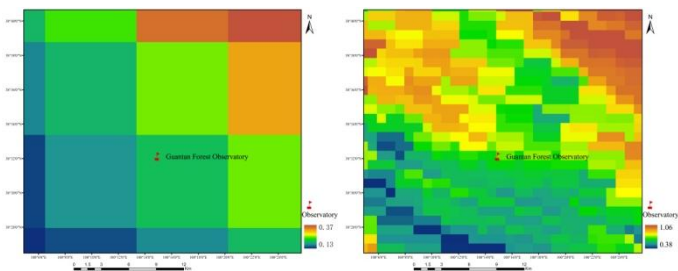


Figure 2. MODIS atmospheric products of aerosol and water vapor. (from left to right)

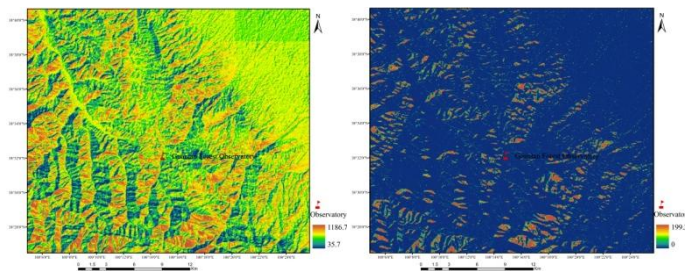


Figure 3. total radiation and surface-reflected radiation (from left to right)

ACKNOWLEDGMENT

The work is supported by the NSFC project – “Heihe Watershed Allied Telemetry Experimental Research” (grant number: 91125001), the “Enhancing the research capability of young teachers project of Northwest Normal University” (grant number: NWNNU-LKQN-10-33). The data used in the paper are obtained from the Watershed Allied Telemetry Experimental Research (<http://westdc.westgis.ac.cn/water/>).

REFERENCES

[1] Dozier, J. and Frew, J., 1990. Rapid calculation of terrain parameters for radiation modeling from digital elevation data. *IEEE Transactions on Geoscience and Remote Sensing*, 28(5): 963-969.

[2] Li, X., Koike, T., and Cheng, G. D., 2002. Retrieval of snow reflectance from Landsat data in rugged terrain. *Annals of Glaciology*, 34: 31-37.

[3] Li Xin, li Xiaowen, li Zengyuan, Ma Mingguo, Wang Jian, Xiao Qing, Liu Qiang, Che tao, Chen Erxue, Yan Guangjian, Hu Zeyong, Zhang Lixin, Chu Rongzhong, Su Peixi, Liu Qinhua, Liu Shaomin, Wang Jindi, Nui Zheng, Chen Yan, Jin Rui, Wang weizhen, Ran Youhua, Xin Xiaozhou, Ren Huazhong., 2009. Watershed Allied Telemetry Experimental Research, *Journal of Geophysical Research*, 114: D22103-1-D22103-19.

[4] Ruiz-Arias, J. A., Cebecauer, T., Tovar-Pescador, J., & Šuri, M., 2010. Spatial disaggregation of satellite-derived irradiance using a high-resolution digital elevation model. *Solar energy*, 84(9), 1644-1657.

[5] Wen, J. G., Liu, Q. H., Liu, Q., Xiao, Q., and Li, X. W., 2009. Parametrized BRDF for atmospheric and topographic correction and albedo estimation in Jiangxi rugged terrain, China. *International Journal of Remote Sensing*, 30(11): 2875-2896.

[6] Yang, K., Huang, G. W., & Tamai, N., 2001. A hybrid model for estimating global solar radiation. *Solar Energy*, 70(1), 13-22.

A Near-lossless Digital Watermarking Algorithm of DEM Based on DCT

Hu Ding

Remote Sensing College
Nanjing University of Information Science&Technology
Nanjing, China
nivsop@gmail.com

Aili Liu

Remote Sensing College
Nanjing University of Information Science&Technology
Nanjing, China
liuaili@nuist.edu.cn

Abstract—A near-lossless watermarking algorithm based on DCT (Discrete Cosine Transform) is presented to protect DEM from theft and illegal reproduction. Due to the high accuracy of the DEM, the focus of this paper is put on ensuring that the watermarked DEM should meet the precision requirement which also means the watermarked DEM should be near-lossless. The contribution of this work is that not only the DEM precision, but also the precision of slope and aspect are considered. In order to improve the robustness, the watermark should be embedded in the terrain lines—the ridge lines and valley lines. The preliminary results show that the error both of the aspect and the slope are very small and the watermarked DEM meets the medium error and maximum error proposed in the national DEM precision criterion. The watermarking can resist the compression and cropping attack.

INTRODUCTION

With the development of earth information technology, high accuracy DEM plays role in construction of National Spatial Data Infrastructure more and more important. Due to the rapid development of digitization and network, the storage, transmission and replication of DEM data are very convenient, and security and copyright issues of DEM have become increasingly salient. For copyright protection of DEM, digital watermarking can provide an effective solution. Since proposed in 1994, digital watermarking technology has developed rapidly. N.Nikolaidis and I.Pitas [1] proposed a robust image watermarking algorithm using pixel modifications, which can resistant to JPEG compression and lowpass filtering. M.Barni and F. Bartolini [2] first proposed "nearly lossless" digital watermarking, and applied it to the copyright protection in remote sensing data. Santi P. Maity and Malay K. Kundu [3] used human visual system (HVS) and the spread transform to improve the ability of watermark against the various unintentional and deliberate attacks. Later M.Kutter etc. [4] introduced the concept of second generation watermarking schemes. The idea of this concept is that watermark should be

embedded in salient parts of the original data to enhance the robustness. A new watermarking algorithm for the digital raster map based on integer wavelets transformation was proposed by Changqing Zhu etc. [5]. This algorithm is robust against various attacks such as JPEG compression, sharpening and cutting. Chengsong Yang and Changqing Zhu [6] presented a watermarking algorithm for vector geo-spatial data based on Invariant Function. This method could resist attacks such as compressing, adding, deleting, clipping, translating, rotating, scaling and complex attacks composited of above. Mi He etc. [7] put forward a DEM watermark algorithm by modifying the generalized histogram of the DEM, which could keep the original shape and relief of the terrain and ensure the high embedding capacity.

Generally, DEM digital watermarking technique has particular requirements. Firstly the embedded watermark should be invisible, as the reason that DEM data is used for terrain visualization. Moreover, watermarked DEM should be near-lossless and meets precision standard because of DEM's important quantitative analysis function. In addition, the watermarking algorithm is required to be robust. Since the conversion of DEM data spatial reference system is essentially realized by translation, rotation and scaling of the data, DEM digital watermarking should be resistant to translation, rotation and scaling [8].

METHODS

This paper proposed a DCT digital watermarking algorithm. That is near-lossless in precision and support of watermark embedding adaptively. As two basis terrain parameters, slope and aspect are important for digital terrain analyst. Therefore, the near-lossless demand of slope and aspect are taken into consideration in this paper.

The proposed algorithm first uses Hash algorithm and MD5 function to scramble the binary watermark picture with copyright

information with three passwords. Then the DEM is divided into 8×8 pixels blocks and transformed by DCT, and the scrambled watermark picture is embedded into each DEM block. Before embedded the watermark, the watermark embedding position needs to be determined. The relationship between the root-mean-square error and the slope are a negative correlation [9]. Therefore, the watermark should not be embedded in flat area. Terrain lines delineate topography relief, therefore, the digital watermark is imposed on DEM's terrain lines in this experiment to enhance the robustness of the watermark [10]. Because different terrain lines of DEM data have different positions, the terrain-line-based digital watermarking algorithm can automatically adapt the position of embedded watermark. Moreover, the watermark is embedded into the medium-frequency area of DEM to better protect the copyright of DEM, the algorithm should ensure that the strength of embedded watermark is strong enough with the constraints that the watermark is invisible and near-lossless in DEM precision. In this paper, invisibility of embedded watermark is realized by Watson visual model. The watermark is embedded in DEM using the additive rule

$$\tilde{I}_w = \tilde{I} + \alpha W, \tag{1}$$

Where \tilde{I} denotes the original DEM data, \tilde{I}_w denotes the DEM with watermark embedded, W represents the watermark signal and α represents watermark embedding strength [11].

To determine the watermark embedding strength, slope and aspect are extracted and root-mean-square error are calculated from the DEM firstly. Secondly, the watermark embedding strength are calculated according to the DEM maximum error, the DEM, slope and aspect root-mean-square error. Then the watermarked DEM is generated using IDCT (Inverse Discrete Cosine Transform).

RESULTS

Results show that the watermarked DEM meets the medium error and maximum error proposed in the national DEM precision criterion. Moreover, by area frequency statistics analyst, the error of the slope and aspect of watermarked DEM are very small. This shows that the algorithm can satisfy the near-lossless requirement of slope and aspect. In addition, watermark can be extracted after compression and cropping attacks to the DEM.

REFERENCES

[1] N.Nikolaidis, and I. Pitas, 1998. "Robust image watermarking in the spatial domain", *Signal Processing* 66:385-403.
 [2] M.Barni, F.Bartolini, V.Cappellini, E.Magli and G.OlmoWilson, 2002. "Near-lossless digital watermarking for copyright protection of

remote sensing images", *Geoscience and Remote Sensing Symposium 3*: 1447-1449.
 [3] Santi P.Maity, and Malay K.Kundu, 2004. "An Image Watermarking Scheme using HVS Characteristics and Spread Transform", *Pattern Recognition* 4:869-871.
 [4] M.Kutter, S.K.Bhattacharjee, and T.Ebrahimi, 1999. "Towards Second Generation Watermarking Schemes". *Proc of ICIP '99(1)*: 320-323.
 [5] Changqing Zhu, Haojun Fu, Chengsong Yang, and Qisheng Wang, 2009. "Watermarking Algorithm for Digital Grid Map Based on Integer Wavelet Transformation". *Geomatics and Information Science of Wuhan University* 35(5): 619-621.
 [6] Chengsong Yang, and Changqing Zhu, 2011. "Robust Watermarking Algorithm for Geometrical Transform for Vector Geo-spatial Data Based on Invariant Function". *Acta Geodaetica et Cartographica Sinica* 40(2): 257-261.
 [7] Mi He, Yong Luo, and Lizhi Cheng, 2007. "Lossless watermarking for digital elevation mode data". *Computer Engineering and Applications* 43(30): 40-43.
 [8] Guonian Lv, and Aili Liu, 2008. "Applicability of Watermarking Techniques to DEM". *Journal of Remote Sensing* 21(5): 810-818.
 [9] Xuejun Liu, Yefei Wang, Caozhi Dong, Junfeng Li and Guoan Tang, 2004. "A Study of Error Spatial Distribution of Slope and Aspect Derived from Grid DEM". *Bulletin of Surveying and Mapping* 12: 11-13.
 [10] Aili Liu, and Guonian Lv, 2008. "Copyright Protection of DEM by Means of DCT-based Digital Watermarking". *Geo-information Science* 10(2): 214-223.
 [11] Lina Wang, Chi Guo, and Peng Li, 2004. "Information Hiding Technology Experimental Course". Wuhan University Press, 300p.

Implementation of a multiple flow algorithm into the dynamic ecosystem model LPJ-GUESS

Jing Tang, Petter Pilesjö

Dept. of Physical Geography and Ecosystem Sciences
Lund University
Lund, Sweden
Jing.Tang@nateko.lu.se

Abdulghani Hasan

Department of Water Resources Engineering,
Duhok University
Duhok, Iraq

Abstract— The dynamic ecosystem model LPJ-GUESS includes explicit representation of vegetation dynamics as well as soil biogeochemistry, and has been widely and successfully implemented in predicting vegetation biomass and carbon cycling at different scales. However, the water cycling for each grid cell in the model is only considering the movement between atmosphere, vegetation and soil, ignoring the lateral water movement between grid cells. A previous study has proposed a distributed scheme in LPJ-GUESS incorporating topographic indices to redistribute lateral water movement, and has demonstrated the impacts on ecological functioning and carbon cycling at the Stordalen catchment, northern Sweden. The topographic indices, extracted based on a Digital Elevation Model (DEM), were based on a single flow (SF) algorithm at 50 m resolution, restricting the flow movement to the downslope cell with maximum gradient. In this study we have incorporated the Triangular Form-based Multiple Flow algorithm (TFM) to redistribute lateral water in LPJ-GUESS and analyzed the influences and differences between the two flow algorithms on runoff prediction as well as carbon cycling estimations. The results indicate that the runoff estimated by the TFM algorithm is more realistic than the SF algorithm. Besides, the comparison with observed runoff data demonstrates the monthly runoff estimated using the SF algorithm tends to overestimate the runoff in May and June as well as in the lower flatter peatland region. For the TFM algorithm, the underestimated runoff during the growing season can be compensated by the decreased soil depth in the elevated area. Moreover, the implementation of the TFM algorithm results in a significant increase of the catchment mean value of vegetation uptake of carbon as well as net ecosystem exchange carbon. We conclude that the advanced multiple flow algorithm (TFM) with more accurate estimation of flow accumulation can improve the hydrological predictions in LPJ-GUESS. Meanwhile, the results have proved that the flow routing algorithms do influence the vegetation pattern estimations for the study area.

INTRODUCTION

LPJ-GUESS is a dynamic ecosystem model, simulating vegetation dynamics as well as soil biogeochemistry [Sitch *et al.*, 2003; Smith *et al.*, 2001]. The model has been successfully implemented in predicting vegetation biomass, carbon balance, and carbon cycling at local and global scales [Ahlström *et al.*, 2012; Hickler *et al.*, 2004]. However, as an ecosystem model, the water cycling [Gerten *et al.*, 2004] is only limited to the interactions between atmosphere, plants and soil [Wolf, 2011]. There is no consideration of lateral water movement. A previous study proposed a distributed scheme by implementing topographic indices to add lateral water movement in LPJ-GUESS to conquer this limitation, and was renamed as LPJ-Distributed Hydrology (LPJ-DH) [Tang *et al.*, In Review]. The topographic indices, including drainage area (*DA*), flow direction (*Fdir*) and slope (*S*) are extracted from a Digital Elevation Model (DEM). Through applying *Fdir* to direct the generated runoff to downslope cells and using *DA* to organize the processing sequence, the new proposed LPJ-DH allows water flow between grid-cells, which is directly influencing the amount of vegetation available water as well as the runoff. The single flow algorithm (SF) [O'Callaghan and Mark, 1984] based on a gridded DEM was chosen for this application, assuming that surface flow only occurs in the steepest downslope direction.

The SF algorithm used in the previous study, in comparison to multiple flow algorithm (MF), restricts the divergence in estimating lateral flow paths [Hasan *et al.*, 2012; Zhou *et al.*, 2011] and therefore could influence the soil moisture and vegetation pattern estimations [Guentner *et al.*, 2004]. Many studies have suggested different methods of handling the multiple flows, and the majority work is based on gridded DEMs. However, due to the regularly spaced samplings on the continuous surface the gridded DEM could produce inconsistent flow paths [Zhou *et al.*, 2011], especially for coarser scales. To overcome the limitations of the gridded structure of the DEM, the newly-developed Triangular Form-based Multiple flow algorithm

(TFM) has been developed, based on the partition of grid cells in the DEM into triangular facets and redistribution of water proportionally to down-hill adjacent cells [Pilesjö and Hasan, 2013]. In this way, the algorithm can better take into consideration the continuity using Triangulated Irregular Network (TIN). Besides, the improvements of flow routing over flat cells from the TFM algorithm was also evaluated [Hasan et al., 2012]. The TFM algorithm then showed the capability of producing the closest and consistent outcomes in relation to theoretical values of specific catchment area (SCA) compared to other methods.

In this paper the TFM algorithm is implemented to estimate topographic indices and adapt the distributed scheme in LPJ-DH to fulfill the divergence flow routing paths. Through comparing the hydrological and ecological estimations after coupling SF and TFM algorithm in LPJ-GUESS (named LPJ-DH-SF and LPJ-DH-TFM, respectively), we aim to answer the question how important the flow routing algorithms is in terms of modeled runoff and hydro-ecological variables at the catchment scale.

METHODS

The implementations of the SF and TFM algorithms are based on the same DEM, with the resolution of 50 m (to be consistent with the resolution of climate data). The main change in the LPJ-DH using the TFM algorithms is that the generated runoff can be directed to multiple downslope cells, instead of just one cell in the SF algorithm. So, the proportions of flow to downslope cells are added to each grid-cell as input attributes. Apart from that, in comparison with the single flow algorithm, the processing sequence of grid-cells for TFM cannot be uniquely determined by the values of DA alone, since some cells flowing to a downslope cell may have higher DA value. To overcome this problem, we found that implementing elevation (from higher to lower) together with DA values (from lower to higher) could uniquely decide the cell sequence for flow accumulation. A Matlab program was developed to test and make sure that the flow accumulation has been accomplished for the “upslope cells” before draining to “downslope cells”.

The sub-surface water routing is also included, and its lateral water redistribution follows the same principles as the surface water part. For the subsurface part, only vertical water movement is considered for unsaturated soil, and the saturated subsurface runoff ($R_{sub}(r,c)$) is estimated by quasi three-dimensional flow developed by Wigmosta et al. [1994]:

$$R_{sub}(r,c) = \frac{K_s}{f} [\exp(-fz_{wt}(i,j)) - \exp(-fD(i,j))] * S(i,j) * w$$

K_s is the saturated hydraulic conductivity varying with different soil types. $z_{wt}(i,j)$ is the distance from the ground surface to the water table (positive downward) and $D(i,j)$ is the total soil depth. f is the decay coefficient of saturated conductivity with depth and

w is the width of the flow. $S(i,j)$ is the slope of the cell. The parameter values of K_s and f are based on the literature.

The modeled runoff is compared with observed runoff measurements and evaluated by the relative root mean square error (RRMSE). The closer value of RRMSE to zero, the better is the model performance [Stehr et al., 2008]. To reveal the different flow algorithms influences on carbon fluxes, the Mann-Whitney U test was used.

$$RRMSE = \sqrt{\frac{\sum_{i=1}^n (S_i - O_i)^2}{n}} * \frac{1}{O}$$

STUDY AREA

Stordalen catchment

The Stodalen catchment is located in northern Sweden, about 9.5 km from the Abisko Research Station (ANS). The whole catchment covers 16 km² and consists of a mountainous area in the southern part, entering into the lower flat peatland area in the north (see Fig.1). The catchment hydrology has been reported by Persson et al. [2012] and Ryden et al. [1980] and water-related carbon fluxes measurements have been presented by Olefeldt et al. [2012] and Lundin et al. [2013]. For this study, measured daily runoff during the year 2007-2009 was provided by Olefeldt et al. [2012] in order to evaluate the model runoff estimations.

RESULTS

Drainage area

Presented in Fig.1, two different drainage patterns are estimated using the TFM (left) and the SF (right) algorithms. Through visual comparison, the TFM extracted drainage pattern shows smoother and more realistically looking spatial patterns than the SF estimated one. Additionally, the values of Ln(DA) from the SF algorithm are not smoothly increasing downhill, and the main drainage is more distinct.

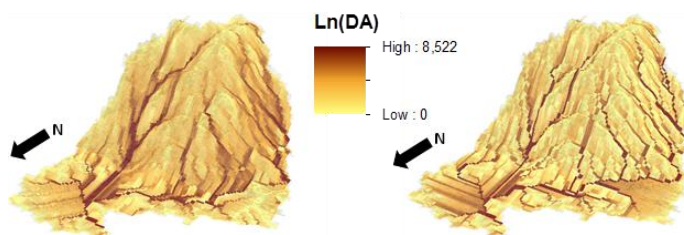


Figure 1. Map of Ln(DA) using the triangular form-based (left) and the single algorithm (right). For each grid-cell, the value 1 is added before calculating the natural logarithm. The map is draped on a digital elevation model (enhanced five times).

TABLE I. STATISTICS OF DRAINAGE AREA FROM TFM AND SF ALGORITHMS

Algorithms	Variables	Mean	Standard variation	Skew
SF	Drainage area(DA)	51.840	303.562	11.274
TFM	Drainage area(DA)	40.770	235.093	12.690

The results in Table 1 show that the TFM algorithm produces lower mean and variance values of DA and the higher and positive skew values indicate more cells with lower DA values when using the TFM algorithm. The allowances of flow divergence and consideration of consistency from the TFM algorithm reduce the DA average as well as the variances among cells.

Monthly runoff comparison

The daily runoff is summed up to get the monthly runoff, and the comparisons between observed and modeled runoff from LPJ-DH-SF and LPJ-DH-MF are presented in Fig. 2. The RRMSE values vary from point to point, but generally, the runoff peak from LPJ-DH-SF is higher than the LPJ-DH-MF, especially for the peatland cell A2. For the point A1, located at the catchment outlet, the LPJ-DH-SF produces lower RRMSE values, which capture the high runoff better in June during the observed years. For the point A2, the overestimation of runoff by LPJ-DH-SF is converse with the underestimation by LPJ-DH-MF during the summer period. For the point B2, with steeper terrain, both models are underestimating the runoff, but the LPJ-DH-SF shows values closer to the observed (RRMSE=4.14). For the relatively dry years (2008 and 2009), the runoff predictions at B2 have larger underestimation bias. For the outlet points A5 and A6, located in the comparatively flat region, both models show almost the same accuracy.

Going through the six measured points, for the LPJ-DH-MF the main discrepancy in runoff compared with observed data are the low runoff estimations in June. When the plants start to grow, there is more water supplying plants' photosynthesis and growth as well as soil evaporation, thus less water can route downslope. The distributed flow used in the TFM makes the available water to the main drainage network even less.

Carbon fluxes comparison

Due to lack of field data of spatially distributed biomass and carbon fluxes, the comparisons are based on the statistical comparison of models estimations over the whole catchment. The Mann Whitney U-tests indicate that the differences are significant for vegetation uptake carbon (VegCflux) and net ecosystem exchange (NEE) for the two models. The LPJ-DH-MF model has around 1.34% and 7.41% increase (more carbon uptake) in VegCflux and in NEE, compared with the LPJ-DH-SF outputs. There is no indication of significant difference of soil respired carbon (SoilCflux) between the two models. However, a distinctively higher soil released carbon can be found for the main drainage network cells from LPJ-DH-SF (see the whisker

extend for SoilCflux in Fig. 3), which is not appearing in LPJ-DH-MF.

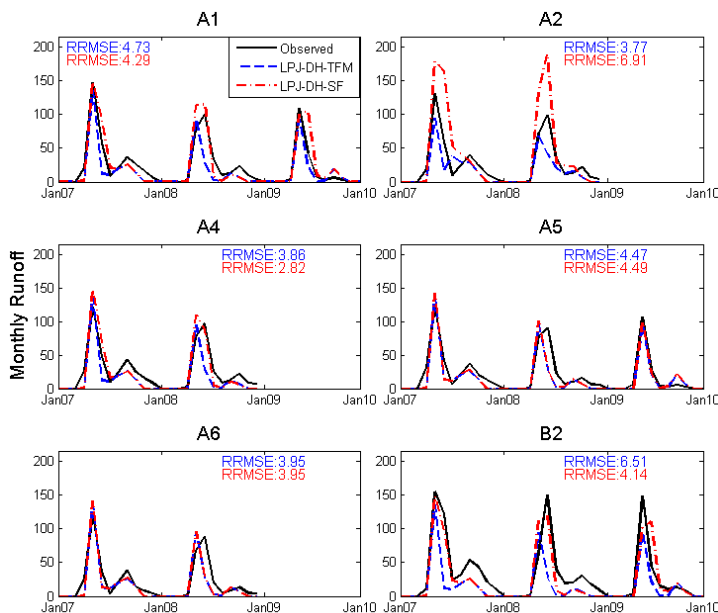


Figure 2. Point runoff comparisons between the modeled and the observed monthly runoff. There are no data for A2, A4 and A6 during the year 2009.

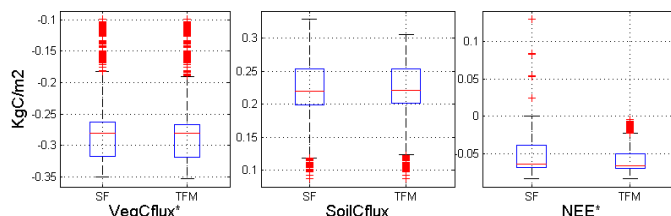


Figure 3. Catchment carbon fluxes diversity during the year 1981-2000. The asterisk (*) represents the statistical significance at the level of 0.05.

DISCUSSION AND CONCLUSION

In this study, the soil depth is set to 1.5 m, as the standard LPJ-GUESS depth, but in reality the soil is quite shallow with bare rocks in the southern mountainous area. The soil depth needs to be adjusted in forthcoming studies for the elevated area of the catchment. With reducing the soil depth, the runoff is expected to increase compared with the models outputs presented in this paper, but to what magnitude is unknown. The current results illustrate that the SF algorithm generally produces higher runoff values than the observed in May and June, with the exception of point B2. When reducing the soil depth in the southern elevated area, the runoff during the high-runoff season will become higher using the SF algorithm since the water is concentrated to the main flow paths. However, that could have less influence for the LPJ-DH-TFM due to the dispersion of water over the catchment

and maybe compensate the underestimated runoff for LPJ-DH-TFM.

The allowance of flow divergence in the TFM makes the upslope area per unit contour length decreasing [Wolock and McCabe Jr, 1995], which means there is less water accumulating for each downslope neighboring cell. In other words, there are more cells that could receive water from upslope cells which results in significant changes in vegetation uptake carbon (total NPP) for LPJ-DH-MF. With larger catchment and water-limited area, the differences of flow routing on vegetation growth will be more pronounced.

It is novel to evaluate two different routing algorithms by implementing them into a process-based ecosystem model. In this way, both the climate conditions and vegetation dynamics are taken into the consideration. Comparing with other studies of utilizing statistical correlations between topographic wetness index (TWI) and vegetation pattern to evaluate different routing algorithms [Kopecký and Čížková, 2010; Sorensen et al., 2006], our method is more accurate and could reveal more detailed flow algorithm differences/influences on hydrological estimations through the seasons. Besides, our method can avoid using TWI as a proxy for soil moisture conditions and can capture the effective contributing area over time. Nevertheless, with increased complexity of model structure, our method needs to be better calibrated before finally concluding which routing algorithm that is the best for different environments.

To summarize, the more advanced multiple flow algorithm (TFM), producing more accurate estimations of flow accumulation can improve the hydrological predictions in LPJ-GUESS. The comparisons of carbon fluxes outputs between LPJ-DH-SF and LPJ-DH-TFM have demonstrated that the flow routing algorithms do matter not only for hydrological variables, but also for ecological estimations, within the study area.

REFERENCES

- [1] Ahlström, A., P. A. Miller, and B. Smith (2012), Too early to infer a global NPP decline since 2000, *Geophys. Res. Lett.*, 39(15), L15403.
- [2] Gerten, D., S. Schaphoff, U. Haberlandt, W. Lucht, and S. Sitch (2004), Terrestrial vegetation and water balance—hydrological evaluation of a dynamic global vegetation model, *Journal of Hydrology*, 286(1-4), 249-270.
- [3] Guentner, A., J. Seibert, and S. Uhlenbrook (2004), Modeling spatial patterns of saturated areas; an evaluation of different terrain indices, *Water Resources Research*, 40(5).
- [4] Hasan, A., P. Pilesjö and A. Persson (2012), Drainage Area Estimation in Practice - how to tackle artifacts in real world data, paper presented at GIS Ostrava 2012-Surface models for geosciences, Ostrava, Czech Republic.
- [5] Hickler, T., B. Smith, M. T. Sykes, M. B. Davis, S. Sugita, and K. Walker (2004), USING A GENERALIZED VEGETATION MODEL TO SIMULATE VEGETATION DYNAMICS IN NORTHEASTERN USA, *Ecology*, 85(2), 519-530.
- [6] Kopecký, M., and Š. Čížková (2010), Using topographic wetness index in vegetation ecology: does the algorithm matter?, *Applied Vegetation Science*, 13(4), 450-459.
- [7] Lundin, E. J., R. Giesler, A. Persson, M. S. Thompson, and J. Karlsson (2013), Integrating carbon emissions from lakes and streams in a subarctic catchment, *Journal of Geophysical Research: Biogeosciences*, n/a-n/a.
- [8] O'Callaghan, J. F., and D. M. Mark (1984), The extraction of drainage networks from digital elevation data, *Computer Vision, Graphics, & Image Processing*, 28(3), 323-344.
- [9] Olefeldt, D., N. Roulet, R. Giesler, and A. Persson (2012), Total waterborne carbon export and DOC composition from ten nested subarctic peatland catchments—importance of peatland cover, groundwater influence, and inter-annual variability of precipitation patterns, *Hydrological Processes*, n/a-n/a.
- [10] Persson, A., A. Hasan, J. Tang, and P. Pilesjö (2012), Modelling Flow Routing in Permafrost Landscapes with TWI: An Evaluation against Site-Specific Wetness Measurements, *Transactions in GIS*, 16(5), 701-713.
- [11] Pilesjö, P., and A. Hasan (2013), A Triangular Form-based Multiple Flow Algorithm to Estimate Overland flow Distribution and Accumulation on a Digital Elevation Model, *Transactions in GIS*.
- [12] Rydén, B. E., L. Fors, and L. Kostov (1980), Physical Properties of the Tundra Soil-Water System at Stordalen, Abisko, *Ecological Bulletins*(30), 27-54.
- [13] Sitch, S., et al. (2003), Evaluation of ecosystem dynamics, plant geography and terrestrial carbon cycling in the LPJ dynamic global vegetation model, *Global Change Biology*, 9(2), 161-185.
- [14] Smith, B., I. C. Prentice, and M. T. Sykes (2001), Representation of vegetation dynamics in the modelling of terrestrial ecosystems: comparing two contrasting approaches within European climate space, *Global Ecology and Biogeography*, 10(6), 621-637.
- [15] Sorensen, R., U. Zinko, and J. Seibert (2006), On the calculation of the topographic wetness index; evaluation of different methods based on field observations, *Hydrology and Earth System Sciences (HESS)*, 10(1), 101-112.
- [16] Stehr, A., P. Debels, F. Romero, and H. Alcayaga (2008), Hydrological modelling with SWAT under conditions of limited data availability: evaluation of results from a Chilean case study, *Hydrological Sciences Journal*, 53(3), 588-601.
- [17] Tang, J., P. Pilesjö, P. Miller, A. Persson, Z. Yang, E. Hanna, and T. V. Challaghan (In Review), Incorporating topographic indices into dynamic ecosystem modeling using LPJ-GUESS, *Ecohydrology*.
- [18] Wigmosta, M. S., L. W. Vail, and D. P. Lettenmaier (1994), A distributed hydrology-vegetation model for complex terrain, *Water Resources Research*, 30(6), 1665-1679.
- [19] Wolf, A. (2011), Estimating the potential impact of vegetation on the water cycle requires accurate soil water parameter estimation, *Ecological Modelling*, 222(15), 2595-2605.
- [20] Wolock, D. M., and G. J. McCabe Jr (1995), Comparison of single and multiple flow direction algorithms for computing topographic parameters in TOPMODEL, *Water Resources Research*, 31(5), 1315-1324.
- [21] Zhou, Q., P. Pilesjö and Y. Chen (2011), Estimating surface flow paths on a digital elevation model using a triangular facet network, *Water Resour. Res.*, 47(7), W07522.

Snow distribution pattern and its influencing factors in a small watershed in Atlantic Canada

Sheng Li

Agriculture and Agri-Food Canada
Fredericton, New Brunswick, Canada
Sheng.Li@agr.gc.ca

Yongbo Liu

University of Guelph
Guelph, Ontario, Canada

Fangzhou Zheng, Zisheng Xing, Fanrui Meng, Karl Butler

University of New Brunswick
Fredericton, New Brunswick, Canada

Abstract—Snowmelt events contribute significantly to surface runoff and sediment and nutrient loadings in cold climate regions such as in most part of Canada. To better understand the snowmelt hydrology, a snow survey was carried out in a small watershed in New Brunswick, Canada in March, 2012. Snow cores were sampled from 33 predetermined locations, covering different land uses and slope positions. The snow depth ranged from 0.17 m to 0.74 m and averaged at 0.36 m. The water equivalent depth of the snow ranged from 0.06 m to 0.23 m and averaged at 0.10 m. Forested area had significantly deeper snow than cropped area. Points on the edge of the forested area had the deepest snow. The variability of snow depth was high and the variation did not correlated well with terrain attributes extracted from a 30 m grid DEM. A Ground Penetrating Radar (GPR) was used to measure the snow depth along transects. The GPR was effective in detecting the soil surface under the snow. The GPR data also demonstrated the strong effect of local topography on snow depth. Future studies are required to examine the use of these data for snow depth predictions.

INTRODUCTION

Studies on watershed hydrology and water quality have focused on rainfall events and rainfall induced runoff. In cold climate regions, such as in most of Canada, a large portion of the annual precipitation is in the form of snow fall. As a result, snowmelt runoff has reported to consist more than 30% of the total runoff at some water monitoring stations in this region (Chow and Rees, 2002) as well as in several other sites in Canada (e.g., Li et al., 2011). However, our knowledge on snowmelt hydrology is limited, which has been identified as a major restriction on the modeling and interpretation of water quality at the watershed scale. One of the limitations is due to the lack of input information on snow distribution, which is normally not uniform in a watershed and is affected by many factors such as climate, topography and land use. The objectives of this study are to measure snow distribution pattern and to determine dominant factors for snow distribution in a small watershed in cold climate region.

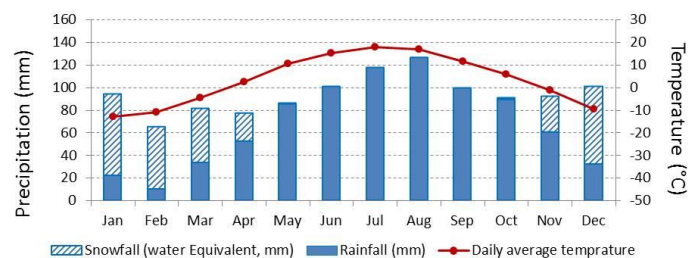


Figure 1. Long-term normal precipitation and mean air temperature at a climate station in Grand Falls, New Brunswick, Canada (data source: Environment Canada website).

MATERIALS AND METHODS

Study site

The study was carried out in the Black Brook Watershed (BBW) in the province of New Brunswick, Canada. The area of BBW is approximately 1,450 ha. The climate in this region is moderately cool boreal, with an average annual temperature of 3.2 °C and approximately 120 frost-free days (Fig. 1). Annual rainfall, snowfall and total precipitation averaged at 769 mm, 354 mm and 1,092 mm, respectively. Elevations in BBW range from 150 to 241 m above sea level (Fig. 2). Most of the area in BBW is undulating to gently rolling with slopes of 1–6% in the upper portion, 4–9% in the central part and 5–16% in the lower part of the watershed. Soils were predominantly moderately well drained Orthic Humo-Ferric Podzols, developed on coarse-textured till. The major land-use within the watershed is agriculture, which accounts for 65% of the total watershed area (Fig. 2). The major crops are potato and barley, followed by other crops in rotation. Approximately 25% of the watershed is forested. Roads, urban areas and streams cover the remaining 10% of the watershed.

Snowmelt discharge and snowmelt erosion play an important role in the BBW. Chow and Rees (2002) reported that approximately 36% of discharge and 39% of sediment loadings measured at the watershed outlet occurred during the snow-

melting period in April. The source of runoff and sediment load coming from snowmelt strongly relies on the spatial distribution of snow cover and watershed characteristics. Therefore, examining the spatial and temporal variations of snow cover over the watershed has both practical and scientific significance in understanding snow hydrology and in particular the management of BMPs related to snowmelt runoff, sediment loading, and water quality.

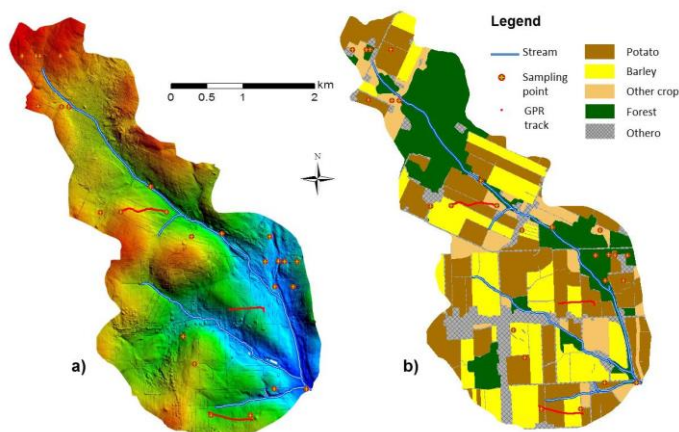


Figure 2. Maps of a) topography; and b) land use in 2002 for the Black Brook Watershed. Manual snow sampling locations and three example Ground Penetrating Radar (GPR) survey tracks were shown in both maps.

Field snow sampling and survey

A field snow sampling and survey campaign was carried out on March 21st and 22nd, 2012. Snow depth (SnD) and weight-based snow water equivalent depth (WED) were measured using a snow sampling kit at 33 predetermined locations (Fig. 2). A snow redistribution model developed by Guelph Watershed Evaluation Group (2010) was used to estimate the general pattern of snow depth as a result of variations in land use and terrain attributes. The terrain attributes were calculated based on a 30 m grid Digital Elevation Model (DEM), which is derived from the lidar data collected in 2007 (approximately 1 – 2 m² per point, error at the level of 0.3 m horizontally). The selected 33 locations represented the major variations of these variables across the landscape. The coordinates of these locations were recorded using a Trimble GeoXH GPS system with a theoretical real-time accuracy at the level of 10 cm.

For detailed in-field snow depth variation, a total of 18 transects were surveyed using a Ground Penetrating Radar (GPR) system (pulseEKKO Pro, Sensors and Software) with a 500 MHz antenna. The GPR unit sends out radio waves and detects the return waves reflected from the snow and ground interface. The time takes for the radio wave to return is converted to the depth of the snow (from snow surface to the snow and ground interface). During the survey, the GPR was secured in a toboggan sled, which is attached to a snowmobile. The snowmobile was moving at a speed of ~10 km hr⁻¹ and point interval for the measurement was approximately 0.2 m. A handheld Garmin GPS with an accuracy of ~5-10 m was connected to the GPR unit to record the coordinates and elevation of each measuring point.

The GPR survey tracks were designed to go through some of the manually measured sampling points so that the GPR data can be calibrated against the manual measurements.

Statistical analyses

The manual sampling points were categorized into three general land use types (i.e., forest, pasture and cropped). Analysis of Variance (ANOVA) was conducted for the snow depth and snow water equivalent depth data to examine the effect of land use. The effect of topography was considered as random noise and was not considered specifically in the ANOVA. A Tukey’s test was used for paired comparisons between the means of different land uses. For each sampling point, a set of terrain attributes—including elevation, aspect and slope gradient and slope curvature along the predominant wind direction (north-west) —were extracted from the 30 DEM derived from the lidar data. The effects of these terrain attributes on SnD and WED were examined using simple linear correlation analyses. The correlation analyses were conducted for all data and also for each sub-dataset for individual land use type. A t-test was used to determine the significance of the correlation coefficients.

RESULTS

Snow depth and snow water equivalent depth both were highly variable across the landscape (Table 1). With all sampling points considered, the coefficients of variation (CVs) for SnD and WED were 41% and 34%, respectively. Within the same land use types, the CV values ranged from 20% to 36%, which were still very high. Despite the high level of variability of the data, the ANOVA tests indicated that for SnD and WED, the effect of land use was significant (P = 0.001 and P = 0.03 for SnD and WED, respectively). The mean SnD and WED both followed the order of Forest > Pasture > Cropped. The Tukey’s test suggested that mean SnD in forest fields was significantly higher than that in Cropped fields, whereas the mean SnD in pasture fields were in between those of the Forest and Cropped fields, but the differences were not statistically significant (Fig. 3). The mean WED values for forest and pasture fields were the same and were significantly higher than that of the cropped field.

TABLE I. SIMPLE STATISTICS FOR THE SNOW DEPTH AND SNOW WATER EQUIVALENT DEPTH DATA MEASURED MANUALLY AT THE SAMPLING POINTS (SD = STANDARD DEVIATION; AND CV = COEFFICIENT OF VARIATION)

	Forest	Pasture	Cropped	All
n	13	6	14	33
Snow Depth				
Mean (cm)	45	38	26	36
SD (cm)	15	13	7	15
CV (%)	34	35	26	41
Water Equivalent Depth				
Mean (cm)	12	12	9	10
SD (cm)	4	3	2	3
CV (%)	36	29	21	34

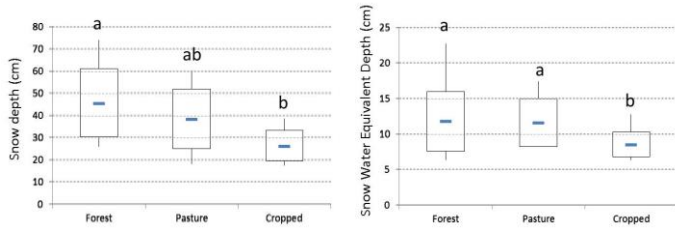


Figure 3. Summary of the snow depth and snow water equivalent depth data and the multiple comparison results based on the Tukey's test. The blue bar indicates the mean value; the upper and lower bounds of the box indicated the values of mean \pm standard deviation, respectively; and the upper and lower ends of the whisker indicate the maximum and minimum values, respectively.

Correlation coefficients between SnD/WED and all four terrain attributes examined in this study were all non-significant at $P = 0.10$ (Table 2). Only a few correlation coefficients were significant even when the significant level was lowered to $P = 0.20$. However, with only one exception, there appeared to be a consistent trend of negative correlations between SnD/WED and slope gradient and between SnD/WED and slope curvature. This suggests that topography may have some profound impact on snow distribution.

TABLE II. CORRELATION COEFFICIENTS (R-VALUES) BETWEEN SNOW DEPTH/SNOW WATER EQUIVALENT DEPTH AND TERRAIN ATTRIBUTES EXTRACTED FROM A 30 M GRID DEM. NO R-VALUE WAS SIGNIFICANT AT $P = 0.10$. BOLD FACED R-VALUES WERE SIGNIFICANT AT $P = 0.20$.

	n	Elevation	Aspect	Slope Gradient [§]	Slope Curvature [§]
Snow Depth					
Forest	13	-0.35	0.04	-0.22	0.20
Pasture	6	0.65	0.65	-0.22	-0.13
Cropped	14	-0.03	-0.37	-0.38	-0.06
All	33	-0.27	0.10	-0.13	0.26
Water Equivalent Depth					
Forest	13	-0.19	0.04	-0.30	-0.16
Pasture	6	0.70	0.15	-0.33	-0.02
Cropped	14	-0.13	-0.14	-0.43	-0.40
All	33	-0.15	0.05	-0.25	-0.03

§ Terrain attributes along the predominant wind direction, i.e. north-west direction

The GPR data provided further evidence of the effects of topography on snow distribution. It appeared that local variations in snow depth is strongly affected by small scale topographic features, in particular some manmade linear features. An example was shown in Fig. 4. The shallow snow depths at location b and e were likely due to the fact that these two locations are on the top of knolls. In contrast, a deep snow depth at location c may be a reflection of the local depression at this location. The effect of man-made linear features are most visible at location a and d, located near an in-field trench-like feature and a field boundary, respectively. In both cases, there were high peaks of snow depth observed.

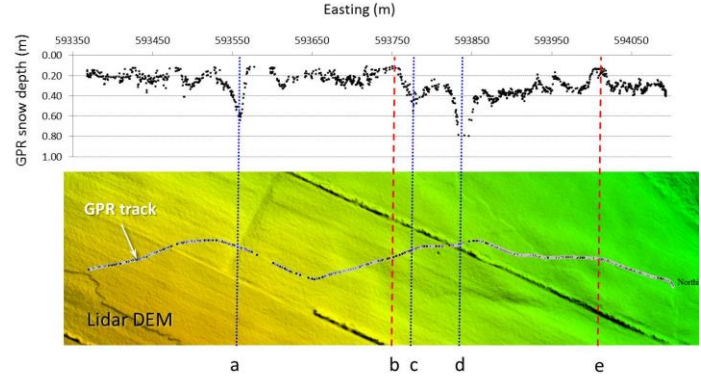


Figure 4. Upper: Snow depth along one of the 18 tracks, determined using a Ground Penetrating Radar unit the Black Brook Watershed; and Bottom: colored shaded relief map showing the topography and the position of the GPR survey track on the ground.

DISCUSSION

The effect of land use on snow distribution was expected. On forest and pasture lands, living plants serve as snow traps and prevent the redistribution of snow by wind. On cropped fields, the ground was mostly bare in the winter and fallen snow can be reactivated and redistributed by wind. The windblown snow can be deposited along field boundaries, roads or forest edges, creating large snow banks along these linear features (e.g., Fig. 4). On the other hand, additional surface roughness created by the living plants on forest and pasture lands may have contributed to the high variations in snow depth (Table 1). It should be noted that the snow survey was carried out in the transition period from winter to spring in BBW, when the snow cover is normally the deepest. However, the temperature rose earlier than normal in 2012 and snowmelt has started before the survey dates. As a result, the measured snow depth was not at its highest level. Also, the snow has high water content, especially towards the bottom of the snow profile, due to the high air temperature. This is evidenced in the high density of the snow (the ratio of WED over SnD is much higher than 0.1, which is the most common factor used to convert SnD to WED). To better understand the dynamic nature of snow redistribution snowmelt, future research is suggested to carry out multiple snow survey campaigns over the period of the snow coverage in the winter.

The non-significant correlations found between SnD/WED and terrain attributes could be due to several reasons. One possible reason is that the random variations of snow depth were too high to detect, with the limited sampling points we had. Another reason could be that there are strong interactions between different terrain attributes such that the effect of any individual terrain attribute was non-linear. Consequently, the simple linear correlation was not suited for the analysis and the coefficients were all non-significant. Lastly, the effect of topography may be scale dependent, as evidenced in the GPR data, which showing the effects of small scale topographic features and man-made linear features on local snow depth variations (Fig. 4). Future study is suggested to consider the use of multivariate models for statistical analysis to account for the interactions among variables and to examine the effects of the

same set of terrain attributes at different scales, extracted from DEMs of different grid sizes.

This study also tested the applicability of GPR on snow depth survey. The 500 MHz antenna appeared to work well with the snow depth range of 0.2 – 1.0 m. Due to the direct reflection of the device, snow depth within 0.1 m is nearly impossible to detect (reflection cannot be separated from the direct reflection from the unit itself). Beyond 2.0 m, return radio signals are mostly being absorbed by the snow and, therefore, are hard to detect. Nevertheless, the GPR did provide detailed snow depth information and can be very useful in future studies of snow depth survey.

CONCLUSIONS

Our field survey data suggested that land use had significant effect on snow distribution. Terrain attributes extracted from a 30 m DEM did not show significant correlations with snow depth but slope gradient and slope curvature did show consistent, although non-significant, negative correlations with snow depth, indicating possible effects of topography on snow distribution. GPR data further proves the strong effect of small scale topography and man-made features on snow distribution pattern.

ACKNOWLEDGMENT

This study is funded by the Watershed Evaluation of Best Management Practices (WEBs) project under the Agriculture and Agri-Food Canada. The authors would like to thank Dr. Wanhong Yang W. from U of Guelph for his valuable inputs, Mr. Andrew Ringeri and Hangyong Zhu from U of New Brunswick and John Monteith, Lionel Stevens and Sylvie Lavoie from the AAFC-PRC for assisting with field work. The author would also like to express their appreciations to the WEBs manage team, particularly Brook Harker, Terrie Hoppe, Irene Hanuta and Terra Jamieson for their continuous support.

REFERENCES

- [1] Chow, T. L. and Rees, H.W. 2002. Impacts of Intensive Potato Production on Water Yield and Sediment Load (Black Brook Experimental Watershed, 1992–2002 Summary). Agriculture and Agri-Food Canada, Fredericton, New Brunswick, 26 pp.
- [2] Guelph Watershed Evaluation Group, 2010. Modifying WetSpa and SWAT for snow redistribution in the Stepler and STC watershed, A Research Report to AAFC.
- [3] Li, S., J.A. Elliot, K.H.D. Tiessen, J. Yarotski, D.A. Lobb and D.N. Flaten. 2011a. The effects of multiple Beneficial Management Practices on hydrology and nutrient losses in a small watershed in the Canadian Prairies. *J. Environmental Quality* 40:1627-1642.
- [4] Yang Qi, Glenn Benoy, Zhengyong Zhao, Thien Lien Chow, Charles P.-A. 2011. Bourque and Fan-Rui Meng, Watershed-level analysis of exceedance frequencies for different management strategies, *Water Quality Research Journal of Canada*, 46, 64-73.

Extraction of loess shoulder-line based on object-based image analysis

Sheng Jiang

Key Laboratory of Virtual Geographic Environment
Nanjing Normal University
Nanjing, China
214230267@qq.com

Abstract—Based on the morphological characteristics of loess hilly and gully areas, a simple and effective method for extracting loess shoulder-lines based on object-based image analysis is proposed. A case study is conducted in the northern Shaanxi Loess Plateau of China and the digital elevation model with a grid size of 5 m is applied as original data in this research. In order to get clear edge of DEM slope, the convolution filter by Gauss Blur is applied to the original DEM. The slope image is calculated on the smoothed DEM. Then the landform DEM objects are obtained by contrast split segmentation. For the standard deviation values between gully-slope land and loess interfluvium are obvious different, the basic loess shoulder-lines could be extracted. While there are still small areas and other disturbing objects, the shoulder-lines will be refined by context and area values. At last, the final results are merged and exported. According to the accuracy assessment, the average extraction accuracies are about 88.7% and it is applicable in the loess area analysis.

diversity of the key structure lines in their spatial distribution could be used for analyzing terrain texture characteristics, which are essential basis for landform recognition and classification.

In recent years, many researches have focused on methods of extracting loess shoulder-lines and their geomorphology significance (Li et al., 2008; Tang et al., 2007; Xiao and Tang, 2007). In this paper, a simple and effective method for extracting loess shoulder-lines based on object-based image analysis (OBIA) is proposed. OBIA usually applies an image segmentation method which divide whole image into image objects. And then the image objects are classified by certain classification and extraction rules. Compared with traditional methods that use grid cell or pixel-based principles, OBIA conduct the operation in the way that reflects the human's vision when identifying image features.

INTRODUCTION

The Loess Plateau of China is a significant topographic area for its typical loess hills and gully landforms (Fu et al., 2000). Many researches have been carried out in the region over the last half a century, including soil erosion (Hessel and van Asch, 2003; Huang, 1955), land evaluation (Qiu et al., 2010; Shi and Shao, 2000) and topographic features (Jiang and Li, 1988; Lo, 1956; Xie et al., 2003), etc. Especially, each loess landform possesses peculiar slope composition which creates corresponding terrain texture on a particular spatial scale, such as platycladus-like texture, petal-like texture and finger-like texture and so on (Liu et al., 2012).

Shoulder-line, one important kind of the structural properties, has great geomorphologic significance in characterizing spatial distribution of terrain elements. The existence of loess shoulder-lines divides the loess surface into positive and negative terrain areas which occupy smooth top ridge land against steep rough valley land respectively. In addition, this zigzag shoulder-line that is a macro and instinctive topographic feature exhibits diverse morphology with different landform. Such similarity and

STUDY AREA AND METHODOLOGY

A. Study Area

The study area is Yijun that situated in the middle of the Loess Plateau, Shaanxi province, China. Yijun is loess residual tableland area and centered on 35°25'22''N, 109°38'52''E. The elevation is from 1125 m to 1742 m, and the gully density is 4.2 km/km². This landform is the residual state of loess tableland and in the later geologic development stage of the landform. Although with a flat top surface with approximately alike height, the overall tableland surface is actually dissevered into separated blocks. The shoulder-lines are in petaloid and finger like structure. The DEM data of Yijun in this research is from the contours of 1:50000 topographical maps and produced by the National Geomatics Center of China with a spatial resolution of 5 m.

B. Work flow of method

Fig. 1 summarizes the methods we used for the extraction method of loess shoulder-lines based on OBIA. The work flow of method is divided into 6 parts.

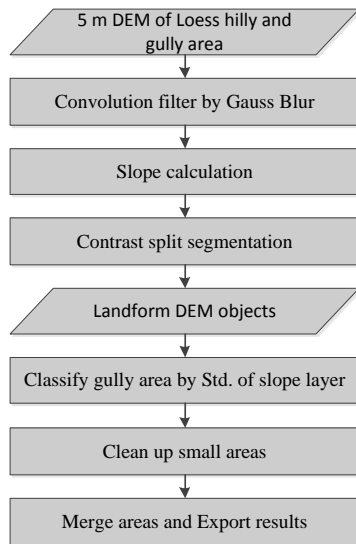


Fig. 1. Work flow of method

C. Contrast Split Segmentation

The contrast split segmentation algorithm divides an image into dark and bright regions. It is based on a threshold that maximizes the contrast between the resulting bright objects (consisting of pixels with pixel values above the threshold) and dark objects (consisting of pixels with pixel values below the threshold). Actually, a DEM is grid cell-based dataset which could be regarded as a specific image, and the common segmentation approach is also suitable for DEM based structural lines extraction.

It achieves the optimization by considering different pixel values as potential thresholds. The test thresholds range from the minimum threshold to the maximum threshold, with intermediate values chosen according to the step size and stepping type parameter. If a test threshold satisfies the minimum dark area and minimum bright area criteria, the contrast between bright and dark objects is evaluated. The test threshold causing the largest contrast is chosen as the best threshold and used for splitting. In this paper, the software eCognition 8.7 is used with this segmentation for the test.

C. Classification by standard deviation

The texture between gully-slope land and loess interfluvial area is obvious different, as shown in Fig. 2, the overall terrain of gully-slope land is more flat than loess interfluvial area. As a result, the standard deviation (Std.) values of DEM objects that obtained by segmentation are also different. According to the analysis and test, the Std. of DEM objects could be a classification criterion for gully-slope land and loess interfluvial area. If the loess interfluvial area has been classified, the loess shoulder-lines are also obtained.

The classification method here is using threshold method. Assign the DEM objects to the class specified by the use class Std. values.

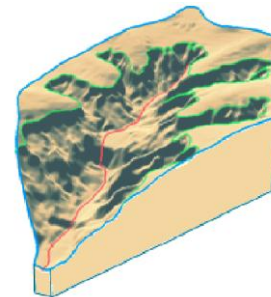


Fig. 2. An illustration of loess gully.

RESULT AND DISCUSSION

To demonstrate the procedure and result of the extraction method proposed, a test region is selected and performed (Fig. 3). As shown in Fig. 3 (a), this region is located in Yijun and it is one part of loess residual tableland. First of all, the DEM is smoothed by convolution filter with Gauss blur operator (Fig. 3b). Then the slope is calculated (Fig. 3c). Based on the slope image, the contrast split segmentation is applied (Fig. 3d). Then we classify gully area by Std. of slope object layer and refine the classification with context and area values (Fig. 3e). At last, the edge of gully area is the shoulder-lines and exported as the final result. Fig. 4 shows the results of other gullies.

In order to verify the extraction accuracy of this paper, the Euclidean Distance Offset Percentage (EDOP) is used for the accuracy assessment. The manually extracted products delineated with high-resolution digital orthophoto map are employed as the criterion which will assess the extraction accuracy. The assessment result is shown by Table 1.

TABLE 1 ACCURACY ASSESSMENT

	Figure Name			
	Fig. 3f	Fig. 4a	Fig. 4b	Average
LS	150.2	318.0	340.0	269.4
LS in EDSL	136.8	277.6	298.2	237.5
EDOP	91.1%	87.3%	87.7%	88.7%

Note: LS= Length of shoulder-lines(m); LS in EDSL= Length of shoulder-lines within EDSL

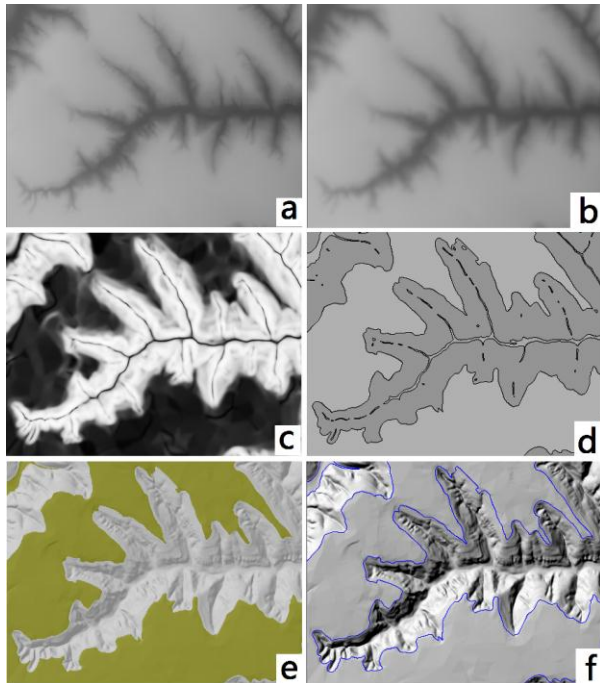


Figure 3. An example of extraction for loess shoulder-lines. a) original DEM; b) results by convolution filter; c) slope image; d) image objects by contrast split segmentation; e) classification result; f) final result.

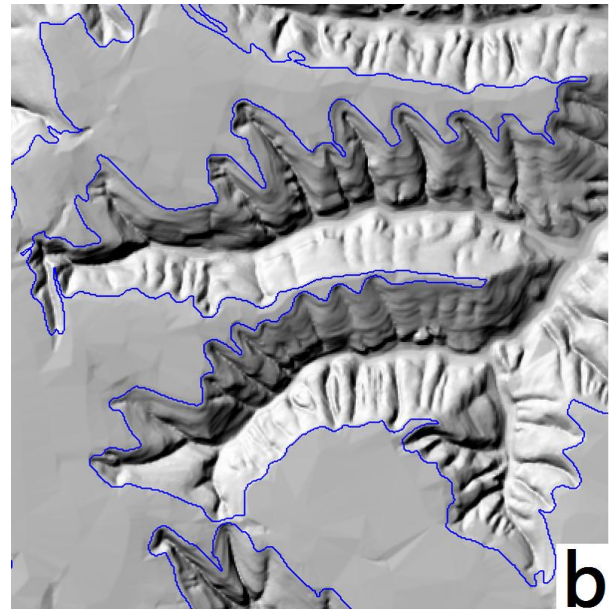
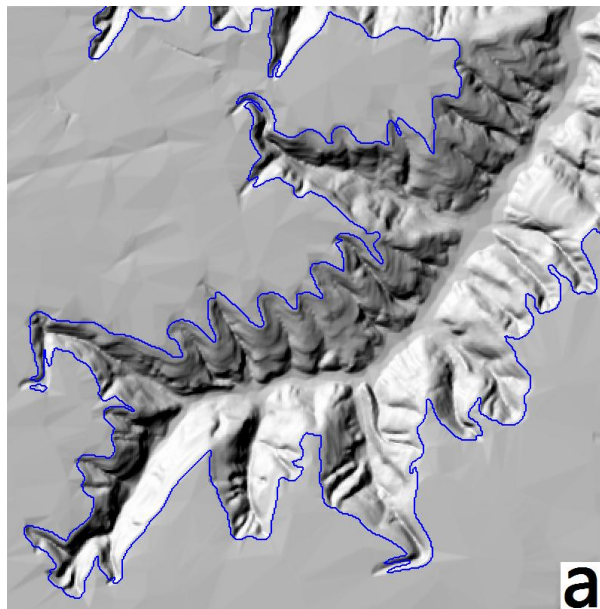


Fig. 4. Results of other gullies.

CONCLUSION

In this paper, a simple and effective method for extracting loess shoulder-lines based on object-based image analysis is proposed. The main conclusion is as follows.

1. The OBIA method offers a simple and effective extraction process of loess shoulder-lines, and its average extracted accuracy is about 88.7%, which is applicable in the loess area analysis.
2. The contrast split segmentation algorithm is useful in the DEM slope. The DEM objects obtained by this segmentation provide fine basis for extraction of loess shoulder-lines.
3. The texture between gully-slope land and loess interfluve is obvious different. As a result, the Std. of DEM objects can be a classification criterion for loess gully.

It should be noted that our research has focused on small region. Therefore, further researches are expected to testify the large area and complex regions. In addition, the formation and development mechanism of loess shoulder-lines are expected to be investigated.

ACKNOWLEDGMENT

This research was supported by the National High Technology Research and Development Program of China (2011AA120303), the National Natural Science Foundation of China (No.40930531, No. 41171320) and the Resources and Environment Information System State Key Laboratory Open Fund Projects (No.2010KF0002SA).

REFERENCES

- [1] Fu, B.J., Chen, L.D., Ma, K.M., Zhou, H.F., Wang, J., 2000. The relationships between land use and soil conditions in the hilly area of the Loess Plateau in northern Shaanxi, China. *Catena* 39, 69–78.
- [2] Hessel, R., van Asch, T., 2003. Modelling gully erosion for a small catchment on the Chinese Loess Plateau. *Catena* 54, 131–146.
- [3] Huang, B.W., 1955. Lessons learnt from mapping regional differentiation of soil losses in the middle reaches of the Yellow River. *Science Bulletin* 6, 15–21. [in Chinese].
- [4] Qiu, Y., Fu, B., Wang, J., Chen, L., Meng, Q., Zhang, Y., 2010. Spatial prediction of soil moisture content using multiple-linear regressions in a gully catchment of the Loess Plateau, China. *Journal of Arid Environments* 74, 208–220.
- [5] Shi, H., Shao, M., 2000. Soil and water loss from the Loess Plateau in China. *Journal of Arid Environments* 45(1), 9–20.
- [6] Jiang, Z., Li, X., 1988. Study on the rainfall erosivity and the topographic factor of predicting soil loss equation in the loess plateau. *Memoir of Northwestern Institute of Soil and Water Conservation Academia Sinica* 7, 40–45. [in Chinese].
- [7] Lo, L.H., 1956. A tentative classification of landforms in the Loess Plateau. *Acta Geographic Sinica* 22(3), 201–222. [in Chinese].
- [8] Xie, K., Wu, Y., Ma, X., Liu, Y., Liu, B., Hessel, R., 2003. Using contour lines to generate digital elevation models for steep slope areas: a case study of the Loess Plateau in North China. *Catena* 54, 161–171.
- [9] Liu, K., Tang, G., Tao, Y., Jiang, S., 2012. GLCM based quantitative of terrain texture form DEMs. *Journal of Geo-information Science* 14(6), 751–760.
- [10] Li, X., Wang, G., Li, R., 2008. A DEM based method for extraction of valley shoulder line and slope heel line. *Bulletin of Soil and Water Conservation* 28 (1), 69–72. [in Chinese].
- [11] Tang, G., Xiao, C., Jia, D., Yang, X., 2007. DEM based investigation of loess shoulder- line. In: *Proceedings of Geoinformatics 2007: Geospatial Information Science*, Nanjing, China, Vol. 6753, pp. 6753.
- [12] Xiao, C., Tang G., 2007. Classification of valley shoulder line in Loess Relief. *Arid Land Geography* 30(5), 646–653. [in Chinese].

Scale-effect of Hypsometric Integral in Loess Plateau

Zhu Shijie

1. Key Laboratory of Virtual Geographic Environment,
Ministry of Education
Nanjing Normal University, Nanjing, China
2. Zhejiang Academy of Surveying & Mapping,
Hangzhou, China
zsjsdx1025@163.com

Tang Guoan

1. Key Laboratory of Virtual Geographic Environment,
Ministry of Education
Nanjing Normal University
Nanjing, China
tangguoan@njnu.edu.cn

Abstract—The Loess Plateau is gully and hilly with serious soil erosion and thus a thorough study on the landscape development and erosion process with the scope of small watershed is of vital importance for ecological restoration of this region. As a macroscopic landscape analyzing method, hypsometric integral could be used for a comprehensive analysis on the development stages and process of small watersheds. Nevertheless, this method could produce distinct scale-effect and consequently an in-depth recognition on the finest analysis scale is a basis for properly understanding the characteristics and development of the watershed. This paper, with small watershed in Loess Plateau as the object of study, elaborately analyzes the scale-effect of hypsometric integral from the perspectives of analysis scale, statistical scale and regional scale based on 5-meter-resolution DEMs. The results show that, with the increase of hypsometric series under analytical scale, the integral value decreases sharply to close to the true value, yet the decreasing range narrows greatly and finally hypsometric curve becomes more accurate. As DEM resolution in statistical scale rises, hypsometric integral value basically remains unchanged, and this value is closely related to the other two land surface parameters, depth of surface cutting and relief height of landscape. Moreover, when considering regional scale in the same landscape, the smaller the analytical area is, the greater the integral value difference will present. At last, the integral value tends to remain steady when analytical area reaches a certain degree. This paper lays a foundation for further analysis of watershed characteristics.

I . INTRODUCTION

Hypsometric integral is a terrain analysis factor with apparent physical and geomorphologic meanings which could reflect the landform erode stage and evolution process. As a macroscopic parameter and method in terrain analysis, the applications of hypsometric integral could reveal the quantitative characteristic of landform evolution in watershed scale.

Horton firstly put forward quantitative indicators to describe watershed morphology in 1932, followed by Strahler (1952, 1963)

and other geomorphologists who constantly improved and complemented the quantitative description indicator system of the watershed (Schumm, 1956; Morisawa, 1964; Lu, 1991). Chen and Jiang (1986) summerized quantitative interrelations between watershed quantitative description indicator system and factors involved in their book Watershed Geomorphologic Mathematic Model. Hypsometric integral, initiated by American geomorphologist Strahler as early in 1952, mainly studied the relationship between regional horizontal section area and hypsometry, which contributes a great deal to the quantitative Davis Theory of Geomorphological Cycle. And later, scholars at home and abroad made further studies on it. Willgoose (1998) analyzed how the watershed morphology and drainage density influenced hypsometric integral. Moreover, Masek (1994) and Montgomery (2001) concluded that different sediments and runoffs had a great impact on hypsometric integral. Chen (2005) analyzed the variations of hypsometric integral from the aspect of drainage area and spatial distribution. Walcott (2008) illustrated specifically the spatial distribution of hypsometric integral in different scales with watershed in southeastern Africa as study object. With respect to the application of losses geomorphy, Wu (1965) comprehensively explained hypsometric integral's application in geography and pointed out its insufficiency mainly related to the conceptual feature of the curve. He held that it could only be used to summarize the characteristics of landform morphology. Besides, Ai (1987, 1988) proposed the comentropy of the watershed erosion system based on hypsometric integral and introduced the concept of linear unbalanced comentropy into the study of watershed system. Li and Lu (1990) developed erosion integral on the basis of hypsometric integral and analyzed the characteristics of watershed development stages from the angle of erosion. In addition, Xin (2008) made a spatial chart of hypsometric integral in losses plateau and drew the conclusion that with the variance of resolution, HI value, short for hypsometric integral, remained steady (100m as a starting point), while as analytical window increases gradually, HI value decreases by power function. Liao (2008) held that hypsometric integral could reflect present landform status and erosive

tendency of the watershed, and the size and changing trend were closely related to whether watershed bottom reached basement.

As scale-effect widely existing in geo-analysis, therefore, a good comprehension on it is the key to providing the basis for thorough understanding of geographical characteristics and geographical phenomenon process. DEM itself depends so heavily on scale that scale-effect is absolutely inevitable while using DEM to calculate hypsometric integral value. Liu (2007) summarized the scale-effect of DEM, analyzed DEM scale conceptual model and scale system, and argued that scale could be classified into two groups, namely, geographical scale and representation scale with the latter including analytical scale, structural scale and sampling scale. This paper, with typical small watershed in loess plateau as a study case and DEM data as basic data source, analyzes basic characteristics of hypsometric integral within small watershed and explores the influence on hypsometric integral posed by analytical scale, digital scale and regional scale contained in application of hypsometric integral.

II. DATA AND METHODS

A. Sample Region and Data

The Loess Plateau is covered with gully and hilly areas and soil erosion is serious. This paper concentrates on severely erosive area in loess plateau and selects typical types of loess landforms with three regions respectively loess tableland, loess ridge and loess hill (Fig.1). Then, based on watershed completeness and data accessibility, taking 1:10000 DEM of national fundamental geographic data as basic data, it extracts three small watersheds and analyzes integrated characteristics and scale-effect of its hypsometric integral.

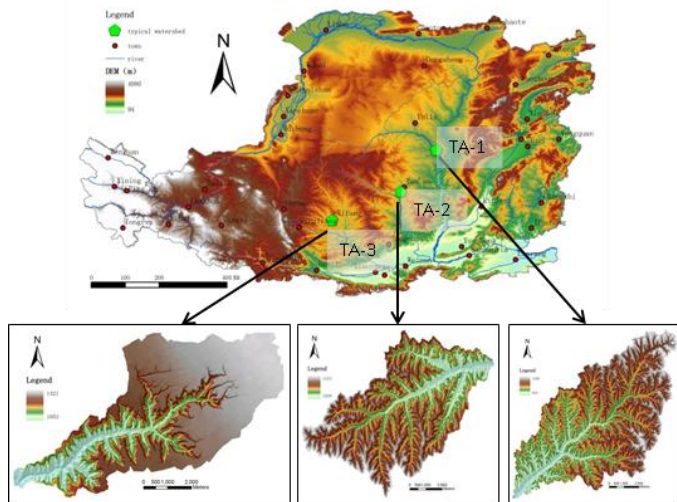


Figure 1. Distribution of test areas on the Loess Plateau

B. Method

The paper takes ArcGIS9.3 as a processing platform for sub-catchment division and DEM re-sampling and programs with MatLab software to calculate hypsometric integral. Firstly, it analyzes the influence produced by hypsometric classification in hypsometric integral calculation and curve plotting, namely analytical scale. Then, with respect to DEM resolution, a discussion is made here on variance of hypsometric integral value with different resolution. Finally, it works out hypsometric integral of sub-catchments differing in watershed area within the small watershed and discusses the issues on regional scale of hypsometric integral.

III. SCALE-EFFECT ANALYSIS

Watershed Size Effect

Hypsometric integral is a regional macro-statistical indicator analyzing landform characteristics within the region. Obviously, analysis results are inevitably diverse with different regions. How to ensure the stability of hypsometric integral under various landforms is a problem we must deal with. Meanwhile, hypsometric integral also serves as an indicator to show development stage of watershed and rectangular window analysis method by no means can summarize its basic characteristics completely. Therefore, the paper, in analysis of integral dependence, calculates integral value by using watershed analysis window with whole watershed as its object. The details are as follows: first, divide small watershed into several sub-watersheds by threshold value, and grant such sub-watersheds corresponding classification according to Strahler's classification and level of catchment network. Then, draw complete sub-watershed in accordance with classification and calculate hypsometric integral value. At the same time, in sub-watershed division, certain inter-areas exist which have a water inlet thus differing from complete watershed. The boundaries of such inter-areas aren't watershed in strict sense due to the existence of the inlet. The inter-areas lie in middle and lower reaches of gully that are traversing across. Compared with higher reaches of the gully, that is gully head areas, the erosion here is relatively weaker and the integral value is lower accordingly, which to some extent shows this type of watersheds maintain stable and stay in their later stage of erosion. Thus, same as the watershed classification, this type of sub-watershed is not considered here.

Three levels of several sub-watersheds can be gained by dividing three small watersheds, hypsometric integral value can thus be figured out. The scatter diagram on the integral value and sub-watershed is as follows (Fig. 2), from which we can see that the range of integral value is wide while the area of sub-watershed is small. With the increasing area of sub-watersheds, its integral value has a trend of convergence. The terrain feature can be displayed by a series of the combination of landform characteristic, which absolutely occupy some space. When its area is smaller than a certain value (stable area), the

geomorphologic feature of the landform types cannot be completely displayed, which will increase the uncertainty of the indicators reflecting the terrain feature. Just like the stability of the slope spectrum (Tang, 2008), the hypsometric integral, as a statistical indicator, also has the inner characteristic of area stability.

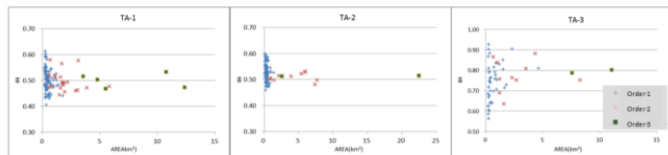


Figure 2. HI against the Watershed Size

IV CONCLUSION

The hypsometric integral value represents a function related to surface cutting depth and relief amplitude, but it is unrelated to its own classification series and DEM resolution. However, it is essential to choose the classification series in drawing the hypsometric curve. With the increase of classification, the integral value figured out on the basis of different levels has a trend of gradual decrease with sharp amplitude. That is, when the classification reaches a certain level, the magnitude is less than five ten thousandth as the integral value only changed very slightly. As a result, the influence on the integral value can be ignored. Similarly, due to the characteristic of hypsometric integral, basically it has the trend of constant arrangement in the calculation of its value with different DEM resolution. However, it also has a certain fluctuation, which is much consistent to the maximum or minimum fluctuations of DEM resolution. This is mainly because the re-sampling method, which, to some extent, has changed the hypsometric extreme value of DEM. When the precision of hypsometric integral is guaranteed, it is reliable to determine the value based on coarse DEM resolution. When the areas of sub-watersheds are small, the differences among the hypsometric integral values are very large in the same type of landforms, mainly because the local area of sub-watersheds is too small to represent and completely reflect the terrain feature of its landform. Consequently, it is necessary to consider its area dependence in order to reveal the development laws of characteristics of watersheds in the analysis of regional difference of landforms using the hypsometric integral method.

ACKNOWLEDGMENT

This research is supported by National Natural Science Foundation of China (No. 40930531, 41071188); Open Foundation of State Key Laboratory of Resources and Environmental Information System (No. 2010KF0002SA).

REFERENCES

- [1] Horton, R.E. 1932. "Drainage basin characteristics". Transactions of the American Geophysical Union.
- [2] Strahler, A.N. 1952. "Hypsometric (area-altitude) analysis of erosional topography". Geological Society of America Bulletin, 63, 1117-1142.
- [3] Strahler, A.N. 1963. "The earth sciences, Harper and Row". Pub New York and London.
- [4] Schumm, S.A. 1956. "The role of creep and rainwash on the retreat of Badland slopes". Amer. Jour. Sci., 254: 693-706.
- [5] Morisawa, M.E. 1964. "Development of drainage systems on an upraised lake floor". Amer. Jour. of Science. 262, 341-354.
- [6] Lu, Z.C., Jia, S.F., Huang, K.X., Yuan, B.Y. 1991. "Watershed Landform System". Dalian: Dalian Press (in Chinese).
- [7] Cheng, J.C., Jiang, M.Q. 1986. "Digital Model of Watershed Landform". Beijing: Science Press (in Chinese).
- [8] Willgoose, G., Hancock, G. 1998. "Revisiting the hypsometric curve as an indicator of form and process in transport limited catchments". Earth Surface Processes and Landforms, 23: 611-623.
- [9] Masek, J.G., Isacks, B.L., Gubbels, T.L., Fielding, E.J. 1994. "Erosion and tectonics at the margins of continental plateaus." Journal of Geophysical Research, 99: 13941-13956.
- [10] Montgomery, D.R., Balco, G., Willet, S.D. 2001. "Climate, tectonics, and the morphology of the Andes". Geology, 29: 579-582.
- [11] Chen, Y.J., Zheng, G.Y., Song, G.C. 2005. Influence of Area and Space Dependence for Hypsometric Integral and its Geological Implications, journal of Geographical Science (Taiwan), 39:53-69. (in Chinese)
- [12] Walcott Rachel C. Summerfield M.A. 2008. "Scale dependence of hypsometric integrals: An analysis of southeast African basins". Geomorphology. 96:174-186.
- [13] Wu, H.H. 1965. "Application of Hypsometric curve". Acta Geographica Sinica, 31(2):157-169. (in Chinese)
- [14] Ai, N.S. 1987. "Comentropy in Erosional Drainage-System". Acta Conservations Soil. 1(2):1-8. (in Chinese)
- [15] Ai, N.S., Yue, T.X. 1988. "Second Discussion of the Comentropy of Drainage-System." Acta Conservations Soil. 2(4):1-9. (in Chinese)
- [16] Xin, Z.B., Xu, J.X., Ma, Y.X. 2008. "Hypsometric Integral Analysis and its Sediment Yield Implications in the Loess Plateau, China." Journal of Mountain Science. 26(3):356-363. (in Chinese)
- [17] Li, Q., Lu, Z.C., Yuan, B.Y. 1990. "Quantitative Study of the Stage of Geomorphological Evolution." Acta Geographica Sinica. 45(1): 110-120. (in Chinese)
- [18] Liao, Y.S., Cai, Q.G., Qin, F., Zhang, J.B., Ding, S.W. 2007. "Study on Topographic Evolution and the Eroding Trend in Hilly Loess Areas, North China." Journal of Mountain Science. 26(3):347-355. (in Chinese)
- [19] Liu, X.J., Lu, H.X. 2007. "Scale Issues in Digital Terrain Analysis and Terrain Modeling." Geographical Research. 26(3): 433-442.
- [20] Tang, G.A., Li, F.Y., Liu, X.J. Research on the Slope Spectrum of the Loess Plateau. Science in China Series E: Technological Sciences, 2008, 51(Supp.1): 175-185.

The scale effect analysis of slope length based on DEM multi-scale representation

Weiling Guo¹, Qinke Yang², Haijiang Wang³,
Rui Li⁴

(1. Anhui University of Science & Technology, Huainan, Anhui, 232001; 2. College of Urban and Environment, Northwest University, Xi'an,

710069, 3. Hebei University of Engineering, Handan, Hebei, 056038; 4. Institute of Soil and Water Conservation Chinese Academy of Sciences Ministry of Water Resources, Yangling, Shaanxi, 712100)

ABSTRACT: It's the only way to extract slope gradient and slope length based on low-resolution DEMs for the studies of regional scale soil erosion modeling. But the slope gradient will reduce and the slope length will enlarge. In Xiannangou catchment, a database of DEM is established by using the wavelet multi-resolution analysis method, which has a gradually-changing resolution and a unified position control base, and effective ability in representing the overall topographic characteristics and landform macro structure. On this basis, we deeply reveal that the variation pattern of the slope length increases as the DEM resolution becomes coarser. The results show that, with DEM resolution become coarser, the gully elevation is rising, while the Liang and Mao top elevation are decreasing, and the small-scale gully, Liang and Mao top are gradually disappeared. Average slope length has a linearly increasing trend with the reduction of DEM resolution, and slope length cumulative frequency curve is moving towards larger value. In general, the overall slope length is enlarged, and the enlarging mainly happens in the middle and bottom of slopes.

Keywords: DEM multi-scale representation, wavelet multi-resolution analysis, slope length increase, scale effect of slope length

INTRODUCTION

Slope gradient and slope length are two of the most important terrain indexes which influence soil erosion^[1]. These two indexes are normally extracted from DEMs with lower resolution in the research of regional soil erosion.

However, slope gradient tends to decrease^[2-8] and slope length tends to increase^[9] as resolution becomes coarser. These make the calculated slope gradient and slope length not accurate enough to describe the real relief of terrain. Thus the accuracy of hydrology and soil erosion model is declined^[8, 10, 11]. At present, the studies on slope gradient decreases are more. For slope length increases, some researchers have paid attention to this phenomenon and its effect, but there are few research reports about scale effect of slope length. Therefore, it has a very important significance for regional scale soil erosion research to study on the rule and mechanism of low-resolution slope length increases.

DEM is the basic data of terrain factor extraction and digital terrain analysis and application^[12, 13]. Multi-scale DEM data in the same area have become the basic DEM data source of terrain factor scale effect analysis. And wavelet analysis method with the reputation of "mathematical microscope" is a striking similarity to the basic idea of spatial data multi-scale representation which provides an effective way to analyze and express different resolution DEMs.

METHOD

The study area and base data

The study area locates in Xiannangou Catchment in Loess Hilly and Gully Region in the Loess Plateau. It is a square area with 25km. The area is a typical Loess Hilly-Gully area with complex terrain surface and intensively soil erosion.

The original DEM data is the

Hydrological-correct DEMs (Hc-DEMs)^[14, 15] of high resolution (2.5m) generated by 1:10 000 scale digital topographic map using AUNDEM software. In addition, taking the Hc-DEM data with the resolution of 10m, 25m and 50m generated by 1:50 000, 1:100 000 and 1:250 000 scale digital topographic map as reference data. The projection is Gauss_Kruger based on the Krasovsky 1940 Datum.

Wavelet transform and slope length extraction

Wavelets are mathematical functions that decompose signals into different frequency components, and represent each component with a resolution matched to its scale. The elegance of the wavelet multi-resolution analysis of $L^2(R)$ comes from the fact that the scaling functions φ generate a set of nested subspaces V_j of $L^2(R), j \in Z$, while the associated wavelets ψ constitute their orthogonal complementary subspaces W_j , i.e. $V_j = V_{j+1} \oplus W_{j+1}$. $f(x)$ is represented with a set of orthonormal basis in V_{j+1} ($\{\varphi_{j+1,k}, k \in Z\}$) and W_{j+1} ($\{\psi_{j+1,k}, k \in Z\}$), i.e.

$$f(x) = \sum_n c_n^{j+1} \varphi_{j+1,n} + \sum_n d_n^{j+1} \psi_{j+1,n} \cdot \quad (1)$$

Here,

$$c_k^{j+1} = \sum_n h_{n-2k} c_n^j, \quad (2)$$

$$d_k^{j+1} = \sum_n g_{n-2k} c_n^j. \quad (3)$$

That is orthogonal wavelet decomposition procedure for discrete signal. Here j are levels of wavelet decomposition; h_{n-2k} is scaling coefficients and g_{n-2k} is wavelet coefficient of a wavelet system, respectively corresponding to low-pass and high-pass filter coefficient.

Since the wavelet transform is a filtering process, it is efficient for wavelet transform to reconstruct the original signal using either

de-convolution or the inverse filter. Wavelet reconstruction function is

$$c_n^j = \sum_{k \in Z} h_{n-2k} c_k^{j+1} + \sum_{k \in Z} g_{n-2k} d_k^{j+1} \quad (4)$$

Where c_k^{j+1} is low-frequency component; d_k^{j+1}

is high-frequency component; c_n^j is wavelet reconstruction component; h_{n-2k} is low-pass filter coefficient of wavelet reconstruction; g_{n-2k} is high-pass filter coefficient of wavelet reconstruction.

The orthogonal wavelet decomposition and reconstruction equations are theories basis of DEM multi-scale representation when DEM is regarded as a discrete signal.

Since DEM multi-scale representation is a process of filtering partial fractal terrain, and considering such as compactly supported, symmetric, orthogonal, regularity and larger cancellation, we select biorthogonal wavelet function bior4.4. In addition, the Radical Law Selection Principles^[16], traditionally feature selection principle used in artificial cartographic generalization, was used to set different scale parameters during the threshold processing on the wavelet high frequency coefficients. i.e.

$$N_b = N_a \sqrt{M_a / M_b} \quad (5)$$

Here, N_a and N_b is respectively the number of high frequency wavelet coefficients of 2.5m resolution and derived DEM. M_a is the scale denominator of the source map; M_b is denominator of scale parameters of the derived DEM used in the implement of wavelet transform.

The calculation method of slope length is runoff accumulation algorithm based on the soil erosion principle^[17], which flow direction algorithm is used by multiple flow direction algorithms (MS)^[18].

RESULTS AND ANALYSIS

A set of DEMs are established by using the

wavelet multi-resolution analysis method, which has a gradually-changing resolution and a unified position control base, and effective ability in representing the overall topographic characteristics and landform macro structure. Fig.1 shows the DEM multi-scale representation.

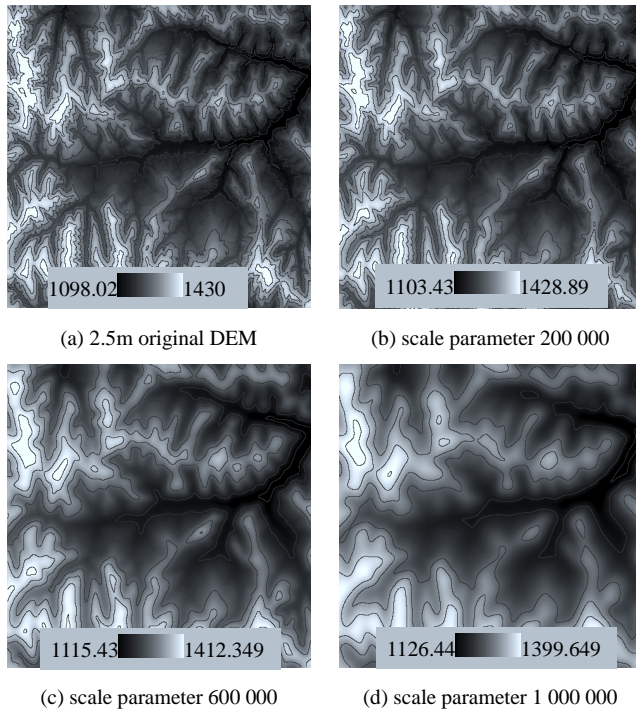


Fig.1 DEM multi-scale representation of different scale parameters with wavelet transform

On this basis, we deeply reveal that the variation pattern of the slope length increases as the DEM resolution becomes coarser. Taking the Hc-DEM data with the resolution of 10m, 25m and 50m generated by 1:50 000, 1:100 000 and 1:250 000 scale digital topographic map using ANUDEM software in Xiannannou Catchment as reference data, the paper evaluates the quality of the generated DEMs, which have different scale parameter and obtained by using wavelet transform method using the elevation shannon, playback contours and slope gradient histogram similarity. Then, the relationship between the scale parameter and resolution is established (Fig.2). Hence, the generation of DEMs with arbitrary coarser resolutions is realized.

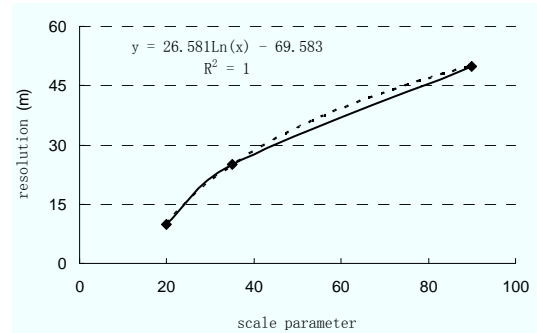


Fig.2 the relationship curve between DEM scale parameters after wavelet transform and DEM resolutions generated by digital topographic map

Based on the multi-resolution database obtained by using wavelet transform, the variation pattern of slope length along with the changing of DEM resolution is analyzed. The results show that with DEM resolution become coarser, the gully elevation is rising, while the Liang and Mao top elevation are decreasing, and the small-scale gully, Liang and Mao top are gradually disappeared. Average slope length has a linearly increasing trend with the reduction of DEM resolution (Fig.3). In general, the overall slope length is enlarged, and the enlarging mainly happens in the middle and bottom of slopes (Fig.4).

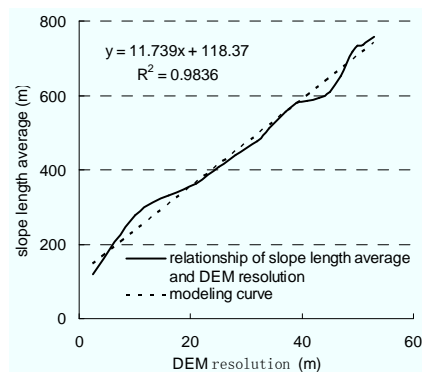
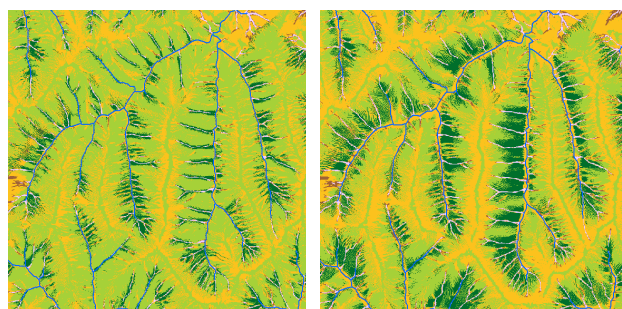


Fig.3 Change trend of average slope length with DEM resolution become coarser



(a) scale parameter 200 000 (b) scale parameter 400 000

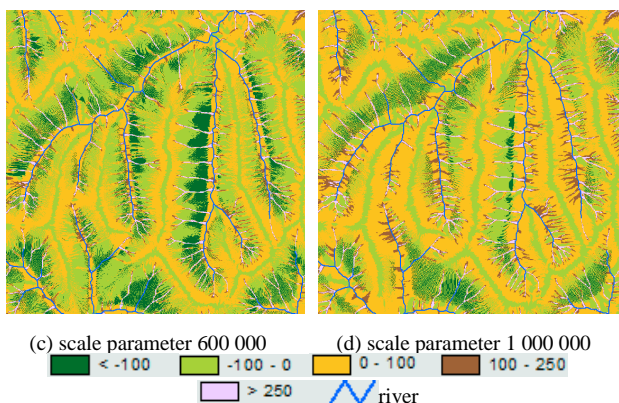


Fig.4 The slope length differential map extracted by DEM of 2.5m resolution and different scale parameter

CONCLUSIONS

With the analyses above, we can conclude that: A database of DEM is established by using the wavelet multi-resolution analysis method, which has a gradually-changing resolution and a unified position control base. Slope length increases along with DEM resolution become coarser and the location of slope length changing is mainly in the middle and bottom of slopes.

DISCUSSIONS

According to this study, slope length on the scale of the DEM resolution has great dependence. Therefore, In large scale range, such as regional scale, it is need to transform slope length extracted from the low resolution DEM to that of the high-resolution with higher accuracy and consistent ability to reflect the terrain relief, so that the Calculated LS factor can be applied for the regional soil erosion evaluation and it has guiding significance for the national soil erosion survey and actual soil and water conservation measures.

ACKNOWLEDGMENT

This study has been financially supported through the projects Estimating Spatially Distributed Slope Length at Watershed for Soil Erosion Assessment (NSFC Project, 41071188) and Study on theoretical distribution model of Slope (NSFC Project, 41301284).

REFERENCES

[1] Wischmeier, W. H. and Smith, D. D. Predicting rainfall

erosion losses from cropland east of the Rocky Mountains: A Guide for soil and water conservation planning. USDA Agriculture Handbook. 1978. 537.

[2] David, M. W. and Gregory, J. M. Differences in topographic characteristics computed from 100- and 1000-m resolution digital elevation model data. *hydrological processes* [J]. 2000, 14: 987-1002.

[3] Gao, J. Resolution and Accuracy of Terrain Representation by Grid DEMs at a Micro-scale. *International Journal of Geographical Information Science* [J]. 1997, 11(2): 199-210.

[4] James, A., Thompson, J. C. B., Charles, A., et al. Digital elevation model resolution: effects on terrain attribute calculation and quantitative soil-landscape modeling. *Geoderma* [J]. 2001, (100): 67-69.

[5] Wolock, D. M. and McCabe, G. J. Differences in topographic characteristics computed from 100- and 1000-m resolution digital elevation model data. *Hydrological Processes* [J]. 2000, (14): 987-1002.

[6] Yang, Q. K., Jupp, D., Li, R., et al., Re-scaling lower resolution slope by histogram matching, in *Advances in Digital Terrain Analysis (Lecture Notes in Geoinformation and Cartography)*, Q.M. Zhou, B.G. Lees, and G.A. Tang, Editors. 2008, Springer. p. 193-210.

[7] Yin, Z. Y. and Wang, X. H. A cross-scale comparison of drainage basin characteristics derived from Digital Elevation Models. *Earth Surface Processes and Landforms* [J]. 1999, (24): 557-562.

[8] Tang, G. A., Zhao, M. D., Li, T. W., et al. Modeling slope uncertainty derived from DEMs in Loess Plateau. *Acta Geographica Sinica* [J]. 2003, 58(6): 824-830.

[9] Guo, W. L., Yang, Q. K., Cheng, L., et al. Re-scaling method of slope length factor in the soil erosion assessment of regional scale. *Science of Soil and Water Conservation* [J]. 2010, 8(4): 73-78.

[10] Tang, G. A., Yang, W. Y., Qin, H. R., et al. An Application of using GIS technology to return hillside cultivated land for forestry and grassland in Loess Plateau region. *Bulletin of Soil and Water Conservation* [J]. 2002, 22(5): 46-50.

[11] Liu, X. H., Yang, Q. K., and Tang, G. A. Extraction and application of relief of China Based on DEM and GIS method. *Bulletin of Soil and Water Conservation* [J]. 2001, 21(1): 57-59, 62.

[12] Pike, R. J., Evans, I. S., and Hengl, T., *Geomorphometry: a brief guide*, in *Geomorphometry: Concepts, Software, Applications*, T. Hengl, Reuter, H. I. (eds), Editor. 2009, Amsterdam: Elsevier p. 3-30.

[13] Wilson, J. P. Digital terrain modeling. *Geomorphology* [J]. 2012, 137(1): 107-121.

[14] Hutchinson, M. F. A new procedure for gridding elevation and stream line data with automatic removal of spurious pits. *Journal of Hydrology* [J]. 1989, 106(3): 211-232.

[15] Hutchinson, M. F. *ANUDEM version 5.1 user guide*. 2004, Canberra: Centre for resource and environmental studies, The Australian National University.

[16] Topfer, F. and Pillewizer, W. The principles of selection, a means of cartographic generalization. *Cartographic Journal* [J]. 1966, 3(1): 10-16.

[17] Yang, Q. K., Guo, W. L., Zhang, H. M., et al. Method of extracting LS factor at watershed scale based on DEM. *Bulletin of Soil and Water Conservation* [J]. 2010, 30(2): 203-206, 211.

[18] Quinn, P., Beven, K., Chevallier, P., et al. The prediction of hillslope flow paths for distributed hydrological modelling using digital terrain models. *Hydrological Processes* [J]. 1991, 5(1): 59-79.

Characterize the spatial patterns of perennial waterlogged cropland using the micro-geomorphology structure in Jiangnan Plain, middle reaches of the Yangtze River

Xiao Fei, Yan Yi, Feng Qi, Ban Xuan

Institute of Geodesy and Geophysics, Chinese Academy of Sciences
Hubei Key Laboratory for Environments and Disaster Monitoring and Evaluating
Wuhan, Hubei Province, P.R.China
xiaof@whigg.ac.cn

Abstract Artificial micro-geomorphology would show increasing potential in understanding the interactions between natural environment and human activities. In this paper, we try to analyze the relationship between the spatial patterns of perennial waterlogged cropland and the micro-geomorphology structure in Jiangnan Plain. The method is an integration of the identifying index of slope position and the calculation of topographic index. The result shows preferable agreement with the waterlogged area identified from remote sensing and soil map. It confirms that the geomorphological methods are effective to simulate the distribution of waterlogged croplands, even in an alluvial plain with complicated hydrogeology regimes.

INTRODUCTION

Currently, activities that humans rearrange and utilize the land have been a more and more powerful geomorphic force, and artificial micro-geomorphology has played an increasing role in the distribution of some disasters. Compared with large scale geomorphological conformations, micro-geomorphology is of small space-scale, and more easily influenced by human activities. However, little has been done to associate geomorphology and natural disasters directly^[1,2]. In this paper, we try to analyze the relationship between the spatial patterns of perennial waterlogged cropland and the micro-geomorphology structure in Jiangnan Plain.

As a kind of agricultural disaster, waterlogging phenomenon is widespread in the earth, especially in some cropping regions of floodplains. Waterlogging poses a serious threat to the world's

productive agricultural land, and these threats have made vast expanses of land totally unsuitable for cultivation. In developing countries which depend heavily on agriculture, the menace of waterlogging is of more immense concern. In china, waterlogging is one of the most harmful disasters comparable with flood in the reaches of Yangtze River^[3].

Because of the violent human activities to geomorphology, there are ferocious complex hydrological regimes in the waterlogging vulnerable areas. Besides, monitoring sites are often scarce in most waterlogging areas. Consequently, it is difficult to use hydrological modeling in this situation, and hardly any existing way is available currently to get a quantificational result. Considering that geomorphology determining topography and the nature of deposits, thus water pathways and residence times, and has a tight connection with human activities, it is assumed here that the spatio-temporal patterns of waterlogging fields could be simulated directly from the geomorphology. Therefore, the aim of this paper is to use the micro-geomorphology structure and some related indexes for the delineation and characterization of waterlogged cropland. Given the wide availability of DEM over the recent years, this method presents the advantage to be easy and possible over large areas integrated with remote-sensing or field surveys. .

STUDY AREA AND DATA

Jiangnan Plain is an alluvial plain formed by the deposition of sediments over a long period of time by the Yangtze and Hanjiang Rivers. Elevations of the most areas in Jiangnan Plain are below 50 m. However, the low-lying fluvial landforms,

abundant rainfall, vast runoff from rivers, and inappropriate land use patterns in some regions of the plain often cause soil saturation and surface flooding. We select a small region as the sampling area in the Jiangnan Plain. Location of the sampling area is shown in figure.1. It is one of the typical geomorphology units in the plain with a shape like dish. Perennial waterlogged croplands are widespread in the plain, and also occurred in this place.

Data used in this research mainly include observations and measurements from different sources: SRTM (Shuttle Radar Topography Mission) DEM, Landsat ETM+ images captured in 2000 and 2004, and soil map, in addition to ground observations.

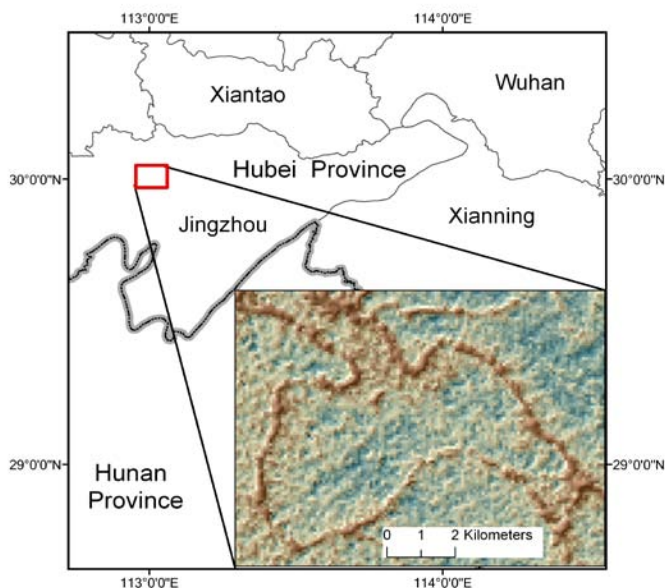


Figure 1. Location of the study area

METHODS

As far as the study methods are concerned, the waterlogging vulnerability is studied mainly by the following methods: numerical simulation from the hydrological and hydraulic modeling, socioeconomic method integrated with meteorological method, and comprehensive analysis of the cause of waterlogging. Those methods requires a lot of data which is lacking in most cases and it is difficult to study the waterlogging risk happened in a broad region. Moreover, waterlogging fields are always located in landscapes with little topographic relief, thus hydrologic modeling in low-lying, flat terrain poses significant difficulties due to a lack of significant topographic gradients.

Because geomorphology is the main factor that determines water pathways, predicting of the spatial distribution of areas with high water content would be through the way by using the geomorphology. Many researchers used the topographic index as an index of saturation. For example, Curie et al. (2007) attempted to predict the extent of waterlogged soils by using the topographic index. At present, there are many other studies of using indirect topographic/landform site factors for the indication of vegetation, soil, snowcover, wetland, etc. They all could show the potential of the quantitative, exclusively geomorphology-based methods for the delineation and characterization of waterlogged cropland.

The research could be made up of three parts: (1) monitoring the spatial patterns of waterlogged fields, (2) interpreting the geomorphology structure and extracting relevant factors, and (3) quantifying and modeling the effects of geomorphology to the distribution of waterlogged fields. The methods are an integration of geomorphology, remote sensing, GIS and geostatistical analysis.

A method is developed by integrating the local topography analysis and the overland flow simulation to extract the structures of artificial micro-geomorphology. Differences between the local elevation of each pixel and the average elevations of around pixels within different distances are calculated first in the local topography analysis process. Then the appropriate distances are evaluated to obtain the size of analysis window. Using the moving window statistics, potential pixels in the structure lines of artificial micro-geomorphology can be filtered from the whole study area. Afterwards, flow simulation was used to identify the real pixels in the structure lines out of the all the potential pixels.

Spatial patterns of waterlogged croplands are identified using remotely sensed images according to its ecological and thermodynamic characteristics. According to field surveys, the characteristics of waterlogged cropland not only show sub-surface physicochemical features, but also show ecological and thermodynamic appearances. We use the time series of indexes including land surface temperature and the Normalized Difference Vegetation Index (NDVI) extracted from Landsat ETM+ images to monitor the waterlogged cropland. The way to retrieve the Land Surface Temperature (LST) using single channel of Landsat scenes is described by Jimenez-Munoz and Sobrino [4]. NDVI are calculated from Landsat images using the formula of $(\text{band } 4 - \text{band } 3) / (\text{band } 4 + \text{band } 3)$.

Parametrization of micro-geomorphology is the key step to characterize the spatial distribution of the waterlogged cropland. Terrain shape characteristics such as slope, peaks, topographic index, and profile curvature, etc could be easily derived from digital elevation models. However, in order to build up geomorphologic models, it is necessary to develop new geometric characteristics [5], and to integrate the existing factors into an effective way. In this paper, we mainly use the index of

slope position and topographic index to model the distribution of waterlogged cropland.

Result and discussion

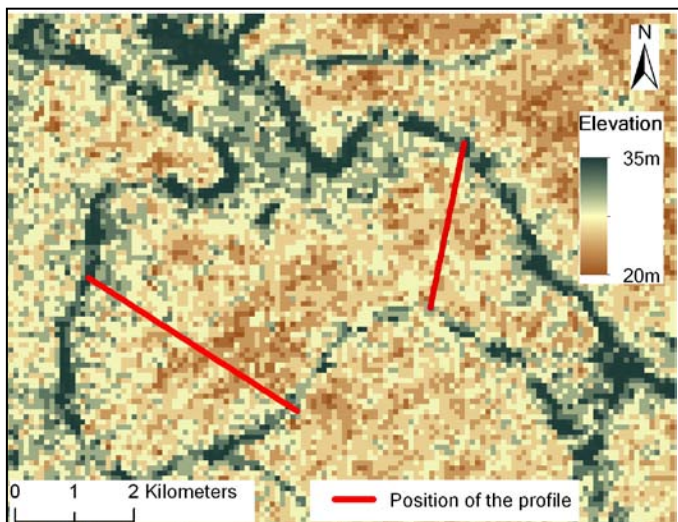


Figure 2. DEM of the study area

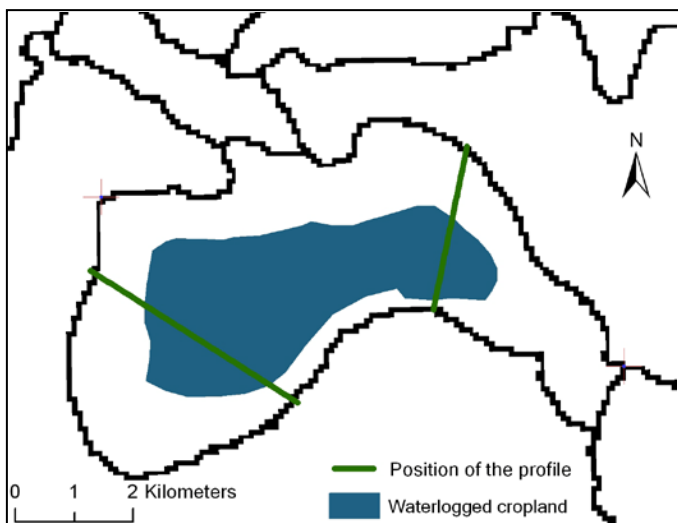


Figure 3. The extracted micro-topography structure and the area of the waterlogged cropland

The typical morphological structure of micro-topography in Jiangnan Plain is characterized by enclosed embankments on the low-lying land. As shown in figure 2, this kind of morphological structure of micro-topography looks like a dish and divides the plain to hundreds of unit. In this sample area, the elevation ranges

from 20m to 35m. Using the method of local topography analysis and the overland flow simulation, the skeleton lines of the enclosed micro-topography structure can be extracted automatically. Figure 3 shows the extracted micro-topography structure with dark line. Waterlogged cropland is extracted using remotely sensed imaged and soil map, and is demonstrated using cyan color in Fig.3. It can be found that the waterlogged cropland is located in the central area of the micro-topography unit.

Fig.4 and Fig.5 shows two profiles of the terrain and the locations of waterlogged cropland in the profiles. Red lines are the fitted quadratic polynomial lines. The positions of the profiles are shown in Fig. 2 and Fig.3. The sections between green lines are the ranges of waterlogged cropland areas in Fig.4 and Fig.5.

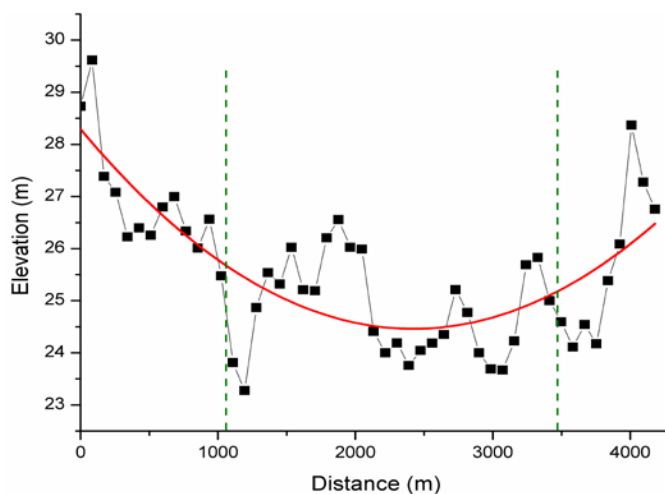


Figure 4. Profile of the terrain and the locations of waterlogged cropland in the profile 1.

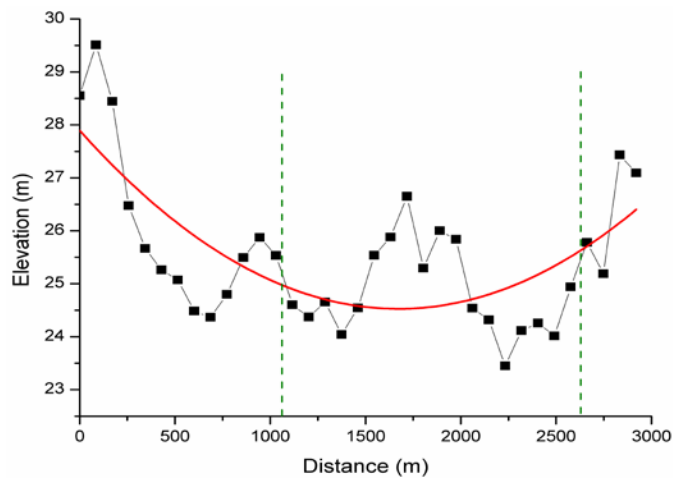


Figure 5. Profile of the terrain and the locations of waterlogged cropland in the profile 2.

It is evident that the waterlogged disaster occurred in the bottom of the pitch arcs of the fitted lines. Therefore, the potential waterlogged area can be identified according to the slope position in the enclosed structure. Topographic index is another way to simulate the distribution of the waterlogged cropland. We calculate the index using multiple-flow-directions algorithm. Afterwards, the two results are compared and integrated to the last simulation result. The simulated waterlogged cropland in the sampling area is shown in Fig.6.

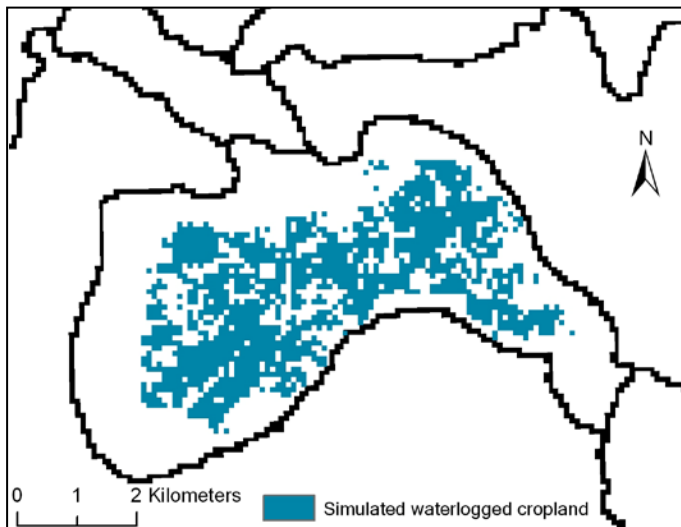


Figure 6. Simulation result of the waterlogged cropland.

CONCLUSION

The result shows acceptable agreement with the waterlogged area identified from remote sensing and soil map. It confirms that the geomorphological methods are effective to simulate the distribution of waterlogged croplands, and the artificial micro-geomorphology shapes the spatial patterns of the waterlogged soil. Even in an alluvial plain with complicated hydrogeology regimes, the micro-geomorphology is still one of the major driving factors for waterlogged croplands distribution, despite that waterlogged soil is essentially induced by high levels of groundwater. Geomorphology methods would be helpful for the estimation of the interactions among disaster spatial patterns, human activities and natural environment.

ACKNOWLEDGMENT

The study was supported by National Natural Science Foundation of China (41271125) and National Program on Key Basic Research Project of China (2012CB417001).

REFERENCES

- [1] Alcántara-Ayala, I., 2002. "Geomorphology, natural hazards, vulnerability and prevention of natural disasters in developing countries." *Geomorphology*, 47p.
- [2] Curie, F., S. Gaillard, and A. Ducharne, 2007. "Geomorphological methods to characterise wetlands at the scale of the Seine watershed." *Science of the Total Environment*, 375p.
- [3] Yin, H., C. Li, 2002. "Human impact on floods and disasters on the Yangtze River." *Geomorphology*, 41p.
- [4] Jimenez-Munoz, J. C., and J. A. Sobrino, 2003. "A generalized single-channel method for retrieving land surface temperature from remote sensing data." *J. Geophys. Res.-Atmos.*, 108p.
- [5] Hörsch, B., 2003. "Modelling the spatial distribution of montane and subalpine forests in the central Alps using digital elevation models." *Ecological Modelling*, 168p.

DEM Based Extraction and Analysis of Loess tableland

Chiming Tong, Cheng Weiming*, Zhang Wenjie

¹ State Key Laboratory of Resource and Environmental Information System,
Institute of Geographic Science and Natural Resources Research, CAS,
Beijing, China

Abstract

Landscape is an important part of the natural environment, it has a significant impact on the formation and development of various surface hydrological processes. So the object of this study is to develop morphology analysis methods for extracting loess tableland automatically. The study area lies between 32° and 41°N, and between 107° and 114°E. The data used includes an ASTER GDEM and geomorphological map. The methodology developed for loess tableland extraction includes preprocessing of the digital data—that is, filtering of the Digital Elevation Model (DEM) for noise removal. A classification technique is then expanded. At the first, DEM is enhanced. For the second, binaryzation is implemented and two terrain factors are assisted in the extraction. For the third, broken patches and boundary lines will be modified. Finally, we used expert knowledge to verify the result. At the end, the extracted loess tableland is compared to the boundary that is delineated manually and the standard deviation between them is satisfactory. Then, we compute some index about the result. And we find that most patches' areas are 1~10km². Beam tablelands' areas are usually less than 5km² and broken tablelands' areas are usually less than 20km². The minimum value of fractal dimension is 1.15, the maximum value is 1.40 and the mean value is 1.27. Edge density is negatively related to the area but shape index is positive correlation.

Keywords: Loess tableland; DEM; morphology

1 INTRODUCTION

Loess plateau is under the action of accumulation and transportation, as well as the impact of wind, water, gravity and human interaction, and is based on the geomorphology of underlying strata, according to a variety of developmental patterns, ultimately forming the basic landscape of the loess plateau and the regular combination of landforms. Loess plateau as the accumulation of the world's largest and youngest plateau, with its unique formation, typical geomorphic features, holds an important role in the ecological environment, and it has attracted the attention of Chinese and many researchers in the world for a long time, and got guiding significance achievements in a lot of production and practice.

Geomorphic type is an important factor for basin erosion and sediment yield in hydrologic model parameters. The traditional landscape classification and cartography mainly adapt the method of topographic map measurement combined with the field survey^[1,2]. But it is low precision and strong subjectivity. Along with the development of computer graphics and GIS technology, people began to use remote sensing, and digital elevation model to extract geomorphic features. By these photos and methods, it has greatly improved the speed and accuracy of the landscape classification^[3].

In 1964, Hammond first suggested automatic classification method for geomorphic types, he pointed out that the slope and relief amplitude in statistical cell can identify types^[4]. This idea was completed by Dikau in 1991^[5] and then it was modified by Brabyn and Morgan^[6,7]. Dikau use a square grid as a statistical unit while Brabyn use a circle one in order to reduce the error when calculated the small relief terrain. Philip T. Giles^[8] use DEM to extract slope unit automatically; Dragut^[9] extracted elevation, slope, profile curvature and plane curvature etc, and then he used image segmentation method to classify. Weiming Cheng^[10] used SRTM-DEM quantitatively extract basic landform types of Chinese landscape. Since then, many experts studied automatic classification of regular statistical unit^[11-14]. All these studies used regular statistical region to calculate all kinds of terrain factors(such as relief degree, surface roughness, elevation etc), and realized the rapid classification. While their disadvantages are obvious.

2 DATA SOURCE

The ASTER Global Digital Elevation Model (ASTER GDEM) is a joint product developed and made available to the public by the Ministry of Economy, Trade, and Industry (METI) of Japan and the United States National Aeronautics and Space Administration (NASA). It is generated from data collected from the Advanced Spaceborne Thermal Emission and Reflection Radiometer (ASTER), a spaceborne earth observing optical instrument. The ASTER GDEM covers land surfaces between 83°N and 83°S and is composed of 22,600 1°-by-1° tiles. Tiles that contain at least 0.01% land area are included. The ASTER GDEM is in GeoTIFF format with geographic lat/long coordinates and a 1 arc-second (30 m) grid of elevation postings. It is referenced to the WGS84/EGM96 geoid. Pre-production estimated accuracies for this global product were 20 meters at 95 % confidence for vertical data and 30 meters at 95 % confidence for horizontal data.

Study Area lies between 32° and 41°N, and between 107° and 114°E. It is situated east of Taihang mountains, west to Riyu mountain in Qinghai, south to Qinling and north to Ordos plateau and occupies an area of about 648700 km².

3 METHODOLOGY

(1) Image enhancement

It is conducive to extract the morphological unit when the line of the morphology cell of the loess plateau is clear. So it uses median filter method to remove noise and keep the image details.

(2) Image binaryzation

After the enhancement, it needs to set a proper threshold to divide the image into black and white. Because the features of the two classifications are very similar, so it is difficult to implement segmentation and there is a need to add additional information. Here we choose slope and relief amplitude to assist the extraction. According to the previous study, we choose 5 degree as the critical point. In this study, we choose 17*17 as the analysis window and then accord to the specific situation in the study area to adjust the threshold. Through many experiments and statistics of each patch, we use 20meters to 100meters as interval.

(3) Morphological filter

There are some broken patches for the extraction due to the grid data feature or arithmetic reason, it is very essential to deal with the result. First, we use boundary clean tool to clean up the outline of the type to smooth it. Then, using region group tool to statistic the number of the pixel in each type, and the result is named of 'RegionGroup'. In the attribute table of statistical result, there is a field named 'COUNT' and we need it to judge a proper threshold to eliminate.

(4) Expert knowledge

The extracted results will be transfer into vector format and then superimposed on the remote sensing image to judge whether the boundary line is right or not.

3.2 Accuracy assessment

Accuracy test is executed from two aspects. It uses the extracted result to compare with the previous work and then computing the error. It should compute the standard deviation between the automatic one and the manual region. In order to make the result more accurate, we choose three regions to test. They are Changwu, Xiaoyi and Yanchang.

(1) Qualitative evaluation

Qualitative evaluation mainly judge whether the automatic one within the corresponding type of the 1:10 000 000 geomorphologic map. And on the other hand, checking whether the outline of automatic one surpass outline of the manul one.

(2) Quantitative evaluation

The extraction accuracy was discussed according to area discrepancy(Ad) between the automatic one and the manual one. Table 1 shows the comparisons of the two results. Both of the results have satisfying accuracy. It is obviously that the main advantage of this approach is good accuracy and good application suitability.

TABLE 1 COMPARISONS OF THE EXTRACTED RESULT BETWEEN AUTOMATIC ONE AND MANUAL ONE

Site	Automatic one (Km ²)	Manual one (Km ²)	Percentage of Ad(%)	Ad (Km ²)
Changwu	140.440	161.071	12.81	20.631
Xiaoyi	9.385	10.264	8.60	0.879
Yanchang	32.657	36	10.24	3.343

4 QUANTITATIVE DEPICT

Systematic indicators are necessary for the depiction of the loess tableland quantitatively. Considering the characteristics of tableland on the Loess Plateau, four indices were proposed to quantitatively depict the geomorphologic landscape properties. Table 2 shows the definition for calculation these indices. Fig.a is curved according to the smallest area and other graphs are curved according to the number of fig.a.

TAVLE 2 DEFINITION FOR TABLELAND INDICATORS

Indicators	Definition	Remark
Area		
Fractal dimension (FD)	$2 * \ln P / \ln A$	P is perimeter A is area
Edge density(ED)	$(P/A) * 10^6$	
Shape index(SI)	$P / 2 \text{Sqrt}(\pi * A)$	

In the study area, small area patches are main part. Less than 10km² area patches are 80.2%。 Among these, most patches area are 1~10km²。 More than 10km² patches are mainly distribute on both sides of

the Weihe river. After superposition 1000000 terrain data and through analysing the corresponding patch on geomorphic types, we find that beam tablelands` area are usually less than 5km² and broken tablelands` area are usually less than 20km², and some famous loess tablelands ,such as Dongzhi tableland and Luochuan tableland, the area of which are more than 100km².

TABLE 3 AREA STATISTICAL

Area (km ²)	<1	1-10	10-100	>100
number	392	516	174	50
percentage (%)	34.6	45.6	15.4	4.4

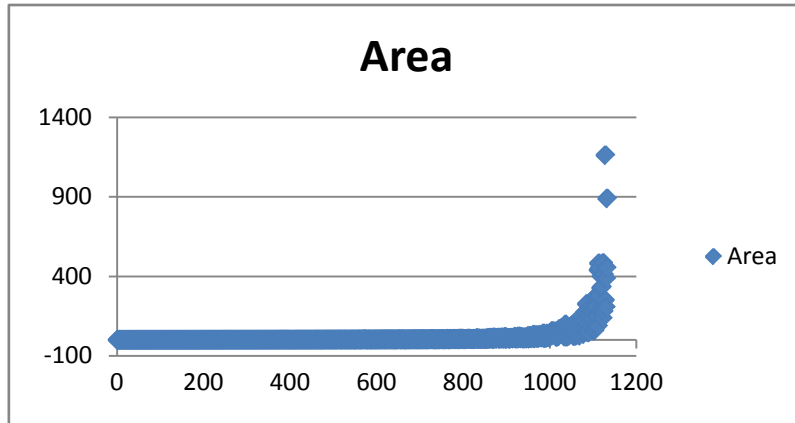


Fig. a

Fractal dimension is an indicator which reflects the shape complexity of the loess tableland. This index reflects the difference between different physiognomy types. The more complex landform is, the bigger the fractal dimension value is. The minimum value is 1.15 ,the maximum value is 1.40 and the mean value is 1.27. This results are almost the same with previous study^[16]. At the same time, Fig.b shows that fractal dimension and graphic area are not correlative. We can deduce that erosion maybe not on the surface in the process of loess tableland.

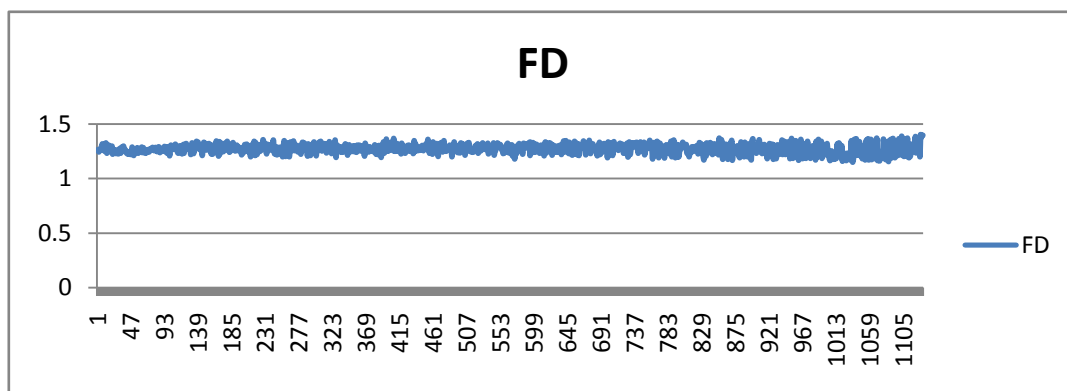


Fig. b

Edge density can quantify the change of the boundary of the loess tableland in the process of relief development. By the Fig.a and Fig.c, we can know that the larger the area of the patches are, their edge density are smaller.

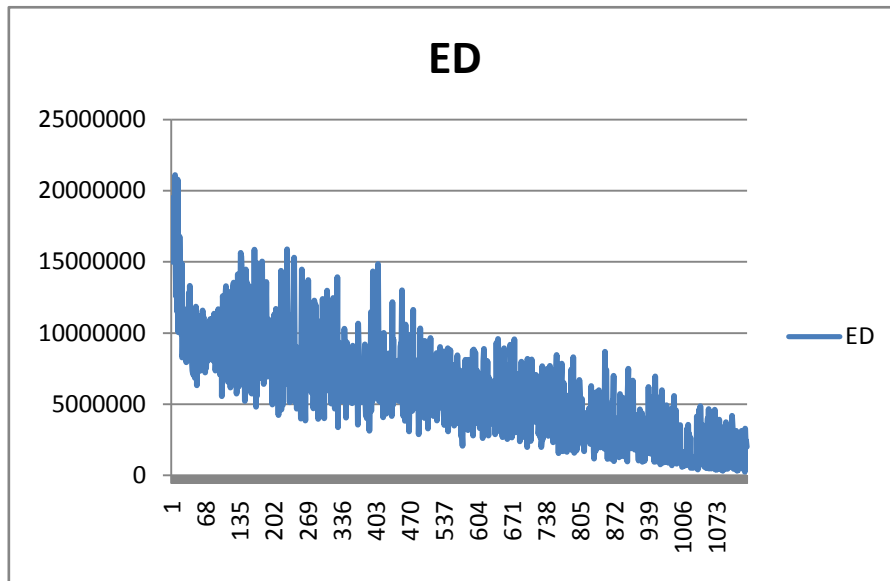


Fig. c

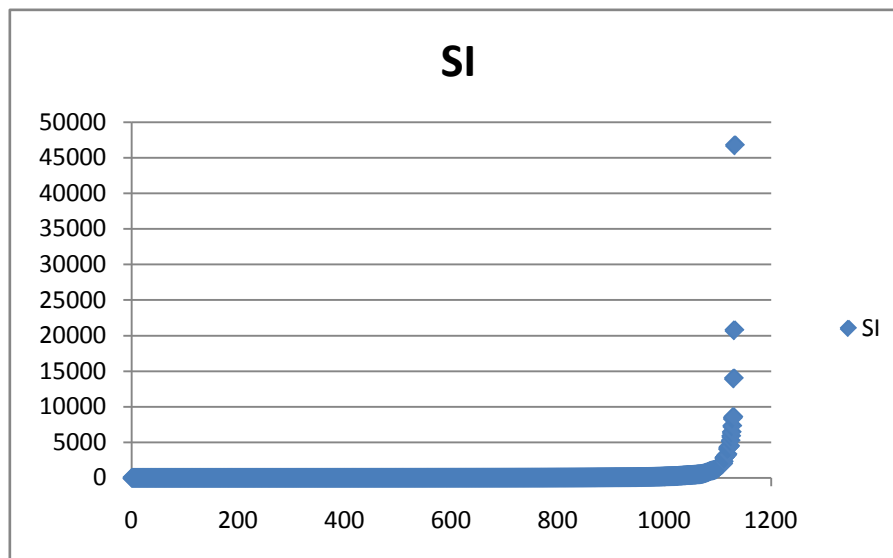


Fig. d

Shape index shows the deviation between patches and the same area circle. Using this index is to quantify the process from complete tableland to beam tableland. When graphic shape is round, its value is one. The more SI is, the greater long and narrow of the graphics. Combining with the area of statistical analysis, fig.d shows that complete tableland which area are more than 100km² increases, the greater deviation from one. But beam tableland and broken tableland are more like circle.

5 CONCLUSIONS

(1) By the technique of GIS and digital terrain analysis, a semi-automatic extraction method based upon the terrain character is proposed. Validation test shows that this method has obvious advantages on extraction accuracy and application adaptability compared with the manual extraction.

(2) Four indices of loess tableland are proposed for quantifying the geomorphologic land, statistical characteristics and spatial distribution characteristics. Most patches's areas are 1~10km². Beam

tablelands` s areas are usually less than 5km² and broken tablelands` s area are usually less than 20km². The minimum value of fractal dimension is 1.15 ,the maximum value is 1.40 and the mean value is 1.27. Edge density is negatively related to the area but shape index is positive correlation.

Since this is just the initial stage of the research, more issues are needed to make deeper cognition on this topic. In the following study, we will further study the morphology of the loess tableland and relative age.

REFERENCES

- [1] SU Shiyu,Li Juzhang.Geomorphological mapping[M].Beijing: Surveying and mapping press, 1999
- [2] P A Burrough, P F M van Gaans, R A Mac Millan.High resolution landform classification using fuzzy k-means[J].Fuzzy Sets and Systems,2000,(113):37-52
- [3] Tang Guoan,Liu Xuejun,Lv Guonian.The principle and method of digital elevation model and geological analysis [M].Beijing: Science press,2005
- [4] Hammond E H. Analysis of properties in landform geography: An application to broad-scale landform mapping[J].Annals of Association of American Geographers,1964(54):11-19
- [5] Dikau R,Brabb E E,Mark R M. Landform classification of New Mexico by computer [M].U.S.Geological Survey,1991.
- [6] Brabyn L.GIS analysis of macro landform[M].//SIRC, The 10th Colloquium of the Spatial Information Research Centre.New Zealand:University of Otago,1998,35-48
- [7] Morgan J M, Lesh A M. Developing landform maps using ESRI's ModelBuilder[C].ESRI User Conference 2005 Proceedings. <http://gis.esri.com/library/userconf/froc05/papers/pap2206.pdf>,2005.
- [8] Philip T.Giles Steven E. Frank lin.An automated approach to the classification of the slope units using digital data[J].Geomorphology, 1998,21:251-264
- [9] Dragut L, Blaschke T, Automated classification of landform elements using object-based image analysis[J].Geomorphology,2006(81):330-344
- [10] CHENG Weiming, ZHOU Chenghu, CHAIHuixia. Quantitative Extraction and Analysis of Basic Morphological Types of Land Geomorphology in China[J]. Geo-Information Science,2009,6(11):725~735
- [11] ZHU Hong-chun, CHEN Nan, LIU Haiying, etc. Research on the relief baesd in 1:10000 DEMs—A case study in the loess plateau of north Shaanxi province[J].Science of Surveying and Mapping,2005,30 (4): 86-88
- [13] LIU Aili, TANG Guoan.DEM Based Auto-classification of Chinese Landform [J]. Geo-Information Science,2006,8(4): 8-14
- [14] LANG Lingling, CHENG Weiming, ZHU Qijiang,etc.A Comparative Analysis of the Multi-criteria DEM Extracted Relief –Taking Fujian Low Mountainous Region as an Example[J]. Geo-Information Science,2007,9(6):1-8
- [15] ZHOU Yi, TANG Guo an, YANG Xin. Positive and negative terrains on northern Shaanxi Loess Plateau[J], Science in China Press,2010,20(1):64-76

Extend the Analysis window to improve the Geo-Computation

ZHAO Mingwei^{1,2}

(State Key Laboratory of Resources and Environment Information System, Institute of Geographic Sciences and Natural Resources Research, CAS, Beijing 10010, China; 2. University of Chinese Academy of Sciences, Beijing 100049, China;)

Many Geo-Science models demand computation of partial derivative, such as slope/aspect model, kinds of curvature model, and the HASM. It is quite obvious that the accuracy of the partial derivative could affect the last computation result. Nowadays, the basic difference scheme to compute partial derivative is central difference, which is simple but the accuracy is also low. So it is important to find new difference scheme that could afford higher accuracy and don't demand more memory and more solution time.

In order to construct the demanded difference scheme, firstly we analyze the error source during the computation of the partial derivative. Take the central difference as example, the computation of central difference is based on 3×3 window (Fig 1).

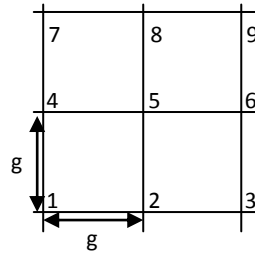


Fig.1 3×3 local moving window

Suppose we have to compute the partial derivative at point 5, considered the Taylor expansion:

$$f(x + g, y) = f(x, y) + f_x(x, y)g + f_x''(x, y)g^2 / 2 + f_x'''(\xi_x, y)g^3 / 3! \quad (1)$$

$$f(x - g, y) = f(x, y) - f_x(x, y)g + f_x''(x, y)g^2 / 2 - f_x'''(\gamma_x, y)g^3 / 3! \quad (2)$$

while, $\xi_x \in (x, x + g)$, $\gamma_x \in (x, x - g)$; f_x , f_x'' , f_x''' are respectively the first, the second, and the third partial derivative. Now we make the (1) subtract the (2), the error of the partial derivative at X direction could be represented as:

$$\begin{aligned} Error_x &= (f(x + g, y) - f(x - g, y)) / 2g - f_x(x, y) \\ &= g^2 [f_x'''(\xi_x, y) + f_x'''(\gamma_x, y)] / (2 \cdot 3!) \end{aligned} \quad (3)$$

Similarly, the error of the partial derivative at Y direction could be represented as:

$$Error_y = (f(x, y + g) - f(x, y - g)) / 2g - f_y(x, y)$$

$$= g^2 \left[f_y'''(x, \xi_y) + f_y'''(x, \gamma_y) \right] / (2 \cdot 3!) \quad (4)$$

while, $\xi_y \in (y, y + g)$, $\gamma_y \in (y, y - g)$; f_y' , f_y'' are respectively the first, the second, and the third partial derivative.

Through (3) and (4), it is obvious that the partial derivative error is directly proportional with the window size g^2 . So the error could be decreased if the window size is cut off. Suppose the new window size is half of the former, then we could get the new presentation of the error of partial derivative at X direction and Y direction:

$$\begin{aligned} Error_x' &= (f(x + g/2, y) - f(x - g/2, y)) / 2 \cdot (g/2) - f_x(x, y) \\ &= (g/2)^2 \left[f_x'''(\bar{\xi}_x, y) + f_x'''(\bar{\gamma}_x, y) \right] / (2 \cdot 3!) \end{aligned} \quad (5)$$

$$\begin{aligned} Error_y' &= (f(x, y + g/2) - f(x, y - g/2)) / 2 \cdot (g/2) - f_y(x, y) \\ &= (g/2)^2 \left[f_y'''(x, \bar{\xi}_y) + f_y'''(x, \bar{\gamma}_y) \right] / (2 \cdot 3!) \end{aligned} \quad (6)$$

while, $\bar{\xi}_x \in (x, x + g/2)$, $\bar{\gamma}_x \in (x, x - g/2)$, $\bar{\xi}_y \in (y, y + g/2)$, $\bar{\gamma}_y \in (y, y - g/2)$.

Suppose the window size is small enough, there are $f_x'''(\xi_x, y) \approx f_x'''(\bar{\xi}_x, y)$,

$$f_x'''(\gamma_x, y) \approx f_x'''(\bar{\gamma}_x, y), \quad f_y'''(x, \xi_y) \approx f_y'''(x, \bar{\xi}_y), \quad f_y'''(x, \lambda_y) \approx f_y'''(x, \bar{\gamma}_y).$$

Then we could get the following equations:

$$\frac{Error_x'}{Error_x} = \frac{1}{4}, \quad \frac{Error_y'}{Error_y} = \frac{1}{4} \quad (7)$$

Combine the (5)、(6)、(7)、(8) and (9), the new partial derivative at X direction and Y direction could be represented as following:

$$f_x(x, y) = \frac{1}{3} \left[4 \times ((f(x + g/2, y) - f(x - g/2, y)) / 2 \cdot (g/2)) - (f(x + g, y) - f(x - g, y)) / 2g \right] \quad (8)$$

$$f_y(x, y) = \frac{1}{3} \left[4 \times ((f(x, y + g/2) - f(x, y - g/2)) / 2 \cdot (g/2)) - (f(x, y + g) - f(x, y - g)) / 2g \right] \quad (9)$$

Since cut off the window size means change the resolution of the origin data such as DEMs, so we construct the new partial derivative model through extending the analysis window (Fig 2). Suppose we compute the partial derivative at point 13, then the partial derivative at X direction and Y direction could be represented as following:

$$\begin{cases} f_x = \frac{1}{3} [4 \times (z_{18} - z_8) / 2g - (z_{23} - z_3) / 4g] \\ f_y = \frac{1}{3} [4 \times (z_{14} - z_{12}) / 2g - (z_{15} - z_{11}) / 4g] \end{cases} \quad (10)$$

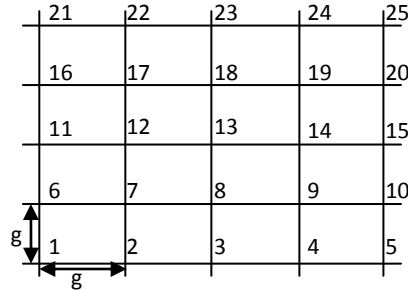


Fig.2 5 × 5 local moving window

We take slope calculation as example to test the accuracy of the new partial derivative computation model. Firstly, a mathematical surface (Fig 3) was selected to test the accuracy of the new model because the mathematical could afford the real slope value.

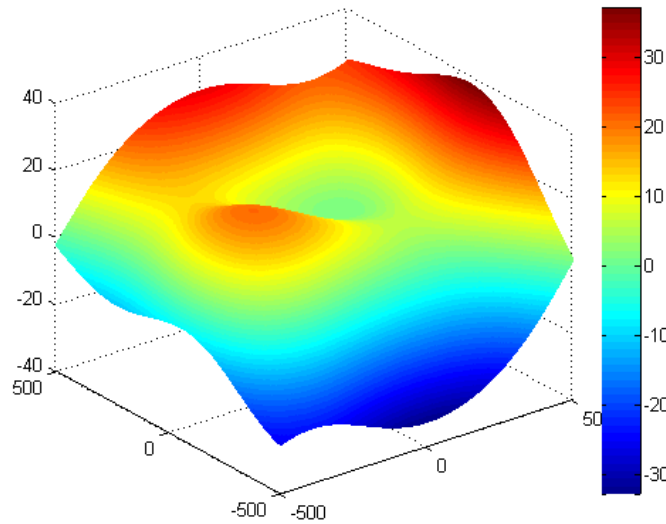


Fig 3 mathematical surface

The equation of the mathematical surface is:

$$f_1(x, y) = 10 \left[3 \left[1 - \left(\frac{x}{500} \right)^2 \right] e^{-\left(\frac{x}{500} \right)^2 - \left(\frac{y}{500+1} \right)^2} - 10 \left[0.2 \left(\frac{x}{500} \right) - \left(\frac{x}{500} \right)^3 - \left(\frac{y}{500} \right)^5 \right] e^{-\left(\frac{x}{500} \right)^2 - \left(\frac{y}{500} \right)^2} - \frac{1}{3} e^{-\left(\frac{x}{500+1} \right)^2 - \left(\frac{y}{500} \right)^2} \right]$$

Two kinds of DEMs with different resolution were generated based on the mathematical surface, one is 1m, and the other is 5m. Then slope was computed respectively use two slope models, one is based on central difference, and the other

is based on the new partial derivative difference scheme put forward in this paper. Table 1 shows the accuracy analysis result (RMSE of the calculation result) of the slope calculation.

Tab.1 Error analysis of slope

DEM resolution	Central difference	New difference scheme
1m	3.40×10^{-5}	4.46×10^{-10}
5m	8.41×10^{-4}	2.77×10^{-7}

The results show that the new model can significantly improve the accuracy of the result compared with the common models. This study enriches the analysis system of the digital terrain analysis system, and provides slope data of high accuracy for many Geo-science models. In addition, except slope, there are many terrain parameters which are calculated through finite difference, such as aspect and various kinds of curvature, and the methods of this paper could afford some useful references in improving the accuracy of such terrain parameters.

Reference:

- [1] LIU Xuejun. On the Accuracy of the Algorithms for Interpreting Grid-based Digital Terrain Model [D]. Wuhan: Wuhan University, 2002. (In Chinese)
- [2] Fleming, M.D., Hoffer, R.M., 1979, Machine processing of Landsat MSS data and DMA topographic data for forest cover type mapping: West Lafayette, IN, Purdue, University, Laboratory for Applications of Remote Sensing, LARS Technical Report 062879.
- [3] Unwin. 1981, *Introductory Spatial Analysis*, Methuen, London and New York.
- [4] Sharpnack, D.A., Akin, G., 1969, An Algorithm for computing slope and aspect from elevations, *Photogrammetric Survey*, 35: 247-248.
- [5] Horn, B.K.P. 1981, Hill shading and the reflectance map, *Proceedings of IEEE*, 69(1): 14-47.
- [6] ZHOU Qi-ming, LIU Xue-jun. Analysis of errors of derived slope and aspect related to DEM data properties [J]. *Computer & Geosciences*, 2004, 30:369-378.
- [7] Hodgson, M.E., 1995, What cell size does the computed slope/aspect angle represent? *Photogrammetric Engineering and Remote Sensing*, 61: 513-517.
- [8] Jones, K.H., 1998, A comparison of algorithms used to compute hill slope as a property of the DEM, *Computer and Geosciences*, 24(4): 315-323.
- [9] Carter, J.R., 1992, The effect of data precision on the calculation of slope and aspect using gridded DEMs, *Cartographica*, 29(1): 22-34.

Transitional relation exploration for typical loess geomorphologic types based on slope spectrum

Shangmin Zhao

Department of Surveying and Mapping, College of Mining
Technology

Taiyuan University of Technology
Taiyuan, China

zhaoshangmin@tyut.edu.cn, zhaosm@lreis.ac.cn

Weiming Cheng

State Key Laboratory of Resources and Environmental
Information System

Institute of Geographic Sciences and Natural Resources
Research, CAS, Beijing, China

chengwm@lreis.ac.cn

Abstract — This research aims to explore the transitional relationships for typical loess geomorphologic types and their sub-types based on slope spectrum. Using the Chinese Geomorphologic Database at 1:1,000,000 scales, the distribution of the typical geomorphologic types, such as loess tableland, loess ridge, loess hill and their sub-types (such as loess terrace, complete tableland, residual tableland, beam tableland, oblique ridge and mao ridge) is acquired; then, based on SRTM (shuttle radar topography mission)-DEM data and topographic analysis methods, the slope spectrums are computed for the loess typical geomorphologic types; through analyzing the slope spectrum characteristics of the loess typical geomorphologic types, the transitional relationships are explored: (1) the loess tableland transits to the loess ridge, and then transits to the loess hill; (2) the transitional order among the subtypes of the typical geomorphologic types is: from loess terrace to complete tableland, to residual tableland, then to beam tableland, to oblique ridge, and then to mao ridge and finally to loess hill.

INTRODUCTION

Slope spectrum, as a microscopic terrain index, can reveal the macro-geomorphologic features, which makes it a valuable topographic index in geomorphologic research [1]. Loess Plateau of China attracts world attention in geographic research because of its unique geomorphologic features. The slope spectrum index is applied in studying the loess geomorphology in many previous researches [2].

In previous researches, the loess geomorphology can be classified by using slope spectrum index. So the slope spectrum is an important topographic index in representing the characteristics of the loess geomorphologic types.

The achievement of the Chinese Geomorphologic Database (CGD) at 1:1,000,000 scales provides the distribution of the loess geomorphologic types; as to the slope spectrum index, it can be computed based on the digital elevation model (DEM) data,

which is shuttle radar topography mission (SRTM) data in this research.

Hence, this research aims to analyze the characteristics of the slope spectrums of the typical loess geomorphologic types using CGD and SRTM-DEM data, and then explore the transitional relationships among the types and their sub-types based on the slope characteristics changing rules.

STUDY AREA AND DATA SOURCES

Study area

This research selects the Loess Plateau of China as the study area, and the transitional relationships among the typical loess geomorphology types and their subtypes are explored.

Located in the upper and middle reaches of Yellow River, Loess Plateau is in the west side of Taihang Mountain, the east side of Qinghai-Tibet Plateau, the north side of Qinling Mountain and the south side of Mongolia Plateau. Loess Plateau is one of the four largest plateaus in China, which distributes the widest and deepest loess in the world, so as to form the most typical loess geomorphology. Loess geomorphology has close relation with soil erosion, which is the one of the most serious problems for ecological and environmental safety in the Loess Plateau. So the research to the loess geomorphology has both scientific significance and economic importance.

Data sources

The main data sources used in this research are the CGD at 1:1,000,000 scales and the SRTM-DEM data.

The CGD data at 1:1,000,000 scales was achieved by using remote sensing visual interpretation and geographic information system methods from multi-source data, such as remote sensing

images, SRTM3-DEM data, published geomorphologic maps, geologic data, and geographic base data and so on [3]. This data is the source data to compile the 1:1,000,000 set of geomorphologic atlas of China [4] and can be divided into seven layers: relief and altitude, genesis, sub-genesis, morphology, micro-morphology, slope and aspect, material and lithology [5]. In this research, the fourth layer — morphology and the fifth layer — micro-morphology are used to acquire the distribution of the typical loess geomorphologic types and their sub-types.

The SRTM-DEM data is the SRTM3-DEM data, which has 3" spatial resolution (SRTM3) and is processed by the Consortium for Spatial Information of the Consultative Group for International Agricultural Research. It can provide continuous elevation surface information and wide coverage (60°N–56°S), so it has been used in many research fields. In this research, the SRTM3-DEM data is the 4th version data, and it is used to compute the slope spectrums for the typical loess geomorphologic types and their subtypes.

METHODOLOGY

Acquisition of the distribution of the typical loess geomorphologic types and their subtypes

The typical loess geomorphology types are loess tableland, loess ridge and loess hill. According to the CGD data, the distribution of the typical loess geomorphologic types is acquired. The areas of the three types are $6.52 \times 10^4 \text{ km}^2$, $9.12 \times 10^4 \text{ km}^2$ and $1.91 \times 10^4 \text{ km}^2$.

The transitional rule among typical loess geomorphologic types is widely acknowledged as: from loess tableland to loess ridge and finally to loess hill [6]. Hence, in this research, the transitional rules of the subtypes of typical loess geomorphology are paid more attention.

Considering the distribution areas and situations of the typical loess geomorphology types, the loess tableland is divided into four subtypes: loess terrace, complete tableland, residual tableland and beam tableland; the loess ridge is divided into oblique ridge and mao ridge; and the loess hill is not divided further. From the CDG data, the distribution of the subtypes of the typical loess geomorphology can be acquired and shown in Figure 1.

Figure 1 shows the distribution of the typical loess geomorphology: loess table mainly distributes in the northern part of Xi'an City and eastern part of the Lanzhou City; besides, there exist spares distribution around Taiyuan City. Loess ridge has the greatest area, which mainly distributes in the eastern part of Lanzhou City and western part of Taiyuan City. Loess hill has the least area, which distributes in the western part of Taiyuan City, the northern part of Xi'an City, and around the Lanzhou City.

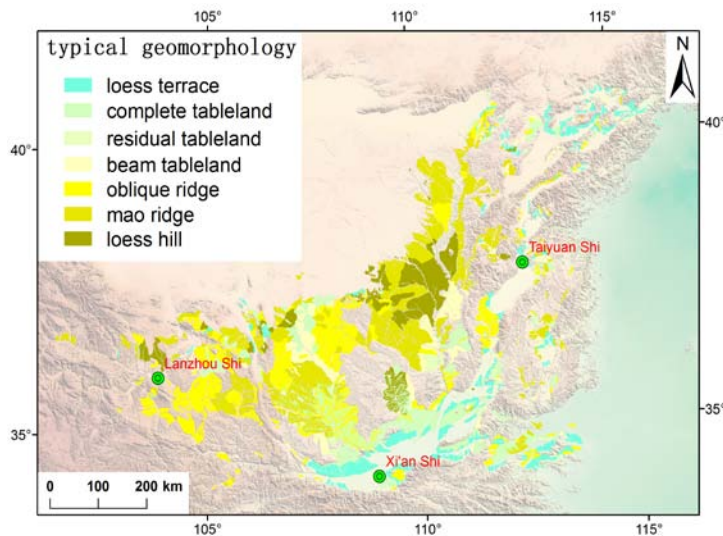


Figure 1. Typical loess geomorphology distribution in the Loess Plateau

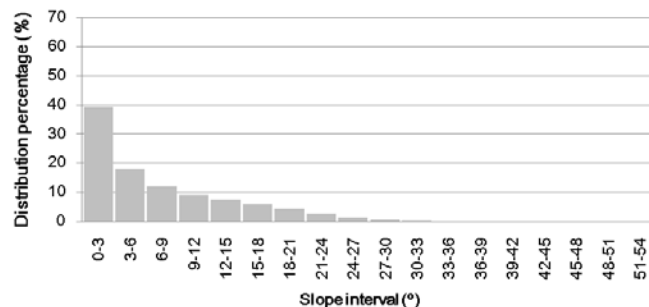
The acquisition of the distribution of the typical loess geomorphology provides the chance to compute the slope spectrum index for every type.

Slope spectrum computation for the typical loess geomorphologic types and their subtypes

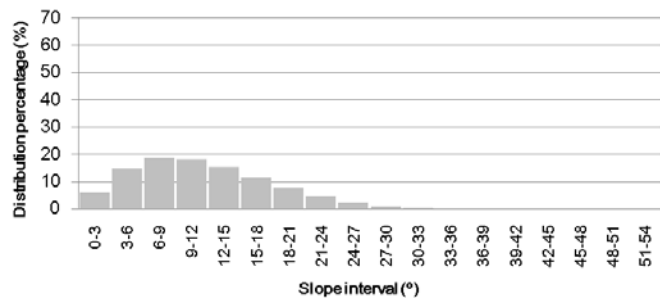
Based on SRTM3-DEM data and topographic analysis method, the slope is computed for the whole Loess Plateau; then, the slope is classified with the interval of 3°; overlapped with the classified slope data and the distribution data of typical loess geomorphologic types, the slope distribution status are acquired for all the types; through numerical statistics, the slope spectrum index is achieved for every type.

RESULTS

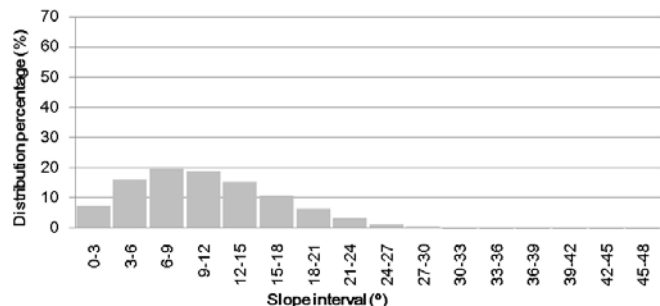
The slope spectrum analysis for the typical loess geomorphologic types



(a) loess tableland



(b) loess ridge



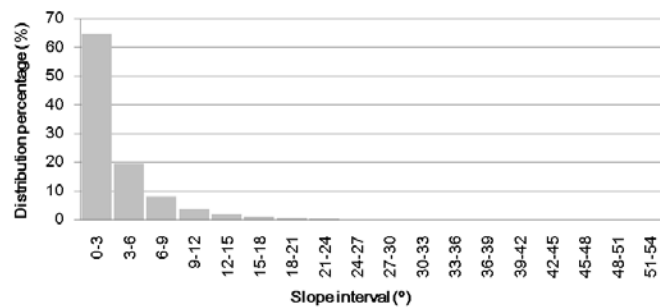
(c) loess hill

Figure 2. Slope spectrum of the typical loess geomorphologic types

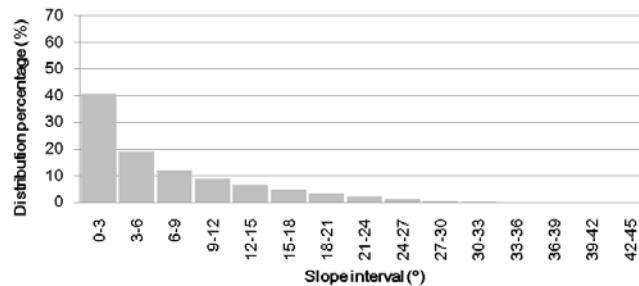
Based on the distribution data of the typical loess geomorphologic types and the slope spectrum computation method, the slope spectrum indexes for the typical loess geomorphologic types are acquired as shown in Figure 2:

Figure 2 shows: the slope spectrum index for the loess ridge is similar to that for the loess hill; the loess ridge is a little steeper than loess hill. As to the loess table, it is much more flatter than other two types. So it has distinct slope spectrum characteristics compared to it for other two typical geomorphologic types.

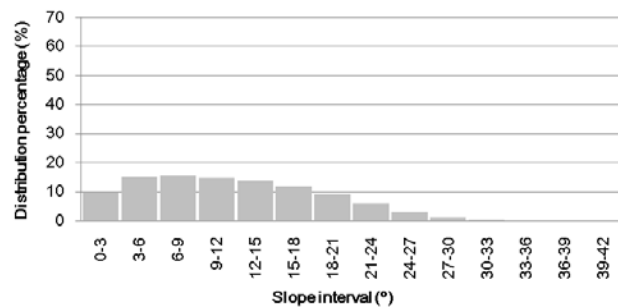
The slope spectrum analysis for the subtypes of typical loess geomorphologic types



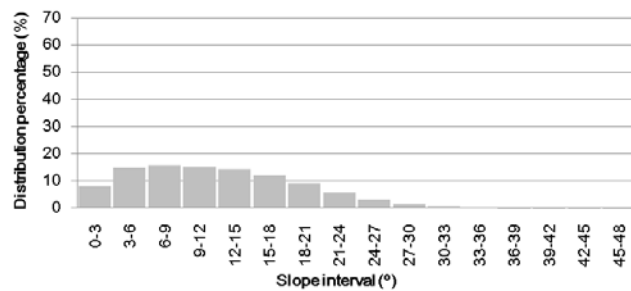
(a) loess terrace



(b) complete tableland



(c) residual tableland



(d) beam tableland

Figure 3. Slope spectrum for the subtypes of the loess tableland

The slope spectrum for the subtypes of the loess tableland is computed as shown in Figure 3:

Figure 3 shows: the loess tableland is divided into 4 subtypes: loess terrace, complete tableland, residual tableland and beam tableland. The loess terrace is the most flattest one; and then the complete tableland, which is similar to the loess tableland; the residual tableland and beam tableland are steep, the slope spectrums for which are similar to that for the loess ridge, especially for the beam tableland.

Figure 4 gives the slope spectrum distribution for the subtypes of the loess ridge. From Figure 4 we can see: the loess ridge is divided into 2 subtypes: oblique ridge and mao ridge; the slope spectrum characteristics for the two subtypes are similar; compared to oblique ridge, the slope for the mao ridge is more similar to that for the loess hill.

DISCUSSIONS

Innovations

This research explores the transitional relationships among the typical loess geomorphologic types and their sub-types based on the slope spectrum index, which gives a way to further study the loess geomorphology.

limitations

Slope spectrum is an important topographic index, but acquiring the transitional relationships only using the slope spectrum perhaps is not enough.

CONCLUSIONS

The transitional relationships among the typical loess geomorphologic types and their sub-types are achieved as the following: for the typical loess geomorphologic types, from loess tableland to loess ridge and finally to loess hill. For the subtypes of the loess tableland, from loess terrace to complete terrace, and then to the residual tableland and finally to beam tableland; as to the loess ridge, from oblique ridge to mao ridge.

ACKNOWLEDGMENT

This research was supported by the National Natural Science Foundation of China (41301469, 41171332) and the National Science Technology Basic Special Project (2011FY110400-2), the strategic plan project of science and technology of Institute of Geographic Sciences and Natural Resources Research (2012ZD009), the National Science Technology Support Plan Project (2012BAH28B01-03). We would like to express our gratitude to the editors and anonymous reviewers for processing our manuscript.

REFERENCES

[1] Tang, G.A., Ge, S.S., Li, F.Y., and Zhou, J.Y., 2005. "Review of Digital Elevation Model (DEM) Based Research on China Loess Plateau." *Journal of Mountain Science*, 2 (3): 265-270.

[2] Tang, G.A., Li, F.Y., Liu, X.J., Long, Y., and Yang, X., 2008. "Research on the slope spectrum of the Loess Plateau." *Science in China Series E: Technological Sciences*, 51: 175-185.

[3] Cheng, W.M., Zhou, C.H., Chai, H.X., Zhao, S.M., and Zhou, Z.P., 2011. "Research and compilation of the Geomorphologic Atlas of the People's Republic of China (1:1,000,000)." *Journal of Geographical Sciences*, 21(1): 89-100.

[4] Li, J.J., Zhou, C.H., and Cheng, W.M., 2009. "Geomorphologic Atlas of the People's Republic of China". Science Press, 200p.

[5] Cheng, W.M., Zhou, C.H., and Li, B.Y., 2011. "Structure and contents of layered classification system of digital geomorphology for China". *Journal of Geographical Sciences*, 21(5): 771-790.

[6] Sang, G.S., Chen, X., Chen, X.N., and Che, Z.L., 2007. "Formation model and geomorphic evolution of loess hilly landforms". *Arid Land Geography*, 30(3): 375-380.

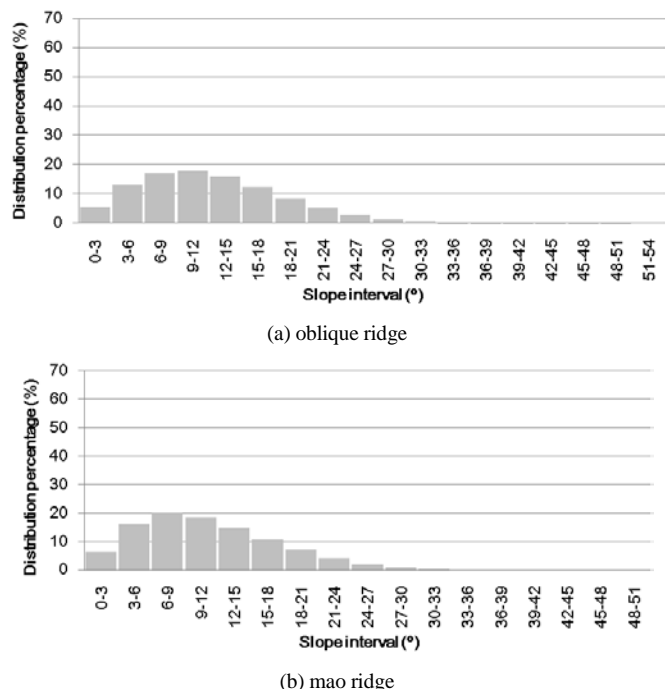


Figure 4. Slope spectrum for the subtypes of the loess ridge

Transitional relationship exploration for the typical loess geomorphologic types

From the slope spectrum characteristics analysis for the typical loess geomorphologic types and their subtypes, the transitional relationship is achieved as shown in Figure 5:

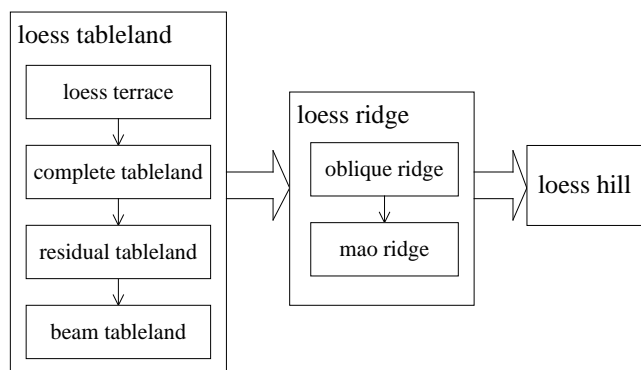


Figure 5. Transitional relationship among typical loess geomorphology

Figure 5 shows: for the loess tableland, the transitional order of the subtypes is: from loess terrace to complete tableland, to residual tableland and beam tableland; for the loess ridge, it is: from oblique to mao ridge; so the beam tableland is the closest subtype to the loess ridge, and the mao ridge is the closest subtype to the loess hill.

Effectiveness of Mitigation Measures on Phosphorus Delivery

Ting Zhang^{1*}, Trevor Page¹, David M. Oliver²

¹ Lancaster Environment Centre, Lancaster University, Lancaster, LA1 4YQ

² Biological & Environmental Sciences, School of Natural Sciences, University of Stirling, Stirling, FK9 4LA, UK

*Corresponding author : email tting.zhang@gmail.com

INTRODUCTION

Diffuse pollution from agricultural land has become the dominant factor controlling freshwater quality in many catchments. Phosphorus (P), as one of the main macronutrients, plays a key controlling role in the eutrophication of surface waters. To meet our environmental management responsibilities there is a need to estimate the likely effect of current and future soil and land management policies on water quality and choose the most effective strategies given catchment characteristics, climate and economic drivers.

Mitigation methods employed to meet standards set to protect ecological function include measures to reduce P inputs to catchment systems (e.g. reduced fertiliser application rates), those to reduce the mobilisation and transport of P from agricultural land to water (e.g. improved soil management) and others to reduce the fluxes of P delivered to waterbodies (e.g. buffer zones and constructed wetlands (CWs) (Cuttle et al., 2006; Daverede et al., 2004; Johnes et al., 2007; Kay et al., 2009)). Where measures to reduce P delivery are used, some farm infrastructures have been proven to be useful such as riparian buffer zones (RBZs) and CWs (Abu-Zreig, 2003; Braskerud, 2005; Kay, 2009; Uusi-Kämpä 2000).

Determining which land management option (or combination of options) is the most effective mitigation strategy for a given catchment or catchment type and what is the likely magnitude of their effect in isolation and in combination is difficult and depends upon factors such as catchment characteristics, climatic conditions and agronomic structure.

A number of phosphorus transport and delivery models have been developed in recent years (Heathwaite et al., 2003; Dougherty et al., 2004; Haygarth et al., 2005; Schärer et al., 2006; Haygarth et al., 2009). However, those of a dynamic, process-based nature can often be over-parameterised. In addition, there are significant uncertainties in representing the

effects of any mitigation. The mitigation process is much more complicated at the catchment scale than it is at the plot scale as there are many factors affecting the effectiveness of mitigation options, such as the localization of preferential surface and subsurface flows in a catchment and the distributed patterns of different soil types (Beven, 2010). The spatial locations of where mitigation measures being installed also affect their effectiveness of reducing P delivery. Without consideration of the uncertainty in our current ability to estimate the behaviour of diffuse pollutants, estimation of the effectiveness of mitigation measures, and hence cost-effectiveness, might be misleading.

In this paper we illustrated how we have incorporated the uncertainties associated with limited information at appropriate scales in the development of fuzzy rules describing the likely effectiveness of CWs within headwater catchments. We used information from literature reviews and expert opinion as a basis for the rules. The expert opinion was derived from the project team and a focused workshop of invited experts. The Critical Source Areas (CSAs) was delimited as the most important area for P delivery by using Digital Elevation Model (DEM) data and the Sensitive Catchment Integrated Modelling Platform (SCIMAP) protocol. The influence of spatial distributions of installed or to be installed mitigation measures was investigated on P delivery. These rules were applied to modify the P delivery coefficient estimates with installed or to be installed mitigation measures depending on catchment characteristics.

MATERIALS

This work used data from five data-rich catchments and seven data-poor catchments. The data-rich catchments refer to catchments with an existing set of time series measurements of high resolution (daily or sub-daily) hydrometric and water quality monitoring data and wide coverage of the Aquatic Landscape classes (Defra, 2003), while the data-poor catchments are those with one year of monitoring data of approximately 10 storms plus

occasional base flow samples. All of these catchments are headwater catchments generally less than 6 km². The 10m resolution DEM data, the land cover map and 30 years annual rainfall data were used to delineate the CSAs.

As we would like to model the likely effect of the mitigation methods on reducing P delivery coefficients, it is ideal if we have monitoring data before any mitigation measure being installed. But in fact, all of our experimental catchments have been installed with several mitigation measures and the monitoring data were collected after their applications. Therefore, P delivery coefficients of current status based on hydrologic and geographic factors are the necessary foundation. Tabulated raw data is available on http://www.lancs.ac.uk/staff/zhangt/Table_Catchment_features_and_phosphorus.htm. It lists the estimated P delivery coefficients without mitigation measure effectiveness (revised results from the PEDAL project, unpublished data), the observed P delivery coefficients and key catchment characteristics (see Defra, 2006).

METHODOLOGY

Model structure

In this paper, the estimated P delivery coefficients without mitigation measure effectiveness in the above link are used as the input. The P delivery coefficient is defined in Equation 1 (Beven et al., 2005; Brazier et al., 2006). DESPRAL is an index of P mobilisation and expressed as a concentration (Withers et al., 2007). The delivery coefficients without mitigation measure effectiveness are also given in the above raw data table link.

$$\text{Phosphorus delivery} = \frac{\text{Annual flow weighted mean (mg l}^{-1}\text{)}}{\text{DESPRAL index value (mg}^{-1}\text{)}} \quad \text{Equation 1}$$

A set of fuzzy rules were built to modify the P delivery coefficients without mitigation measures effectiveness, as there might be installed or to be applied mitigation measures affecting the P delivery results. We constructed a fuzzy-rule base to implement a modification of the fuzzy delivery coefficients. Figure 1 (see in full version of the paper) shows the model structure schematically and demonstrates how the likely effects of CWs are implemented in the model. The model took the P delivery coefficients without mitigation measure effects as inputs, established a set of fuzzy rules for P reduction rate of each mitigation method, the control areas effects, the effect of catchment properties and installed mitigation measures, and exported the revised P delivery coefficients as outputs. The model also has the facility to incorporate information on existing mitigation measures (e.g. by visual assessment of fields where possible) that may have a significant impact on effectiveness

(e.g. in the extreme the effectiveness of additional measures may be zero where optimal mitigation exists).

Critical Source Areas

To ensure the most efficient deployment of mitigation effort, it is important to focus upon those parts of a catchment where restoration is likely to give the greatest added value. Certain areas are diffuse pollution hotspots, where high nutrient inputs and/or inappropriate land use generate a significant nutrient source that is also connected with a hydrological flow path to the drainage network. Evidence suggests that this delivery process may be conditioned by local, often sub-field scale hydrology (e.g., Blackwell *et al.*, 1999; Burt *et al.*, 1999; Quinn, 2004) and nutrient transformation processes (Harris and Heathwaite, 2005). These patterns of runoff generation and hydrological connection occur at spatial scales of the order of ≤ 10 m (Western *et al.*, 1999, 2001; Lane *et al.*, 2004; Heathwaite *et al.*, 2005), often related to quite subtle topographic attributes.

A set of DEM data with 10m resolution, the land cover map and annual rainfall data were used to generate a risk based critical source areas, which gave the most risk parts of the catchment for P delivery. Topographic wetness index was calculated from DEM data and land cover erosion risk was derived from the land cover map and rainfall data. Both the risk indices were used to give the risk map of P delivery at given catchment. The critical source areas was delineated based the risk map and field visits at wet conditions. Mitigation measures, such as wetlands, installed within CSAs will be given high weight when calculating its effectiveness of reducing P delivery.

Mitigation measure effectiveness rule

Stevens and Quinton (2009a, 2009b) reported that observations of the reduction efficiency of diffuse pollution mitigation measures show highly variable results for TP. This variability is highlighted in Figure 2, which shows the broad distribution of the reduction efficiency of CWs (1% to 91%) on TP flux from published sources. Using the information presented in Figure 2, a fuzzy rule was constructed for mitigation measure effectiveness applied to the a priori estimated delivery coefficient distribution. The fuzzy rule is of the type:

Rule 1:

If the estimated P delivery coefficient is A and mitigation option reduction efficiency is B, then the final P delivery coefficient is $A \times (1-B)$.

1- reduction efficiency (B) refers to the delivered P passing through CWs. Fuzzy multiplication of two fuzzy membership functions refers to the fuzzy union of every point from the multiplicand membership function multiplied by the multiplier membership function (Beven, 2009). Fuzzy membership function

refers to a curve or function that specifies the degree to which a given input belongs to a set or is related to a concept.

Fuzzy membership function for wetlands was built and is presented in Figure 3.

Control area rule

Every mitigation measure has an upslope control area. When mitigation measures are installed in a catchment, parts of the area in the catchment will be covered and protected. If the whole catchment has already been controlled and protected by the installed mitigation measures, there will be the minimum need for a new mitigation measure.

The catchment control area is estimated based on Visual Assessment (VA) (Kovacic et al., 2000) information reported in Defra (2006). Table 1 shows the installed mitigation measures and the estimated catchment control areas in experimental catchments.

A fuzzy range is been given based on Table 1 and a fuzzy trapezoidal shaped membership function is adopted to represent the fuzzy control areas of experimental catchments (Figure 5).

Apart from catchment control areas, the control area of each mitigation measure affects how much delivered P it can reduce and eventually affects the delivered P at the outlet. Due to the limited information, an expert opinion is applied here. We assume every installed mitigation measure works at its maximum effectiveness. A trapezoidal shaped fuzzy membership function is built as below (Figure 6), in which, n means the number of mitigation measures within the catchment control area. As n varies in different catchments, the fuzzy membership function in Figure 6 will change accordingly.

Spatial pattern rule

When multiple mitigation options are combined in the same catchment, there will be an interacting effect between them. The spatial distributions of mitigation measures will lead to different effectiveness on P delivery.

We assume that all the mitigation measures work equally well on diffuse P pollution. The interacting effect could be an additive or multiplication relationship that depends on the spatial locations of the mitigation options. Figure 7 is an example of how spatial location affects the mitigation measure effectiveness. When two mitigation measures are implemented in the same sub-catchment, they may work as a multiplicative relationship if implemented in series; otherwise an additive relationship if in parallel. When they are in different sub-catchments, an additive relationship occurs. The combination effect is also closely related to whether or not the critical source areas (CSAs) (Maas et al., 1985; Gburek & Sharpley, 1998; Pionke et al., 2000) have been mostly covered by installed mitigation measures. If the CSAs have been fully covered by installed mitigation measures, the

combination effect between a new mitigation measure and installed ones will be minimal. That is to say, a new mitigation in the catchment would not be expected to have a significant impact.

In this situation, information about the installed mitigation measures is required. This will normally be assessed by making a VA of the catchment of interest (Defra, 2006). There may be several levels of VA information that could be collected. First of all, a partial level of VA information as to whether or not there is any mitigation measure currently installed; then a full level of VA information extending to the catchment characteristics and mitigation measure properties (like the buffer strip length and its location). An example is shown below how partial level VA information will be incorporated into the fuzzy rule model.

Due to the limited VA information, we could only give a range of possibilities covering the minimum and maximum situations. The fuzzy rule is of the type:

Rule 2:

If two mitigation measures are in the same sub-catchment, they work as a multiplication or additive relationship depending on whether they work as in series or parallel.

If they are in different sub-catchments, an additive relationship occurs.

Combination effect depends on the spatial locations of mitigation options and whether or not the CSAs have been fully covered by installed mitigation options.

Final fuzzy rules

Final fuzzy rules for mitigation methods are the combination of fuzzy rule 1, rule 2, rule 3, control area rule and the up-scaling rule:

If there are CWs in the catchment, the estimated P delivery coefficient is A, wetlands' P loss reduction proportion is B, the catchment control area is CA, the mitigation measure control area is CC and the combination effect is C, then the final P delivery coefficient is $A \times CC \times (1-B) \times CA \times C$.

RESULTS AND DISCUSSIONS

The results of applying the proposed fuzzy rules are presented in Figure 9. Figure 9a and 9b and 9c demonstrate P delivery coefficients where without mitigation measures effectiveness, taking installed mitigation measures effects into account and applying a new CW at the catchments respectively. It is clearly shown from the comparison of these three figures that P delivery has been much improved at these catchments after the mitigation measures being installed. As it is shown, where there is installed RBZs or much more RBZs than wetlands installed, applying a new CW is more effective than applying in those catchments

with several CWs installed. We assume every mitigation measure work effectively and we don't take time lag effect into account in the model. Besides, as we do not have enough information of the installed mitigation measures, we do not know which kind of combination relationship the installed mitigation measures have. Therefore, a full range of possibilities is given in the model covering both the multiplicative and additive relationships. In this case, detailed information about the spatial locations of installed mitigation measures is required in the future.

As we have limited VA information about the installed mitigation measures, a full range of possibilities instead of accurate estimations of the combination effect is given in the paper. The combination effect of multiple mitigation measures is not only related to the spatial location but also related with CSA and mitigation measures properties (like the area ratio of wetlands to the catchment). For example, if the CSAs have been fully covered by the wetlands, then there is no need for a new wetland to be installed; but if there is a large proportion of CSA not being protected, then extra mitigation measures will be needed.

Other than CSAs, the wetland surface-area/watershed-area ratio plays an important role in wetlands' retention ability (Uusi-Känpää et al., 2000). The timing issue is also important for the combination effect. The time when installed mitigation measures are implemented and VA information and samples are collected should be recorded appropriately.

Besides this, pollution swapping can occur when one mitigation option applied to reduce one pollutant leads to an increase in a different pollutant (Stevens and Quinton, 2009a). We have little evidence on the full range of impacts these mitigation measures have on different diffuse agricultural pollutants. Further research will be needed in the future.

Some of the variation associated with factors mentioned above has been included in the range of the effectiveness data we have used. However if supplementary field visits and experimental campaigns are targeting on these factors in future then more accurate simulations of mitigation strategies effectiveness will be achieved. The combination effect rules could be used to evaluate not only installed but also to be installed mitigation methods' efficiency when considering land management strategies.

CONCLUSIONS

This study has provided a first approximation of how CWs (i.e. delivery mitigation features) affect P delivery coefficients by coupling expert knowledge with data from twelve catchments studied. A set of fuzzy rules of P trapping efficiency, control area rule and the combination effect for CWs were built. These fuzzy rules were incorporated into a fuzzy model of P delivery coefficient from the previous PEDAL project (Defra, 2006). The

results demonstrated how effective each mitigation method could be for reducing the P delivery coefficient and that mitigation options should be selected according to catchment properties. These fuzzy rules can be applied for the evaluation of the effect of installed and to be installed mitigation measures on P delivery coefficient and give support for land management strategies. As the fuzzy rule model is a learning process, its accuracy is based on the raw data. Optimized results will be provided to land management policy makers when more detailed VA data become available.

ACKNOWLEDGEMENTS

The work reported in this paper was funded by Defra within the Delivery of Phosphorus and Faecal Indicator Organisms from Agricultural Sources to Watercourses project (WQ0129) and University of Lancaster. We also thank all experts who contributed to the workshop: Richard Brazier, Clare Deasy, Phil Jordan, Neil Preedy, John Quinton, Paul Scholefield, Luke Spadavecchia and Paul Withers.

Research on Terrain Landscape System based on Complex network

TIAN Jian¹

1. School of Resources and Environment Engineering Hefei University of Technology,
193 Tunxi Road, Hefei 230009, China
E-mail: tianjian.1999@163.com

Abstract—This paper described study hilly area of the Loess Plateau watershed system using complex network theory, and terrain landscape network was established. Some indexes such as degree, average path length and clustering coefficient were selected as measure. Some results included that terrain landscape network is the typical small world characteristic network, has disassotativity characteristic, and is not a kind of scale-free network. The topology feature of terrain landscape is not affected by the geographic scale. Under the artificial modification, the terrain landscape network had been changed the topology structure of network. Its average degree was reduced and its clustering coefficient was increased. The watershed hydrological characteristics about system had been influenced because of the change of system structure. It was shown that complex network is a new method for studying the landscape evolution on the drainage basin.

I. INTRODUCTION

On the Loess Plateau, There are many styles of landform, and the skeleton of terrain is constructed by terrain feature points and lines. The terrain features such as peaks; runoff nodes occupy the transfer of terrain energy, and reflect the different hydrological characteristics on the local terrain landscape system. The structure of terrain landscape on the Loess Plateau is marvelous and complex. In the system opinion, many complex systems in nature can be described by network, e.g. river network, transport network and social network [1-3]. Geomorphic systems consist of coupled subsystems with trait of small world networks, characterized by tightly connected clusters of components. This spatial complex network showed that these networks have nodes and links which are constrained by some geometry and are usually embedded in three dimensional spaces and this has important effects on their topological properties and consequently on process which take place on them.

Terrain landscape system as a kind of geomorphic system can be characterized as a set of interconnected components,

which may be objects, process or regimes, or nature phenomena or events. These components are connected by fluxes of matter and energy, feedbacks, spatial or temporal sequencing or connectivity and process-response relationships. This paper discussed a novel method based on complex network theory, to analyze terrain landscape system function change after artificial affect. For purposes of illustration, the method is applied to landform landscape system on the Loess plateau.

II. DATA AND METHODS

A. Data

The study area is located on Suide County in China. The experimental data was obtained from digitized contour of topographic map at a scale of 1:10000 and 5m resolution. The projection of DEM is Gauss-Kruger. DEM data is provided by Shaanxi Bureau of Surveying and Mapping.

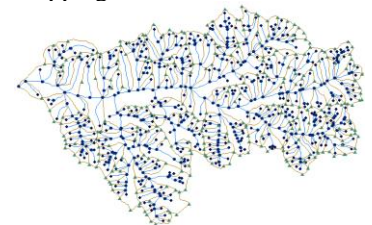


Fig1. DEM of test area

Fig2. All nodes of network

In terrain landscape, many feature points control the distribution of watershed energy, which include the peak and node of ridge on the positive terrain, gully head and runoff node on the negative terrain. So complex network for terrain landscape can be abstracted as follows:

TNet = network (peak, gully head, runoff node)

All feature points of terrain landscape system need to be connected. Edges of network included as follows rules:

- (1) The edge is between peaks with points of ridge intersection in the positive landform.
- (2) The edge is between peaks and points of ridge intersection in the positive landform with runoff node and gully head in the negative landform.
- (3) The edge is between gully head with runoff node in the negative landform.

All nodes and edges of network were extracted by DEM data, which was adopted by method of digital terrain analysis.

B. METHODS

Method of complex network is abstractly reflected natural system using network elements (nodes, edges), and expressed the link of various objects in reality. These types of networks were termed “small-world” networks [4]. There short cuts across the graph to different clusters of vertices introduced a level of efficiency not predicted in the ER model, and showed the first signs of self-organization in complex networks. In 1999, Barabási found scale-free network that its degree distribution is not a Poisson or exponential distribution [5], but a power law distribution. Meanwhile, complex networks of grow over time, and new vertices attach preferentially to already well-connected vertices in the network.

When examining dynamical terrain landscape systems connected by a network of interactions, two aspects of the problem can be considered independently. These are the dynamics of the individual uncoupled subsystems, and the topology of the interaction network. A network about terrain landscape on the Loess plateau consists of N nodes or vertices and m edges (the connections or relationships among components). The abstract networks may be directed, signifying the direction of causality or influence, or undirected, simply signifying that many components are related. A net is considered connected if it is possible to follow a path of one or more edges between any two vertices.

Some important characteristics of complex network include average degree, degree distribution, average path length, clustering coefficient and assortative coefficient.

III. RESULTS

A. Statistic terrain landscape network

The complex network of terrain landscape had been established depended on DEM, and its network expressed the structure of natural drainage system. The characteristic of complex landscape network is that node is 921, edge is 1778, average degree is 3.77, clustering coefficient is 0.22, and average path length is 14.82. The clustering coefficient and average path length of this random network is 0.004 and 5.14

respectively. From it, one clearly appreciates that the values of the clustering coefficient are much larger than those corresponding to the associated classical random graphs. The values of the average path length are also to be very small. Thus, terrain landscape networks are in fact small world network. At the same time, we could be found that the distribution of node is exponential type, and is not power law distribution (figure 3). The networks have not scale free feature. However, runoff node as only node in this network (figure 4), this node is obey power law distribution and it can be as a kind of scale free network.

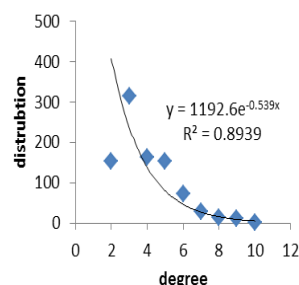


Figure3. Degree distribution of all nodes

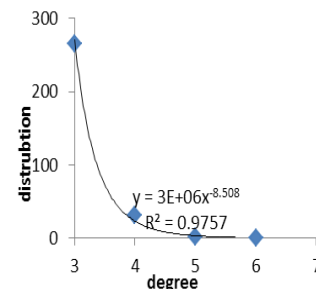


Figure4. Degree distribution of runoff nodes

In order to measure the link of all nodes about terrain landscape network, assortative coefficient is special index. In this network, its value was -0.19 and it was shown that the network is classified as dissortative network. Nodes whose degrees were high is priority to be connected with nodes whose degree was low. In complex terrain, degrees of some nodes were relatively high, and it controlled rather large geographical range. However, many nodes have low value of degrees, and all kinds of degree were spatial distribution of equilibrium.

B. Analysis of network evolution

In order to soil and water conservation, some bars were constructed at the outlet of drainage, so that the original terrain landscape network had been changed in structure of natural system aspect. Fig.4 showed the distribution of bars. The completely continuous watershed system was dissected with 13 sub-watershed system. In this network, elevation about 13 nodes was heightened, so that control ranges of nodes were enhanced. Function of terrain network had been changed by human activity, and surface process was influenced in the watershed system.

From table1, clustering coefficient was lager and average path length on all 13 sub-networks was less than corresponding to the random graph. It was showed that 13 sub-networks were accord with small world network feature, and it was consistent with the whole terrain landscape network. So we can be

concluded that the characteristic of network was not varied with geographical scales. In specific geographic space, network nodes were randomly distributed state with the drainage area was smaller. When watershed scale is become larger, small-world feature was increasingly presented. All of sub-networks in degree distribution aspect were not power law rules.

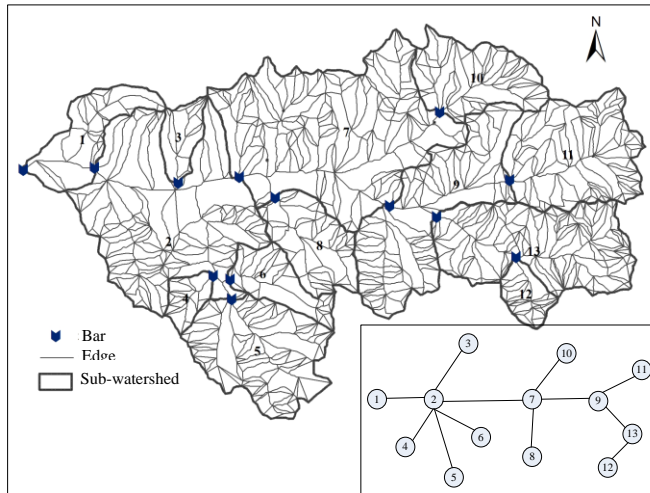


Figure5. Terrain landscape networks under artificial modification

Table1. the characteristic result of sub-network about watershed average degree, D , average path length, L , (corroding with random graph, L_r), the clustering coefficient, C , (compared with those of the random graphs, C_r)

ID	Area (km ²)	D	L	L_r	C	C_r
1	0.55	3.69	3.3	2.65	0.38	0.12
2	2.13	3.59	6.1	3.88	0.2	0.03
3	0.23	3.24	2.65	2.59	0.19	0.15
4	0.17	3.42	2.78	2.58	0.25	0.14
5	1.08	3.78	5.5	3.41	0.26	0.04
6	0.37	3.43	3.8	2.88	0.27	0.10
7	2.50	3.47	7.37	4.21	0.17	0.02
8	0.59	3.40	4.68	3.35	0.31	0.06
9	1.35	3.50	6.92	3.88	0.19	0.03
10	0.71	3.70	4.67	3.13	0.29	0.06
11	1.14	3.65	5.81	3.58	0.28	0.04
12	0.21	4.08	2.63	2.26	0.4	0.17
13	1.52	3.76	6.51	3.73	0.23	0.03

When human behavior was active on the watershed system, some topology characteristic of network would be changed. The average degree of network after artificial modification was 3.6, which is less than original network, and nodes relationship in network was weaken. The outlet

importance of 13 sub watershed was stronger than the other nodes, breaking the distribution of the original network energy. Average path length became decrease with network scale lessening, and the connectivity of sub network was reducing, so that coupling feature about terrain landscape system was weak. Under the artificial effect, the modular of terrain landscape network was significant. When the structure of basin system had changed, the runoff slope length was reduced, and system hydrological function had been influenced.

According to the soil and water conservation data from Suide station, it was indicated that the hydrology and sediment transport function of this basin has been changed obviously. The measures for soil and water conservation is rather good, runoff modulus decreased by 24% and sediment transport module reduced 50%.

IV. CONCLUSION

We have discussed the spatial complex network approach to shed new light on complexity of the phenomenon about terrain landscape system. The topological properties of terrain network constructed from DEM on Suide County have been analyzed. We have shown that the terrain landscape is “small-world” networks. The local network about runoff node is scale-free network characterized by the power law connectivity distribution. Geographical scale changes have little effect on the structure characteristic of complex terrain landscape network. After artificial modification, complex network of terrain landscape have evolved as for some bars embed in the spatial network. These key nodes controlled surface network process, changed local base level of erosion, and influenced the hydrological feature in this watershed system. It was our expectation that spatial complex network approach may lead to deeper understanding of terrain landscape system.

ACKNOWLEDGMENT

This research is supported by National Natural Science Foundation of China (No. 41101365).

REFERENCES

- [1]. Carmi, S., S. Havlin, et al. Energy-landscape network approach to the glass transition [J]. Journal of Physics a-Mathematical and Theoretical, 2009, 42(10): 1-9
- [2]. S. Abe, N. Suzuki. Complex-network description of seismicity [J]. Nonlinear Processes in Geophysics, 2006, 13(2):145-150.
- [3]. Zhao ling, Deng Min, Wang jia-qiu etal. Structural property analysis of urban street networks based on complex network theory. Geography and Geo-information Science, 2010,26(5): 11-15.
- [4]. Watts DJ, Strogatz SH (1998) Collective dynamics of small-world networks. Nature 363:202-204

- [5]. Barabasi A, Albert A (1999) Emergence of scaling in random networks. *Science* 286:509–512

Fractal analysis of the Loess Plateau in China

Kamila Justyna Lis
Nanjing Normal University
kamikabo@gmail.com

Tang Guoan
Nanjing Normal University
tanguoan@njnu.edu.cn

Abstract—Fractal dimension is an important indicator for the understanding the loess plateau geographic features. This study employed this method to investigate this. The preliminary results show that terrain in the study area has a complex landscape structure based on the fractal dimensions evaluated. The final work is to integrate the fractal dimension and slope for the test sites to showcase how these landscape parameters can help define the landform evolution in the Loess plateau.

Keywords—integration, dimension; slope; DEM; bathymetry

I. INTRODUCTION

The field of remote sensing and geographic information systems (GIS) continues to grow rapidly as computer and mathematics profession get an informed understanding of the earth surface and its physical features. The study of landforms for example has been a prime issue of concern and importance in the geomorphometry [1-3].

Loess plateau belongs to the family of landforms that has been of strategic important to the Chinese Government and have attracted several studies about its natural features, underlying geomorphology, the climate conditions and accumulation of soil deposits [4-8]. Though, a large number of studies have been conducted in loess plateau, the employment of fractal dimension originally develop by Mandelbrot [9] to describe accurately and precisely natural physical features in this plateau has been limited. Therefore, this study employed the fractal dimension technique to extract the physical features in this zone. The study conducted this in four test cases located in the Shaanxi Province of China. It is expected that this study would provide baseline understanding of the use of fractals in this region and further, boosts the informed understanding of the evolution of the loess plateau.

II. MATERIALS AND METHODS

A. Data Sources

The digital elevation models (DEMs) were obtained from the Shaanxi project conducted using bathymetry. These included two test sites – Changwu and Chunhua.

B. Methods

The method employed in this study is the implementation of the fractal dimension technique. In fractal analysis, the fractal dimension (D) is estimated as follows:

$$D_f = \lim_{r \rightarrow 0} \frac{\log N_r}{\log \left(\frac{1}{r} \right)} \quad (1)$$

Where

$$N_r = \sum_{i,j}^M n_r(s, s) \quad (2)$$

And

$$n_r(s, s) = L - K + 1 \quad (3)$$

Where, (s, s) is the size of the box counter and in this case was adopted as 250 x 250.

III. RESULTS

The preliminary results about the fractal analysis for the test sites have been presented in figure 1. The complete work is to consider the effects of D_f and slope variation in the test sites and how these two help to describe the complexity of a landscape.

IV. CONCLUSION

The adoption of fractals is important in understanding the different anthropogenic activities in the Loess Plateau. This study used bathymetry studies conducted in four test sites. The comparison of the fractal dimension and slope maps shows distinctive differences. The slope show the general existing conditions of the landscape while the fractals determined the degree of anthropogenic of each of these attributes described by the slope map. Therefore, it is anticipated the employment of the fractal and slope attribute for the analysis of DEM can provide useful information for an in-depth classification of the loess plateau.

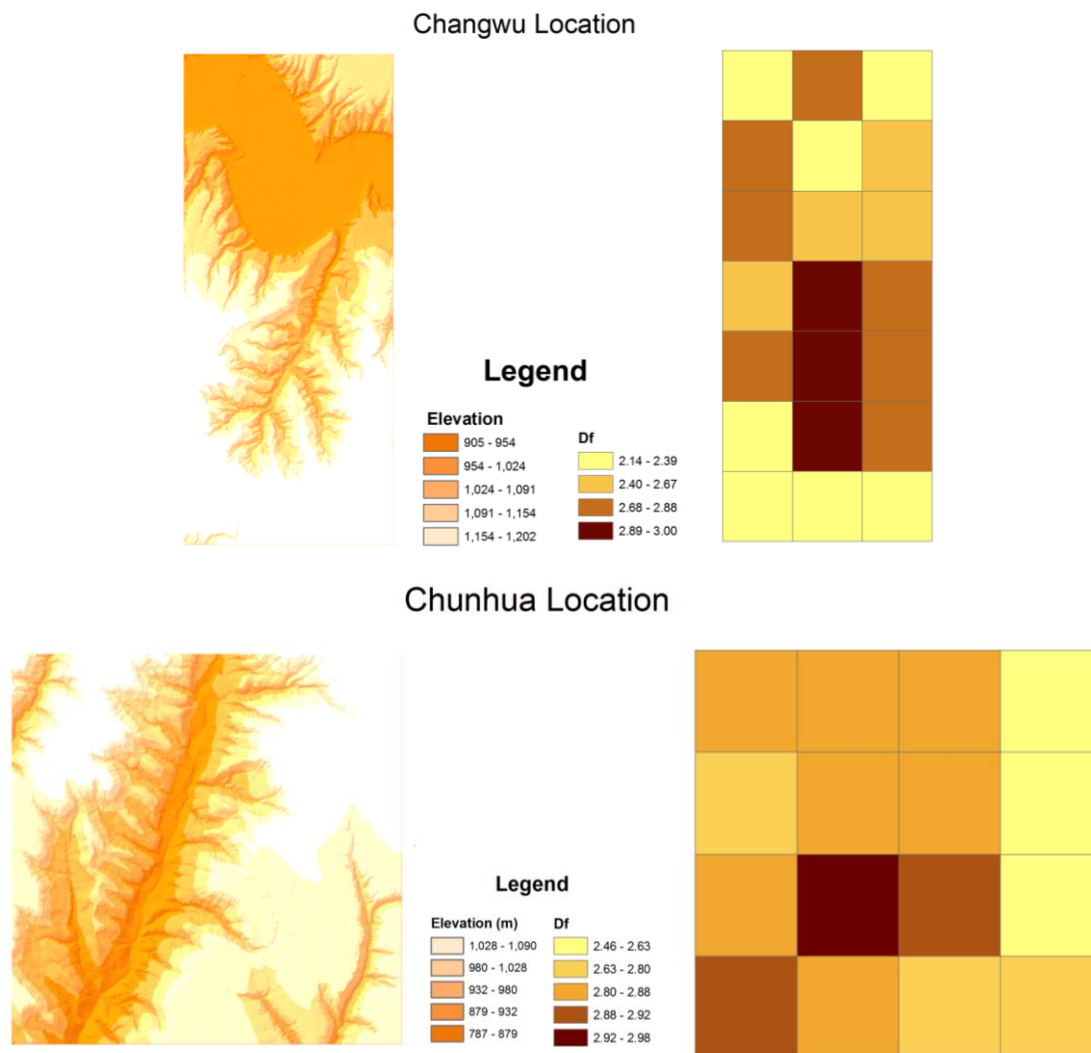
ACKNOWLEDGMENT

The authors wish to extend the kind support of the staff and students of the Department of Geography at the Nanjing Normal University who have worked so hard to provide all these bathymetry DEM. The authors also thank the sponsors of the project in Shaanxi.

REFERENCES

- [1] Qiming, Z., B.G. Lees, and T. Guo-an, Advances in digital terrain analysis: the TADTM initiative. *Advances in Digital Terrain Analysis*, 2008: p. 3-10.
- [2] Bolongaro-Crevenna, A., et al., Geomorphometric analysis for characterizing landforms in Morelos State, Mexico. *Geomorphology*, 2005. 67(3): p. 407-422.
- [3] MacMillan, R. and P. Shary, Landforms and landform elements in geomorphometry. *Developments in Soil Science*, 2009. 33: p. 227-254.
- [4] Fu, B. and H. Gulink, Land evaluation in an area of severe erosion: the Loess Plateau of China. *Land Degradation & Development*, 1994. 5(1): p. 33-40.
- [5] Hessel, R., et al., Soil erosion simulations of land use scenarios for a small Loess Plateau catchment. *Catena*, 2003. 54(1-2): p. 289-302.
- [6] Zhou, Q., B. Lees, and G. Tang, *Advances in digital terrain analysis*. 2008: Springer Verlag.
- [7] Tang, G.A., et al., Research on the slope spectrum of the Loess Plateau. *Science in China Series E: Technological Sciences*, 2008. 51: p. 175-185.
- [8] Chen, Y., et al., The Positive and Negative Terrain of Loess Plateau Extraction Based on the Multi-azimuth DEM Shaded Relief [J]. *Scientia Geographica Sinica*, 2012. 1: p. 105-109.
- [9] Mandelbrot, B.B., How long is the coast of Britain. *Science*, 1967. 156(3775): p. 636-638.
- [10] Beyer, H.L., *Hawth's analysis tools for ArcGIS*. 2004.
- [11] Odeh, I., A. McBratney, and D. Chittleborough, Spatial prediction of soil properties from landform attributes derived from a digital elevation model. *Geoderma*, 1994. 63(3): p. 197-214.
- [12] Guoan, T., et al., Simulation on slope uncertainty derived from DEMs at different resolution levels: a case study in the Loess Plateau. *Journal of Geographical Sciences*, 2003. 13(4): p. 387-394.
- [13] Hunter, G.J. and M.F. Goodchild, Modeling the uncertainty of slope and aspect estimates derived from spatial databases. *Geographical Analysis*, 1997. 29(1): p. 35-49.

Figure 1. Preliminary results of spatial fractal dimension for study sites



Generalizing Resolution-assignable DEM Based on Rational-dilation Wavelet Transform and Sampling Theory

Haijiang Wang¹, Qinke Yang^{2,3*}

1. College of Urban and Environmental Science, Shanxi Normal University, Linfen 041004, China; 2. College of Urban and Environment, Northwest University, Xi'an,

Shaanxi, 710127, China; 3. Institute of Soil and Water Conservation Chinese Academy of Sciences Ministry of Water Resources, Yangling, Shaanxi, 712100

Abstract: The digital elevation model (DEM) is widely used in various geographic researches and investigations. However, the scale-effect of the model deeply impacts the suitability and reliability of its application. The studies on the scale-effect of DEM thus have becoming focuses of researches. As these studies require the DEM dataset with continuously-changeable resolutions and uniformly spatial-location base in analysis and evaluation and the present method can not scientifically and systematically meet the required, we propose an effective DEM generalization method to obtain lower-resolution DEM based on higher-resolution DEM.

The method is based on the sampling theory and a kind of wavelet transform. The relation between the horizontal resolution of DEM and its max frequency in frequency domain is firstly analyzed according to the sampling theory which is used in signal resampling as a fundamental principle. We then propose a new method to obtain the DEM with assignable resolution by quantitatively decreasing the highest frequency of the original DEM. After studying the idea of this proposed method, we improve a kind of rational-dilation wavelet transform (RWT) to meet the requirement of the proposed DEM generation method. The original RWT, whose Q-factor can be tuned before decomposition, has a finer time-frequency localization ability than common dyadic wavelet transform. However, its fixing employment of Q-factor in all decomposition level greatly restricts its decomposition freedom in frequency-domain partition, and also the up-sampler and down-sampler in its decomposition destroys its translation-invariant property. We analyze the decomposition and reconstruction of the original RWT, and then construct a new transform scheme that provides a tunable Q-factor in each level and keeps the translation-invariant property as well. Also, this new RWT method is expanded to two-dimensional case by using tensor-product transform approach for image signal processing. After studying and evaluating the freely and finely time-frequency decomposition ability of the constructed RWT, we propose an energy-based threshold processing method used in the decomposition domain of the RWT. The method implements threshold processing to different

frequency-band obtained from the decomposition of the RWT. With the method, the most significant spatial-domain features in the original data are preserved and at the same time, it is ensured that the DEM data obtained can meet the requirement of the sampling theory. The generalization method to generate resolution-assignable DEM is finally obtained.

With the DEM generation method, from a high-resolution DEM, we can obtain a DEM dataset of which the resolutions change from fine to coarse. Moreover, the validity of the assigned resolution, the spatial location consistency and the effectiveness of generalization are all analyzed and evaluated. The result shows the resolution of the obtained DEM are all satisfied with the sampling theory and the ratio of their sampling rate to their max frequency are all very close to that of original high-resolution DEM. Those show the reasonability of the resolution of the obtained DEM dataset. To evaluating the spatial location consistency, we analyze the contour overlay status of the DEM dataset obtained by using the proposed method, and the result shows the overlay status is more reasonable than those of the DEM obtained based on interpolation of multi-scalar topographic map. The generalization effect is evaluated by visually comparing, analyzing hillside images, elevation statistics, slope frequency distribution curves and cumulative slope frequency distribution curves, curvature frequency distribution curves and cumulative curvature frequency distribution curves, total contour lengths and total river network length. The evaluation results show that as the resolution of the obtained DEM changes from finer to coarser, the local detail of terrain is gradually eliminated, while in this process, the overall structure of the terrain is still retained. We even compare our generated DEM data of different resolution with DEM data obtained by interpolation of topographic map, and find that for a certain resolution, the DEM obtained by our method have similar terrain characteristics (including visual observation, elevation statistics, slope frequency distribution curves and cumulative slope frequency distribution curves, curvature frequency distribution curves and cumulative curvature frequency distribution curves, total contour lengths and total river network length) as that of

topographic map interpolation. In addition, we evaluate the generation error of the obtained DEM by analyzing their mean square error. We find the results generalized have desirable generation precision and in most case, their generation errors are lower than those of the interpolated DEM obtained by using conventional interpolation methods (e.g., bilinear interpolation and bicubic interpolation).

In this paper, we study the relation between the spatial horizontal resolution of DEM and its effective max-frequency in frequency domain based on sampling theory. We proposed a DEM generalization method by which one can obtain DEM data with coarse and assigned resolution from original DEM with fine resolution. Our experiment results show that with the method proposed, one can obtain the DEM data which has the goal resolution assigned in advance. Also, the generalization effect of method is reasonable, the spatial-location base consistency of the DEM dataset and the generalization precision is more desirable than other conventional methods. This study provides methodological supports to digital terrain analysis, researches and investigations.

Key words: DEM, generalization, Rational-dilation wavelet transform, Resolution, Q-factor

The elevation error of DEMs caused by grid size

Lei Wang

College of Urban and Environment
Northwest University
Xi'an, China
montez@nwu.edu.cn

Yong qing Long

College of Urban and Environment
Northwest University
Xi'an, China
sjzxlyq@126.com

Abstract—Based on the DEM generated by the full digital photogrammetry and field measurements in Yaojiawangou watershed, Suide, Shaanxi Province, the relationship between the elevation error of GRID DEMs and grid size is discussed. The influence of grid size on the elevation error of DEMs is shown as follows: the elevation on a grid is overestimated in down-slope direction, while underestimated in up-slope direction. As a result, the value of elevation error on a grid is decided by the slope gradient, while the complication of distribution of elevation error is decided by the size of grid. The analysis of elevation error calculated from the DEMs series generated by sampling directly shows that the RMSE and the maximum error of elevation increase with the grid size in the way that is a quadratic function. The maximum error on a grid far exceeds the 2 times of RMSE. Consequently, the grid size of DEMs should be as small as possible according to the precision in the application of DEMs.

INTRODUCTION

As well known, the grid size of DEMs influence the result of terrain analysis seriously [1-6]. However, the way and the extent of the influence are still not clear. In fact, most the changes of terrain parameters along with grid size, such like slope gradient, could be attributed to the changes of grid height along with grid size when the algorithm of those parameters are taken in account carefully. As the most basic attribute of DEMs which is a kind of model to simulate the surface of ground, the heights on the grid themselves don't change once the DEMs were created. However, the change of grid size or sampling interval alter the scope represented by one grid height if one grid is regarded as a flatten surface. Therefore, the error of elevation on one grid will change with grid size. According to the analysis mentioned above, the reason of the change of elevation error could be explained; however, the quantities and the distribution of elevation error caused by grid size should be discussed further. This paper aims to this problem to quantifies the elevation error on one grid and summary the spatial pattern of the elevation error based on the DEM which has a fine grid size and was generated by the full

digital photogrammetry and field measurements in Yaojiawangou watershed, Suide, Shaanxi Province.

BASIC METHOD

A. Data extraction

Use the full digital photogrammetry to create a DEM with 1 meter grid size as the reference data in study area. And then, base on this data; use the method of direct sampling to obtain a DEMs series which have the same vertical precision with varying grid size.

B. Elevation error calculation

Use the DEMs with different grid size in the DEMs series one by one to minus the 1 meter DEM which is taken as "true" value. The result could be thought as the elevation error of the DEMs on every grid

BASIC RESULT AND DISCUSSION

A. Data extraction

Fig.1 shows that the RMSE of Elevation increases with the grid size increasing in the way that is a quadratic function which is very similar with linear relationship. While Fig. 2 describe the relationship between the range of elevation error on one grid and the grid size. It is consistent with the result showed in Fig. 1.

According to the result showed in Fig. 1 and Fig. 2, the RMSE of elevation and the range caused by grid size could be estimated, Although the RMSE of elevation caused by grid size coincident with the specification in the standards CH/T9008.2-2010 and CH/T9009.2-2010[7-8], the maximum error far exceed the 2 times of RMSE which is specification in the standard. In fact, the mean of maximum error on grids is in 2 times of RMSE. The area with big maximum error usually occurs in the part with large slope gradient on the surface.

Fig. 3 shows the relationship among the RMSE, the scale ratio of grid size and the original grid size. The relationship could be represented with the formula as follow:

$$RMSE=0.2386m+0.0826d-0.0137m^2-0.002d^2+0.1738md$$

Where the m is the scale ratio and the d is the original grid size.

This relationship indicates that the result of Fig. 1 is correct no matter how big the sampling interval is. For instance, if the DEM with 5 meters grid size is taken as the original data and is thought as "true" value, the RMSE of elevation of DEM also increase with the increasing of grid size in a way of quadratic function which is similar with the result of Fig. 1.

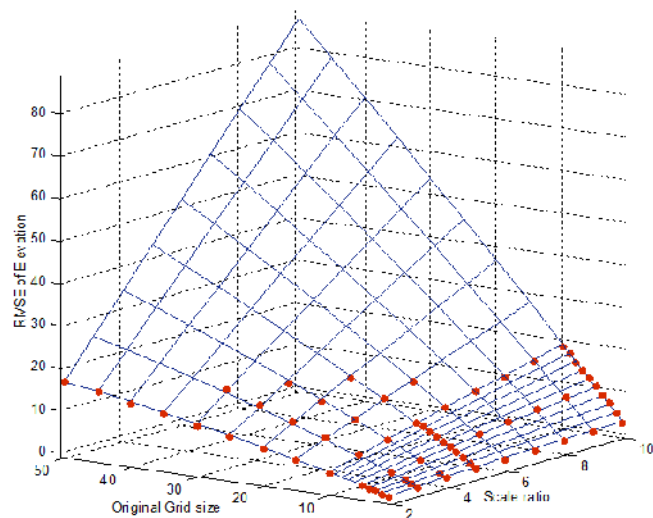


Figure 3 The relationship among the RMSE, the scale ratio of grid size and original grid size

BASIC CONCLUSION

The result mentioned above explained that the elevation error of DEMs cause by grid size could be estimated once the grid size and the complication of terrain are specified. RMSE can only express the global accuracy of DEMs while the local accuracy in the complicated topography areas usually far exceeds the RMSE. In fact, the terrain parameters extracted from DEMs in these areas often influence the final conclusion of terrain analysis. The result of this paper could estimate the elevation error of DEMs caused by the grid size, and could help to make the right choice of grid size according to the precision in the application of DEMs.

REFERENCES

- [1] Horritt M. S.,Bates P. D. Effects of spatial resolution on a raster based model of flood flow. Journal of Hydrology, 2001, 253(1-4): 239-249.
- [2] Thompson James A., Bell Jay C.,Butler Charles A. Digital elevation model resolution: effects on terrain attribute calculation and quantitative soil-landscape modeling[J]. Geoderma, 2001, 100(1-2): 67-89.
- [3] Wu Wei, Fan Yan, Wang Zhengyin, et al. Assessing effects of digital elevation model resolutions on soil-landscape correlations in a hilly area[J]. Agriculture, Ecosystems & Environment, 2008, 126(3-4): 209-216.
- [4] Liu Xuejun and Zhang Ping. Effective Scale of Slope and Aspect Derived from Grid-based Digital Elevation Mode. Geomatics and Information Science of Wuhan University, 2008, 33(12): 1254-1258.
- [5] Wu XianFeng, Liu Changming, Wang zhonggen, et al. Effect of horizontal resolution of raster DEM on drainage basin characteristics. Journal of Natural Resources, 2003, 18(02): 148-154.

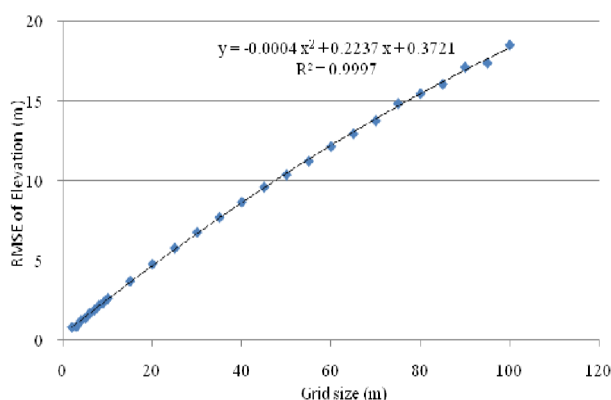


Figure 1. The relationship between the RMSE of Elevation and grid size

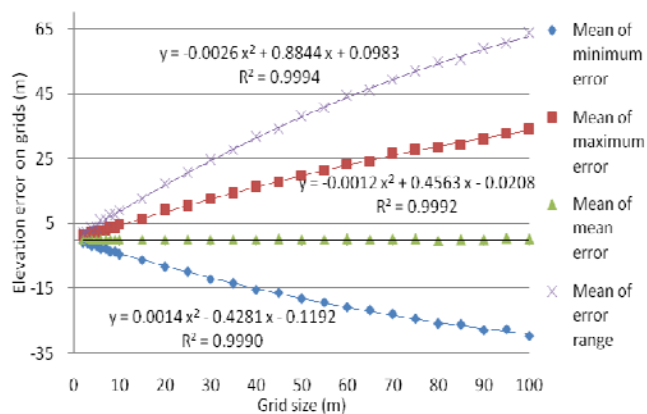


Figure 2. The relationship between the mean range of error on the grid and the grid size

- [6] Sørensen Rasmus, Seibert Jan. Effects of DEM resolution on the calculation of topographical indices: TWI and its components[J]. Journal of Hydrology, 2007, 347(1-2): 79-89.
- [7] CH/T9008.2-2010 Digital products of fundamental geographic information 1:500 1:1000 1:2000 digital elevation models[s]. Beijing: Surveying and Mapping Press, 2010.
- [8] CH/T9009.2-2010 Digital products of fundamental geographic information 1:5000 1:10000 1:25000 1:50000 1:100000 digital elevation models[s]. Beijing: Surveying and Mapping Press, 2010.

Construction of Information Capacity Model for Evaluation on the Land Surface Complexity using Remote Sensing Imagery

Wang XuHong, Zhang zhe, Li Fei
 College of Urban and Environmental Science,
 Northwest University
 No. 129, Taibai Road, BeiLin District, Xi'an 710069, China
 jqy_wxh@163.com

Abstract—An new model--Information Capacity was proposed in this study, which characterizing effectively the land surface (landscape complexity) by used remote sensing imagery. Information capacity is a quantity unit of pixel density information. Center pixel and neighboring pixels will all be taken into account in the calculation of information capacity. The value of Information Capacity is closely related to the image gray levels. The more the gray level is, the greater the information capacity value will be. Thus, information capacity can objectively and effectively characterize the land surface spatial structural complexity. However, the core of the information capacity theory is the selection of the constraint domain and the determination of parameters. In this study, two different constraint domains of information capacity were designed and analyzed.

1 INTRODUCTION

Information capacity is a quantity unit of pixel density information in the field of image processing. It can be used for image quality evaluation by statistics of the cumulative frequency of the local scatter of two-dimensional histogram^[1-3]. However, remote sensing imagery is highly structured and contiguous pixels of spatial domain have strong correlations, which contains abundant information of the land surface structure features and electromagnetic radiation features^[4]. In this model, the features of the local region of pixels are taken into account in the calculation. So it can represent objectively land surface features and spatial characteristics.

2 METHODOLOGY

Calculation of information capacity

Information capacity is obtained by the followed definition: Generally, the cumulative sum of a k-dimensional logarithmic

peak normalized histogram within constraint domain $\omega \subseteq \Omega$, is defined as the information capacity. The cumulative sum of the histogram is logarithmically transformed, which can be expressed as follows:

$$C_{info} = \text{Log}_2[1 + \sum_{\omega} \text{Norm}_{\text{Log}}(G_1, G_2, \dots, G_k)] \quad (1)$$

where C_{info} represents information capacity, the unit is bit. Cumulative constraint domain ω represents measure of the histogram definition domain.

Constraint Domain of Information Capacity

The constraint domain of information capacity is a measure domain of a histogram. If a constraint domain is selected large enough, and the correlation coefficient of the histogram within the domain is higher, the evaluation results of information capacity will be consistent with human vision. However, if the constraint domain is too large, it would loss visual response characteristics. Because the low-frequency information of imagery in the calculation of information capacity has first visual response, the peak value of a normalized histogram should be cumulated and then transformed logarithmically. The constraint domain evaluating on image quality and describing image complexity is expressed as follows:

$$\omega = \left\{ \begin{array}{l} \left| G_1 - \frac{1}{2}(G_{\max} + G_{\min}) \right| \leq T_1 \\ |G_1 - G_2| \leq T_2 \end{array} \right. \quad (2)$$

with the transformation processes of histograms, information capacity can not only be suitable to human vision, but it can also reflect the sensitivity of local gray leap and adaptability of the whole image (as shown in Figure 1-a).

In order to improve the effectiveness of information capacity describing the land surface complexity in flat landform areas, such as Plain, Basin and Loess Plateau. Another algorithm of information capacity constraint domain had been proposed. Taking into account the higher correlation coefficient of gray in a histogram's diagonal domain, the constraint domain is expressed as follows:

$$\omega = \left\{ \begin{aligned} & \left| G_1 - \frac{1}{2}(G_{\max} + G_{\min}) \right| \leq T_1 \\ & T_2 \leq |G_1 - G_2| \leq T_3 \end{aligned} \right. \quad (3)$$

where T_1 represents the difference between maximum and minimum of gray values of the image; T_2 and T_3 represents the difference of gray values of two adjacent pixels. And both T_1 and T_2 are non-negative in the formula. The constraint domain ω is near diagonal within a parallelogram (as shown in Figure1-b).

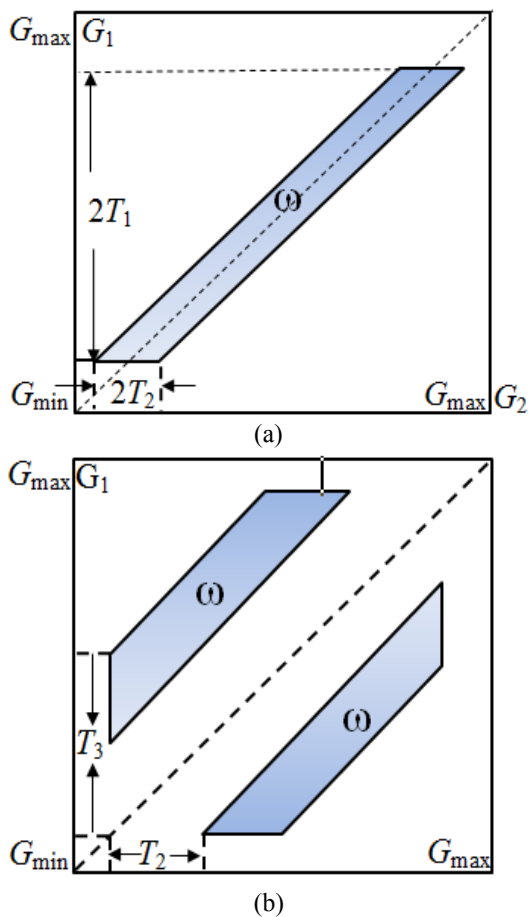


Figure 1. Constraint Domain based on two-dimensional histogram of the remote sensing image (G_1 is the vertical axis, G_2 is the horizontal axis, Fig.1-a, 1-b, indicates Constraint Domain)

3 RESULTS AND ANALYSIS

By elaborating the scientific characterization of information capacity theory, two constraint domains were proposed which can be used to evaluate image quality and describe spatial complexity of the imagery. After experimental examining the ETM+ and SPOT5 imagery, we set the parameters of the two constraint domains, respectively. The algorithm of two constraint domains is developed and optimized. In this study, 56 different landform areas of Shaanxi province were selected as test areas, using ETM+ and SPOT5 as experimental data. Two different calculation method of constraints domain of information capacity were adopted by using comparative analysis and mathematical statistics, which analyzed constraint domain selection and spatial distribution of information capacity. All these experimental results show that information capacity can reflect the land surface spatial structure complexity to a certain extent.

4 CONCLUSION

In this study, information capacity is adopted to analyse remote sensing image information in geosciences. Based on quantitative analysis of information capacity, the relationships between information capacity and surface landscape complexity in different LULC areas have been studied. The main results show that there is strong correlation between information capacity and surface complexity. In principle, information capacity based on a multi-dimensional histogram is an expression of spatial form entropy in a broad sense, reflecting the quantity and proportionality of geographic area system elements. Finally, our results support the hypothesis that information capacity is a new index for characterizing image complexity, and has great potential in characterizing landscape patterns for global environmental studies using remote sensing imagery and describing terrain complexity for digital terrain analysis using Dem.

5 ACKNOWLEDGMENT

Thanks for financially support from the National Natural Science Foundation of China (No. 41071271).

REFERENCES

- [1] Yin,D.K, Yu B.Z., and Dong M.A., 1996, "How to Measure the Thermal Image Quality". *Laser and infrared*, 26, pp. 75-79.
- [2] Yin,D.K and Yu B.Z.,1996, "Image Quality Metrics Based on Multi-dimensional Histogram". *Pattern Recognition and Artificial Intelligence*, 9, pp. 265-270.
- [3] Qu, Y.G., Zeng, G.S., and Xia, D.S., 2002, "Appraise the CBERS - 1 image quality with image information capacity and power spectrum". *Spacecraft Recovery & Remote Sensing*,23, pp. 40-45.
- [4] Wang X.H., Qin H.J., Jia B.J.. 2010 "Analysis on correlation between Information Capacity of NDVI and fractal dimension at different landscape zones," *Proceedings of the 2nd International Conference on Information Science and Engineering: IEEE*, Vol.1, 6446-6450.

Vegetation Pattern Topographic Differentiation of YaoXian county , shaanxi province, China

Li Xiao-yin
Resource and Environment College
University of Jinan
Jinan, China

Abstract—Based on the theory of landscape ecology and plant geography, taking Yaoxian county, Shaanxi province, China as the sample region, with 1:50000 DEM and vegetation map as data source, using DEM terrain analysis technology, GIS spatial analysis technology, and mathematical statistics analysis technology, this paper firstly studied the relationship between vegetation and elevation, slope and aspect, and on this basis, according to elevation, slope, and aspect three terrain factors, divided Yaoxian county into low, medium, high, gentle slope, steep slope, sunny slope, non-sunny slope, comprehensive studied vegetation distribution in different regions under the combination, finally, according to landform classification theory, extracted ditch land, ditch slopes land, gap land between ditch, mountain valley area, loess plateau hilly-gully region and flat area etc. landform type, researched vegetation distribution characteristics under different geomorphic types. Come to the conclusion:

(1) Vegetation show some distribution rules along with the change of elevation, slope and aspect. Vegetation has certain elevation living space, with Green bush and grass in Summer with fallen leaves biggest, followed by farmland, typical meadow, evergreen coniferous forest, with vegetable plot least. Evergreen coniferous deciduous mixed forests distribute in highest region of the terrain, followed by deciduous broad-leaved forest, evergreen coniferous forest. Vegetable plot and orchard distribute in the lower farmland. Farmland, Vegetable plot and orchard mainly distribute in gentle slope area. Other vegetation has less dependence on the slope. In the category of farmland, irrigated land and paddy field are mainly distributed in flat area, and dependence of dry field on slope additionally reduces. Farmland, vegetable plot and orchard is higher to the sun, other vegetation significantly reduce to the sun. In general, natural vegetation is less than artificial vegetation to the sun.

(2) Farmland mainly distribute in gentle slope, low and middle ground. Evergreen coniferous forest and evergreen coniferous and deciduous broad-leaved mixed forest is mainly distributed in steep slope, middle ground and highland. Deciduous broad-leaved forest is mainly distributed in steep slope and highland. Deciduous broad-leaved shrubs are mainly distributed in steep slope and middle ground. Green bush and grass in summer with fallen leaves is mainly distributed in steep slope and lowland. Typical meadow mainly distribute in the highland. Plantation mainly distribute in steep slope and middle ground. Farmland mainly distribute in gentle slope, middle and lower

land. Vegetable plot, orchard are mainly distributed in gentle slope and lowlands.

(3) In flat areas, other kinds of vegetation have its distribution in addition to evergreen coniferous forest, evergreen coniferous and deciduous broad-leaved mixed forests, deciduous broad-leaved forest and typical meadow. Ditch slopes land is mainly distributed by green bush and grass in Summer with fallen leaves and farmland. Gap land between ditch is mainly distributed by farmland, then followed by vegetable plot, Green bush and grass in Summer with fallen leaves. Ditch land is mainly distributed by Green bush and grass in Summer with fallen leaves and farmland. Farmland mainly distributed in gap land between ditch, followed in ditch land s, ditch slopes land. Vegetable plot, orchard only between distributed in gap land between ditch. Deciduous broad-leaved shrubs, green bush and grass in Summer with fallen leaves, plantation mainly distributed in ditch slopes land, followed by ditch lands and gap land between ditch.

(4) In loess plateau hilly-gully region, other kinds of vegetation has its distribution in addition to deciduous broad-leaved forest. Ditch slopes land is mainly distributed by Green bush and grass in Summer with fallen leaves, followed by farmland, deciduous broad-leaved shrubs and plantation. Gap land between ditch is mainly distributed by farmland, followed by Green bush and grass in Summer with fallen leaves, deciduous broad-leaved shrubs and plantation. Ditch land is mainly distributed by Green bush and grass in Summer with fallen leaves and farmland, followed by deciduous broad-leaved shrubs and plantation. Evergreen coniferous forest is mainly distributed in ditch slopes land, followed by Ditch land, gap land between ditch. Evergreen coniferous and deciduous broad-leaved mixed forest is mainly distributed in gap land between ditch, followed by ditch slopes land, Ditch land. Deciduous broad-leaved shrub, plantations and Green bush and grass in Summer with fallen leaves mainly distributed in ditch slopes land, followed by Ditch land, gap land between ditch. typical meadow Mainly distributed in ditch slopes land, followed by gap land between ditch ,Ditch land. farmland is mainly distributed in gap land between ditch, followed by ditch land , ditch slopes land. Vegetable plot is mainly distributed in ditch land, followed by gap land between ditch, ditch slopes land. Orchards are mainly distributed in gap land between ditch, followed by ditch land, ditch slope.

(5) In Mountain valley area, vegetation type per unit area is the most, vegetation coverage is the most reasonable, landscape diversity is the

biggest and the degree of vegetation landscape fragmentation is the largest, followed by the loess plateau hilly-gully region, plat areas. In the loess plateau hilly-gully region, vegetation patch shape is more complex, followed by plat area, Mountain valley area.

Keywords: DEM; GIS; Vegetation; Topographic Differentiation